

# An introduction to Multiphase Pipe Flow

Ruben Schulkes

August 18, 2010

# Contents

<b>1</b>	<b>Introduction</b>	<b>3</b>
<b>2</b>	<b>Preliminaries</b>	<b>6</b>
2.1	Introduction . . . . .	6
2.2	Conservation Equations . . . . .	6
2.3	Interfacial boundary conditions . . . . .	10
2.4	Single phase, laminar flow . . . . .	13
2.4.1	Single phase, laminar flow: hydraulic model . . . . .	15
2.5	Single phase, turbulent flow . . . . .	16
2.5.1	Phenomena of turbulent flow . . . . .	16
2.5.2	Reynolds equations . . . . .	17
2.5.3	Turbulent channel and pipe flow . . . . .	20
2.6	Friction factors . . . . .	24
2.7	Exercises . . . . .	26
<b>3</b>	<b>Multiphase flow phenomena and experimental techniques</b>	<b>28</b>
3.1	Introduction . . . . .	28
3.2	Gas-liquid flow . . . . .	29
3.3	Liquid-liquid flow . . . . .	33
3.4	Averages . . . . .	38
3.5	Measuring Techniques . . . . .	40
3.6	Exercises . . . . .	43
<b>4</b>	<b>Two-Fluid Model</b>	<b>45</b>
4.1	Introduction . . . . .	45
4.2	The phase function . . . . .	45
4.3	Conservation equations for a two-fluid mixture . . . . .	49
4.4	Area-averaged two-fluid model . . . . .	52
4.5	Area-averaged model for stratified flow . . . . .	55
4.6	The drift-flux model . . . . .	60
4.7	Area-averaged model for dispersed flow . . . . .	62
4.8	The Control Volume Method . . . . .	66
4.9	Exercises . . . . .	69
<b>5</b>	<b>Fully developed stratified Flow</b>	<b>71</b>
5.1	Introduction . . . . .	71
5.2	Stratified, laminar flow between two parallel plates . . . . .	71
5.2.1	Stratified, laminar flow: hydraulic model . . . . .	74
5.3	Stratified, laminar flow in a circular pipe . . . . .	75
5.4	Stratified pipe flow: one dimensional models . . . . .	77
5.5	Solutions of the holdup equation and the Lockhart-Martinelli parameter	82
5.6	Stratified, turbulent flow between two parallel plates . . . . .	84
5.7	Exercises . . . . .	88
<b>6</b>	<b>Dispersed Flow</b>	<b>90</b>
6.1	Introduction . . . . .	90
6.2	The motion of a spherical particle in an infinite fluid . . . . .	90
6.3	The effective viscosity of a dilute suspension . . . . .	96
6.4	The formation of drops and bubbles in turbulent flows . . . . .	104
6.5	The cross-sectional distribution of a dispersed phase . . . . .	107
6.6	Exercises . . . . .	110

<b>7 Slug Flow</b>	<b>112</b>
7.1 Introduction . . . . .	112
7.2 The motion of elongated bubbles . . . . .	113
7.2.1 Closure relations for the distribution and drift coefficients . . . . .	116
7.3 The slug front . . . . .	118
7.3.1 Pressure jump at the slug front . . . . .	118
7.3.2 Slug body holdup and gas entrainment . . . . .	121
7.4 Slug statistics . . . . .	124
7.5 The unit slug model . . . . .	127
7.6 Exercises . . . . .	131
<b>8 Interfacial waves</b>	<b>133</b>
8.1 Introduction . . . . .	133
8.2 Stability of stratified, frictionless shear flow . . . . .	133
8.3 Well-posedness of two-fluid equations . . . . .	138
8.4 Linear stability of interfacial waves . . . . .	143
8.5 Exercises . . . . .	147
<b>9 Flow Regime Transitions</b>	<b>149</b>
9.1 Introduction . . . . .	149
9.2 The transition criteria for (near) horizontal flow . . . . .	150
9.3 The transition criteria for vertical flow . . . . .	151
<b>10 High-inclination multiphase flow</b>	<b>153</b>
10.1 Introduction . . . . .	153
10.2 Upward flow . . . . .	153
10.3 Downward flow . . . . .	153

# 1 Introduction

The simultaneous flow of mixtures of different components is probably one of the most common types of flow. Indeed, in most practical systems it is rare to have only one pure component which flows under the action of external forcing. Dust clouds swept up by blowing wind or sediments displaced by flowing rivers are every-day examples of multi-component flow systems. However, in the case where one of the components in the flow has such a low concentration so as not to influence the overall flow in a major way, one may make approximations which allow the flow to be treated as a pure, single-component, system. However relatively small particles in large concentrations, can have a significant influence on large-scale flow structures. This is exemplified by strong wind casts that may precede heavy rain showers.

When multiple components are present and when the motion of one component influences that of the other component (and vice versa) we find that it is no longer possible to study the components separately. It is at this point where we enter the realm of multiphase flow. Multiphase flow is a term which is used to describe multi-component systems in which the interaction between the different components has a major influence on the overall flow structure. A well-known example of multiphase flow is the combined flow of gas and liquid in a pipe. This type of flow is a huge importance in the nuclear industry, the oil industry and the general process industry. In the oil- and process industry it also occurs frequently that two immiscible liquids are transported or processed. In such cases we also use the term multiphase flow although strictly speaking this would be a single-phase, multi-component system.

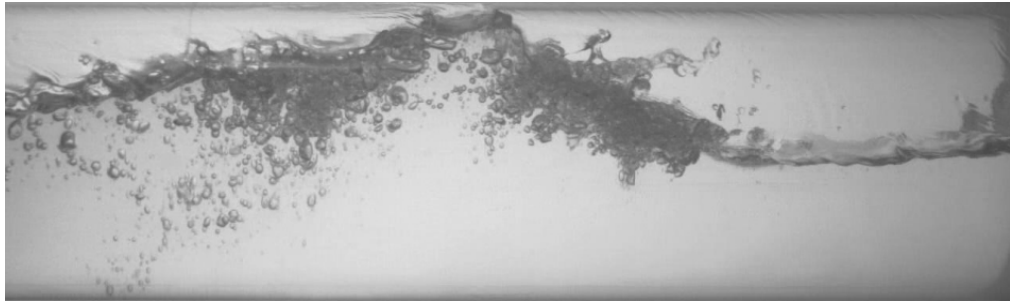


Figure 1.0.1: Wave motion in gas-liquid pipe flow (picture by P. Andersson, IFE).

Surface waves on the ocean, generated by the interaction between ocean and air currents provide another example of multiphase flow. This example is illustrative of the complexity of flow phenomena that occur at the interface separating the two different phases: complex wave motion, breaking waves which entrain gas, one phase dispersed in the other with large variations in the dispersed phase concentration. It is to a large extent these complexities which are central to many of the challenges which we face in dealing with multiphase flow problems, see for example figure 1.0.1.

Single-phase flow problems, while generally difficult enough, often allow simplifications which enable us to obtain information about main features of the flow structure. A nice example of such a simplification in single phase flow concerns turbulent flows in ducts and pipes. While our understanding of turbulent flow is by no means complete, we are able to describe characteristics of turbulent flow in pipes by using our knowledge of boundary layers and by applying simplifying approximations which hold in the case of pipe flow. Unfortunately, there are very few cases in multiphase flow in which the problem can be simplified significantly while still retaining most of the essential physics. The main reason for this is precisely the presence of liquid-liquid or gas-liquid interfaces that can undergo enormous deformations as a result of forces induced by the fluid motion: the position of the gas-liquid or liquid-liquid interface is not known *a priori* and has to be found as part of the solution of the problem. This is a challenging problem even for the

case where there is only one simply-connected interface. In the case where the interface consists of main discrete parts (in the form of drops or bubbles), often modified by the action of turbulent forces, the moving boundary problem becomes fiendishly hard. Our ability to model such flows is limited and even with the most powerful modern computational tools we are currently (and in the foreseeable future) only able to simulate highly simplified systems.

Despite the difficulties mentioned above, it is possible to formulate mass and momentum conservation equations for a multiphase system. Mass and momentum conservation in a multiphase system is, in principle, not different from that in a single phase system. Namely, even in a multiphase flow system it is possible to identify regions in which only one phase is present. For example, in a bubbly flow we have a matrix that consists only of fluid and we have the bubbles that consist only of gas. If we could solve the conservation equations in each of these regions which contain only one phase and apply the appropriate boundary conditions at the interfaces where the two phases meet, our problem would be solved. Quite beside the fact that we are, in general, not interested in knowing in detail what happens in each and every bubble, there are enormous practical difficulties associated with this approach. It is, unfortunately a fact of life that the general equations governing the motion of liquid or gas can only be solved numerically and even then often only by applying simplifying assumptions. Simulations of a gas-liquid systems in which multiple deformable interfaces are present is currently only possible for highly idealized systems. As computational algorithms become more advanced and computers become more powerful, we may expect to be able to resolve ever-increasing details of multiphase flows. Even so, it is not realistic to expect that we will be able to perform fully three-dimensional simulations of multiphase flow systems in a long transport pipe line in the near future.

As an example, consider a 100 m long pipe section which has an inner diameter of 15 cm. A cell size of  $1 \times 1 \times 1$  cm would yield  $O(10^6)$  computational cells. In a transient simulation we would require a numerical time-stepping scheme in order to advance the solution in time. The maximum time step that we can use is dictated by the grid size which is used and by the typical fluid velocity. Indeed, it is usually demanded that over the length of one time step in a numerical simulation, a fluid particle moves a distance which is smaller than the grid size (this is the so-called Courant-Friedrichs-Lewis condition). Assuming a typical velocity of 1m/s it follows that the maximum time step in such a simulation would be  $\Delta t < 0.01$  s. Even with the most powerful computers currently available, a problem of this size will take an enormous amount of time to solve. And even if we were prepared to make the effort we would still be faced with the most difficult problem of all: complex closure relations are required since a cell size of  $1 \times 1 \times 1$  cm is by no means small enough to resolve the (important!) small scale turbulent and dispersed-phase features. This implies that for quite some time to come, multiphase flow simulators that aim at predicting flow regimes, pressure drops etc. in long pipe lines, will be based on simplified models in which details of the dispersed phase and the turbulent flow structure are dealt with in some averaged way. This is the starting point of so-called hydraulic or one-dimensional models. The advantage of this approach is computational speed but the large drawback is that fundamentally three-dimensional phenomena must be squeezed into a one-dimensional straight-jacket. Despite the fact that research into various aspects of multiphase pipe flow has been ongoing for at least 50 years, there are very few books which can be regarded as providing a unified introduction to the area of hydrodynamic aspects of multiphase pipe flow. The earliest, and so far only, unified presentation is given by G.B. Wallis (1969) in the book "One-dimensional two-phase flow". The book gives a thorough exposition of aspects of multiphase flow as known up to the 1960's. However, our knowledge of various aspects of multiphase flow phenomena has advanced significantly since Wallis' book was published. In recent years a number of books have appeared which address different aspects of the multiphase flow. In the recent text by Drew and Passman (1999), "Theory of multicomponent fluids" a mathematical approach is taken in deriving the general conservation equations for a multi-component system. Drew & Passman do

not delve into aspects of multiphase pipe flow but we note that the derivation of the conservation equations as presented by Drew & Passman is closely followed in this course. The book by N. Kolev (2002) "Multiphase flow dynamics 2" is an engineering-like text where numerous multiphase phenomena are discussed, including closure relations. With regards to dispersed flow systems, two excellent and highly readable books have appeared in recent years. In "Fundamentals of multiphase flow" Brennen (2005) introduces details of the physics and modelling issues related to dispersed phase systems. Ishii & Hibiki (2006) present a thorough derivation of the two-fluid equations based on a time-averaging approach. In addition they discuss detailed models for the dispersed phase closure relations.

## 2 Preliminaries

### 2.1 Introduction

The solution of any flow problem requires the following steps. First the relevant conservation equations must be defined. Mass and momentum conservation are always required and in some cases also energy conservation needs to be considered (for example, where temperature effects are relevant). Secondly, appropriate boundary and initial conditions need to be imposed. Finally, when the governing equations and boundary conditions are in place, the equations have to be solved. This last step is often the most challenging since the governing equations are in general nonlinear.

The procedure for solving any multiphase flow problem is in principle not different from that described above. Namely, in each region where only one phase is present (within each bubble and drop, for example), the conservation equations for single phase flow are valid. However, since it is neither feasible nor desirable to model the evolution of each bubble or drop in detail, we mostly work with conservation equations that are averaged in some way. These equations will be derived in later chapters but are, of course, based on the fundamental conservation equations for pure (that is, single phase) fluids. For that reason we start with an outline of the conservation equations for a single phase fluid. Special care will be taken in deriving the boundary conditions that are required at interfaces which separate fluids with different physical properties.

It turns out, as will be seen later, that we often need to rely on known relations derived for single-phase systems when dealing with multiphase flow problems. This is in particular the case when the final closure relations have to be supplied. For this reason that we devote some attention to aspects of flow hydraulics in single phase flow systems in the final sections in this chapter.

### 2.2 Conservation Equations

If we in some way could mark all the particles in a certain blob of fluid (by giving them a specific colour, for example), we would find that in any fluid flow this particular blob of fluid particles would deform as it follows the flow. Provided the blob of fluid is not torn apart, the total number of coloured particles within the blob of fluid will remain constant. This means, for example, that the total mass of the blob containing coloured particles would be constant even though large deformations of the blob may occur, see for example figure 2.2.1. In continuum mechanics, any such connected volume of a given collection of fluid particles has a special name: it is called a *material volume*.

The concept of a material volume is important in the derivation of the conservation equations as was clear from our blob of coloured particles: the mass of a material volume is constant. In deriving the conservation equations we will see shortly that time-derivatives of material volume integrals are required. That is, we have to find expressions for integrals of the form

$$\frac{d}{dt} \int_V \theta dV$$

in which  $\theta$  denotes some intensive property of the fluid (a property is called intensive if it can be defined at a point within the material volume  $V$  and if it is independent of the magnitude of  $V$ : examples of intensive properties are pressure, temperature and velocity). In general,  $\theta$  is a function of position and time while also the shape of the material volume is a function of time. This means that the above time derivative must include two effects: those related to changes in  $\theta$  and those related to shape changes of  $V$ . These two effects are contained within the following result, known as Reynolds transport theorem. The theorem is one of the corner stones in continuum mechanics and it states that

$$\frac{d}{dt} \int_V \theta dV = \int_V \left( \frac{\partial \theta}{\partial t} + \nabla \cdot (\theta \mathbf{v}) \right) dV \quad (2.2.1)$$



Figure 2.2.1: Colliding water drops present nice examples of material volumes - during the collision the drops can undergo large deformations but at all times each drop will contain the same fluid particles (picture by R.W. Park, 1970)

in which  $\mathbf{v}$  is the velocity of the fluid. The first term under the integral sign on the right-hand-side of the above equation deals with temporal variations of  $\theta$  while the second term deals with changes in the volume  $V$  (essentially the flux of  $\theta$  through the surface bounding the volume  $V$ ).

Let us return to the problem of mass conservation. Consider a material volume  $V$ , bounded by a surface  $S$ . If  $\rho$  denotes the density of the material within  $V$  then the total mass contained within  $S$  is given by  $\int_V \rho dV$ . Since  $V$  is a material volume, there is no mass flux through  $S$  (by definition) so that the only change of mass can be due to the presence of mass sources within  $V$ . If we assume, as is usual, that mass is neither created nor destroyed, it follows that

$$\frac{d}{dt} \int_V \rho dV = 0$$

Using Reynolds transport theorem and taking  $\theta = \rho$ , it follows immediately that the equation for mass conservation as given above can be written like

$$\int_V \left( \frac{\partial \rho}{\partial t} + \nabla \cdot (\rho \mathbf{v}) \right) dV = 0$$

Since the above relation holds for any volume  $V$  (we have not put any restrictions on the type of volume to obtain (1)) it follows that the above equation can only be satisfied if the integrand is identically zero, that is

$$\frac{\partial \rho}{\partial t} + \nabla \cdot (\rho \mathbf{v}) = 0 \tag{2.2.2}$$

An interesting special case of the mass conservation equation occurs when the density is constant since in that case the above equation reduces to  $\nabla \cdot \mathbf{v} = 0$ . In its differential form, it may not be immediately obvious that the statement  $\nabla \cdot \mathbf{v} = 0$  is in any way related to mass conservation. However, let us integrate this equation over some volume

$V$  which is bounded by a surface  $S$ . On using the divergence theorem we find that  $\int_V \nabla \cdot \mathbf{v} dV = \int_S \mathbf{v} \cdot \mathbf{n} dS = 0$  showing that the nett flux through the surface  $S$  is identically zero. This then implies that material contained within the volume bounded by the surface will remain there: this is precisely what mass conservation implies.

The procedure as outlined above for obtaining the mass conservation equation may be repeated to obtain the momentum and energy conservation equations. It is, however, beneficial to exploit the fact that a generic conservation equation can be derived where mass, momentum and energy conservation are just special cases of this generic conservation equation. To this end we consider the conservation of the total amount of some extensive property  $\int_V \rho \Psi dV$  (an extensive property is, in contrast to an intensive property, a property that is proportional to the extent of the system: examples are mass, volume and kinetic energy). The time rate of change of  $\int_V \rho \Psi dV$  is then equal to the sum of all sources acting on the volume  $V$ : surface sources acting on the surface  $S$  plus volume (or body) source terms which act on the total volume contained within  $V$ . Mathematically this can be written like

$$\frac{d}{dt} \int_V \rho \Psi dV = \int_S \mathbf{J} \cdot \mathbf{n} dS + \int_V \rho \phi dV \quad (2.2.3)$$

in which  $\mathbf{J} \cdot \mathbf{n}$  denotes a surface source,  $\mathbf{n}$  denotes a unit normal vector to  $S$  and  $\phi$  denotes a general body-source term. In order to arrive at a general conservation equation we apply Reynolds transport theorem (1) to the left hand side of the above equation. In addition we use the divergence theorem to convert the surface integral involving the flux term into a volume integral. After some algebra we find that the conservation equation (2.2.3) may be written in the form

$$\int_V \frac{\partial}{\partial t} (\rho \Psi) dV + \int_V \nabla \cdot (\rho \Psi \mathbf{v}) dV - \int_V \nabla \cdot \mathbf{J} dV - \int_V \rho \phi dV = 0 \quad (2.2.4)$$

Note that we only have volume integrals in (2.2.4) such that all the terms in the equation may be collected under one large volume integral. Since the volume  $V$  in the above equation is arbitrary it follows that the integrand must be identically zero, resulting in the general conservation equation

$$\frac{\partial}{\partial t} (\rho \Psi) + \nabla \cdot (\rho \Psi \mathbf{v}) - \nabla \cdot \mathbf{J} - \rho \phi = 0 \quad (2.2.5)$$

Conservation equations for mass, momentum and energy can be obtained by choosing appropriated expressions for  $\Psi$ ,  $\mathbf{J}$  and  $\phi$ . Note that the mass conservation equation (2.2.2) is obtained from the above equation by taking  $\Psi = 1$  and  $\mathbf{J} = \phi = 0$ . Table 2.1 shows how  $\Psi$ ,  $\mathbf{J}$  and  $\phi$  must be chosen in order to obtain the conservation equations for momentum and energy. In the table,  $\mathbf{T}$  denotes the stress tensor,  $\mathbf{g}$  denotes the gravitational force,  $e = u + \frac{1}{2} \mathbf{v} \cdot \mathbf{v}$  denotes the total energy ( $u$  being the internal energy),  $\mathbf{q}$  denotes the heat flux and  $r$  denotes the distributed heat source per unit mass.

Conservation principle	$\Psi$	$\mathbf{J}$	$\phi$
Mass	1	0	0
Momentum	$\mathbf{v}$	$\mathbf{T}$	$-\mathbf{g}$
Energy	$e$	$\mathbf{T} \cdot \mathbf{v} - \mathbf{q}$	$\mathbf{g} \cdot \mathbf{v} + r$

**Table 2.1** Definition of  $\Psi$ ,  $\mathbf{J}$  and  $\phi$  for given conservation principles.

Using Table 2.1 it follows that the momentum conservation equation is given by

$$\frac{\partial}{\partial t} (\rho \mathbf{v}) + \nabla \cdot (\rho \mathbf{v} \mathbf{v}) = \nabla \cdot \mathbf{T} - \rho \mathbf{g} \quad (2.2.6)$$

where the tensor  $\rho\mathbf{v}\mathbf{v}$  has components  $(\rho\mathbf{v}\mathbf{v})_{ij} = \rho v_i v_j$ . The above expression is nothing more than Newton's second law (mass  $\times$  acceleration = sum of forces) although it may not immediately be recognized as such. To see that the above equation is indeed an expression of Newton's second law we first look at the physical meaning of the stress tensor. On any surface, a stress (force per unit area) can act in three independent directions: normal to the surface and in two independent directions in the plane of the surface. A stress tensor therefore has nine components since each component of the stress must be defined not only by the direction in which it acts but also by the orientation of the surface upon which it acts. Thus, a given component  $T_{ij}$  of a stress tensor denotes the  $i^{th}$  component of a force per unit area on a surface whose outward normal points in the  $j^{th}$  direction, see figure 2.2.2.

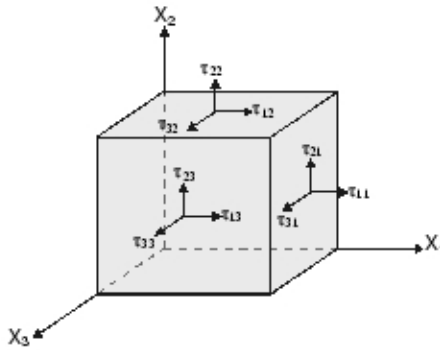


Figure 2.2.2: Shear stresses on an infinitesimal cube whose surfaces are parallel to the coordinate system.

Let us return to the momentum conservation equation (2.2.6). With the meaning of the stress tensor clarified, we note that the terms of the right-hand-side of this equation represent forces acting on a fluid particle: forces due to shear stresses (surface forces) and forces due to the action of gravity (body forces). Furthermore, when we use the mass conservation equation (2.2.2) it is readily found that the left-hand-side of (2.2.6) can be written like

$$\frac{\partial}{\partial t}(\rho\mathbf{v}) + \nabla \cdot (\rho\mathbf{v}\mathbf{v}) = \rho \frac{\partial \mathbf{v}}{\partial t} + \rho(\mathbf{v} \cdot \nabla)\mathbf{v} = \rho \frac{D\mathbf{v}}{Dt}.$$

The material (or convective) derivative  $\frac{D}{Dt} = \frac{\partial}{\partial t} + v_j \frac{\partial}{\partial x_j}$  describes the time derivative in a system which follows the motion of the fluid so that in such a system  $\frac{D\mathbf{v}}{Dt}$  denotes the acceleration of a fluid particle. It is now clear that the terms on the left hand side of (2.2.6) represent mass times acceleration while the terms on the right hand side represent forces acting on a continuum.

It can be shown (see for example Batchelor, 1967) that conservation of angular momentum implies that the stress tensor is symmetric, that is  $\mathbf{T} = \mathbf{T}^T$ . In addition it can be shown that for a Newtonian, incompressible fluid, the stress tensor is of the form

$$\mathbf{T} = -p\mathbf{I} + \mu(\nabla\mathbf{v} + (\nabla\mathbf{v})^T) \quad (2.2.7)$$

in which  $p$  denotes the static pressure,  $\mathbf{I}$  denotes the unit tensor,  $\mu$  denotes the fluid viscosity. It is common to write the stress tensor in the form  $\mathbf{T} = -p\mathbf{I} + \mathbf{D}$  in which  $\mathbf{D}$  is called the *deviatoric part* of the stress tensor. With reference to (2.2.7) it is clear that the deviatoric part of stress tensor is entirely due to the presence of velocity gradients.

In a static fluid, the deviatoric part of the stress tensor is identically zero and the stress tensor reduces to  $\mathbf{T} = -p\mathbf{I}$ . This essentially means that at a given point in the fluid, the normal force (that is, pressure per unit area) which a measuring device would register, is independent of the orientation of the device.

For the special case in which the fluid is incompressible , the mass and momentum conservation equations become respectively

$$\nabla \cdot \mathbf{v} = 0 \quad (2.2.8)$$

and

$$\rho \frac{\partial \mathbf{v}}{\partial t} + \rho(\mathbf{v} \cdot \nabla)\mathbf{v} + \nabla p = \mu \nabla^2 \mathbf{v} - \rho \mathbf{g} \quad (2.2.9)$$

Equation (2.2.9) is often referred to as the Navier-Stokes equation for an incompressible fluid. In the special case where the flow is stationary ( $\frac{\partial}{\partial t} = 0$ ) and where viscous effects can be neglected ( $\mu \nabla^2 \mathbf{v} = 0$ ), the Navier-Stokes equation can be written in a particulary simple form. Namely, using these simplifications and standard identities from vector analysis we find that (2.2.9) reduces to

$$\frac{1}{2} \rho \mathbf{v} \cdot \mathbf{v} + p + \rho \mathbf{g} \cdot \mathbf{x} = \text{Constant} \quad (2.2.10)$$

The above equation is known as Bernoulli's equation and is essentially a statement of conservation of energy along a streamline in the flow.

The mass and momentum conservation equations need to be augmented by appropriate boundary and initial conditions in order to be able to solve these equations. On solid boundaries the boundary conditions are usually easy to specify since we demand that in a viscous fluid, fluid particles close to the boundary will move with the same velocity as the boundary. For example, on a solid, stationary boundary, we take the fluid velocity  $\mathbf{v} = 0$ . The situation is different when the boundary is not solid and deforms under the action of fluid motion - a typical situation at gas-liquid or liquid-liquid interfaces. In a multiphase system we can have many such deforming interfaces and some care has to be taken in specifying the appropriate boundary conditions. The mass and momentum conservation equations (2.2.2) and (2.2.6) still specify the fluid motion in each phase but at the interfaces where two different phases meet, special boundary conditions are required. In the following section, these boundary conditions are studied in some detail.

### 2.3 Interfacial boundary conditions

The general conservation equation (2.2.5) holds in any material volume  $V$  and right up to the boundary  $S$  of  $V$ . However, as we cross the surface we may move from a fluid with one set of intrinsic properties to a fluid with a different set of intrinsic properties. This implies that a step-change in, for example, the density may occur as we cross the surface  $S$ . Thus, the surface  $S$  represents a discontinuity and it is clear that special care needs to be taken in deriving the boundary conditions at the surface  $S$ .

As with the derivation of the conservation equations, here we also require a form of transport theorem akin to Reynolds transport theorem (1). However, the interface separating the two regions with different properties need not be a material surface. Can we apply the transport theorem in that case? It turns out that we can indeed formulate a generalized transport theorem on a domain which is not a material volume. The only restriction which is required, is that the normal component of the velocity of any particle on the boundary is equal to the normal component of the boundary velocity (see Slattery, 1999). Thus we use the generalized form of (1) where we allow for the

fact that the boundary velocity is not necessarily the material velocity. The generalized transport theorem can be written like

$$\frac{d}{dt} \int_{V_u} \theta dV = \int_{V_u} \frac{\partial \theta}{\partial t} dV + \int_{S_u} \theta \mathbf{u} \cdot \mathbf{n} dS \quad (2.3.1)$$

in which  $V_u$  denote a region whose boundary  $S_u$  is moving with a velocity  $\mathbf{u}$  (not necessarily a material velocity). Applying the divergence theorem to write the last term in the above equation as a volume integral and setting  $\mathbf{u}$  equal to the material velocity  $\mathbf{v}$  we see that (2.3.1) indeed reduces to Reynolds transport theorem (1).

We next consider a material region  $V$  which is divided into two distinct regions  $V_1$  and  $V_2$  by a singular surface  $\Sigma$  moving with a velocity  $\mathbf{v}_i$  see figure 2.3.1. The part of  $\Sigma$  contained within  $V$  is denoted by  $\Lambda$ . Since  $V$  is a material region it follows that the boundaries of  $V$  move with the material velocity  $\mathbf{v}$  so that  $\mathbf{u} = \mathbf{v}$  on  $S_{1,2}$ . On the surface  $\Lambda$  we have  $\mathbf{u} = \mathbf{v}_i$ .

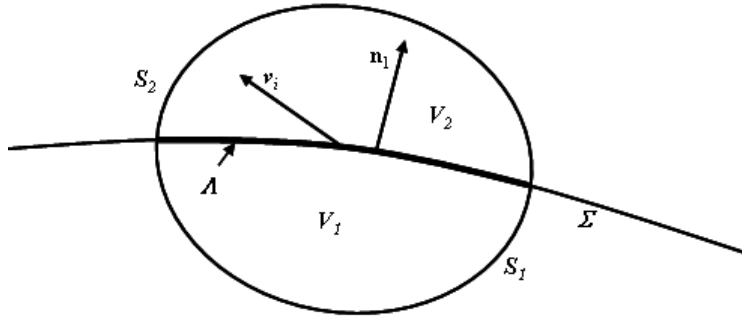


Figure 2.3.1: A schematic diagram showing a singular surface  $\Sigma$  which intersects with a material region  $V$ .

We now apply (2.3.1) in each of the material regions  $V_{1,2}$ . Adding the resulting equations and choosing the unit normal on  $\Lambda$  to be the outward normal to  $V_1$ , the following equation is obtained

$$\frac{d}{dt} \int_{V_u} \theta dV = \int_{V_u} \frac{\partial \theta}{\partial t} dV + \int_{S_u} \theta \mathbf{v} \cdot \mathbf{n} dS + \int_{\Lambda} [\theta] \mathbf{v}_i \cdot \mathbf{n}_1 dS \quad (2.3.2)$$

in which  $[\theta] = \theta_1 - \theta_2$  denotes the *jump* of the quantity  $\theta$  across the singular surface  $\Sigma$ . We now define  $\theta = \rho\Psi$  and we use the conservation equation (2.2.3) combined with (2.3.2), giving

$$\int_{V_u} \left( \frac{\partial}{\partial t} (\rho\Psi) - \rho\phi \right) dV + \int_{S_u} \rho\Psi \mathbf{v} \cdot \mathbf{n} dS - \int_{S_u} \mathbf{J} \cdot \mathbf{n} dS + \int_{\Lambda} [\rho\Psi] \mathbf{v}_i \cdot \mathbf{n}_1 dS = 0$$

The next step in the derivation of the jump conditions, involves shrinking the domain  $V_u$  until it collapses onto the surface  $\Sigma$ . To this end we now consider the volume  $V_u$  to be a pill-box shaped volume as shown in Figure 2.3.2. The pill-box has a thickness equal to  $\delta$  which we let go to zero.

Note that in taking this limit, the volume of  $V_u$  will reduce to zero such that the volume integral in the above equation vanishes. In addition, the bounding surface of  $V_u$  will collapse onto  $\Lambda$  such that the two surface integrals will reduce to surface integrals over  $\Lambda$ . Defining, as before, the unit normal on  $\Lambda$  to be the normal pointing outwards from  $V_1$  it follows that in the limit  $\delta \rightarrow 0$  the integral given above reduces to

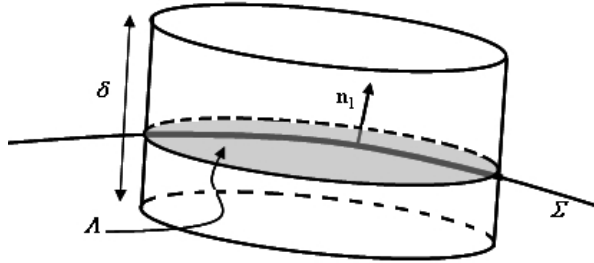


Figure 2.3.2: The *pill-box* volume intersecting the singular surface  $\Sigma$ .

$$\int_{\Lambda} ([\rho\Psi]\mathbf{v} \cdot \mathbf{n}_1 - [\mathbf{J}] \cdot \mathbf{n}_1 - [\rho\Psi]\mathbf{v}_i \cdot \mathbf{n}_1) dS = 0$$

Since the area element  $\Lambda$  is arbitrary it follows that the integrand in the above equation must vanish. This then yields the general jump condition

$$[\rho\Psi(\mathbf{v} - \mathbf{v}_i) - \mathbf{J}] \cdot \mathbf{n}_1 = 0,$$

which the intensive quantity  $\Psi$  must satisfy when the domain on which  $\Psi$  is defined is intersected by a singular surface. In the presence of surface sources  $\mathbf{m}_i$  the jump condition can be shown (see e.g. Slattery, 1999) to be given by

$$[\rho\Psi(\mathbf{v} - \mathbf{v}_i) - \mathbf{J}] \cdot \mathbf{n}_1 = \mathbf{m}_i \quad (2.3.3)$$

Referring to Table 2.1 it follows that for the case of mass conservation ( $\Psi = 1, \mathbf{J} = 0, \mathbf{m}_i = 0$ ) the jump condition reduces to

$$[\rho(\mathbf{v} - \mathbf{v}_i)] \cdot \mathbf{n}_1 = 0 \quad (2.3.4)$$

The jump condition as given above states that the mass flow (per unit area) leaving phase 1 must equal the mass flow (per unit area) entering phase 2. In the special case where  $\mathbf{v} = \mathbf{v}_i$  the surface  $\Sigma$  is a material surface and the jump condition is trivially satisfied. It should be noted that (2.3.4) does not yield any information about tangential velocities at the interface. For viscous fluids we have an additional relation called the *no-slip condition*. This condition states that at the interface separating two viscous fluids, the velocity tangential to the interface is continuous across the interface. Thus,

$$\mathbf{v}_1 \cdot \mathbf{t} = \mathbf{v}_i \cdot \mathbf{t} = \mathbf{v}_2 \cdot \mathbf{t} \quad (2.3.5)$$

in which  $\mathbf{t}$  denotes a unit vector tangential to the interface. The no-slip condition does not follow directly from conservation equations and is essentially a constitutive relation similar to the no-slip condition as specified on solid boundaries.

In the presence of surface tension forces, the interfacial momentum source can be shown to be of the form

$$\mathbf{m}_i = \mathcal{C}\sigma\mathbf{n}_1 + \nabla_S\sigma$$

in which  $\mathcal{C}$  denotes the total curvature of the surface  $S$ ,  $\sigma$  denotes the coefficient of surface tension and  $\nabla_S$  denotes the gradient operator acting along the surface  $S$ . For

flat surfaces, the curvature term is identically zero and the interfacial momentum source is related to surface tension gradients. In the absence of surface tension gradients the interfacial momentum source is governed by the curvature of the interface: a large curvature implies a large interfacial surface force. For the case of momentum conservation we have (see Table 2.1)  $\Psi = \mathbf{v}$  and  $\mathbf{J} = \mathbf{T}$  so that the jump condition becomes

$$[\rho\mathbf{v}(\mathbf{v} - \mathbf{v}_i) - \mathbf{T}] \cdot \mathbf{n}_1 = \mathcal{C}\sigma\mathbf{n}_1 + \nabla_S\sigma \quad (2.3.6)$$

Let us now consider the meaning of the jump conditions as specified above for a number of illustrative cases. We will restrict ourselves to the case in which the interface is a material surface, that is  $\mathbf{v} = \mathbf{v}_i$ . When, in addition, the surface tension forces are completely neglected ( $\sigma \equiv 0$ ), the momentum jump condition reduces to  $[\mathbf{T}] \cdot \mathbf{n}_1 = 0$  which is a statement of continuity of stresses on the interface, see exercise 2.1. Neglecting just the effects of surface tension gradients (which are generally due to concentration gradients of surface-active chemical components) the last term in (2.3.6) vanishes. By writing the stress tensor in the form  $\mathbf{T} = -p\mathbf{I} + \mathbf{D}$  we can separate the components which are normal and tangential to the interface, to obtain

$$[p] - [d_n] = \mathcal{C}\sigma \text{ and } [\mathbf{d}_s] = 0 \quad (2.3.7)$$

In the above equation we have used  $\mathbf{D} \cdot \mathbf{n}_1 = \mathbf{d}_n = d_n\mathbf{n}_1 + \mathbf{d}_s$ , where  $\mathbf{d}_n$  denotes the stress vector (giving the magnitude and direction of the stress on a surface with normal  $\mathbf{n}_1$ ),  $d_n$  denotes the normal component of the stress vector and  $\mathbf{d}_s$  denotes the tangential stress vector. In the case where the fluid is static (for example, a gas-liquid interface in a still fluid) we have  $d_n = \mathbf{d}_s = 0$  and it follows that  $[p] = \mathcal{C}\sigma$ . The normal stress condition therefore shows that in a static situation, there is a jump in the pressure when crossing an interface on which surface tension forces are present. Furthermore, this pressure jump is proportional to the curvature of the interface. The mean curvature of a surface at a specific point is given by  $\mathcal{C} = \frac{1}{R_1} + \frac{1}{R_2}$  in which  $R_1$  and  $R_2$  denote the principle radii of curvature. For the special case of a spherical drop with radius  $a$ , the total curvature becomes  $\mathcal{C} = 2/a$ . Hence, the jump condition (2.3.6) specifies that a jump with the pressure equal to  $[p] = 2\sigma/a$  is experienced when crossing a surface bounding a spherical bubble or drop in a quiescent fluid.

The presence of a deformable interface highlights an interesting characteristic of multiphase flow problems. Namely, even if the volumes of the gas and liquid phases are specified on a given domain, it is by no means always clear where the interface will be situated. The position of the interface is namely determined by the motion in each of the phases as well as by the interfacial conditions. If the one of the phases has sufficient inertia, the gas-liquid interface may break up such that it is not longer simply-connected: bubbles and/or liquid drops may be formed. Even in the case where the gas and liquid phases are entirely at rest, finding the shape of the gas-liquid interface may not be trivial. For example, when surface tension forces dominate gravitational forces, the interfacial curvature may be large resulting in complex gas-liquid interfaces.

## 2.4 Single phase, laminar flow

Before we try to deal with all the complexities which a deformable interface introduces, we first study some simple flow problems. The motion of a viscous fluid between two infinite parallel plates is such a problem. The lower plate is situated at  $z = 0$  while the upper plate is situated at  $z = H$  and between the plates there is a viscous fluid flowing in the positive  $x$ -direction, driven by a constant pressure gradient, see figure (2.4.1). We may assume that, at some point a long way away from the inlet, the flow is developed and fully one-dimensional, giving  $\mathbf{v} = (u(x, z), 0, 0)$ .

The fluid is assumed to have a constant density so that mass conservation implies  $\nabla \cdot \mathbf{v} = 0$ . Together with the uni-directional flow assumption this yields immediately  $u =$

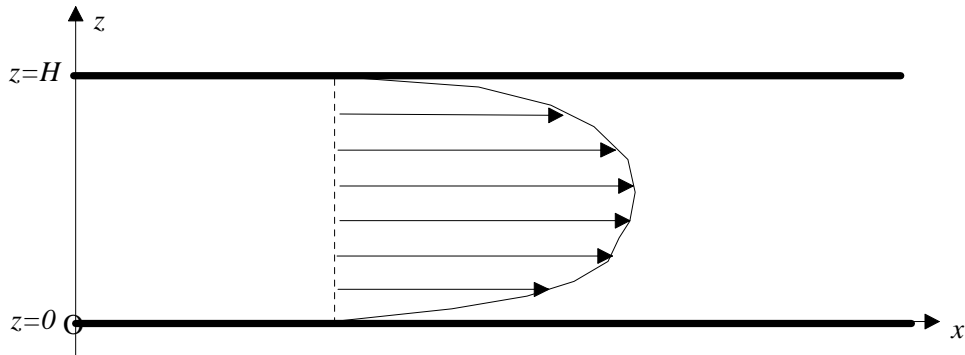


Figure 2.4.1: Geometry of 2-dimensional flow problem.

$u(z)$ . We now turn to the momentum equation as given by (2.2.6). Assuming steady state removes the time-derivative term in (2.2.6) while the non-linear convective term is identically zero due to the unidirectional flow assumption. This then implies that the momentum equation reduces to the simple form

$$\nabla \cdot \mathbf{T} - \rho \mathbf{g} = 0,$$

Using the velocity field  $\mathbf{v} = (u(z), 0, 0)$  in the constitutive relation (2.2.7), it follows that the  $x$ - and  $z$ -components of the momentum equation become respectively

$$-\frac{\partial p}{\partial x} + \mu \frac{\partial^2 u}{\partial z^2} = 0,$$

$$-\frac{\partial p}{\partial z} - \rho g = 0.$$

The  $z$ -component of the momentum equations yields immediately  $p(x, z) = -\rho g z + P(x)$ . Substituting this expression for the pressure into the  $x$ -component of the momentum equation and solving the differential equation for  $u(z)$  yields  $u(z) = -\frac{\Theta}{2\mu} z^2 + Az + B$ . In this expression  $A$  and  $B$  are integration constants and we have introduced  $\Theta = -dP/dx$ . The two integration constants are determined by applying the no-slip conditions at the lower and the upper boundaries. Doing so we finally obtain the desired velocity profile between the two plates, namely

$$u(z) = \frac{\Theta}{2\mu} z(H - z). \quad (2.4.1)$$

Knowledge of the velocity profile allows us to compute a quantity of central interest in pipe or duct flow, namely the stress which the fluid motion exerts on the solid pipe wall. To that end we consider the stress vector  $\mathbf{T} \cdot \mathbf{n}$ . On the lower surface  $\mathbf{T} \cdot \mathbf{n}|_{z=0} = (\mu \frac{du}{dz}, 0, 0)$  while on the upper surface  $\mathbf{T} \cdot \mathbf{n}|_{z=H} = (-\mu \frac{du}{dz}, 0, 0)$ . Using (2.4.1) we find that the  $x$ -component of the stresses on the lower and the upper plate are identical and equal to  $\tau_w = \frac{1}{2}\Theta H$ . The quantity  $\tau_w$  is referred to as the wall shear stress and is evidently directly proportional to the pressure gradient.

In a typical engineering problem, the volume flow of a given fluid is specified and the pressure drop over a given transport length has to be found. Alternatively, the pressure drop is given (based on, for example, pump characteristics) and the volume flow of liquid delivered by the pump has to be computed. In both cases the mean velocity of

the liquid has to be related to the pressure drop. This relation is obtained directly from (2.4.1) since the mean velocity, defined via  $\bar{u} = \frac{1}{H} \int_0^H u(z) dz$ , is given by

$$\bar{u} = \frac{\Theta}{12\mu} H^2.$$

Using the expression for the wall shear stress as obtained earlier, we find that the wall shear stress can be expressed in the form

$$\tau_w = \frac{6\mu\bar{u}}{H} \quad (2.4.2)$$

We see that for the case of laminar flow, the wall shear stress is directly proportional to the mean velocity. This is an interesting result. Namely, in general, the shear stress is proportional to the velocity gradient at the wall and in flow problems with complicated geometries, all details of the flow field have to be resolved in order to find the shear stress. However, in flow systems where the velocity is predominantly in one direction (such as in the case of pipe flow) the wall shear stress can generally be expressed in terms of mean flow properties. This fact forms the basis of hydraulic flow models.

#### 2.4.1 Single phase, laminar flow: hydraulic model

Hydraulic models are of use in flow problems where the geometry is such that a typical length scale in the flow direction is much larger than the length scale perpendicular to the flow direction. With the hydraulic modelling approach in mind, let us approach the problem of flow between parallel plates in a somewhat different manner. A straightforward force balance in the  $x$ -direction dictates that pressure differences that drive the flow are balanced by wall shear stresses. Thus, the pressure force per unit width of the channel, given by  $H(P(x) - P(x + \Delta x))$ , is balanced by shear forces (also per unit width) on the top and bottom plates equal to  $\Delta x(\tau_{top} + \tau_{bottom})$ . Our analysis above has shown that shear stresses on the top and bottom plate are identical, that is  $\tau_{top} = \tau_{bottom} = \tau_w$  (this result also follows directly from our assumption of fully developed flow). Hence, the force balance implies  $H(P(x) - P(x + \Delta x)) = 2\Delta x\tau_w$  which, on taking  $\Delta x \rightarrow 0$ , yields

$$-H \frac{dP}{dx} = 2\tau_w$$

In hydraulic problems it is common to relate the wall shear stress to the mean fluid velocity in the following way

$$\tau_w = \frac{1}{8}\rho\bar{u}^2 f, \quad (2.4.3)$$

in which  $f$  is a dimensionless parameter called the Darcy friction factor. Let us now find out how the friction factor is related to the parameters defining our flow problem. Combining the above equation with (2.4.2) yields immediately

$$f = \frac{48}{Re} \quad (2.4.4)$$

where we have introduced the Reynolds number  $Re = \rho H \bar{u} / \mu$ . The above result shows an important general characteristic of the friction factor: it is dependent on the Reynolds number of the flow and it decreases for increasing Reynolds numbers. This is true for laminar flows, as shown here, but also for turbulent flows as we will see shortly.

For the case of laminar flow in a circular pipe it is easy to show (see exercise 2.3 ) that the friction factor becomes  $f = 64/\text{Re}$  where the pipe diameter is used as the length scale in the definition of the Reynolds number. The friction factor is an important parameter in hydraulic computations for two reasons. Firstly, given the pressure drop and the volume flow rate, the friction factor can be determined experimentally. Secondly, it is a dimensionless parameter. This last fact means that once the friction factor is determined for a given geometry by performing experiments with a given fluid, we can apply the friction factor to flows with other fluids in geometries which have a similar shape. We will come back to friction factors later in this chapter.

## 2.5 Single phase, turbulent flow

The short introduction to turbulence which will be given here serves only to highlight some of the special features of turbulent flow that will be required at later stages. For those interested in a more in-depth and complete treatment of turbulent flows, a few introductory and numerous specialized books are available. The classic text of Tennekes & Lumley (1972) is still one of the most readable introductions to this rather difficult topic. A more in-depth treatment of turbulent flows is given in the books by Hinze (1975) and Monin & Yaglom (1973). Nieuwstadt (1992) has also written a clear introduction to turbulence but, unfortunately, this Dutch book has not been translated into English.

### 2.5.1 Phenomena of turbulent flow

Turbulence is a property of the flow, not of the fluid. A precise definition of turbulence is difficult to give but it is tempting to say that turbulence is that what a laminar flow is not. In a laminar flow, the flow is structured with fluid particles travelling along well-ordered stream lines. One result of this well-orderedness is the fact that the exchange of information in the direction perpendicular to the stream lines is rather slow. For example, if we were able to heat-up a small parcel of fluid on a given streamline then this small patch of warm fluid would flow along the streamline while slowly losing heat to its surroundings through the process of molecular diffusion. This is in stark contrast to what would happen in a turbulent flow. Namely, one of the defining characteristics of a turbulent flow is rapid mixing. This then necessarily implies that, unlike laminar flows, turbulent flows are unordered and chaotic with a relatively fast exchange of information even perpendicular to the main direction of the flow. A nice visualization of this property of turbulence is given in the 500 year old drawing by Leonardo da Vinci shown in figure 2.5.1. Here we see a flow which is *irregular* but not *random*. In the drawing we see large whirls and small whirls which, interestingly, is still one of the starting points of present-day turbulence modelling. The large whirls, or "eddies" as they are usually called, define the macro structure of a turbulent flow. We can define a typical length scale  $\mathcal{L}$  and velocity scale  $\mathcal{U}$  associated with these large eddies. The Reynolds number of these large eddies, namely  $\text{Re} = \mathcal{L}\mathcal{U}/\nu$ , is large which implies that viscous effects are negligible for these eddies.

It will be clear that the large eddies are responsible for one of the defining characteristics of a turbulent flow, namely the rapid mixing or diffusion as mentioned earlier. The turbulent diffusion coefficient  $\mathcal{K}$  is related to the length-scale and velocity-scale of the large eddies via

$$\mathcal{K} \sim \mathcal{L}\mathcal{U}. \quad (2.5.1)$$

Comparing the magnitude of the molecular diffusion coefficient  $k$  with that of the turbulent diffusion coefficient we find  $\mathcal{K}/k \sim \text{Re} \gg 1$ , provided the Prandtl number  $\text{Pr} = \nu/k \simeq 1$ . Clearly, turbulent diffusion completely dominates molecular diffusion which is in line with every-day observations: turbulent flows are efficient at mixing. The mixing processes require energy if the mixing is to be sustained. On the other hand, if no energy is supplied to the flow, the turbulent eddies will rapidly lose their energy



Figure 2.5.1: A drawing by Leonardo da Vinci showing turbulence generated by flow into a pool

and the mixing efficiency will also be reduced. It is therefore natural to ask how fast a turbulent flow will lose its ability to mix, that is, how long will large eddies survive, if no energy is supplied. A large turbulent eddy with a kinetic energy (per unit mass) equal to  $e \sim \mathcal{U}^2$  will lose its energy on a time scale  $T \sim \mathcal{L}/\mathcal{U}$ . Thus, roughly speaking, a turbulent eddy will lose its energy when it has "gone round" once. It follows that the rate of dissipation of turbulent energy, denoted by  $\varepsilon$ , is related to the properties of the large eddies via

$$\varepsilon \propto \frac{e}{T} = \frac{\mathcal{U}^3}{\mathcal{L}} \quad (2.5.2)$$

This is one of the corner stones of turbulence theory and is known as Kolmogorov's relation.

The question is now - what happens to the large eddies when they loose their energy? It turns out that energy is transferred to smaller length-scales by means of break-up of the large eddies. As the eddies get smaller and smaller through repeated break-up of the remaining eddies (a process known as the energy cascade), they are finally so small that viscous effects become completely dominant. At this smallest length scale, termed the micro scale, the kinetic energy of turbulence is dissipated into heat through the action of viscous forces. It is now natural to ask which physical processes determine the length-scale of these final small-scale eddies on which dissipation to heat occurs. We have already found out that viscous effects will be dominant on these smallest length scales so we expect the kinematic viscosity  $\nu$  to play an important role. In addition, we have assumed that dissipation of energy occurs primarily on the smallest scales. This then implies that the dissipation rate  $\varepsilon$  will also play a role. It turns out that both a length-scale and a time-scale can be obtained from these two parameters, namely  $\lambda = (\nu^3/\varepsilon)^{1/4}$  and  $\tau = (\nu/\varepsilon)^{1/2}$ . A velocity-scale for the smallest eddies follows immediately from these two scales, namely  $v = \lambda/\tau = (\nu\varepsilon)^{1/4}$ . When we now compute the Reynolds number for the micro scale we find  $\text{Re} = \lambda v / \nu = 1$ . This interesting result shows that viscous effects completely dominate the micro structure. The length- and time-scales of the micro structure are known as the Kolmogorov micro scales.

### 2.5.2 Reynolds equations

Turbulence is an inherently dynamic phenomenon - something like steady state turbulence does not exist. Turbulent eddies lead to velocity fluctuations which everybody, who has been in an aeroplane, must have noticed (sometimes unpleasantly so). Hence, a description of turbulence requires tools that allow us to deal with these fluctuations in

a satisfactory manner. As a starting point we decompose the velocity field into a contribution which describes some sort of mean flow and a contribution which is indicative of the fluctuations relative to this mean flow. Thus for the velocity field we would write

$$\mathbf{v} = \bar{\mathbf{v}} + \mathbf{v}' \quad (2.5.3)$$

in which an averaged quantity is denoted with an over bar and a dashed quantity denotes the fluctuating part. The type of average which we use is not entirely arbitrary since the averaging operator is required to fulfill a number of conditions. We will suffice by stating that we will use the averaging technique called ensemble averaging . In the next chapter the ensemble average is defined in more detail (together with space and time averages) and there we will also show the properties of the ensemble average as listed in the table below.

<b>1. Linearity</b>	$\bar{c_1 \mathbf{v}_1} + \bar{c_2 \mathbf{v}_2} = c_1 \bar{\mathbf{v}}_1 + c_2 \bar{\mathbf{v}}_2$
<b>2. Average of Average</b>	$\bar{\bar{c_1 \bar{\mathbf{v}}}} = \bar{c_1} \bar{\bar{\mathbf{v}}} = c_1 \bar{\mathbf{v}}$
<b>3. Derivative</b>	$\partial_\xi \bar{\mathbf{v}} = \bar{\partial_\xi \mathbf{v}}$

**Table 2.2** In the above table,  $c_1$  and  $c_2$  are constants and the differential operator  $\partial_\xi$  can be both a time- or a space-derivative.

Taking the average of equation (2.5.3) and using property 2 in table 2.2, it follows immediately that  $\bar{\mathbf{v}'} = 0$ . Let us return to the conservation equations as derived in section 2.2. We assume that the density of the fluid is constant so that mass conservation reduces to the simple equation  $\nabla \cdot \mathbf{v} = 0$ . Substituting (2.5.3) into this equation and taking the average we find

$$\nabla \cdot \bar{\mathbf{v}} = 0 \quad (2.5.4)$$

Using now the mass conservation equation for the sum of the mean and the fluctuating part and subtracting the above result we also obtain

$$\nabla \cdot \mathbf{v}' = 0 \quad (2.5.5)$$

We now turn our attention to the Navier Stokes equation (2.2.9). Due to the fluctuating velocity, it is clear that the pressure will also experience fluctuations. For the pressure we write, in analogy with the velocity,  $p = \bar{p} + p'$ . For the Navier-Stokes equation we use the same procedure as for the mass conservation equation: we substitute (2.5.3) and the expression for the pressure into the equation and we take the average. Note that when taking the averages we make extensive use of properties 1 and 3 in table 2.2. After some algebra we obtain

$$\rho \frac{\partial \bar{\mathbf{v}}}{\partial t} + \rho (\bar{\mathbf{v}} \cdot \nabla) \bar{\mathbf{v}} + \rho \overline{(\mathbf{v}' \cdot \nabla) \mathbf{v}'} + \nabla \bar{p} = \mu \nabla^2 \bar{\mathbf{v}} + \rho \mathbf{g} \quad (2.5.6)$$

Using the mass conservation equation (2.5.5) it is easy to show that the term  $\rho \overline{(\mathbf{v}' \cdot \nabla) \mathbf{v}'}$  can be written like  $\rho \nabla \cdot (\overline{\mathbf{v}' \mathbf{v}'})$  or in component form  $\rho \frac{\partial}{\partial x_j} (\bar{v}'_i v'_j)$ . At this stage it is worthwhile to point out that a new term has appeared in our equation but we have not, at the same time, obtained an extra conservation equation. Of course, a conservation equation for the fluctuating component  $\mathbf{v}'$  is easily obtained: use (2.5.3) in the Navier-Stokes equation and subtract (2.5.6) from the resulting equation. However, by trying to rewrite this equation as a conservation equation for terms of the form  $\bar{v}'_i v'_j$  we soon discover that ever more complex terms appear which involve higher-order products of the fluctuating components  $v'_i$ . We have arrived at the root of what is called the closure problem: the nonlinear convective term in the momentum equation leads to

the appearance of new terms for which we have no equation. Essentially, the closure problem tells us that information which has been filtered out of the equations through the averaging process has to be put back into the problem. This is done by trying to relate the new terms for which we have no equation, to the known variables for which we have equations. This is what turbulence modeling is all about.

Let us now turn our attention to the physical meaning of the term  $\overline{v'_i v'_j}$ . This term can be interpreted as transport in the  $j$ -direction of momentum (per unit mass) in the  $i$ -direction. This type of momentum transport results in a stress and for this reason the term  $\overline{v'_i v'_j}$  is called the Reynolds stress. We can thus introduce a turbulent stress tensor  $T_{ij}^{(t)} = -\rho \overline{v'_i v'_j}$ . The modeling task is now to relate the terms in this stress tensor to the averaged variables  $\bar{\mathbf{v}}$  and  $\bar{p}$ . To that end, let us briefly return to the expression for the stress tensor in a Newtonian fluid, given by (2.2.7). There we saw that this stress tensor can be written like  $\mathbf{T} = -p\mathbf{I} + \mathbf{D}$  where the deviatoric contribution  $\mathbf{D}$  is related to velocity gradients and the pressure term is related to the normal stresses. It is tempting to draw a parallel between the deviatoric tensor  $\mathbf{D}$  and the Reynolds stress tensor since both are related to changes in the fluid velocity (velocity gradients in the case of the deviatoric tensor and velocity fluctuations in the case of the Reynolds stress tensor).

Let us now assume that the normal stresses in the Reynolds stress tensor, namely the diagonal terms  $-\rho \overline{v_1'^2}$ ,  $-\rho \overline{v_2'^2}$  and  $-\rho \overline{v_3'^2}$  contribute little to the transport of mean momentum (which is valid in many flows) so that they can be neglected. We now take a bold step and, in analogy with the form of the deviatoric stress tensor for an incompressible flow, we write

$$T_{ij}^{(t)} = -\rho \overline{v'_i v'_j} = \rho \mathcal{K} \left( \frac{\partial \bar{v}_i}{\partial x_j} + \frac{\partial \bar{v}_j}{\partial x_i} \right) \quad (2.5.7)$$

Note that in the above equation, the turbulent diffusion coefficient  $\mathcal{K}$  has taken the place of the kinematic viscosity. The above relation is known as the Boussinesq closure hypothesis and it gives us precisely what we want: turbulent quantities expressed in terms of the averaged variables. The turbulent viscosity  $\mathcal{K}$  was introduced earlier and was shown to be related to the velocity and length scales of the turbulent eddies. For this reason,  $\mathcal{K}$  is often referred to as the *eddy viscosity*. As yet we have no explicit expression for  $\mathcal{K}$  since (2.5.1) assumes that we have information about the size and velocity of typical eddies - this information is not available. Hence, we have to do some further modeling work to close the problem completely.

It is found that it is not easy to define an eddy viscosity relation which has a general validity and we will therefore restrict this discussion to the so-called Prandtl mixing length hypothesis. For simplicity, we further restrict ourselves to the case to be discussed in the next section, namely a one-dimensional shear flow where  $\bar{\mathbf{v}} = (u(z), 0, 0)$ . According to the Prandtl mixing length hypothesis, the velocity scale  $\mathcal{U}$  associated with the large eddies can be estimated via  $\mathcal{U} \sim \mathcal{L} |\frac{\partial u}{\partial z}|$  so that

$$\mathcal{K} = \mathcal{L} \mathcal{U} = \mathcal{L}^2 \left| \frac{\partial u}{\partial z} \right|. \quad (2.5.8)$$

The length scale of the eddies  $\mathcal{L}$  is still undefined but this length scale turns out to be dependent of the details of the velocity field close to the solid boundary as will be shown in the next section.

In the current and the preceding section, we have presented some of the fundamentals of turbulence modelling. For our purpose it is not necessary to delve into more details since the structure established so far allows us to arrive at the results which we need at later stages. The interested reader can find more information about turbulence modelling in the books mentioned at the start of this section.

### 2.5.3 Turbulent channel and pipe flow

We will now study turbulence in the case where a fluid flows between two infinite, parallel plates, see figure (2.4.1). At a point far from the inlet, we may assume that the *mean* flow is stationary (that is  $\partial/\partial t = 0$ ) and fully developed (that is  $\partial/\partial x = \partial/\partial y = 0$ ). Note that the mean flow direction is parallel to the plates but, since the flow is turbulent, fluctuations may occur in a direction perpendicular to the mean flow direction. When we now apply the mass conservation equation (2.5.4) we obtain immediately that for the mean flow field we have  $\bar{\mathbf{v}} = (\bar{u}(z), 0, 0)$ . We next turn to the momentum equation (2.5.6) and apply the Boussinesq assumption (2.5.7). Like in the case of laminar flow (c.f. section 2.4), we find that the non-linear convective term is identically zero due to the fact the mean flow field is one-dimensional. Without much difficulty it can now be shown that the  $x$ - and  $z$ -components of the momentum equation reduce to respectively

$$0 = -\frac{\partial \bar{p}}{\partial x} + \frac{\partial \tau_t}{\partial z} \quad (2.5.9)$$

in which the total shear stress  $\tau_t = -\rho \bar{u}' \bar{w}' + \mu \partial \bar{u} / \partial z$  and

$$0 = -\frac{\partial \bar{p}}{\partial z} - \rho \frac{\partial \bar{w}'^2}{\partial z} - \rho g$$

Integrating the last equation yields immediately  $\bar{p} + \rho \bar{w}'^2 + \rho g z = P_0(x)$ . Since we have assumed fully developed flow it follows that  $\bar{w}'^2$  is independent of  $x$  and hence  $\partial \bar{p} / \partial x = dP_0 / dx$ .

Symmetry considerations tell us that the shear stress  $\tau_t$  must be zero at the centre of the channel at  $z = \frac{1}{2}H$ . Using this condition allows us to integrate (2.5.9), giving

$$\tau_t = \rho u_*^2 \left( 1 - \frac{2z}{H} \right) \quad (2.5.10)$$

where we have introduced the friction velocity  $u_*^2 = -\frac{H}{2\rho} \frac{dP_0}{dx}$ . From the above equation it follows immediately that the friction velocity is related to the shear stress at the wall via  $\rho u_*^2 = \tau_t(0)$ . Since turbulent fluctuations vanish at the wall, it follows that  $\tau_t(0) = \tau_w$  with  $\tau_w$  denoting the wall shear stress. We note in passing that the relation between the friction velocity and the pressure gradient is nothing other than a simple force balance which we have seen before in section 2.4.

Up to this point the results are exact but in order to obtain information about the velocity profile in the channel, we have to introduce closure relations that help us deal with the Reynolds stress term  $\bar{u}' \bar{w}'$ . In the previous section we were made familiar with the Boussinesq hypothesis, which for the case under consideration reduces the turbulent stress tensor to

$$T_{13}^{(t)} = -\rho \bar{u}' \bar{w}' = \rho \mathcal{K} \frac{\partial \bar{u}}{\partial z}$$

Using the Prandtl mixing length model to give us an explicit expression for the turbulent diffusion coefficient, we end up with  $-\rho \bar{u}' \bar{w}' = \rho \mathcal{L}^2 \left| \frac{\partial \bar{u}}{\partial z} \right| \left| \frac{\partial \bar{u}}{\partial z} \right|$ . Substituting this result into equation (2.5.10) we obtain the following differential equation for the profile of the mean velocity between the plates

$$\mathcal{L}^2 \left| \frac{\partial \bar{u}}{\partial z} \right| \left| \frac{\partial \bar{u}}{\partial z} \right| + \nu \frac{\partial \bar{u}}{\partial z} = u_*^2 \left( 1 - \frac{2z}{H} \right) \quad (2.5.11)$$

The boundary condition required to close the problem is the usual no-slip condition on the lower solid wall, namely  $\bar{u}(0) = 0$ .

It turns out that in turbulent channel flow, three relatively well-defined regions exist with distinct flow characteristics. In what follows, these three regions are discussed in some detail.

### The viscous sub-layer

As pointed out before, very close to the wall, turbulent fluctuations must vanish simply because the fluid velocity tends to zero due to the no-slip condition. This then implies that, close to the wall, the turbulent stress term on the left hand side of (2.5.11) is completely dominated by the viscous term (this is equivalent to stating that the Reynolds number is small close to the wall). Very close to the wall we have  $z \ll H$  and hence it follows that in this region the equation to be solved reduces to the simple form

$$\nu \frac{\partial \bar{u}}{\partial z} = u_*^2$$

with solution

$$\bar{u} = \frac{u_*^2}{\nu} z \quad (2.5.12)$$

We see that in the region very close to the wall, called the viscous sub-layer, the velocity increases linearly with the distance from the wall. When we return to section 2.4 we see that a similar relation was observed in the case of laminar flow (equation 2.4.1). Hence, in the viscous sub-layer the flow resembles the characteristics of laminar flow. The flow is, however, not truly laminar: it turns out that turbulent fluctuations from the region above the viscous sub-layer penetrate into the viscous sub-layer. In the viscous sub-layer it is natural to use  $u_*$  as a velocity scale and, hence, introduce the dimensionless velocity  $u_+ = \bar{u}/u_*$ . From (2.5.12) it follows that a natural expression for the dimensionless length associated with the viscous sub-layer is given by

$$z_+ = z \frac{u_*}{\nu}$$

The dimensionless variables  $u_+$  and  $z_+$  are often referred to as wall variables.

### The wall region

As we move away from the wall, the turbulent fluctuations start to dominate the viscous effects. As a result we can neglect the molecular viscosity term in equation (2.5.11). However, since we are still in the region where the presence of the wall influences the flow, we expect that the size of the eddies is modified by the wall. We therefore write

$$\mathcal{L} = \kappa z$$

in which the constant  $\kappa$  is called the Von Karman constant. Experimentally it is found that  $\kappa \approx 0.4$ . In the wall region we still have  $z \ll H$ , so that the equation to solve becomes

$$\kappa^2 z^2 \left| \frac{\partial \bar{u}}{\partial z} \right| \left| \frac{\partial \bar{u}}{\partial z} \right| = u_*^2$$

which has the solution

$$\bar{u}(z) = \frac{u_*}{\kappa} \ln(z) + u_W \quad (2.5.13)$$

with  $u_W$  being an integration constant. Evidently, in the wall region the velocity profile is logarithmic which is one of the most profound properties of wall-bounded turbulent flows.

We have obtained this fundamental result by applying the mixing length model and assuming that in the wall region the size of the turbulent structures decreases linearly as the wall is approached. The benefit of this approach is that it is rather intuitive. However, it should be pointed out that the logarithmic profile can be recovered without specifying anything about the size of the turbulent structures. In fact Millikan (1939) showed that the logarithmic profile can be obtained by means of matched asymptotics. A natural question which then arises is the following - if the logarithmic profile can be obtained without recourse to the mixing length model, what type of mixing length is obtained when the logarithmic profile is assumed as being the fundamental input? Going back to equation (2.5.11) we find, on using equation (2.5.10) and neglecting the molecular viscosity term, that it can be written like

$$\mathcal{L} \left| \frac{\partial \bar{u}}{\partial z} \right| = \sqrt{\frac{\tau_t}{\rho}}$$

Using now the logarithmic profile as given by (2.5.13) in the above equation and using this equation to compute the mixing length, we find

$$\mathcal{L} = \frac{\kappa z}{u_*} \sqrt{\frac{\tau_t}{\rho}} = \kappa z \sqrt{\frac{\tau_t}{\tau_w}} \quad (2.5.14)$$

We see that a mixing length for the wall region is obtained which is similar to the one used earlier with the difference that the mixing length is modified by the ratio of the turbulent and wall shear stresses. Close to the wall where  $\tau_t \approx \tau_w$  we regain the original model.

### The core region

When we move still further from the wall, the size of the turbulent eddies is no longer dictated by the distance from the wall, but instead, by the overall dimension of the cross sectional flow area. Hence, for the length scale of the eddies we write  $\mathcal{L} = \theta H$  which implies that the size of the eddies in the core region scales with the size of the channel. The solution of the differential equation is easily shown to be

$$\bar{u}(z) = u_H - \frac{2}{3} \frac{u_*}{\theta} \left( 1 - \frac{z}{H} \right)^{3/2} \quad (2.5.15)$$

with  $u_H$  denoting the velocity at the centre line of the channel.

With the velocity profiles in the viscous sub layer, the wall region and the core region known, we have an almost complete description of the velocity profile in a turbulent channel flow. When we go back to equations (2.5.13) and (2.5.15) we note that there are two, as yet undefined, integration constants in these equations, namely  $u_W$  and  $u_H$ . These integration constants are found but "matching" the velocity profiles in the three regions such that a continuous velocity profile over the whole channel cross section is obtained. First consider the overlap between the viscous sub-layer and the wall region. Figure (2.5.2) shows experimental data of the dimensionless velocity profile as a function of the wall coordinate  $z_+$ . We note that the viscous sub-layer is valid in the region  $z_+ < 5$  while the logarithmic profile characteristic of the wall region holds for  $z_+ > 30$ . It turns out that a best fit with experimental data is obtained when we match the two profiles at  $z_+ = 11$ . This then determines the integration constant  $u_W$  and the dimensionless velocity profiles become

$$\begin{aligned} u_+ &= z_+ && \text{for } 0 < z_+ < 5 \\ u_+ &= 2.5 \ln(z_+) + 5 && \text{for } z_+ > 30 \end{aligned}$$

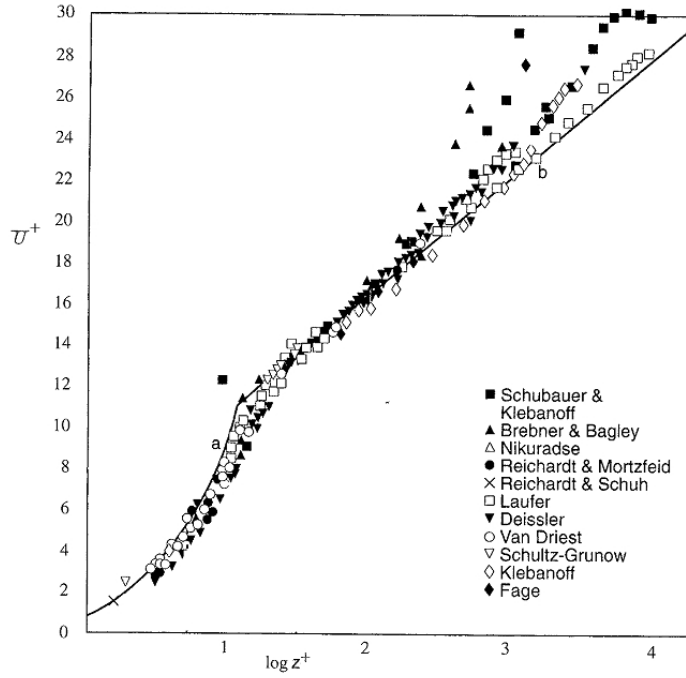


Figure 2.5.2: The dimensionless velocity profile in a turbulent channel flow (from Monin & Yaglom, 1973)

In a similar manner we can determine the integration constant  $u_H$  by matching the velocity profile of the wall region with that of the core region. We choose to match the profiles at  $z = \theta H$  which gives the following equation for  $u_H$

$$u_H = u^* \left[ 2.5 \ln \left( \frac{\theta H u^*}{\nu} \right) + 5 \right] + \frac{2}{3} \frac{u^*}{\theta} (1 - \theta)^{3/2} \quad (2.5.17)$$

The parameter  $\theta$  is still unknown and we need additional experimental data to determine it.

The above equation is known as a logarithmic friction law which essentially relates the pressure gradient to the flow velocity and the channel geometry. In order to see this we first note that (2.5.17) can be written like

$$\frac{u_H}{u^*} = \frac{1}{k} \ln(\text{Re}^*) + C$$

in which  $C$  is some constant and  $\text{Re}^* = Hu^*/\nu$  denotes the Reynolds number. Using the definition of  $u^*$  we can easily reformulate this equation to give

$$-\frac{dP_0}{dx} = \frac{1}{2H} \rho u_H^2 \times f$$

in which the function  $f = 4 \left( \frac{1}{k} \ln(\text{Re}^*) + C \right)^{-2}$  is commonly referred to as a friction factor. Friction factors will be discussed in more detail in the next section and there we will meet some commonly-used logarithmic friction factors. We see that the logarithmic friction factor is intimately related to the velocity profile in a turbulent channel (or pipe) flow - this is important to realise!

The analysis presented above for channel flow can be repeated for the case of pipe flow. It turns out (see Tennekes & Lumley, 1972) that the momentum equation for the case

of pipe flow is identical to equation (2.5.11) when we replace  $H$  with  $2r$ . This implies that all the results obtained for channel flow also hold for pipe flow. In particular it is found that in the viscous sub layer and the wall layer the velocity profiles are identical for channel flow and pipe flow. The reason for this is, of course, that these layers have a thickness which is much smaller than the pipe diameter so that the curvature of the pipe is negligible in the flow regions close to the wall.

## 2.6 Friction factors

In the previous section we have seen that for a number of simple flow geometries (flow between parallel plates and flow in long pipes) it is possible to compute the velocity profile when the flow is fully developed. For these simple cases it is then possible to extract the information which is of most importance in many practical situations, namely the pressure drop as a function of the volume flow rate. It will, however, be no surprise that there are only a few cases where this information can be obtained analytically. Indeed, in many situations of practical interest it is not possible to obtain this information analytically and one either has to rely on numerical techniques (Computational Fluid Dynamics) or on experimental measurements to get this information. Experiments may be expensive to perform and it is natural to search for ways in which data from previous experiments can be used to obtain the information we are after.

Let us, to start with, focus on the problem of finding the pressure gradient in a circular pipe in which only one phase flows. We now ask the question: "on which parameters does the pressure gradient depend?" When a differential pressure measurement is performed over a length  $L$  we may use our knowledge of the physics of fluid flow to guess that the measured pressure gradient will depend on the fluid density  $\rho$ , the fluid viscosity  $\mu$ , the average fluid velocity  $\bar{U}$  and the pipe diameter  $D$  (note that the average velocity is easily determined when we know the volume flow entering the pipe as well as the cross sectional area of the pipe). In addition, it is natural to assume that the wall roughness  $\epsilon$  will also influence the pressure gradient. Therefore, in general we would expect

$$-\frac{dp}{dx} = F(\rho, \bar{U}, D, \mu, \epsilon) \quad (2.6.1)$$

where  $F$  is some, as yet unknown, function. We now use standard arguments from dimensional analysis to rewrite the right hand side in the above equation. To this end we note that  $\rho$ ,  $\bar{U}$  and  $D$  are the parameters with independent dimensions (namely, Length, Time and Mass) while the dimensions of remaining two parameters ( $\mu$  and  $\epsilon$ ) can be expressed in terms of the dimensions of the first three. It is also easy to establish that the dimensions of pressure gradient (Pa/m) can be obtained from the three parameters with independent dimensions via  $\rho\bar{U}^2/D$ . Since the function  $F$  contains 3 parameters with independent dimensions, the 5 parameters in  $F$  yield  $5-3=2$  dimensionless groups and (2.6.1) can be written in the form

$$-\frac{dp}{dx} = \frac{\rho\bar{U}^2}{D}\Phi\left(\text{Re}, \frac{\epsilon}{D}\right) \quad (2.6.2)$$

in which  $\text{Re} = \rho\bar{U}D/\mu$  denotes the Reynolds number. The function  $\Phi$  in the above equation can be regarded as a dimensionless pressure gradient and it should come as no surprise that  $\Phi$  is related to the friction factor which was introduced in section 2.4. There it was also shown that a simple force balance in the case of flow between parallel plates, yields a direct relation between the pressure gradient and the wall shear stress. For the case of a pipe with a constant cross section equal to  $A$  this force balance yields a relation

$$-A\frac{dp}{dx} = \pi D\tau_w$$

Using the force balance as given above together with the definition of the wall shear stress as in (2.4.3), it is easy to show that the function  $\Phi$  and the friction factor  $f$  are related via  $\Phi = \frac{1}{2}f$ . Equation (2.6.2) shows that the friction factor is only dependent on the Reynolds number of the flow and on the dimensionless wall roughness. For smooth walls where  $\varepsilon = 0$  it follows that the friction factor is only dependent on the Reynolds number. Let us now briefly return to section 2.4 where we calculated the friction factor for the case of laminar, fully developed flow. There it was shown (see equation (2.4.4) and exercise (2.3)) that for the case of laminar flow, the friction factor is of the form  $C/\text{Re}$  where the constant  $C$  is dependent on the geometry. What this means in practice is that the friction factor can be determined by doing experiments in one single pipe with a given diameter with one given fluid: for a given wall roughness, the Reynolds number can be varied by changing the velocity of the fluid flowing through the pipe. The friction factor thus obtained can now be used in other pipes with any diameter or any other fluid, provided the dimensionless wall roughness is the same. Clearly it is possible in the case of single phase flows to perform experiments in 'model systems' in order to obtain information about flow characteristics in a system that has different dimensions and/or different fluid properties. The fundamental reason for this property of single phase flows is the fact that the Reynolds number is the only dimensionless group which appears in the Navier-Stokes equations. Flows with equal Reynolds numbers are said to be dynamically similar, implying that the relative importance of the forces acting on the flows (viscous and inertia forces) is the same in the different flows. Unfortunately, as we will see, this is a property only of single phase flows. The existence of the so-called Moody-chart in which the friction factor is plotted as a function of the Reynolds and the relative wall roughness, is essentially a consequence of (2.6.2): for single phase flow the friction factor is completely determined by only these two parameters.

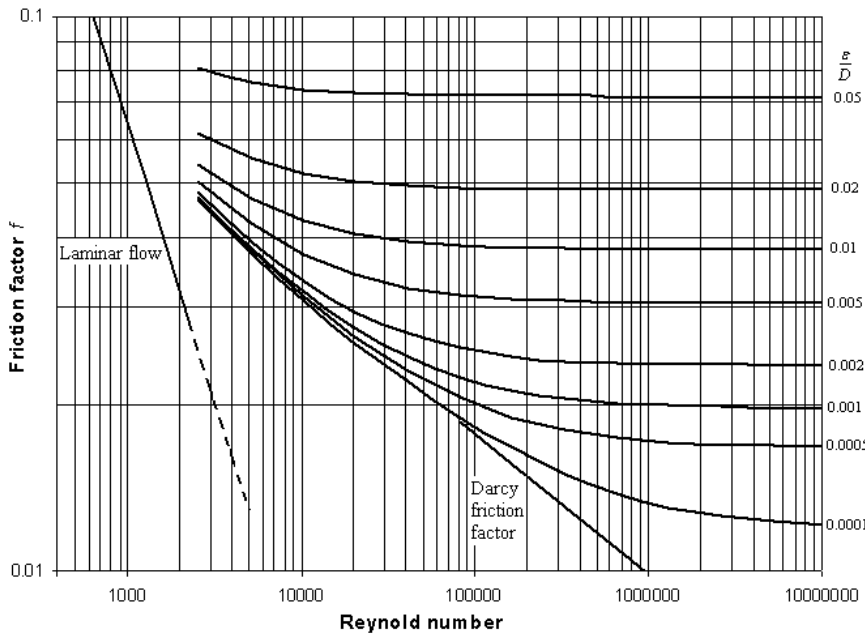


Figure 2.6.1: The Moody chart - the Darcy friction factor as a function of the Reynolds number and the relative wall roughness for round pipes.

At this point it is important to mention that two different friction factors are in use: the Darcy and the Fanning friction factor. These friction factors are related via  $f_{\text{Darcy}} = 4 \times f_{\text{Fanning}}$ . While we will consistently use the Darcy friction factor, it is an unfortunate (and often confusing) fact of life that both the Darcy and the Fanning friction factors are used actively in the literature. In the hydraulic literature, the friction factor is sometimes

referred to as the Chezy coefficient.

Some commonly-used friction factors are listed in Table 2.3. The Colebrook, Haaland and Blasius friction factors are valid only for turbulent flow while the Blasius friction factor is valid only for smooth pipes. Note that the Colebrook friction factor is given implicitly (the friction factor has to be determined iteratively). Only the friction factor for laminar flow is exact, the friction factors for turbulent flow are (at least partly) based on experimental observations.

Friction Factor	Expression
Colebrook Friction Factor	$\frac{1}{\sqrt{f}} = -2 \log_{10} \left( \frac{\epsilon}{3.7D} + \frac{2.51}{\text{Re} \sqrt{f}} \right)$
Haaland friction factor	$f = \left[ 1.8 \log_{10} \left( \frac{6.9}{\text{Re}} + \left( \frac{\epsilon}{3.7D} \right)^{1.11} \right) \right]^{-2}$
Blasius Friction Factor	$f = 0.316 / \text{Re}^{0.25}$
Friction Factor for laminar flow	$f = 64 / \text{Re}$

**Table 2.3:** Some commonly-used friction factors for single-phase pipe flow.

## 2.7 Exercises

**Exercise 2.1** Show that in the case with no mass transfer across a flat interface without surface tension gradients, the jump condition for the momentum equations reduces to

$$[\mathbf{T}] \cdot \mathbf{n} = \mathbf{0}$$

Using the constitutive relation for an incompressible ( $\nabla \cdot \mathbf{v} = 0$ ), viscous flow shows that the above jump condition reduces to

$p^+ - p^- = 0$  and  $\left( \mu \frac{\partial v}{\partial y} \right)^+ = \left( \mu \frac{\partial v}{\partial y} \right)^-$  in the case whether the flow is purely in the  $x$ -direction, parallel to a flat surface in the  $x - z$  plane.

**Exercise 2.2** The curvature of a surface is given by  $C = -\nabla \cdot \mathbf{n}$  where  $\mathbf{n}$  denotes the unit normal to the surface. When the position of a 2-dimensional surface is specified the function  $y = f(x)$ , show that the curvature can be written like

$$H = \frac{d^2 f}{dx^2} / \left( 1 + \left( \frac{df}{dx} \right)^2 \right)^{\frac{3}{2}}$$

Derive an approximation to the curvature in the case where the surface gradients are small.

**Exercise 2.3** Consider a long pipe with a constant diameter  $D$ . The axis of the pipe is placed along the  $x$ -axis. For the case of fully-developed unidirectional flow along the axis of the pipe, write down the momentum equations. Show that under the given assumptions the  $x$ -component of the momentum equation is given by

$$\frac{dP}{dx} = \mu \frac{1}{r} \frac{d}{dr} \left( r \frac{du}{dr} \right)$$

in which  $P = P(x)$  and  $u(r)$  denotes the  $x$ -component of the velocity. Applying the no-slip condition at the solid wall and the symmetry condition at the centre line of the pipe, integrate the above equation to find  $u(r)$ . Compute subsequently the mean velocity,  $\bar{u}$ , and the the wall shear stress. Hence show that the Darcy friction factor is equal to  $f = 64 / \text{Re}$ .

**Exercise 2.4** The profile coefficient is defined via

$$c_v = \frac{1}{\bar{u}^2} \frac{1}{A} \int_A u^2 dA$$

and it measures of the "flatness" of the velocity profile. Show that for the case in which the velocity is equal to a constant over the cross section  $A$ , we have  $c_v = 1$ . Use the velocity profile and the mean velocity found in the previous exercise to show that for laminar flow the profile coefficient is equal to  $c_v = \frac{4}{3}$ . For single phase turbulent flow we typically have  $c_v \approx 1.1$ .

**Exercise 2.5** In the operation of subsea oil fields, chokes are operated using hydraulics. Suppose that the length of the hydraulic line is 250km and that the internal diameter of the line is 2cm. The hydraulic fluid in the line has a density of  $800\text{kgm}^{-3}$  and a viscosity of  $10\text{cP}$ . If it is possible to establish a pressure difference of 700bar over the total length of the line, compute the mean velocity of the hydraulic fluid in the line. Assuming the flow to be laminar (what is the Reynolds number?), show that the maximum velocity of the hydraulic fluid is twice the mean velocity..

**Exercise 2.6** Suppose water flows through a pipe at a volume flow rate equal to  $100\text{m}^3\text{hr}^{-1}$ . The pipe has an internal diameter of 15cm and a wall roughness equal to  $2 \times 10^{-5}\text{m}$ . Compute the Reynolds number and the Haaland friction factor. Hence compute the pressure gradient. Compute the pressure gradient once again but now using the Blasius friction factor.

### 3 Multiphase flow phenomena and experimental techniques

#### 3.1 Introduction

The complexity of multiphase flow problems is such that we still rely heavily on experimental measurements in order to obtain insight into flow structures and phenomena which can not be predicted by present-day models. By doing experiments in virtually any system containing different phases (gas/liquid) or components (liquid/liquid), one is often struck by the bewildering complexity of the flow. The presence of a deformable interface (gas-liquid or liquid-liquid) means that different flow structures (so-called, flow regimes) may be observed: dispersed flow at high flow rates and stratified flow at low flow rates, for example. Before we attempt to model different aspects of multiphase flow, it is instructive to spend some time discussing the different phenomena that are observed in experiments. In this chapter we shall therefore focus on experimental observations related to different aspects of multiphase pipe flow. In addition, we will discuss some measuring techniques that are often applied in multiphase flow experiments. The reason for doing this is that most measurement techniques yield some kind of space, time or ensemble average of velocity, density or pressure measurements. There is, therefore, a natural coupling between the equations that are to be derived later and the measured quantities which one obtains from experiments.

Before we consider multiphase flow phenomena and experimental techniques, it is interesting to look at the multiphase flow problem from a completely different angle. In section 2.6 we considered the problem of finding the pressure drop for the case of single phase pipe flow. Using arguments based on dimensional analysis we found that for the case of single phase flow, the pressure drop was only dependent on two dimensionless parameters: the Reynolds number and the dimensionless wall roughness. This dimensional analysis is supported by experimental measurements leading to the well-known Moody chart shown in figure 2.6.1. It is obvious to attempt a similar analysis when dealing with multiphase pipe flow. For example, for the case of stratified gas-liquid flow in a pipe we can once again ask the question "on which parameters does the pressure gradient depend?" Now we have two different fluids flowing in the pipe so it is reasonable to expect that the parameters related to the different fluids (that is density, viscosity, velocity) influence the measured pressure gradient. In addition interfacial waves may occur and these will also influence the pressure gradient. This implies that the surface tension coefficient  $\sigma$  and the gravitational constant  $g$  will have to be included in our parameter list. Finally, it will be evident that the pipe inclination  $\theta$  will be important. Hence we obtain

$$\frac{dp}{dx} = F(\rho_L, v_L, \mu_L, \rho_G, v_G, \mu_G, D, \epsilon, \sigma, g, \theta)$$

The 11 parameters in the function  $F$  contain only 3 independent dimensions (Mass, Length and Time) so that  $10 - 3 = 8$  dimensionless groups are obtained! Without having any knowledge of multiphase flow phenomena it is easy to draw one immediate conclusion: the equivalent of a Moody chart for multiphase flow is unlikely to exist. Namely, even if it was possible to find meaningful dimensionless groups, constructing a Moody chart for a two-phase system would entail performing so many experiments that identifiable surfaces in a 8-dimensional space would be obtained. This is clearly an unrealistic task.

All this is quite beside the fact that meaningful dimensionless groups are very problem-dependent. As an example we take the influence of surface tension coefficient in problems where the governing length scale is denoted by  $L$ . Four commonly-used dimensionless groups involving the surface tension coefficient are the Bond or (Eötvös) number  $\rho g L^2 / \sigma$ , the Weber number  $\rho L v^2 / \sigma$ , the Ohnesorge number  $\mu / \sqrt{\sigma \rho L}$  and the Capillary number  $\mu L \dot{\gamma} / \sigma$ ,  $\dot{\gamma}$  denoting the shear. The Bond number represents the ratio between gravitational and

surface tension forces and is a relevant parameter in small-diameter pipes. In the case of bubbly flow, the bubble size is determined by the ratio between inertia and surface tension forces and hence the Weber is the relevant dimensionless group (the length scale being the bubble diameter). The Ohnesorge number represents a balance between viscous, surface tension and inertia forces and is relevant when a liquid is dispersed (the length scale being the drop diameter). Finally, the Capillary number is a ratio of viscous shearing forces and surface tension forces, important when considering drop/bubble formation in a strong shearing flow (the length scale being the drop/bubble diameter). We come to the conclusion that a general application of dimensional analysis in multiphase flow is unlikely to be successful since details of the flow have to be known before meaningful dimensionless groups can be identified. Many researchers have (independently) reached this conclusion.

In the following sections, various multiphase flow phenomena will be presented. There it will become clear that the presence of a deformable gas-liquid or liquid-liquid surface is one of the principal reasons behind the fact that dimensional analysis, as a general tool, is of limited value in the area of multiphase flow.

### 3.2 Gas-liquid flow

Gas-liquid flow is the most-studied type of all multiphase flow systems. Gas-liquid flow also exhibits one of the most striking properties of multiphase flow systems, namely different types of flow regimes. In figure 3.2.1 we show the most common flow regimes observed in a co-flowing gas-liquid system in horizontal and vertical pipes. Let us first consider the case of flow in horizontal pipes. It turns out that for a given gas/liquid system, different flow regimes occur for different relative combinations of the volume flow of each phase.

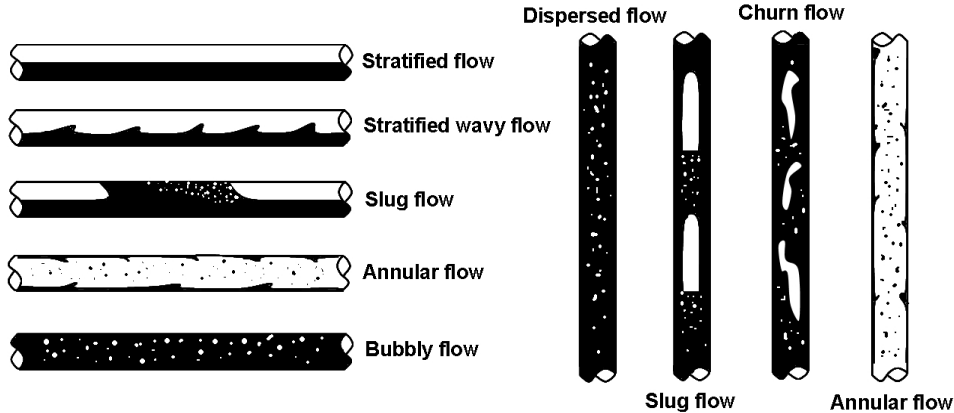


Figure 3.2.1: Flow regimes observed for horizontal and vertical gas-liquid pipe flow.

For example, at low values of the gas and the liquid flow rates, a situation is observed in which the gas and liquid are nicely separated, each flowing in the same direction but with different velocities. For horizontal flows, the least viscous phase (the gas) usually flows faster than the more viscous phase (the liquid). This implies that at the surface separating the two phases there is a shearing force. When this shearing force becomes large enough, waves will occur at the gas-liquid interface. Depending on the physical properties of the liquid phase and on the velocity difference between the gas and the liquid phase, the waves may be nice and regular or may be more chaotic. For relatively large shearing forces, the waves will start to overturn or break. The physics here is similar to what can be observed on the surface of a lake when the wind picks up: waves

with increasing amplitudes form and at some point white tops appear, the unmistakable sign of wave-breaking.

Under the right conditions, wave amplitudes become so large that the wave blocks the cross section of the pipe (see figure 7.1.1). When this happens, the pressure behind the blockage builds up since the gas which was passing over the liquid, suddenly finds its path blocked. Due to the pressure difference over the liquid plug, the plug will accelerate and grow in size by scooping-up slower-moving liquid ahead of the plug: a liquid slug is generated.

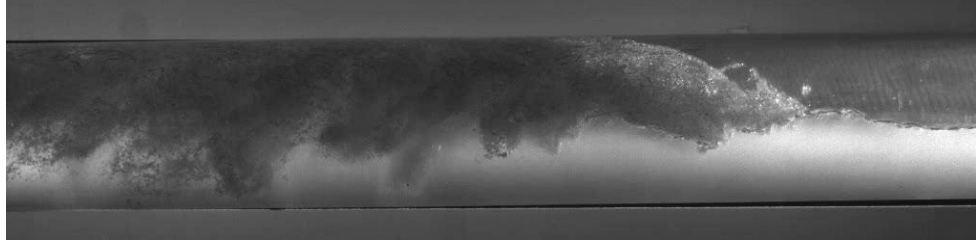


Figure 3.2.2: Gas entrainment at the slug front (picture by P. Andersson, IFE).

The process of slug formations is exceedingly rapid and many details are still poorly understood. Once a slug is formed, a liquid plug starts propagating through the pipe. For a stable slug to exist, the velocity of the slug front and the slug tail have to be identical. This does not mean, however, that the front and the tail of a slug look similar. While the tail of a slug is often well-defined, the slug front may be difficult to locate exactly due to the fact that it often consists of a long frothy region. The slug front can be regarded as a propagating, breaking wave where the over-turning motion of fluid may lead to the capture of a sizable amount of gas, see figure 3.2.2. This process is called gas entrainment, probably one of the most difficult and least understood processes in multiphase flow. Slug flow in which no gas entrainment occurs is called elongated bubble flow. This is a flow pattern which is often visible in a garden hose where discrete pockets of air are transported by the liquid phase.

In the case where the volume flow rate of gas is much larger than that of liquid, a flow pattern called annular flow may occur. Annular flow can be regarded as a type of stratified flow with the exception that in the case of annular flow (most of) the inner circumference of the pipe is covered with a thin layer of liquid. For annular flow to occur, the gas velocity must be significantly larger than the liquid velocity. This leads to large shear stresses at the gas-liquid interface and, as a consequence, a chaotic and rough interface. As a result, a significant degree of liquid is sheared off the interface and is transported in form of droplets in the fast-moving gas core. In the case where the liquid flow rate dominates the gas flow rate, something called dispersed bubble flow occurs. In this case, the turbulence forces in the liquid phase break up the larger pockets of gas and a dispersion of small gas bubbles is formed.

As was discussed in the preceding paragraphs, the flow regimes as shown in figure 3.2.1 are to a large extent (but not solely) determined by the relative volume flow rates of each phase. In figure 3.2.3 we have plotted a so-called flow regime maps for horizontal and vertical flow. These maps are representative for gas-liquid systems in relatively small pipes (diameters less than 10cm) and physical properties similar to that of air and water at atmospheric conditions. The units on the axis in the flow regime maps are the often-used superficial gas and liquid velocities. These are defined via  $U_{SG} = Q_G/A$  and  $U_{SL} = Q_L/A$  with  $Q_G$  and  $Q_L$  denoting the gas and liquid volume flow rates and  $A$  denoting the total cross sectional area of the pipe. We see that different flow regimes occur in well-defined areas on the each map but that the maps for horizontal and vertical flow are markedly different. One benefit of this type of map is that it represents a nice visualization of the different regimes that may occur. The large drawback of these maps is that the boundaries between the different flow regimes are dependent on the physical

properties of the liquid and the gas phase (in particular the viscosity and the density) and on the inclination of the pipe (recall that a complete description of multiphase flow requires the identification of surfaces in a 8-dimensional space)

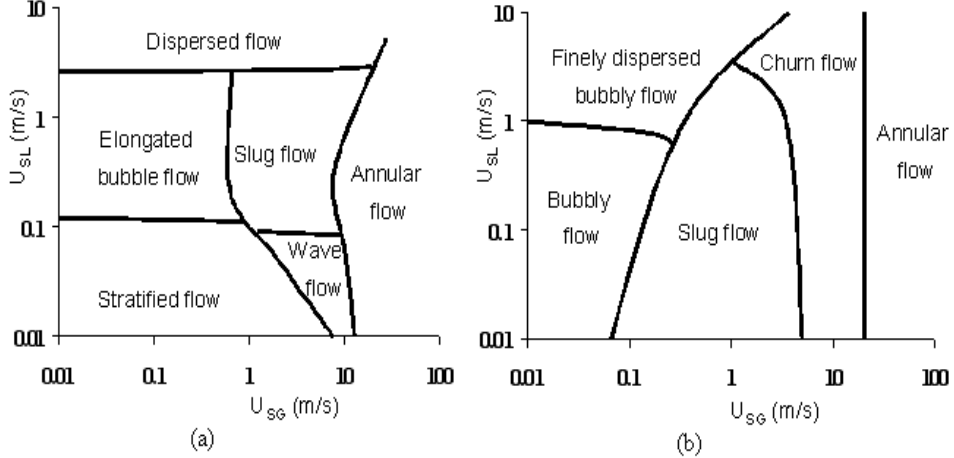


Figure 3.2.3: Flow pattern maps for horizontal (a) and vertical (b) gas-liquid pipe flow.

The inclination of the pipe has a big influence on the flow regimes and its boundaries. When going from horizontal to vertical pipes, entire flow regimes disappear (stratified, and elongated bubble flow) while a new regime (churn flow) appears. It is an interesting fact of life that flow pattern boundaries are very dependent on the inclination of the pipe when this inclination is in the interval  $[-10^\circ, 10^\circ]$ . Outside this range the effect of inclination is much less pronounced. This relates in particular to the boundary between stratified and slug flow. In order to understand why this is so, we consider a quantity called the liquid holdup. The liquid holdup is nothing other than the fraction of liquid in a given section of a pipe. Using density measurements it is possible to measure the liquid fraction as a function of time at a given cross section of the pipe: this provides the so-called the in-situ liquid holdup. In most flows, the in-situ holdup will be time-dependent due to, for example, wave motion at the gas-liquid interface. An average holdup can be obtained by taking some average of the time-dependent signal. It will be no surprise that the average liquid holdup is very dependent on relative flow rates of gas and liquid, pipe inclination and physical properties of both the gas and the liquid. When we measure the average liquid holdup as a function of the pipe inclination for given input liquid fractions, we obtain data as shown in figure 3.2.4.

We see that the liquid holdup is very dependent on the pipe inclination when the pipe is nearly horizontal. For inclinations larger than 30 degrees the holdup hardly varies. It is important to note that the holdup which is measured, is in almost all instances significantly different from the input liquid fraction. The physical reason for this is the velocity difference between the gas and the liquid phase, the so-called slip. Once the average in-situ holdup is known, the average in-situ phase velocities can be determined. For example, if in a stratified flow the average liquid holdup is found to be  $H_L$  then the in-situ liquid velocity is equal to  $u_L = U_{SL}/H_L$ . The in-situ gas velocity can be determined likewise and subsequently the slip ratio  $S = u_G/u_L$  can be determined. For upward or horizontal flows, the slip ratio is generally larger than unity while for downward flows the slip ratio may be less than unity.

Due to the difference in velocity between the different phases, there is a shearing force at the surface separating the gas and the liquid phases. When the gas moves faster than the liquid (that is, when  $S > 1$ ), the liquid is dragged along by the gas phase. When the pipe has an upward inclination, gravity will act to pull the liquid phase downwards. Thus, the total force dragging the liquid up the inclined pipe is now reduced due to the

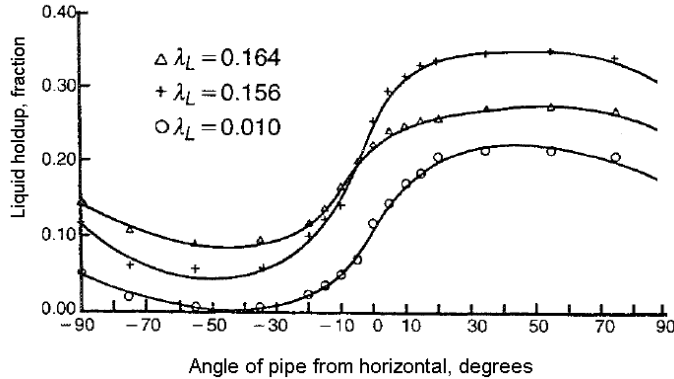


Figure 3.2.4: The liquid holdup as a function of the pipe inclination for different values of the input liquid fraction as indicated in the plot (Beggs & Brill, 1973)

action of the gravitational force. As a result, the liquid moves slower. With a constant volume flow of liquid and conservation of mass, a lower in-situ liquid velocity implies that the cross section of the pipe occupied by the liquid phase must increase. In other words, the liquid holdup increases. When the pipe is inclined downwards, the opposite will happen: gravity works in the same direction as the shearing force of the gas and the liquid holdup may be less than the input liquid fraction.

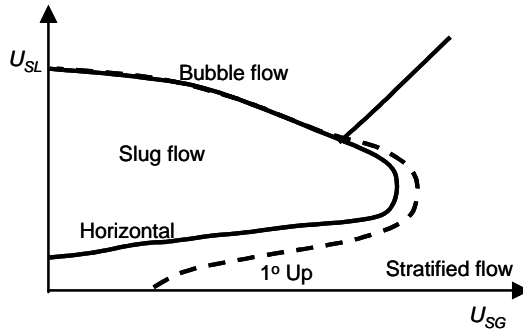


Figure 3.2.5: The influence of pipe inclination on the boundary separating stratified and slug flow.

We have seen that the flow pattern map is significantly different for horizontal and vertical pipes. How does the flow pattern change when the pipe is inclined only slightly? Figure 3.2.5 shows the change in the slug flow boundary when the pipe is inclined upwards by 1 degree. We observe a significant reduction of the region in which stratified flow is observed while the slug flow region is increased equivalently. The physical reason for the increasing occurrence of slug flow for upwardly inclined pipes is very much related to the strongly increasing liquid holdup for slightly inclined pipes. Namely, the increased liquid holdup means that the area available to the gas phase is reduced equivalently. For a constant volume flow rate of gas, a reduced area implies an increasing gas velocity. We now have two effects which enhance the possibility of slug flow occurring. To start with we have increased the relative velocities between the gas and the liquid phases, leading to increased shear at the gas-liquid interface and therefore an increase in shear-induced wave motion. Secondly, the gas-liquid interface has moved closer to the top of the pipe. This then means that waves which are generated, will more easily lead to liquid blockages which may grow into slugs.

The liquid holdup was shown to be very dependent on the inclination of the pipe but

it should be no surprise that the gas velocity also influences the holdup. Through the shearing motion at the gas-liquid interface, momentum is transferred from the gas to the liquid (when the gas moves faster than the liquid) implying an increasing liquid velocity. When the volume flow of the liquid is held constant, a faster moving liquid means that the liquid holdup must decrease. Therefore, an increasing gas velocity must lead to a decreasing liquid holdup. Experimental measurements of this effect are shown in figure 3.2.6. Important quantities which are related to the liquid holdup are the gas-oil-ratio, or GOR, defined via  $GOR = U_{SG}/U_{SL}$  and the liquid fraction, defined via  $X = U_{SL}/(U_{SL} + U_{SG})$

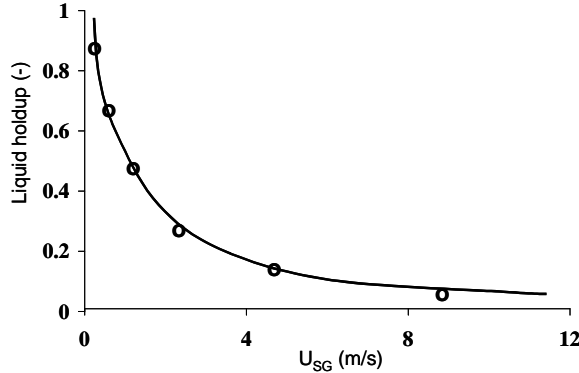


Figure 3.2.6: The measured liquid hold-up as a function of the superficial gas velocity. The liquid volume flow is held constant

The flow regime diagram in figure 3.2.3 shows that for sufficiently high superficial gas velocities, annular flow will occur. The transition from stratified (wave) flow to annular flow is, however, a gradual process. As the gas velocity increases, the gas-liquid surface deforms such as to minimise the surface area of the gas in contact with the liquid relative to the flow area available to the gas. This means that the gas-liquid surface becomes increasingly curved such that the cross sectional flow area occupied by the gas phase becomes increasingly circular. Indeed, for a circular cross section, the ratio of the circumference and cross sectional area is minimal. In this manner the gas and the liquid is transported with a minimum loss of energy (minimal pressure loss). In figure 3.2.7, measurements of the increasing curvature of the gas-liquid interface are shown.

In addition to the inclination of the pipe, physical properties also influence the boundaries separating the flow regimes in the flow regime diagram. To illustrate this we look at the influence of the density on the flow regime boundaries. Figure 3.2.8 shows that with increasing pressure (that is, increasing gas density), the region in which slug flow occurs is strongly reduced while regions with bubble and annular flow increase in size. The reason for the marked increase of the region with annular flow can be related to the increasing shear at the gas-liquid interface when the density increases. Namely, the interfacial shear is proportional to the density of the gas. Thus, when the interfacial shear is increased, the transfer of momentum from the gas to the liquid phase increases so that the liquid velocity increases. With a constant volume flow rate for the liquid phase, an increase in the liquid velocity means that the area occupied by the liquid decreases. This then means that the mean thickness of the annular film of liquid decreases and hence, it becomes more difficult to generate large-amplitude waves which will form blockages, leading to slugs.

### 3.3 Liquid-liquid flow

In the previous section we have seen that gas-liquid flow exhibits different flow regimes. We have also seen that the flow regime boundaries are very dependent on pipe inclination

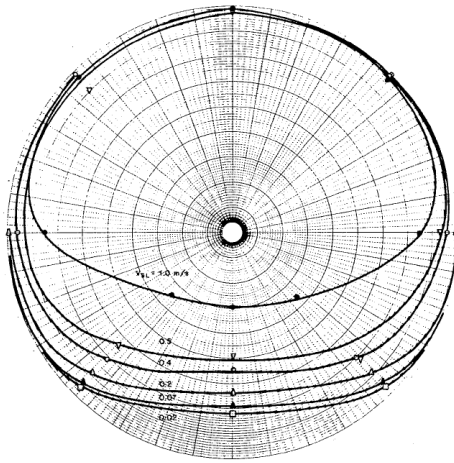


Figure 3.2.7: The measured liquid distribution in an 8-inch pipe for the case where  $U_{SG} = 7 \text{ ms}^{-1}$  while  $U_{SL}$  varies in the range  $0.02-1.0 \text{ ms}^{-1}$  (Wu *et al*, 1987).

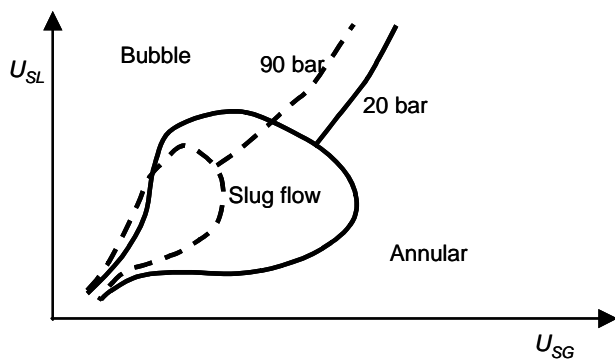


Figure 3.2.8: Flow regime diagram showing the influence of the pressure on the region with slug flow for the case of vertical flow.

and physical properties. It is then natural to expect similar features in the case of flows containing two immiscible liquids. As we will see shortly, there are indeed flow regimes in the case of liquid-liquid flow but the flow regimes are quite different from those observed in the case of gas-liquid flow. There are a number of reasons for this and these reasons are closely related to the main differences between gas-liquid and liquid-liquid systems. To start with, the density difference between the two components is generally much less for the case of liquid-liquid flow. In the case of oil-water mixtures, the density difference between the different fluids is generally less than  $300\text{kg/m}^3$  while for gas-liquid systems this difference is often much larger than  $700\text{kg/m}^3$  (exceptions are cases where the system pressure is very high).

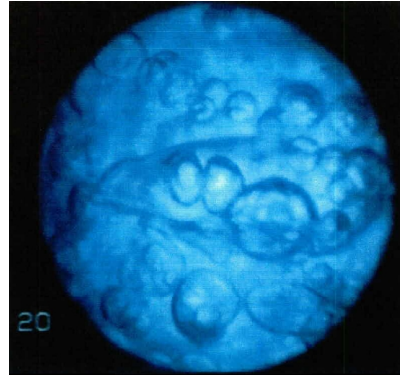


Figure 3.3.1: Water drops in oil-continuous flow at 20% watercut. (Soleimani, 1999).

The relatively small density difference in liquid-liquid systems means that it is comparatively easy to disperse one phase into the other. When this happens, a dispersion is obtained as shown in figure 3.3.1. A stable dispersion is often called an emulsion. Depending on the size of the drops of the dispersed phase, the density difference and the presence of surface-active chemical components (usually called surfactants), the emulsion may be stable or not. An emulsion is stable when the drop size is more or less fixed as a function of time. In an unstable emulsion the drop size varies continuously: drops grow in size due to coalescence events and drops break up due to the action of shearing forces and turbulence-induced fluctuations.

The presence of surfactants, and thus the ease with which different drops coalesce, is an important factor determining the flow regime diagram of liquid-liquid flows. Generally, the more refined an oil is, the less surfactants are present. Different crude oils can have quite different levels of surfactants and hence, the emulsion forming tendencies of crude oils exhibits large variations. This implies that the flow regime map for a liquid-liquid system is dependent on the properties of the fluids. An example of a flow regime map, for oil-water flow in a horizontal pipe, is shown in figure 3.3.2. As a unit on horizontal axis in the flow regime map, the so-called watercut is used. The watercut is the expression often used for the input water fraction. The unit on the vertical axis is taken to be the mixture velocity defined via  $U_{mix} = (Q_O + Q_W)/A$  with  $Q_O$  and  $Q_W$  denoting the oil and water volume flows respectively.

At relatively low velocities we see that stratified flow occurs without the dispersion of oil drops in the water phase or water drops in the oil phase. Apparently, at these low velocities the dispersive turbulent forces are not large enough to keep a significant fraction of drops entrained. Some drops will be formed at the oil-water interface (due to, for example, wave breaking) but the buoyancy forces will transport the drops back to the interface (see figure 3.3.3a). At larger mixture velocities three different flow patterns can be obtained. Common for all these flow patterns is the fact that turbulent forces are now large enough to counteract the buoyancy forces. Firstly, at low watercuts, all the water will be dispersed and the water-continuous layer is no longer present (see figure

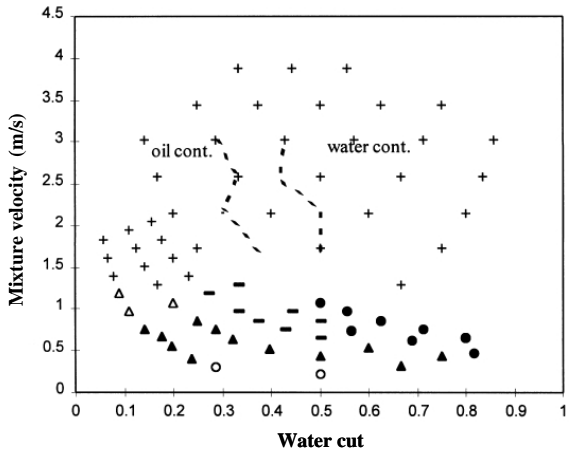


Figure 3.3.2: Observed oil/water flow patterns in pipe flow (Angeli & Hewitt, 2000a). The symbols indicate the following flow patterns:  $\circ$ , stratified wavy; — three layers;  $\triangle$  stratified mixed/oil;  $\blacktriangle$  stratified wavy/drops;  $\bullet$ , stratified mixed/water; + mixed (dispersed oil- or water-continuous)

3.3.3b). At intermediate watercuts (see figure 3.3.3c) there will be clearly identifiable layers of water and oil. In each of these layers drops of the other component will be dispersed. Finally, at high watercuts, all the fluid in the oil-continuous layer has been dispersed (see figure 3.3.3d) and oil appears in the form of drops in a water-continuous matrix.

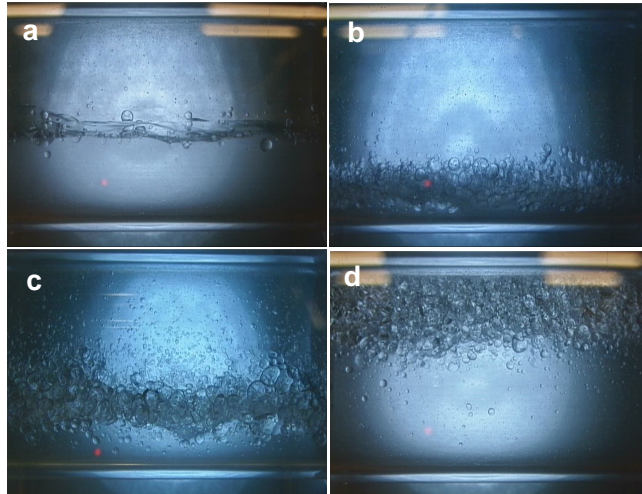


Figure 3.3.3: Pictures of oil-water flow. Stratified flow without dispersions (a), dispersed oil-continuous flow (b), stratified flow with dispersions in both phases (c) and dispersed water-continuous flow (d) (pictures by H.K.Kvandal).

It is important to realise that when the flow pattern is dispersed oil-continuous, the dispersion need not be homogeneously distributed over the cross section of the pipe. This is very clear from figure 3.3.3d. Here, droplet breakup events dominate coalescence events and hence an oil-continuous layer is not formed. Even so, the turbulence-induced velocity fluctuations are not large enough to give a homogeneous dispersion over the cross section of the pipe. The dispersion becomes increasingly homogeneous over the pipe cross section with increasing mixture velocities. The same is true for a oil-continuous

dispersion as seen in figure 3.3.3b.

One rather striking feature of dispersed liquid-liquid flows is the possibility that the effective viscosity of the mixture may vastly exceed the viscosity of either of the phases. This effective viscosity, often called the emulsion viscosities, is the result of droplet-droplet interactions. A typical example of this effect is shown in figure 3.3.4. The data is obtained by recirculating a crude oil/water mixture in a closed loop system at different input water fractions. Based on pressure gradient measurements, the effective viscosity can be determined. We observe that the mixture viscosity can be at least one order of magnitude higher than the pure oil viscosity.

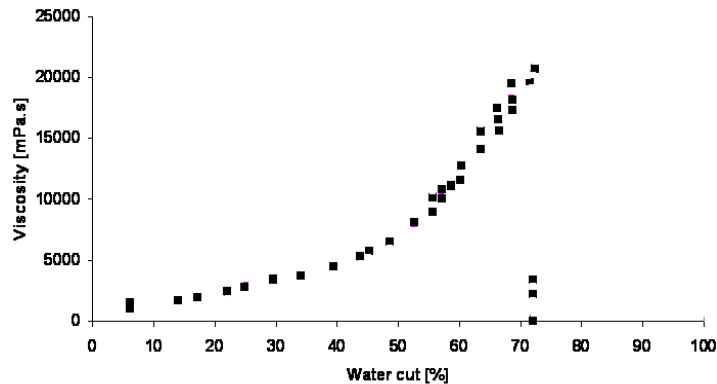


Figure 3.3.4: Viscosity as a function of the water cut for a heavy crude oil-water system (K. Pettersen, Statoil).

Measurements show that the water phase is dispersed in the oil when the wattercut is below 70%. The increase in the measured pressure gradient is thus the result of an increased effective viscosity resulting from interaction of the dispersed droplets. At the point where the emulsion viscosity drops significantly in figure 3.3.4, the flow regime changes from an oil-continuous dispersed flow (for wattercuts below 70%) to a water-continuous flow.

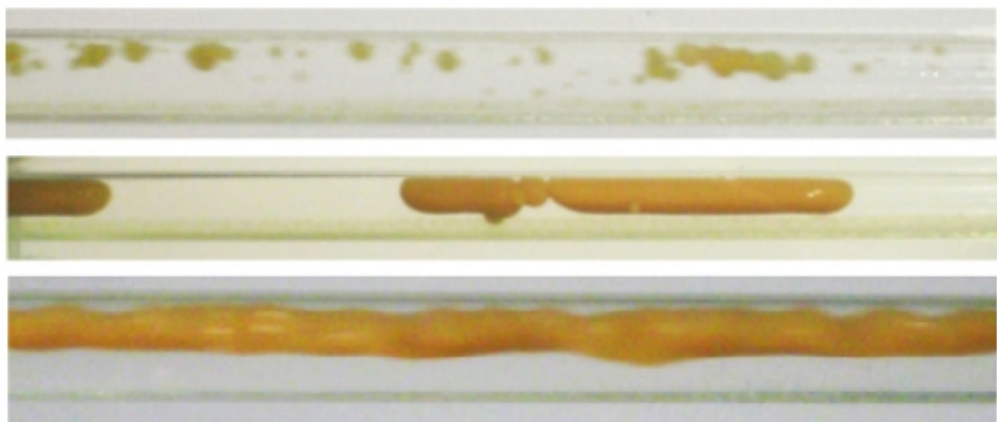


Figure 3.3.5: Examples oil-water flow patters with high-viscosity oil showing dispersed flow, oil slugs in water and core-annular flow (Grassi et al, 2008).

The flow patterns in an oil-water system as described above are representative for the case where the oil viscosity is of the same order of magnitude as the viscosity of the water phase. When the oil viscosity is large (typically 4-5 orders of magnitude larger than that of water), completely different types of behaviour are observed. Characteristic

of these high oil-viscosity systems is the fact that the oil phase is not easily dispersed by the actions of turbulent fluctuations in the water phase. In fact, over a significant range of parameters, the oil is hardly dispersed at all. In figure 3.3.5 we show some examples. Oil is transported in the form of large coherent blobs or in the form of an oil-continuous core, surrounded by an annulus of water, so-called core-annular flow. Only at very low or high waters cuts and at large mixture velocities we find flow patterns similar to those observed in the low-viscosity systems.

### 3.4 Averages

In order to obtain information about the structure of a flowing multiphase mixture it is possible to perform measurements that provide different degrees of information. For example, one can perform point measurements to provide information about the local variations of the flow. Most multiphase flow problems are stochastic in nature so that the only meaningful measurements are those which say something about the probability of finding phase  $X$  at point  $Y$ , say. This means that point measurements are usually performed over a given time interval where the sampling rate is such that meaningful statistical sample is obtained. The measured quantity,  $F(\mathbf{x}, t)$  say, is then averaged to obtain the time average

$$\tilde{F}(\mathbf{x}) = \frac{1}{\Delta T} \int_T^{T+\Delta T} F(\mathbf{x}, t) dt \quad (3.4.1)$$

If the position at which the measurement is taken, is fixed in space then the average is called an Eulerian average. On the other hand, if the position vector  $\mathbf{x}$  is some material coordinate (that is, a coordinate moving with the fluid) then the average is called a Lagrangian average. In order to obtain meaningful measurements, it is important that the length of the measurement interval  $\Delta T$  is large compared with temporal variations induced by the structure of the flow. For example, if  $L$  denotes the dimension of a typical flow structure (slug or bubble size) and  $U$  denotes a typical transport velocity of this structure, then we require  $\Delta T \gg L/U$ .

Line, area or volume measurements are also commonly performed (more about these in the next section). These measurements naturally yield spatial averages of the form

$$\tilde{F}(t) = \frac{1}{\partial\Omega} \int_{\partial\Omega} F(\mathbf{x}, t) d\mathbf{x}$$

in which the domain  $\partial\Omega$  may represent a line, area or volume element. Owing to the stochastic nature of multiphase flow it is often necessary to combine space and time averages, such as performing area measurements over a given time interval. For example, suppose we are interested in finding the mean liquid content in a mixture of gas and liquid flowing in a pipe. To obtain this information one can measure the density  $\rho(x, y, z, t)$  at some point  $x = X$  in the  $y, z$ -plane (assuming the flow is in the  $x$ -direction) over a given length of time to obtain

$$\tilde{\rho}(X) = \frac{1}{\Delta T} \int_T^{T+\Delta T} dt \frac{1}{A} \int_A \rho(x = X, y, z, t) dy dz \quad (3.4.2)$$

where  $A$  denotes the area which is scanned by the density meter. With knowledge of the density of each phase, (3.4.2) will provide information about the mean liquid content in the pipe.

Averages, simply by virtue of the fact that they are obtained by means of space and/or time integrals, smooth out most of the high-frequency variations that may be present in the flow. It is, therefore, evident that the space and time resolutions of the averaged measurements are limited. For the density average as given in (3.4.2) spatial variations

with a length scale less than  $\max [O(\sqrt{A}), U\Delta T]$  and temporal variations with a time scales less than  $O(\Delta T)$  are meaningless ( $U$  denotes a typical velocity scale for the flowing mixture). An in-depth discussion of time-averaging in general and time-averaging related to the development of conservation equations in two-fluid mixtures, is given by Ishii & Hibiki (2006).

A type of average which is often used in the multiphase flow context is the ensemble average. The concept of an ensemble average will now be introduced by taking as an example the way the liquid content (or holdup) in a slug is often determined. When one is interested in the liquid holdup in a slug, one usually measures some averaged density profile as a function of time. However, owing to the stochastic nature of slug flow, one will find that the measured average density will vary significantly from one slug to the next, clearly seen in figure 3.4.1.

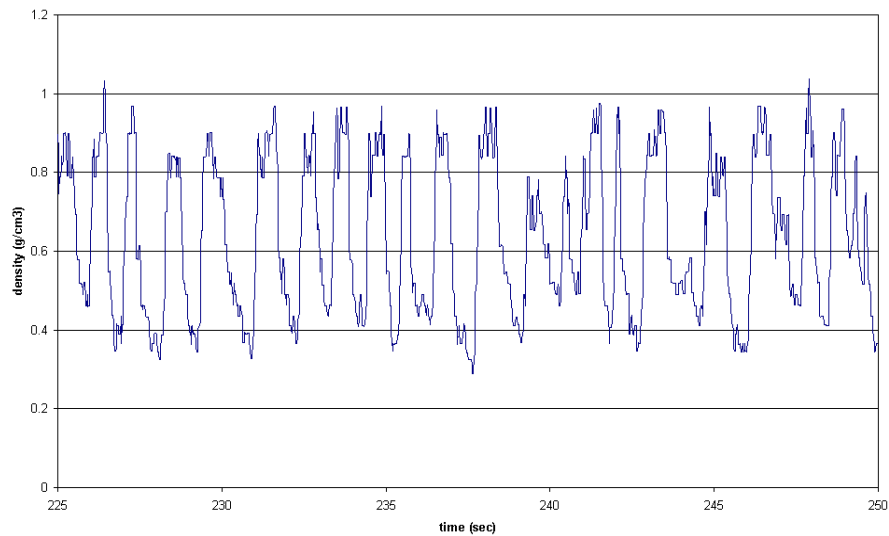


Figure 3.4.1: A gamma-ray signal for slug flow showing the measured mixture density ( $\text{mg}/\text{cm}^3$ ) versus time (s). In the time trace shown, approximately 20 slugs pass the gamma-ray instrument.

Thus, in order to obtain a meaningful measure of the liquid holdup, it is necessary to perform density measurements over many slugs and take some sort of statistical average. Assume now that we have a time series which contains density measurements over  $N$  discrete slugs. The density measurement for slug  $i < N$  is termed a *realization* denoted by  $R_i$ . The set of all realizations is called an ensemble. For the case under consideration the ensemble consists of the density measurements of the  $N$  discrete slugs as covered by the time series. It is natural to ask what sort of average we can define on our ensemble. Now assume that the probability of observing realization  $R_i$  is equal to  $\mu(R_i)$  with  $\sum_{i=1}^N \mu(R_i) = 1$ . We define the ensemble average of the measured densities to be

$$\bar{\rho}(X) = \sum_{i=1}^N \tilde{\rho}_i(X) \mu(R_i), \quad (3.4.3)$$

where  $\tilde{\rho}_i(X)$  denotes the measured density for realization  $R_i$ . For the case in which each realization has an equal probability of being observed it follows that  $\mu(R_i) = \frac{1}{N}$  and (3.4.3) reduces to the arithmetic mean. This particular case is interesting since it allows us to establish a link between the ensemble average and the time average. Namely, suppose we are able to perform a large number of measurements ( $N \gg 1$ ) at short,

equally-spaced time intervals, one after the other. Since the outcome of each measurement is equally-probable we have  $\mu(R_i) = \frac{1}{N} = \Delta t$  in which  $\Delta t$  denotes the time spacing between each measurement. In this case it is evident that the ensemble average (3.4.3) approaches the time average (3.4.1). This would be an example of what is called an ergodic process: average values (and moments) are independent of whether time averaging or ensemble averaging is used. When employing ensemble averaging in multiphase flow applications we implicitly assume the validity of the so-called ergodic hypothesis. This hypothesis essentially states that all realisations have an equal probability of occurring. For a strongly turbulent, homogenised flow this is evidently a reasonable assumption but for intermittent flow regimes the validity may be less easy to justify.

Since computing an average (time, space or ensemble) constitutes a linear operation it is trivial to show the validity of the following properties

<b>Linearity</b>	$c_1\rho_1 + c_2\rho_2 = c_1\bar{\rho}_1 + c_2\bar{\rho}_2$	where $c_1$ and $c_2$ are constants;
<b>Average of Average</b>	$\bar{\rho}_1\bar{\rho}_2 = \bar{\rho}_1\bar{\rho}_2 = \bar{\rho}_1\bar{\rho}_2$	

**Table 3.1:** Properties of averaging procedures.

### 3.5 Measuring Techniques

Experimental measuring techniques in multiphase pipe flow can be divided into four different categories. The first category consists of point measurements in which flow related quantities are measured at one point in space. Examples of such point measurements are: Laser Doppler Velocimetry (LDV), Particle Image Velocimetry (PIV) and conductivity measurements. Both LDV and PIV measurements are able to supply a detailed picture of the both velocity field and turbulent quantities, see figure 3.5.1. Unfortunately LDV and PIV measurements are generally limited to single phase flows or liquid-liquid flows in which the different fluids have matching refractive indices. In gas-liquid flows LDV measurements are of limited use owing to the scattering of light caused by the presence of the gas bubbles. Point pressure measurements can be obtained by means of Pitot tubes. Pitot tubes may be used to determine the direction of the flow which is not always a self-evident in the case of fluids with different densities flowing in inclined pipes. Conductivity measurements are able to provide information about the position of an oil-water interface: salted water being conductive while oil is not.

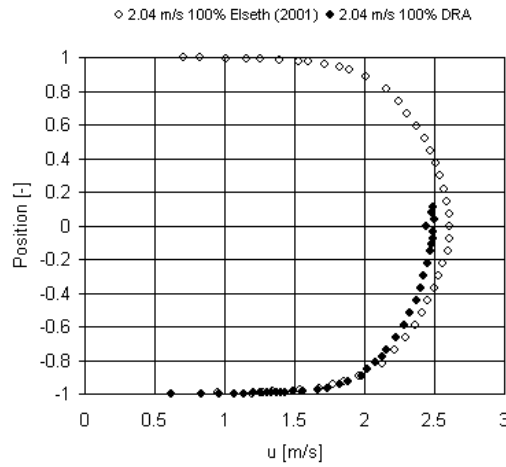


Figure 3.5.1: LDV measurements showing the measure velocity profile in a 5 cm pipe (Elseth, 2001).

Point measurements can supply detailed information about the spatial structure of the flow, simply by taking point measurements at different positions. In multiphase flow

applications, the point measurements will exhibit significant temporal variations. Therefore, in order to obtain meaningful measurements it is generally necessary to perform the point measurements at a single point over a time interval which allows enough samples to be taken to obtain statistically significant results. The structure of the flow (that is bubble sizes, slug frequencies, etc.) in addition to the sampling frequency will determine the time interval over which measurements must be performed.

The second category of measurements techniques consists of line measurements. A typical example of a line measurement is obtained by means of a narrow beam  $\gamma$ -ray. A properly calibrated  $\gamma$ -ray instrument can determine the mean density of the fluid through which the  $\gamma$ -ray passes. Since we may expect significant temporal variations, the narrow beam  $\gamma$ -ray measurements are usually performed over a certain time interval to obtain statistically meaningful results. We therefore see that measurements with a narrow beam  $\gamma$ -ray provide an example of a combined line-average and time-average. By traversing the  $\gamma$ -ray it is possible to obtain information about the vertical density variation in, for example, three phase pipe flow. In figure 3.5.2 an example is shown of the vertical density profile as obtained from a system consisting of water, condensate and gas in a pipe with a circular cross section. On the vertical axis the position of the  $\gamma$ -ray beam is shown while the horizontal axis shows the measured intensity of the beam that has traversed the gas or liquid phase. The three bold, drawn lines show the calibration lines for the different fluids: the red-dotted line for the gas phase, the green-dotted line for the condensate and the yellow-dotted line for the water phase. The symbols show the measured line- and time-averaged densities. The measurements show the presence of a gas phase in the top of the pipe, a pure condensate phase starting somewhat above the middle of the pipe and a water phase in the lowest 20% of the pipe cross section.

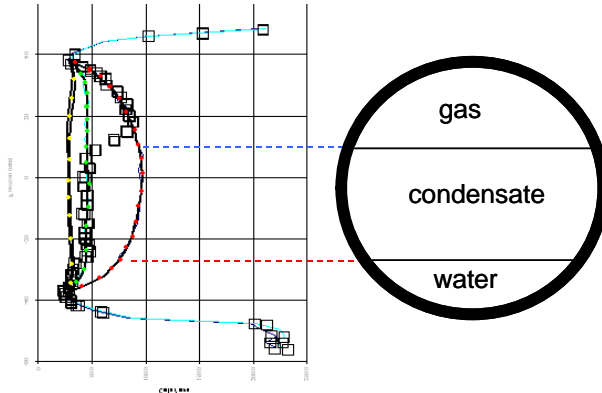


Figure 3.5.2: Measurements using a 2-energy  $\gamma$ -ray beam in a system consisting of water, condensate and gas.

Area measurements are obtained by performing measurements with a wide-beam  $\gamma$ -ray instrument. Since it is not possible distinguish details which have a dimension less than the width of the beam, the wide beam  $\gamma$ -ray provides essentially an area-averaged density. A typical application of wide beam  $\gamma$ -ray measurements is in the field of slug flow where one parameter of interest is the gas content in the liquid slug. Based on time-series analysis of the  $\gamma$ -ray signal it is possible to determine the mean density of the gas-liquid mixture in the slug and thereby infer the gas fraction in the slug. Figure 3.4.1 shows a typical  $\gamma$ -ray signal as a function of time for the case of slug flow. It is evident that in order to obtain statistically meaningful results it is necessary to perform measurements of a large number of slugs. This is therefore an example of a case where a combination of area averages and ensemble averages are used.

In recent years, tomographic techniques have been developed which provide more detailed information about the cross-sectional distribution of flow phenomena. All tomographic techniques are essentially based on the collection of projection data from mul-

tiple directions. The data which is collected is subsequently processed (reconstructed) in order to provide a picture of the area which was scanned. Different types of physical principles are used to obtain the basic tomographic data in multiphase systems. Narrow beam  $\gamma$ -ray or X-ray measurements are used as well as electrical capacitance measurements. Figure 3.5.3 shows an example of the type of information which can be obtained using tomographic techniques. The images are obtained using electrical capacitance measurements of gas-oil flow in a 76mm pipe and show a passing slug.

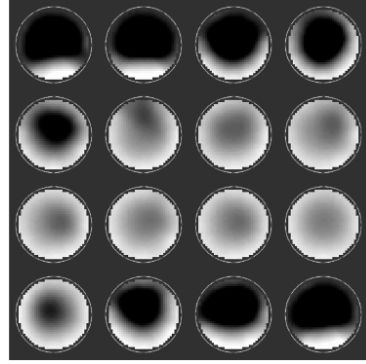


Figure 3.5.3: Tomographic images of slug flow. The time sequence starts at top left and proceeds from left to right, 50ms between each image. The sequence of images shows a passing slug (Gamio *et al*, 2005).

Cross sectional information about the flow structure can also be obtained by inserting a fine wire mesh in the cross section of the pipe. By measuring the conductivity changes in the wire mesh it is possible to determine which phase (locally) passes the wire mesh. Depending on the spacing of the wires and the sampling rate of the sensors, it may be possible to identify small bubbles. Figure 3.5.4 shows an example of the type of information that may be obtained in this manner. The figure shows reconstructed images of vertical two-phase pipe flow at varying superficial gas velocities.

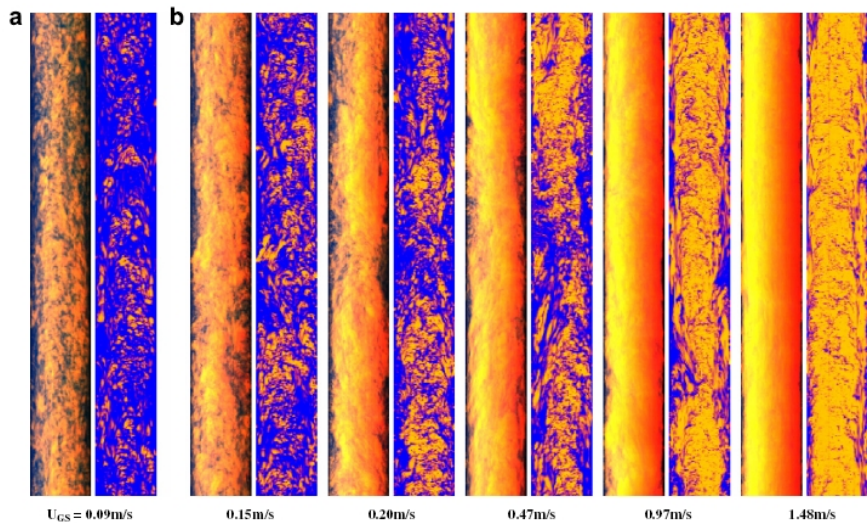


Figure 3.5.4: Flow structure in vertical gas-liquid pipe flow. Virtual side projection (a) and sectional side views (b) for superficial liquid velocity of 0.01m/s (Omebere-Iyari *et al*, 2008).

Employing a set of rapidly closing valves it is possible to determine a **volume average**.

For example, if one is interested in finding out what the mean liquid content is in a bubbly flow, one can trap a given volume of this gas-liquid mixture between two rapidly closing valves and simply measure the volume of liquid after the phases have separated. In this case, as in the measurements mentioned above, it is necessary to perform repeated experiments in order to obtain statistically meaningful results. This then provides an example of a combined volume average and ensemble average. Figure 3.5.5 shows the measured void fraction in repeated experiments (Banerjee & Chan, 1980). The void fractions are measured by trapping a flowing air-water mixture between two rapidly closing valves, the same experiments being repeated several times. In the figure, the diamonds denote the measured void fraction in each experiment, the triangles denote the average after each new experiment and the dashed line denotes the average after 7 experiments. It is clear that the average void fraction approaches the asymptotic average after only 4 experiments, despite the fact that there are significant variations in the measured void fraction between each experiment.

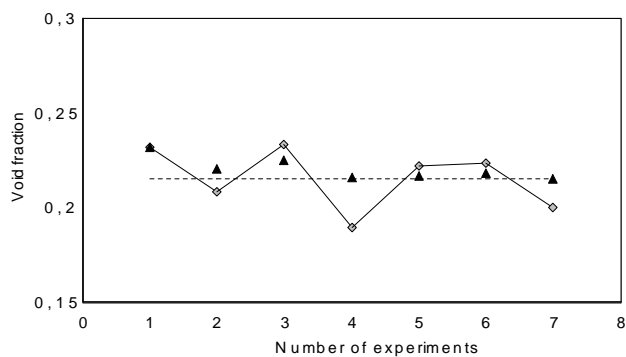


Figure 3.5.5: Void-fraction measurements obtained by trapping a flowing mixture of air and water between two rapidly closing valves. The symbols are explained in the text.

A detailed overview of novel measuring techniques, including magnetic resonance imaging, ultrasonic pulsed Doppler velocimetry and electrical impedance tomography is given by Powell (2008).

### 3.6 Exercises

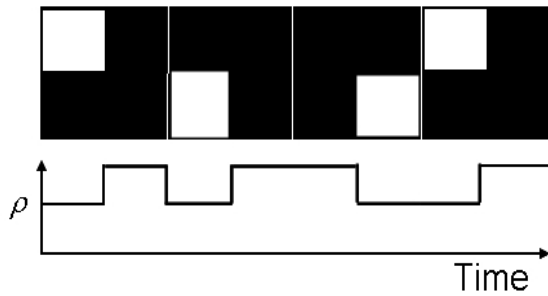
**Exercise 3.1** Show that

$$\overline{\frac{\partial F}{\partial t}} = \frac{\partial \bar{F}}{\partial t}$$

in which the bar denotes the ensemble average. Hint: use linearity properties of the ensemble average. Show in a similar way that  $\nabla \bar{F} = \bar{\nabla F}$  where  $\nabla$  denotes the usual gradient operator.

**Exercise 3.2** Show that the "linearity" and "average of average" relations (table 3.1, 3.4) are valid for time, space and ensemble averages.

**Exercise 3.3** In order to establish the relation between time, ensemble and volume averages, consider the figure shown below. The upper figure shows a schematic representation of pipe flow with large "bubbles" present. Assume that the regions occupied by the dark fluid have a density equal to  $\rho = 1$  while the light bubbles have a density equal to  $\rho = 0$ . The time trace of a density measurement is given in the lower figure.



Assume that a camera take 4 separate pictures of the flow (pictures demarkated by the thin vertical lines). Each picture can be regarded as a realisation of the flow. Show that the density of each realisation is equal to  $\frac{1}{4}$ . Assuming next that each realisation has a similar probability of occurring, show that the ensemble-averaged density is equal to  $\bar{\rho} = \frac{1}{4}$ . Based on the time trace of the measured density shown, show that the time-averaged density is equal to  $\bar{\rho} = \frac{1}{4}$ . Finally, if the section of the flow as shown was captured between two rapidly closing valves, show that the volume-averaged density is equal to  $\bar{\rho} = \frac{1}{4}$ .

## 4 Two-Fluid Model

### 4.1 Introduction

For most practical multiphase systems it is neither desirable nor feasible to determine exactly how the different phases are distributed in time and space. To see this we only need consider the case of a bubbly flow in a pipe. Here, the distribution of the bubbles is governed on the one hand by buoyancy forces trying to move the bubbles upwards and, on the other hand, by turbulent forces trying to disperse the bubbles in the direction of decreasing concentration gradients. Knowing exactly where each bubble is at any given time instant is clearly a tremendous task which has limited benefits. Generally, what we really would like to know is the profile of the bubble concentration which is indicative of the probability of finding a given bubble fraction at some point in space and time. It is precisely this probabilistic description which forms the basis of multiphase flow models. Starting with the local instant conservation equations for mass and momentum we want to develop a set of equations that give us the probability of finding a given phase at some given point in space and time.

The equations to be derived in this chapter can be obtained in different ways. Ishii & Hibiki (2006) show how the equations can be derived by means of taking time averages while volume averages are applied by Banerjee & Chan (1980), among others. It will be clear that the choice of an averaging procedure in the case of non-stationary or spatially non-uniform flows, is not trivial. For example, suppose time-averaging is employed to derive the averaged equations. The resulting equations still contain time derivatives even though time-averaging has removed some of the temporal variations present in the flow. The time derivatives will thus only show significant gradients on time scales that are large compared with the typical time interval on which the averaging is performed. Hence, we have the rather awkward situation that the dimension of the time-interval used in the averaging procedure influences model predictions. A similar situation occurs when we consider the spatial derivatives in relation to the volume-averaging procedure. The derivation of the averaged equations presented in this chapter is based on ensemble-averaging, closely following the derivation presented by Drew & Passman (1999) and Drew & Wood (1985). By using ensemble averaging we formally side-step the problems related to time- and volume-averaging as mentioned above but we lean heavily on the validity of the ergodic hypothesis.

### 4.2 The phase function

In a multiphase flow we have a distribution of two or more phases or components flowing simultaneously in a given domain. The dynamics in each of the phases is governed by the conservation equations and jump conditions as derived in chapter 2. In general it is neither possible nor desirable to try to describe the motion and deformation of each bubble or droplet in the flow. It is therefore clear that some sort of formalism has to be established which enables us to deal with the different phases in some averaged or statistical manner. For example, if we were interested in computing the density of the liquid-liquid mixture shown in figure 4.2.1 we would have to try to determine how much of each phase was present in a given volume of the mixture. We would have to determine the volume of each drop and add all the drop volumes to yield the total volume of the dispersed phase. This volume, together with the total volume from which the sample was taken and the known densities of each phase, would allow us to compute the mixture density. In a picture like 4.2.1 it is possible to determine the size of each drop since the boundary of each drop is clearly visible. Indeed, it would be possible to develop an image analysis program that would find the boundary of a drop and, based on this, compute the volume of each drop. Based on the presence of a visible boundary, the program would thus be able to compute the mixture density. In the development of the two-fluid model we need something similar. Namely, we need a function which allows us to distinguish between different phases or components in the mixture under

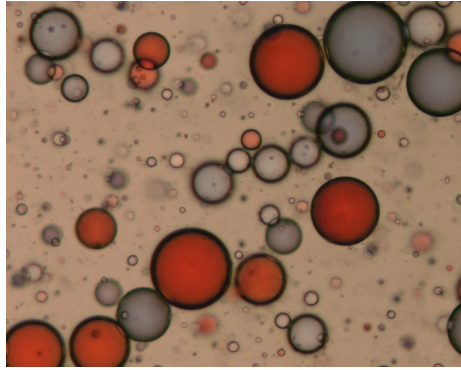


Figure 4.2.1: Coloured water drops in silicon oil (Bremond *et al.*, 2008).

consideration.

To this end we introduce the *phase function*  $X_k$ . The function  $X_k$  has the following property

$$X_k(\mathbf{x}, t; R_i) = \begin{cases} 1 & \text{if } \mathbf{x} \text{ is within phase } k \text{ in realization } R_i \\ 0 & \text{otherwise} \end{cases}$$

When we return to our image analysis program and reconsider figure 4.2.1, the meaning of the phase function becomes clear. Figure 4.2.1 represents one realization of a liquid-liquid dispersion and our program would assign different properties to the phase within a drop and the phase outside the drop. For example, if  $X_D$  were to denote the drop phase, our program would give the phase function  $X_D$  a value 1 whenever we are inside a drop while outside the drop the phase function would be assigned the value 0. Likewise, the phase function for the liquid,  $X_L$ , would be assigned as value equal to 1 or 0 depending on whether we are inside or outside the fluid surrounding the drop. Once the phase functions have been assigned values for a given realization, the density for this realization can be written like

$$\rho(\mathbf{x}, t) = \rho_{liquid} X_L(\mathbf{x}, t) + \rho_{drop} X_D(\mathbf{x}, t) \quad (4.2.1)$$

By employing (4.2.1) the density is thus specified in the whole of the domain, except at the exact location of the boundary of the drop. It may seem rather strange to emphasize that the boundary has not been included since the density is a property associated with the volume of a certain body and the boundary, being a surface, does not have any volume. However, the boundary, being characterized by a step-change in the phase function, does play a rather special role in the development of our formalism for dealing with multiphase flows (this was already evident when formulating the interfacial boundary conditions in chapter 2). A special way to indicate that the boundary between the phases is not included in the mixture density formulation (4.2.1) is to say that the mixture density as given by (4.2.1) is specified *almost everywhere*. In the case of a two-phase flow we have  $X_1 + X_2 = 1$  *almost everywhere* and any intensive property  $\Psi$  of the two-phase mixture can be written like

$$\Psi(\mathbf{x}, t) = \Psi_1(\mathbf{x}, t) X_1 + \Psi_2(\mathbf{x}, t) X_2$$

where  $\Psi_1$  is defined only in phase 1 and likewise for  $\Psi_2$ .

In the development of the two-fluid model, special attention is required with respect to the position of the interface that separates the two phases. The question now is, how can we relate the interface to the phase function  $X_k$ ? In order to answer this question, we

need to understand what the derivative of the phase function can be. To this end, let us go back to the image analysis program we discussed earlier. When we look at the picture of the drops we see that the boundary of each drop is clearly visible since it is notably darker than the regions inside and outside the drop. One way for our image analysis program to detect a bubble boundary would thus be to take a certain pixel  $P_0$  in the picture and determine the colour of this pixel. We then look at the neighbouring pixels and we compare the colour of these pixels with the pixel  $P_0$ . If one of the neighbouring pixels,  $P_1$  say, is notably darker than  $P_0$  it may be that we have detected a boundary. We now have to apply the same procedure to  $P_1$  and determine whether or not one or some of its neighbouring pixels are even darker than  $P_1$ . Proceeding in this manner, all dark pixels can be identified and the domain enclosed by a curve of dark pixels would be a drop. In order to make sure that we detect only drops, we have to write our program such that a drop boundary is identified only when the relative change in pixel colour between neighboring pixels exceeds a certain threshold: gradual changes in pixel colours will thus not be associated with boundaries. In this way, a boundary is identified by a certain gradient in the pixel colour - as we approach the boundary from either side the gradient will increase, while at the middle of the boundary the colour gradient would be zero (in the middle of the boundary all the neighboring pixels would be dark). Figure 4.2.2 shows what the colour gradient could look like if the dark colours would be given a high value while the lighter colours would be assigned a low value. Regardless of the actual values of the colour gradients, it will be clear that a boundary will be identified by large colour gradients.

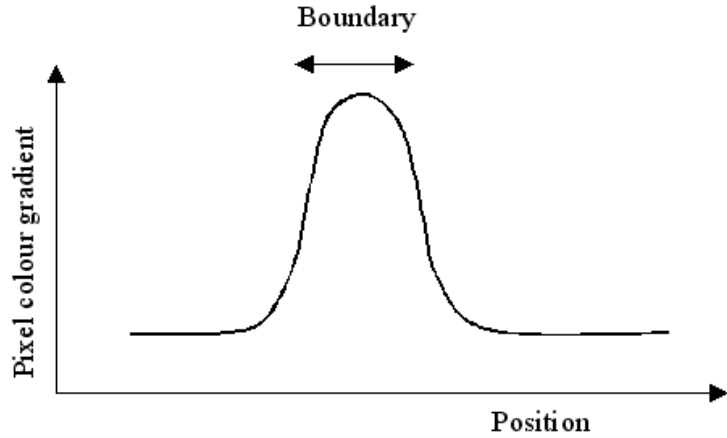


Figure 4.2.2: A schematic plot of the gradient of the pixel colour when crossing the boundary of a given droplet in one specified direction.

We now return to the derivative of the phase function  $X_k$ . By definition, the phase function is equal to unity in the domain  $\Omega_k$ , say, while it is zero outside of  $\Omega_k$ . The derivative of such a function can not be found in the classical way since a step change occurs over an infinitesimal distance (essentially giving "infinite" gradients). However, the so-called Dirac  $\delta$ -function gives us the means to define the derivative of the phase function. This rather special function has the following properties. If  $\mathbf{x}_{k,i}$  denotes the position vector of the boundary of  $\Omega_k$  then

$$\int_{\Omega} \delta(\mathbf{x} - \mathbf{x}_{k,i}) \Psi(\mathbf{x}) d\mathbf{x} = \int_{\partial\Omega_k} \Psi_{k,i} ds \quad (4.2.2)$$

In the above equation  $\Psi_{k,i} = \Psi(\mathbf{x} = \mathbf{x}_{k,i})$ . It is clear that the Dirac  $\delta$ -function has the property that it "focusses" values of an integral on points or lines which lie within the

domain of the integral; in (4.2.2) the action of the  $\delta$ -function selects the boundary of the domain  $\Omega_k$ . The  $\delta$ -function is a function which is zero everywhere with a "spike" at those positions at which the argument in the  $\delta$ -function is zero, thus:  $\delta(\mathbf{y}) = 0$  for  $\mathbf{y} \neq 0$  and  $\delta(\mathbf{y}) \rightarrow \infty$  at  $\mathbf{y} = 0$  while in addition  $\int_{\Omega} \delta(\mathbf{x}) d\mathbf{x} = 1$ . The  $\delta$ -function has a shape similar to that shown in figure 4.2.2 but the width of the function would be infinitesimal while its height would be infinite. With the Dirac  $\delta$ -function available, we can now write the gradient of the phase function  $X_k$  as follows

$$\nabla X_k = -\mathbf{n}_k \delta(\mathbf{x} - \mathbf{x}_{k,i}) \quad (4.2.3)$$

To show that the above result is indeed correct we first have to introduce the concept of a test function. A test function  $\phi$  is a function with the following specific properties:

- (1)  $\phi$  and all its derivatives are continuous;
- (2)  $\phi$  is non-zero on a finite domain contained within  $\Omega$  (a function with this property is said to have "compact support");
- (3)  $\phi \rightarrow 0$  as  $t \rightarrow \pm\infty$ .

Let us return to (4.2.3), multiply both sides of the equation by a test function  $\phi$  and integrate the result over the domain  $\Omega$ . Proceeding as outlined we obtain for the left-hand side of (4.2.3)

$$\begin{aligned} \int_{\Omega} \phi \nabla X_k d\mathbf{x} &= - \int_{\Omega} X_k \nabla \phi d\mathbf{x} \\ &= - \int_{\Omega_k} \nabla \phi d\mathbf{x} \\ &= - \int_{\partial\Omega_k} \phi \mathbf{n}_k ds \end{aligned} \quad (4.2.4)$$

To obtain the above results we have gone through the following three steps: firstly we have applied the fact that  $\phi$  has compact support, secondly we have used the fact that  $X_k$  is non-zero only when  $X_k \in \Omega_k$  and finally we have applied Green's theorem ( $\mathbf{n}_k$  denotes the outward unit normal to  $\Omega_k$ ). By virtue of the property (4.2.2) we can write the surface integral (4.2.4) like

$$\int_{\partial\Omega_k} \phi \mathbf{n}_k ds = \int_{\Omega} \mathbf{n}_k \phi \delta(\mathbf{x} - \mathbf{x}_{k,i}) d\mathbf{x} \quad (4.2.5)$$

Combining (4.2.4) and (4.2.5) yields the desired result when we realise that the domain of integration is arbitrary. In the derivation of the conservation equations we will require an expression for the time-derivative of  $X_k$  as well as the product rule involving  $X_k$ . It is left as an exercise to show that the following relations hold

$$\frac{\partial X_k}{\partial t} + \mathbf{v}_i \cdot \nabla X_k = 0 \quad (4.2.6)$$

$$\nabla(X_k f) = f_{k,i} \nabla X_k + X_k \nabla f \quad (4.2.7)$$

$$\frac{\partial}{\partial t} (X_k f) = f_{k,i} \frac{\partial}{\partial t} X_k + X_k \frac{\partial}{\partial t} f \quad (4.2.8)$$

Before we leave the  $\delta$ -function and its properties, it is important to note that this function has a dimension equal to  $L^{-1}$ . This follows immediately from property (4.2.2).

### 4.3 Conservation equations for a two-fluid mixture

In order to arrive at the conservation equations for a two-fluid mixture we take the generic conservation equation (2.2.5) as a starting point. We now multiply (2.2.5) by the phase function  $X_k$  and we manipulate each of the terms in the resulting equation using the product rules (4.2.7) and (4.2.8). The time-derivative, convective and diffusive terms become respectively

$$\begin{aligned} X_k \frac{\partial}{\partial t} (\rho\Psi) &= \frac{\partial}{\partial t} (X_k \rho\Psi) - (\rho\Psi)_{k,i} \frac{\partial}{\partial t} X_k \\ &= \frac{\partial}{\partial t} (X_k \rho\Psi) + (\rho\Psi)_{k,i} \mathbf{v}_i \cdot \nabla X_k \\ X_k \nabla \cdot (\rho\Psi \mathbf{v}) &= \nabla \cdot (X_k \rho\Psi \mathbf{v}) - (\rho\Psi \mathbf{v})_{k,i} \cdot \nabla X_k \\ X_k \nabla \cdot J &= \nabla \cdot (X_k \mathbf{J}) - \mathbf{J}_{k,i} \cdot \nabla X_k \end{aligned}$$

where (4.2.6) has been used to remove the time derivative of  $X_k$ . We now substitute the expressions as given above into the conservation equation and take the ensemble average of the whole equation. Using the linearity property of the averaging procedure and the fact that the average of a space- or time-derivative is equal to the space- or time-derivative of the average (cf. exercise 3.1), we obtain

$$\frac{\partial}{\partial t} (\overline{X_k \rho\Psi}) + \nabla \cdot (\overline{X_k \rho\Psi \mathbf{v}}) - \nabla \cdot (\overline{X_k \mathbf{J}}) - \overline{X_k \rho\phi} = \overline{(\rho\Psi (\mathbf{v} - \mathbf{v}_i) - \mathbf{J})_{k,i} \cdot \nabla X_k} \quad (4.3.2)$$

It is worthwhile to point out the similarity between the term on the right hand side in the equation given above and the general jump condition as given in equation (2.3.3). Evidently and not surprisingly, the jump conditions are a natural and integral part of multiphase flow models.

The mass conservation equation was obtained from the general conservation equation by taking  $\Psi = 1$  and  $\mathbf{J} = 0$ . Using this in the above equation we obtain

$$\frac{\partial}{\partial t} (\overline{X_k \rho}) + \nabla \cdot (\overline{X_k \rho \mathbf{v}}) = \overline{\Gamma}_k \quad (4.3.3)$$

in which

$$\overline{\Gamma}_k = \overline{(\rho (\mathbf{v} - \mathbf{v}_i))_{k,i} \cdot \nabla X_k} \quad (4.3.4)$$

denotes the interfacial mass transfer rate. The momentum conservation equations are obtained by taking  $\Psi = \mathbf{v}$  and  $\mathbf{J} = \mathbf{T}$  and  $\phi = -\mathbf{g}$ . Substituting into (4.3.2) yields

$$\frac{\partial}{\partial t} (\overline{X_k \rho \mathbf{v}}) + \nabla \cdot (\overline{X_k \rho \mathbf{v} \mathbf{v}}) - \nabla \cdot (\overline{X_k \mathbf{T}}) + \overline{X_k \rho \mathbf{g}} = \overline{\mathbf{v}}_{k,i}^m \overline{\Gamma}_k + \overline{\mathbf{M}}_{k,i} \quad (4.3.5)$$

where

$$\overline{\mathbf{M}}_{k,i} = -\overline{\mathbf{T}}_{k,i} \cdot \nabla X_k \quad (4.3.6)$$

denotes the interfacial momentum source associated with shearing motion and

$$\overline{\mathbf{v}}_{k,i}^m \overline{\Gamma}_k = \overline{(\rho \mathbf{v} (\mathbf{v} - \mathbf{v}_i))_{k,i} \cdot \nabla X_k} \quad (4.3.7)$$

denotes the interfacial momentum source associated with transfer of mass between the phases.

Before we proceed, let us try to understand the physical meaning of the terms on the right-hand-side of the momentum equation (4.3.5). The momentum source  $\bar{\mathbf{M}}_{k,i}$  is clearly related to the interfacial stress since it contains the stress tensor and the operator  $\nabla X_k$  which, by virtue of (4.2.3), selects the interface. We are no longer modelling each bubble of drop individually but the collective interfacial shear associated with the presence of these bubbles or drops is captured in  $\bar{\mathbf{M}}_{k,i}$ . The momentum source  $\bar{\mathbf{v}}_{k,i}^m \bar{\Gamma}_k$  is related to the mass transfer between the phases. This term denotes therefore momentum exchange resulting from mass exchange. Consider, for example, the case of stratified gas-liquid flow where liquid droplets from a slow-moving liquid layer are entrained in a fast-moving gas layer. The entrainment process (mass transfer of liquid to the gas layer) slows down the mean velocity in the gas layer since the slower moving liquid particles have to be dragged along by the gas. This effect is captured in the term  $\bar{\mathbf{v}}_{k,i}^m \bar{\Gamma}_k$ . Let us next turn our attention to the interfacial (jump) conditions. From equation (2.3.3) we recall that the generic jump condition can be written in the form  $[\chi] \cdot \mathbf{n}_1 = \mathbf{m}_i$  where  $[\chi]$  denotes the jump of a quantity  $\chi = \rho\Psi(\mathbf{v} - \mathbf{v}_i) - \mathbf{J}$  over the interface. In order to derive the averaged jump conditions we take the jump condition as given in (2.3.3) and multiply it by  $\mathbf{n}_1 \cdot \nabla X_1 = -\delta(\mathbf{x} - \mathbf{x}_i)$  (c.f. equation (4.2.3)). Since  $[\chi] \cdot \mathbf{n}_1 = \chi_1 \cdot \mathbf{n}_1 - \chi_2 \cdot \mathbf{n}_1 = \chi_1 \cdot \mathbf{n}_1 + \chi_2 \cdot \mathbf{n}_2$  it follows that

$$\begin{aligned} [\chi] \cdot \mathbf{n}_1 (\mathbf{n}_1 \cdot \nabla X_1) &= \chi_1 \cdot (-\mathbf{n}_1 \delta(\mathbf{x} - \mathbf{x}_1)) + \chi_2 \cdot (-\mathbf{n}_2 \delta(\mathbf{x} - \mathbf{x}_2)) \\ &= \chi_1 \cdot \nabla X_1 + \chi_2 \cdot \nabla X_2 \end{aligned}$$

Using the above result and taking averages it follows that the general jump conditions can be written like

$$\overline{[\chi] \cdot \mathbf{n}_1 (\mathbf{n}_1 \cdot \nabla X_1)} = \overline{\chi_1 \cdot \nabla X_1} + \overline{\chi_2 \cdot \nabla X_2} = \bar{\mathbf{m}}_i \quad (4.3.8)$$

in which we have defined the mean interfacial source of mass or momentum via  $\bar{\mathbf{m}}_i = \overline{\mathbf{m}_i (\mathbf{n}_1 \cdot \nabla X_1)}$ . For the specific case of mass conservation we take  $\Psi = 1, \mathbf{J} = 0$  and  $\mathbf{m}_i = 0$ , giving

$$\overline{\rho(\mathbf{v} - \mathbf{v}_i) \cdot \nabla X_1} + \overline{\rho(\mathbf{v} - \mathbf{v}_i) \cdot \nabla X_2} = 0$$

Using (4.3.4) it follows that the equation above can be written in the form

$$\bar{\Gamma}_1 + \bar{\Gamma}_2 = 0 \quad (4.3.9)$$

This equation states simply that in order to conserve mass, the amount of mass leaving phase 1 must equal the amount of mass entering phase 2.

For the case of momentum conservation we take  $\Psi = \mathbf{v}, \mathbf{J} = \mathbf{T}$  and  $\mathbf{m}_i \neq 0$  (cf. equation (2.3.6)). Using (4.3.6)-(4.3.8) it follows readily that the interfacial momentum jump condition becomes

$$\bar{\mathbf{v}}_{1,i}^m \bar{\Gamma}_1 + \bar{\mathbf{v}}_{2,i}^m \bar{\Gamma}_2 + \bar{\mathbf{M}}_{1,i} + \bar{\mathbf{M}}_{2,i} = \bar{\mathbf{m}}_i \quad (4.3.10)$$

The conservation equations (4.3.3) and (4.3.5) together with the interface conditions (4.3.9) and (4.3.10) are the basic equations required for the development of the two-fluid model.

Some work still has to be done before we have a model that can be used as a predictive tool. To start with, we need to interpret averaged quantities like  $\overline{X_k \rho}$  and  $\overline{X_k \rho \mathbf{v} \mathbf{v}}$  which appear in the conservation equations. To this end we define a general weighted mean value (also called a Favré average) of a quantity  $\Psi$  according to

$$\overline{\Psi}^w = \frac{\overline{w\Psi}}{\overline{w}}$$

in which  $w$  is some scalar. By taking  $w = X_k$  we obtain the phase-weighted mean

$$\overline{\Psi}_k^x = \frac{\overline{X_k \Psi}}{\overline{X_k}}$$

In order understand the meaning of the phase weighted mean as defined above, we need to understand the meaning of  $\overline{X}_k$ . Since  $X_k$  indicates the presence of phase  $k$  in the domain of interest, it follows naturally that mean value  $\overline{X}_k$  should be identified with the average fraction of occurrences of component  $k$ . It has become customary to refer to

$$\overline{X}_k = \overline{\alpha}_k$$

as the volume fraction even though the volume fraction is formally a quantity related to volume averaging. The phase-averaged density is then defined via

$$\overline{\rho}_k^x = \frac{\overline{X_k \rho}}{\overline{\alpha}_k} \quad (4.3.11)$$

In the conservation equation we consider the conservation of a quantity  $\rho\Psi$ . For this reason it is useful to introduce the mass-weighted average.

$$\overline{\Psi}_k^{x\rho} = \frac{\overline{X_k \rho \Psi}}{\overline{\rho X}_k} \quad (4.3.12)$$

We now consider the mass conservation equation (4.3.3) and use (4.3.11) and (4.3.12) to obtain

$$\frac{\partial}{\partial t} (\overline{\alpha}_k \overline{\rho}_k^x) + \nabla \cdot (\overline{\alpha}_k \overline{\rho}_k^x \overline{\mathbf{v}}_k^{x\rho}) = \overline{\Gamma}_k \quad (4.3.13)$$

The momentum conservation equation (4.3.5) can be reformulated in a similar way but before doing so we need to consider the non-linear convective term  $\overline{X_k \rho \mathbf{v} \mathbf{v}}$  in some detail. In general, the simultaneous flow of multiple phases is not steady due to the presence of turbulent fluctuations. This means that, in line with standard procedures in turbulent flow modelling (see section 2.5.2), we write the velocity as the sum of a mean and a fluctuating component. Thus  $\mathbf{v} = \overline{\mathbf{v}}_k^{x\rho} + \mathbf{v}'_k$  in which we demand that  $\overline{X_k \rho \mathbf{v}'} = 0$ . It is easy to show that the convective term becomes

$$\overline{X_k \rho \mathbf{v} \mathbf{v}} = \overline{\alpha}_k \overline{\rho}_k^x \overline{\mathbf{v}}_k^{x\rho} \overline{\mathbf{v}}_k^{x\rho} - \overline{\alpha}_k \overline{\mathbf{T}}_k^{\text{Re}} \quad (4.3.14)$$

in which we have defined the Reynolds stress  $\overline{\mathbf{T}}_k^{\text{Re}}$  in the usual manner, namely

$$\overline{\mathbf{T}}_k^{\text{Re}} = -\frac{1}{\overline{\alpha}_k} \overline{X_k \rho \mathbf{v}'_k \mathbf{v}'_k}$$

Using (4.3.11), (4.3.12) together with (4.3.14) in the conservation equation (4.3.5) we obtain

$$\frac{\partial}{\partial t} (\bar{\alpha}_k \bar{\rho}_k^x \bar{\mathbf{v}}_k^{x\rho}) + \nabla \cdot (\bar{\alpha}_k \bar{\rho}_k^x \bar{\mathbf{v}}_k^{x\rho} \bar{\mathbf{v}}_k^{x\rho}) - \nabla \cdot (\bar{\alpha}_k \bar{\mathbf{T}}_k) - \nabla \cdot (\bar{\alpha}_k \bar{\mathbf{T}}_k^{\text{Re}}) + \bar{\alpha}_k \bar{\rho}_k^x \bar{\mathbf{g}}_k^{x\rho} = \bar{\mathbf{v}}_{k,i}^m \bar{\Gamma}_k + \bar{\mathbf{M}}_{k,i} \quad (4.3.15)$$

in which we have defined avarage mass-weighted body force  $\bar{\mathbf{g}}_k^{x\rho} = \frac{\bar{X}_k \rho \mathbf{g}}{\bar{\alpha}_k \bar{\rho}_k^x}$  and the average phase-weighted stress tensor  $\bar{\mathbf{T}}_k = \frac{\bar{X}_k \mathbf{T}}{\bar{\alpha}_k}$ . The general two-fluid model is now given by the conservation equations (4.3.13) and (4.3.15) together with the interface (jump) conditions (4.3.9) and (4.3.10).

It will be clear that the general conservation equations for a two-fluid mixture, as derived above, is still some way removed from a predictive model. Namely, new terms (like  $\bar{\mathbf{M}}_{k,i}$ ) have appears in the equations but no additional equations have been obtained. This means that additional modelling work has to be performed in order to relate these new terms to known variables. This is the familiar closure problem which we encountered earlier in our treatment of turbulence in section 2.5.2. Since the modelling of terms like  $\bar{\mathbf{M}}_{k,i}$  is problem-specific we will henceforth focus on the problems of primary interest here: multiphase flow in a pipe-like geometry. For this reason it is natural to consider simplifications of the general two-fluid model derived in this section. This will be the topic of the following two sections.

#### 4.4 Area-averaged two-fluid model

In the oil and gas industry, it is very common to deal with the combined transport of liquid and gas in pipelines that have a diameter less than a meter but a length extending to many tens of kilometers. It is natural to ask how flow models in such systems can be developed, which in some way represent a simplification of the full 3-dimensional models as presented in the previous section. Indeed, simplified models are likely to be possible if the typical length scale of the flow structure in the pipe is much larger than the pipe diameter. We know that in a pipe, momentum is transported predominantly along the axis of the pipe. This observation is the starting point of so-called hydraulic models: models in which only spatial variations along the axis of the pipe are considered. In order to develop such models we start with the general conservation equations derived in the previous section and derive area-averaged equations. To that end, consider a pipe with a constant cross section denoted by  $A$  and assume that the axis of the pipe points in the direction of the positive  $x$ -axis. We define the area average of a quantity  $f(\mathbf{x}, t)$  via

$$\langle f \rangle = \frac{1}{A} \int_A f(\mathbf{x}, t) da$$

Note that the area average  $\langle f \rangle$  is a function of  $x$  and  $t$  only. If the area  $A$  is taken to be constant in time then it follows immediately that

$$\frac{\partial}{\partial t} \langle f \rangle = \left\langle \frac{\partial f}{\partial t} \right\rangle \quad (4.4.1)$$

The divergence of a quantity  $\mathbf{F}$  can be written as  $\nabla \cdot \mathbf{F} = \frac{\partial}{\partial x} \mathbf{F} \cdot \mathbf{i} + \nabla_{yz} \cdot \mathbf{F}$  in which the operator  $\nabla_{yz}$  denotes the divergence operator in the  $y$ - $z$  plane and  $\mathbf{i}$  denotes a unit vector in the direction of the positive  $x$ -axis. Taking the area average of the quantity  $\nabla \cdot \mathbf{F}$  and using Green's theorem we obtain

$$\langle \nabla \cdot \mathbf{F} \rangle = \frac{\partial}{\partial x} \langle \mathbf{F} \cdot \mathbf{i} \rangle + \frac{1}{A} \int_{\partial A} \mathbf{F} \cdot \mathbf{n} ds \quad (4.4.2)$$

The surface integral in (4.4.2) is a surface integral along the cross-sectional perimeter of the pipe and the unit normal  $\mathbf{n} = (0, n_y, n_z)$ .

We now turn to the mass conservation equation (4.3.13). Taking the area average of this equation and using (4.4.1) and (4.4.2) it follows that the area-averaged mass conservation equation becomes

$$\frac{\partial}{\partial t} \langle \bar{\alpha}_k \bar{p}_k^x \rangle + \frac{\partial}{\partial x} \langle \bar{\alpha}_k \bar{p}_k^x \bar{\mathbf{v}}_k^{x\rho} \rangle \cdot \mathbf{i} = \langle \bar{\Gamma}_k \rangle \quad (4.4.3)$$

The surface integral along the perimeter of the pipe vanishes owing to the fact that  $\bar{\alpha}_k \bar{p}_k^x \bar{\mathbf{v}}_k^{x\rho} \cdot \mathbf{n} = 0$  which states that the pipe walls are impenetrable. We now introduce the following variables:

The area-averaged volume fraction

$$\alpha_k = \langle \bar{\alpha}_k \rangle$$

The density

$$\rho_k = \frac{1}{\alpha_k} \langle \bar{\alpha}_k \bar{p}_k^x \rangle$$

The area-averaged cross-sectional velocity

$$u_k = \frac{1}{\alpha_k \rho_k} \langle \bar{\alpha}_k \bar{p}_k^x \bar{\mathbf{v}}_k^{x\rho} \rangle \cdot \mathbf{i}$$

The area-averaged rate of mass transfer

$$\Gamma_k = \langle \bar{\Gamma}_k \rangle$$

With these definitions, the mass conservation equation (4.4.3) becomes

$$\frac{\partial}{\partial t} (\alpha_k \rho_k) + \frac{\partial}{\partial x} (\alpha_k \rho_k u_k) = \Gamma_k \quad (4.4.4)$$

We next turn our attention to the momentum equation. As specified above, we are dealing with a pipe whose axis is aligned with the  $x$ -axis of our coordinate system. This implies that it is natural to focus on the area average of the  $x$ -component of the momentum equation. This is achieved by first taking the inner product of the momentum equation (4.3.15) with the unit vector  $\mathbf{i}$  and subsequently performing area-averaging operation. We obtain

$$\begin{aligned} \frac{\partial}{\partial t} \langle \bar{\alpha}_k \bar{p}_k^x \bar{\mathbf{v}}_k^{x\rho} \rangle \cdot \mathbf{i} + \frac{\partial}{\partial x} \langle \bar{\alpha}_k \bar{p}_k^x \bar{\mathbf{v}}_k^{x\rho} \bar{\mathbf{v}}_k^{x\rho} \rangle : \mathbf{ii} &= \frac{\partial}{\partial x} \left\langle \bar{\alpha}_k \left( \bar{\mathbf{T}}_k + \bar{\mathbf{T}}_k^{\text{Re}} \right) \right\rangle : \mathbf{ii} \\ &+ \frac{1}{A} \int_{\partial A} \bar{\alpha}_k \bar{\mathbf{T}}_k : \mathbf{ind}s - \langle \bar{\alpha}_k \bar{p}_k^x \bar{\mathbf{g}}_k^{x\rho} \rangle \cdot \mathbf{i} \\ &+ \langle \bar{\mathbf{v}}_{k,i}^m \bar{\Gamma}_k \rangle \cdot \mathbf{i} + \langle \bar{\mathbf{M}}_{k,i} \rangle \cdot \mathbf{i} \end{aligned} \quad (4.4.5)$$

We have introduced the following short-hand notation  $\mathbf{A} : \mathbf{in} = \sum_k \sum_l A_{kl} i_l n_k$ . In order to obtain a scalar equation in the desired form we introduce the profile parameter (required because the average of a product is not the same as the product of averages)

$$c_{uk} = \frac{1}{\alpha_k \rho_k u_k^2} \langle \bar{\alpha}_k \bar{p}_k^x \bar{\mathbf{v}}_k^{x\rho} \bar{\mathbf{v}}_k^{x\rho} \rangle : \mathbf{ii}$$

The profile coefficient is indicative of how far the velocity profile is removed from a flat, plug-like profile. For a completely flat profile we would have  $c_{uk} \equiv 1$  while for turbulent flows we typically have  $c_{uk} \simeq 1.2$ . We now introduce the stresses

$$\begin{aligned} T_k &= \frac{1}{\alpha_k} \langle \bar{\alpha}_k \bar{\mathbf{T}}_k \rangle : \mathbf{ii} \\ T_k^{\text{Re}} &= \frac{1}{\alpha_k} \left\langle \bar{\alpha}_k \bar{\mathbf{T}}_k^{\text{Re}} \right\rangle : \mathbf{ii} \end{aligned}$$

the perimeter-averaged wall stress

$$T_{kw} = \frac{1}{\alpha_{kw}} \frac{D_H}{4A} \int_{\partial A} \bar{\alpha}_k \bar{\mathbf{T}}_k : \mathbf{ind}s$$

in which we have used the hydraulic diameter  $D_H = 4A/\int_{\partial A} ds$  and the perimeter-averaged volume fraction

$$\alpha_{kw} = \frac{D_H}{4A} \int_{\partial A} \bar{\alpha}_k ds$$

Furthermore, we define the body force

$$g_k = \frac{1}{\alpha_k \rho_k} \langle \bar{\alpha}_k \bar{\rho}_k \bar{\mathbf{g}}_k^{x\rho} \rangle \cdot \mathbf{i}$$

the interfacial force density

$$M_k = \langle \bar{\mathbf{M}}_{k,i} \rangle \cdot \mathbf{i}$$

and the interfacial mass transfer velocity

$$v_k^m = \frac{1}{\Gamma_k} \langle \bar{\mathbf{v}}_{k,i}^m \bar{\Gamma}_k \rangle \cdot \mathbf{i} \quad (4.4.7)$$

Using the definitions as given above in the momentum equation (4.4.5) yields

$$\begin{aligned} \frac{\partial}{\partial t} (\alpha_k \rho_k u_k) + \frac{\partial}{\partial x} (c_{uk} \alpha_k \rho_k u_k^2) &= \frac{\partial}{\partial x} [\alpha_k (T_k + T_k^{\text{Re}})] + \frac{4}{D_H} \alpha_{kw} T_{kw} \\ &\quad - \alpha_k \rho_k g_k + v_k^m \Gamma_k + M_k \end{aligned} \quad (4.4.8)$$

It is important to note that the mass and momentum conservation equations (4.4.4) and (4.4.8) exact conservation equations in the sense that no approximations have been introduced in deriving these equations. It is only at a later stage when explicit expressions for the wall and interfacial shear stresses are required that approximations have to be made.

The jump condition (4.3.9) becomes on taking the area-average

$$\Gamma_1 + \Gamma_2 = 0 \quad (4.4.9)$$

The jump condition (4.3.10) needs to be treated with some care since it is a vector equation and it thus contains information about changes over the interface in the normal and tangential directions. For this reason we write

$$\bar{\mathbf{M}}_{k,i} = \bar{\mathbf{M}}_{k,i}^{(n)} + \bar{\mathbf{M}}_{k,i}^{(t)}$$

in which the superscripts  $n$  and  $t$  indicate normal and tangential components. If one assumes that mass transfer occurs mainly normal to the interface (this is equivalent to assuming that the direction of  $\bar{\mathbf{v}}_{k,i}^m$  is almost perpendicular to the interface), then the jump condition (4.3.10) can be decomposed into the two principal components: the component normal to the interface

$$\bar{\mathbf{v}}_{1,i}^m \bar{\Gamma}_1 + \bar{\mathbf{v}}_{2,i}^m \bar{\Gamma}_2 + \bar{\mathbf{M}}_{1,i}^{(n)} + \bar{\mathbf{M}}_{2,i}^{(n)} = \bar{\mathbf{m}}_i^{(n)} \quad (4.4.10)$$

and the tangential component

$$\bar{\mathbf{M}}_{1,i}^{(t)} + \bar{\mathbf{M}}_{2,i}^{(t)} = \bar{\mathbf{m}}_i^{(t)} \quad (4.4.11)$$

in which  $\bar{\mathbf{m}}_i^{(n)} = \overline{C\sigma\nabla X_1}$  and  $\bar{\mathbf{m}}_i^{(t)} = \overline{\nabla_s\sigma(\mathbf{n}\cdot\nabla X_1)}$  denote the normal and tangential components of the interfacial momentum source (c.f. equation (2.3.6)). Generally, the surface tension gradient effects are considered to be small in addition to the fact that their orientation can be assumed to be random. This then justifies the approximation  $\overline{\nabla_s\sigma(\mathbf{n}\cdot\nabla X_1)} \simeq 0$ . Defining  $M_k^{(n)} = \langle \bar{\mathbf{M}}_{k,i}^{(n)} \rangle \cdot \mathbf{i}$  and likewise for  $M_k^{(t)}$  as well as  $m_i^{(n)} = \langle \bar{\mathbf{m}}_i^{(n)} \rangle \cdot \mathbf{i}$ , it follows that the jump conditions (4.4.10) and (4.4.11) become

$$v_1^m \Gamma_1 + v_2^m \Gamma_2 + M_1^{(n)} + M_2^{(n)} = m_i^{(n)} \quad (4.4.12)$$

$$M_1^{(t)} + M_2^{(t)} = 0 \quad (4.4.13)$$

The conservation equations (4.4.4) and (4.4.8) together with the interfacial conditions (4.4.9), (4.4.12) and (4.4.13) constitute the full set of area-averaged two-fluid equations. Before we can apply these equations to actual problems it is necessary to consider the specific forms of these equations for different flow regimes. This will be our next focus.

## 4.5 Area-averaged model for stratified flow

In this section we take as a starting point the area-averaged conservation equations for the two-fluid model as derived in the previous section. The equations will be manipulated in order to give us the governing equations for stratified flow in a circular pipe. Two important simplifying assumptions will be made:

1. There is no exchange of mass between the phases  $\Rightarrow \Gamma_k = 0$ .
2. There is no dispersion of phases: no gas bubbles in the liquid phase and no liquid drops in the gas phase.

The problem under consideration is thus shown schematically in figure 4.5.1.

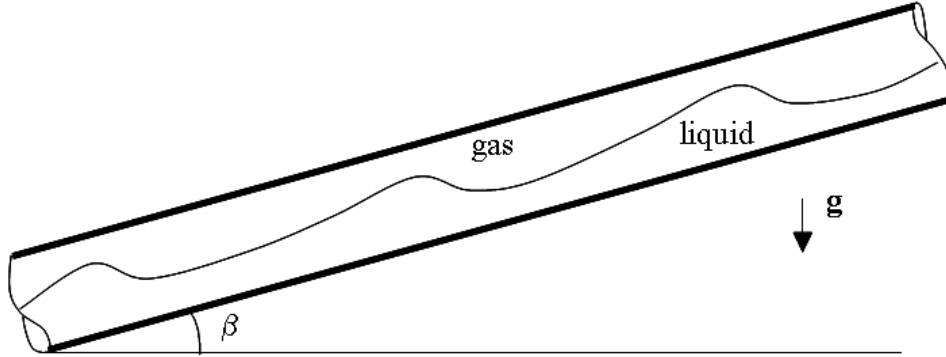


Figure 4.5.1: Schematic diagram of stratified gas-liquid flow in circular pipe.

Taking the mass conservation equation (4.4.4) and multiplying it by the cross sectional area  $A$  of the pipe, we obtain for the liquid and gas phase respectively

$$\frac{\partial}{\partial t} (A_L \rho_L) + \frac{\partial}{\partial x} (A_L \rho_L u_L) = 0 \quad (4.5.1a)$$

$$\frac{\partial}{\partial t} (A_G \rho_G) + \frac{\partial}{\partial x} (A_G \rho_G u_G) = 0 \quad (4.5.1b)$$

in which  $A_k = \alpha_k A$ ,  $k = L, G$ .

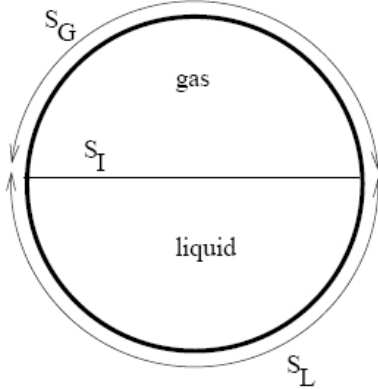


Figure 4.5.2: Diagram showing geometry for stratified flow.

Next we consider the momentum conservation equations as given in (4.4.8). Two terms on the right-hand-side in the momentum equations require some special attention. These are the interfacial momentum transfer term  $M_k$  and the term containing the wall shear stress  $T_{kw}$ . Let us first consider the interfacial momentum term. With the stress tensor of the usual form  $\mathbf{T} = -p\mathbf{I} + \mathbf{D}$  it follows from (4.3.6) and the definition of  $M_k$  that

$$M_k = \langle \bar{\mathbf{M}}_k \rangle \cdot \mathbf{i} = \langle p \nabla X_k \rangle \cdot \mathbf{i} - \langle \bar{\mathbf{D}} \cdot \nabla X_k \rangle \cdot \mathbf{i} \quad (4.5.2)$$

From (4.2.3), we know that  $\nabla X_k$  is an operator that selects the interface which separates the phases. The term  $p \nabla X_k$  is thus related to the interfacial pressure which may be assumed to be a constant in a cross section of the pipe. Thus

$$\langle p \nabla X_k \rangle \cdot \mathbf{i} \equiv \frac{1}{A} \int_A p \frac{\partial X_k}{\partial x} da \simeq p_{kI} \frac{\partial}{\partial x} \left( \frac{1}{A} \int_A \bar{X}_k da \right) = p_{kI} \frac{\partial \alpha_k}{\partial x}$$

in which  $p_{kI}$  denotes the mean interfacial pressure. The second term on the right-hand-side of (4.5.2) becomes

$$\langle \bar{\mathbf{D}} \cdot \nabla X_k \rangle \cdot \mathbf{i} \equiv -\frac{1}{A} \int_A \bar{\mathbf{D}} : \mathbf{n}_k \mathbf{i} \delta(\mathbf{x} - \mathbf{x}_{k,i}) da \simeq \pm \tau_{kI} \frac{1}{A} \int_A \delta(\mathbf{x} - \mathbf{x}_{k,i}) da = \pm \tau_{kI} \frac{s_I}{A}$$

in which the mean interfacial shear stress  $\tau_{kI} = \pm \bar{\mathbf{D}} : \mathbf{n}_k \mathbf{i}$  is assumed to be constant and  $s_I$  denotes the width of the interface separating the liquid and the gas, see figure 4.5.2. Recall that the delta-function has a dimension of  $L^{-1}$  so that  $\int_A \delta(\mathbf{x} - \mathbf{x}_{k,i})$  has the dimension of length, as required. Note also that on the interface separating the two phases,  $\mathbf{n}_1 = -\mathbf{n}_2$  explaining the appearance of the  $\pm$ -sign in front of the interfacial shear stress term. Combining the results given above it follows that (4.5.2) becomes

$$M_k = p_{kI} \frac{\partial \alpha_k}{\partial x} \pm \frac{1}{A} \tau_{kI} s_I \quad (4.5.3)$$

Next we consider the wall shear stress term. From the definition of  $T_{kw}$  given in the previous section, it follows that

$$\frac{4}{D_H} \alpha_{kw} T_{kw} = \frac{1}{A} \int_{\partial A} \bar{\alpha}_k \bar{\mathbf{T}}_k : \mathbf{i} n ds$$

Only the deviatoric part of the stress tensor contributes to the line-integral given above and we assume that the wall shear stress  $\tau_{kw} = -\bar{\mathbf{T}}_k \cdot \mathbf{i}$  is constant on the perimeter wetted by a given phase. Given our assumption that the two phases are not dispersed it follows that  $\alpha_L = 1$  when the perimeter is in the liquid phase and zero otherwise and likewise for  $\alpha_G$ . Thus

$$\frac{1}{A} \int_{\partial A} \bar{\alpha}_k \bar{\mathbf{T}}_k : \mathbf{n} ds \simeq -\frac{\tau_{kw}}{A} \int_{\partial A} \bar{\alpha}_k da = -\frac{1}{A} \tau_{kw} s_k \quad (4.5.4)$$

in which  $s_k$ ,  $k = G, L$  denotes the perimeter wetter by phase  $k$ , see figure 4.5.2. Using (4.5.3) and (4.5.4) together with the form of the stress tensor as given earlier, it follows that the momentum equation can be written as

$$\begin{aligned} \frac{\partial}{\partial t} (\alpha_k \rho_k u_k) + \frac{\partial}{\partial x} (c_{kv} \alpha_k \rho_k u_k^2) &= -\frac{\partial}{\partial x} (\alpha_k p_k) + \frac{\partial}{\partial x} [\alpha_k (D_k + T_k^{\text{Re}})] \\ &\quad - \frac{1}{A} \tau_{kw} s_k - \alpha_k \rho_k g \sin \beta \\ &\quad + p_{kI} \frac{\partial \alpha_k}{\partial x} - \frac{1}{A} \tau_{kI} s_I \end{aligned} \quad (4.5.5)$$

in which  $\alpha_k D_k = \langle \bar{\alpha}_k \bar{\mathbf{D}}_k : \mathbf{i} \rangle$ . It can be shown that (see exercise 4.3)

$$-\frac{\partial}{\partial x} (\alpha_k p_k) + p_{kI} \frac{\partial \alpha_k}{\partial x} = -\alpha_k \frac{\partial p_{kI}}{\partial x} - \rho_k g \alpha_k \cos \beta \frac{\partial h}{\partial x} \quad (4.5.6)$$

in which  $h(x, t)$  denotes the height of the gas-liquid interface above the bottom of the pipe. From the definition for the deviatoric part of the stress tensor in an incompressible flow it follows that  $D_k = 2\mu_k \frac{\partial u_k}{\partial x}$ . The Reynolds stress term is modelled in the usual way using Boussinesq assumption, namely  $T_k^{\text{Re}} = 2\mu_k^t \frac{\partial u_k}{\partial x}$  in which  $\mu_k^t$  denotes the turbulent viscosity in phase  $k$ . Using these results, together with (4.5.6) in (4.5.5) and multiplying the resulting equation by  $A$ , we obtain the following momentum conservation equations

$$\begin{aligned} \frac{\partial}{\partial t} (A_L \rho_L u_L) + \frac{\partial}{\partial x} (c_{Lv} A_L \rho_L u_L^2) &= -A_L \frac{\partial p_{LI}}{\partial x} + 2 \frac{\partial}{\partial x} \left( A_L \mu_L^e \frac{\partial u_L}{\partial x} \right) \\ &\quad - \rho_L g' A_L - \tau_{Lw} s_L + \tau_{LISI} \end{aligned} \quad (4.5.7a)$$

$$\begin{aligned} \frac{\partial}{\partial t} (A_G \rho_G u_G) + \frac{\partial}{\partial x} (c_{Gv} A_G \rho_G u_G^2) &= -A_G \frac{\partial p_{GI}}{\partial x} + 2 \frac{\partial}{\partial x} \left( A_G \mu_G^e \frac{\partial u_G}{\partial x} \right) \\ &\quad - \rho_G g' A_G - \tau_{Gw} s_G - \tau_{GISI} \end{aligned} \quad (4.5.7b)$$

In the above equations  $\mu_k^e = \mu_k + \mu_k^t$  denotes the effective viscosity in phase  $k$  and  $g' = g (\cos \beta \frac{\partial h}{\partial x} + \sin \beta)$ . Note that we have chosen the positive sign for the interfacial shear stress in the liquid phase while the negative sign is chosen for the gas phase. The reason for this is that the gas phase usually moves faster than the liquid phase thus exerting a positive force in the  $x$ -direction on the liquid phase.

In order to complete the model, we need to consider the jump conditions. Since we have assumed that there is no mass transfer between phases, that is  $\Gamma_k = 0$ , it follows that the jump condition (4.4.9) is satisfied identically. With the assumption of no mass transfer, the normal component of the momentum jump condition given by (4.4.12) reduces to  $M_1^{(n)} + M_2^{(n)} = m_i^{(n)}$ . Using the constitutive relation (2.2.7) and the definition of  $\bar{\mathbf{M}}_k$  it follows that  $\bar{\mathbf{M}}_k^{(n)} = \overline{-p \nabla X_k + \mathbf{d}_{nk} \delta(\mathbf{x} - \mathbf{x}_i)}$  and  $\bar{\mathbf{M}}_k^{(t)} = \overline{\mathbf{d}_{tk} \delta(\mathbf{x} - \mathbf{x}_i)}$  in which  $\mathbf{d}_{nk}$  and  $\mathbf{d}_{tk}$  denote the normal and tangential components of the stress vector  $\mathbf{D} \cdot \mathbf{n}_k$ . Considering the normal component of the momentum jump condition, we make the approximation

that the normal stress term  $\overline{\mathbf{d}_{nk}\delta(\mathbf{x} - \mathbf{x}_i)}$  is small compared with the pressure term  $p\overline{\nabla X_k}$ . This assumption is usually valid for liquid-liquid or liquid-gas interfaces since a free surface will deform under the action of fluid motion so that large normal velocity gradients are uncommon near a free surface. Thus

$$M_k^{(n)} = \langle \overline{\mathbf{M}}_k^{(n)} \rangle \cdot \mathbf{i} \simeq -\langle p\overline{\nabla X_k} \rangle \cdot \mathbf{i} \simeq -p_{kI} \langle \overline{\nabla X_k} \rangle \cdot \mathbf{i} \quad (4.5.8)$$

with  $p_{kI}$  denoting the mean interfacial pressure in phase  $k$ . We also have  $\overline{\mathbf{m}}_i^{(n)} = \overline{\sigma C \nabla X_1} \simeq \sigma \overline{C} \langle \nabla X_1 \rangle$  with  $\overline{C}$  denoting the mean curvature of the interface so that

$$m_i^{(n)} = \langle \overline{\mathbf{m}}_i^{(n)} \rangle \cdot \mathbf{i} = \sigma \overline{C} \langle \nabla X_1 \rangle \cdot \mathbf{i} \quad (4.5.9)$$

Combining (4.5.8) and (4.5.9) it follows that the normal component of the jump condition reduces to

$$p_{LI} - p_{GI} = \sigma \overline{C} \quad (4.5.10)$$

We finally consider the tangential components (4.4.13) of the jump conditions. With the definitions given earlier, it follows that the interfacial stress vector can be written like  $\mathbf{D} \cdot \mathbf{n}_k = \mathbf{d}_{nk} + \mathbf{d}_{tk}$  so that

$$M_k^{(t)} = \langle \overline{\mathbf{M}}_k^{(t)} \rangle \cdot \mathbf{i} = \langle \overline{\mathbf{d}_{tk}\delta(\mathbf{x} - \mathbf{x}_i)} \rangle \cdot \mathbf{i} = \langle \overline{\mathbf{D} \cdot \mathbf{n}_k - \mathbf{d}_{nk}\delta(\mathbf{x} - \mathbf{x}_i)} \rangle \cdot \mathbf{i}$$

If we now assume that  $\mathbf{n}_1 \cdot \mathbf{i} \ll 1$  it follows that  $\mathbf{d}_{nk} \cdot \mathbf{i} \ll 1$  and hence (4.4.13) reduced to the continuity of shear stress condition

$$\tau_{LI} = \tau_{GI} \quad (4.5.11)$$

While the assumption  $\mathbf{n}_1 \cdot \mathbf{i} \ll 1$  may appear arbitrary it is, in fact, central to the development of a hydraulic model for pipe flow. Namely, central to the model development is the assumption that the mass and momentum fluxes are primarily aligned with the axis of the pipe. It can be shown formally that this assumption is equivalent to demanding that interfacial gradients are small, that is  $\mathbf{n}_1 \cdot \mathbf{i} \ll 1$ .

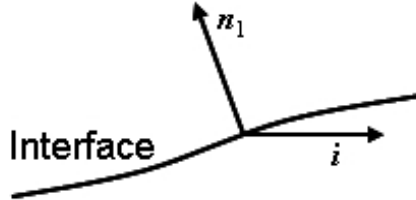


Figure 4.5.3: Interfacial configuration. The hydraulic model requires  $\mathbf{n}_1 \cdot \mathbf{i} \ll 1$ .

This completes the general two-fluid model for the case of stratified flow and the governing equations are summarized in table 4.1. Note that the two-fluid model is still not fully specified by the equations listed in Table 4.1 since important *closure relations* are required which link the interfacial and wall shear stresses to the mean liquid and gas velocities. The closure relations will be discussed in some detail in chapter 5.

Mass Conservation
$\frac{\partial}{\partial t} (A_L \rho_L) + \frac{\partial}{\partial x} (A_L \rho_L u_L) = 0$
$\frac{\partial}{\partial t} (A_G \rho_G) + \frac{\partial}{\partial x} (A_G \rho_G u_G) = 0$
Momentum Conservation
$\frac{\partial}{\partial t} (A_L \rho_L u_L) + \frac{\partial}{\partial x} (c_{Lv} A_L \rho_L u_L^2) = -A_L \frac{\partial p_{LI}}{\partial x} + 2 \frac{\partial}{\partial x} \left( A_L \mu_L^e \frac{\partial u_L}{\partial x} \right) - \rho_L g' A_L - \tau_{Lw} s_L + \tau_{LIsI}$
$\frac{\partial}{\partial t} (A_G \rho_G u_G) + \frac{\partial}{\partial x} (c_{Gv} A_G \rho_G u_G^2) = -A_G \frac{\partial p_{GI}}{\partial x} + 2 \frac{\partial}{\partial x} \left( A_G \mu_G^e \frac{\partial u_G}{\partial x} \right) - \rho_G g' A_G - \tau_{Gw} s_G - \tau_{GISI}$
Jump Conditions
$p_{LI} - p_{GI} = \sigma \bar{C}$
$\tau_{LI} = \tau_{GI}$

**Table 4.1** Summary of the two-fluid equations for stratified flow. The reduced gravity is defined via  $g' = g \left( \cos \beta \frac{\partial h}{\partial x} + \sin \beta \right)$ .

Before we proceed, it is important to retrace our steps and recall how these equations were obtained. Starting with the general conservation equations for mass and momentum, we derived the conservation equations for a two-fluid mixture. These mixture equations were subsequently reduced to a one-dimensional set of conservation equations through the process of area averaging. However, each time we perform an averaging operation we have to make sure that the terms we retain in the equations are consistent with the averaging procedure. Let us therefore focus on the area-averaging operation. We have to keep in mind that through the area-averaging we essentially remove all information about spatial variations which occur on a length scale less than one pipe diameter. Physical effects on these short length scales can not be modelled by the one-dimensional equations.

The terms containing the highest spatial derivatives in physical models, are the terms associated with physical effects on the smallest length scales. For this reason, the axial diffusion term in the momentum conservation equations and the surface tension term in the interfacial jump condition have to be examined more carefully. Let us start with the axial diffusion term. If  $\mathcal{L}$  denotes the length scale associated with axial diffusion term, then for the liquid phase this term scales as  $\frac{\partial}{\partial x} (A_L \mu_L^e \frac{\partial u_L}{\partial x}) \sim A_L \mu_L^e u_L / \mathcal{L}^2$ . This term should be retained in the momentum equation if it is of the same order of magnitude as other terms that can not be neglected with certainty. A term that must be retained is the wall shear stress term which scales as  $\tau_{Lw} s_L \sim \rho_L u_L^2 f D$  in which we have used the closure relation (2.4.3). In order for the diffusive term and the wall shear stress term to be similar in magnitude, the length scale  $\mathcal{L}$  must scale as

$$\mathcal{L} \sim D \times f^{-1/2} \times \text{Re}_L^{-1/2}$$

in which the Reynolds number is defined via  $\text{Re}_L = \rho_L u_L D / \mu_L^e$ . In most cases the Reynolds number of the flow will be large which implies that length scale  $\mathcal{L}$  will be much smaller than the pipe diameter. This observation is clearly problematic: we have retained a term in the equations that can not be justified in view of the area-averaging process. The analysis shows that strictly-speaking, the axial diffusion terms should be removed from the momentum equations. A similar analysis shows that the term containing the surface tension coefficient should also be removed (see exercise 4.6).

So, why not simply remove the terms in the equations that cannot be justified? It turns out that without the axial diffusion terms included, the mathematical properties of the equations as given in table 4.1, are such that numerical solutions of these equations may exhibit unphysical effects. The reason for these unphysical effects is related to the fact that without the higher-order derivatives included, there are no mechanisms in the equations that remove or dampen small-scale disturbances. Without any damping, these

small-scale (arbitrary and unphysical) disturbances will grow in amplitude and will lead to meaningless solutions. A more in-depth discussion of this problem will be given in chapter 8.

## 4.6 The drift-flux model

The area-averaged two-fluid model as presented in previous sections represents the most complete hydraulic formulation for two phases flowing simultaneously in a pipe. Compared with solving the full three-dimensional multiphase problem, it is evident that solving the coupled set of partial differential equations as specified in table 4.1 represents a significant simplification. Even so, solving the full two-fluid problem numerically is not trivial. It is, therefore, natural to ask how this model can be simplified while retaining most of the essential physics captured by the model. One step in this direction is achieved by assuming that the two phases behave as some sort of mixture and that this mixture can be modelled by a single "equivalent" momentum equation. The idea here is to focus on the relative motion of the phases rather than on the motion of the individual phases. Since the mixture we will be dealing with is not homogeneous, we need to retain the separate mass conservation equations for each of the phases. Hence, subject to the assumption that there is no exchange of mass between the phases, we obtain from (4.4.4)

$$\frac{\partial}{\partial t} (\alpha_1 \rho_1) + \frac{\partial}{\partial x} (\alpha_1 \rho_1 u_1) = 0 \quad (4.6.1a)$$

$$\frac{\partial}{\partial t} (\alpha_2 \rho_2) + \frac{\partial}{\partial x} (\alpha_2 \rho_2 u_2) = 0 \quad (4.6.1b)$$

It should be pointed out that the drift flux-model can describe stratified as well as dispersed flow so that no explicit assumption is required about the cross-sectional phase distribution at this stage. We next add the momentum equations as given in (4.4.8) to yield

$$\begin{aligned} \frac{\partial}{\partial t} (\alpha_1 \rho_1 u_1 + \alpha_2 \rho_2 u_2) + \frac{\partial}{\partial x} (\alpha_1 \rho_1 u_1^2 + \alpha_2 \rho_2 u_2^2) &= \\ - \frac{\partial p}{\partial x} - g(\rho_1 \alpha_1 + \rho_2 \alpha_2) \sin \beta - \frac{4}{D} \tau & \end{aligned} \quad (4.6.2a)$$

The following simplifications have been made in order to obtain the equivalent momentum equation as given above. For the profile coefficients we have taken  $c_{uk} = 1$  and by neglecting the axial momentum diffusion terms, we obtain  $\frac{\partial}{\partial x} \Sigma \alpha_k (T_k + T_k^{\text{Re}}) \simeq \frac{\partial}{\partial x} p$ . In addition we have introduced the notation  $\alpha_{1w} T_{1w} + \alpha_{2w} T_{2w} = \tau$  with  $\tau$  denoting the wall shear stress. Finally, (4.4.12) and (4.4.13) have been used and we have assumed that the interfacial momentum source  $m_i^{(n)}$  may be neglected in comparison with the other source terms on the right hand side of (4.6.2a). The shear stress is then modelled in the usual manner given by (2.4.3) with appropriate expressions for the mixture density, mixture velocity and friction factor.

By adding the two momentum equations we have essentially obtained a momentum equation for a mixture in which the void fraction is not constant. However, the model is not complete since we are lacking an equation for  $u_1$  (or  $u_2$ ): information has to be supplied in order to make up for the loss of one of the momentum equations. This information is supplied in terms of an equation that tells us something about the relative velocity of the different phases. This important equation is called the slip law and it is essentially a closure relation that needs to be determined experimentally. In order to understand the physical meaning of the slip law it is instructive to consider the concentration profile of a dispersed bubble phase in a vertical flow. To that end consider a bubble in a region near the pipe wall where there is a velocity gradient.

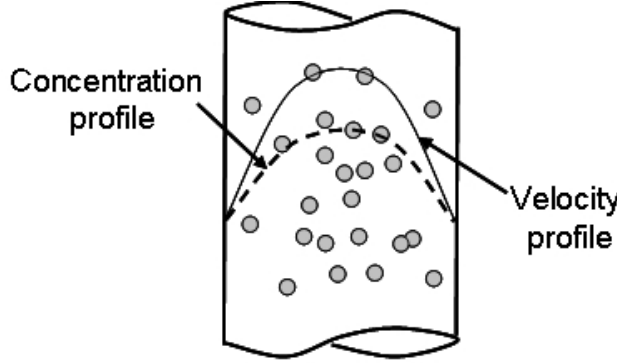


Figure 4.6.1: Dispersed phase concentration profile in a vertical flow.

A force balance shows that there is a force on the bubble pointing away from the pipe wall, perpendicular to the lines of constant shear. This force, called the Saffman lift force, is due to the pressure distribution developed on the bubble resulting from rotation induced by the shearing forces. The slightly higher fluid velocity on the side of the bubble facing away from the wall leads to a lower dynamic pressure on this side thus forcing the bubble away from the pipe wall. As a result of the Saffman lift force, the dispersed bubble concentration near the centre of the pipe is larger than that near the pipe walls. Hence, when averaged across the area of the pipe, the velocity of the dispersed gas phase exceeds the mixture velocity. This is the case, even when there is no velocity difference between the bubbles and the local liquid velocity. The question is now how to quantify this effect. In order to answer this question, we start by defining the flux of phase  $k$  via

$$\bar{q}_k = \bar{\alpha}_k \bar{\mathbf{v}}_k^{x\rho} \cdot \mathbf{i}$$

The total flux along the axis of the pipe is then given by  $\bar{q} = \sum_k \bar{\alpha}_k \bar{\mathbf{v}}_k^{x\rho} \cdot \mathbf{i}$  and it is easy to show that the mixture velocity and the area-averaged flux are related via  $U_{1SL} + U_{2SL} = \langle \bar{q} \rangle$  in which  $\langle \cdot \rangle$  denotes the area-average. Henceforth the notation introduced in section 4.4 will be used, thus  $\langle \bar{q} \rangle = q$  and  $\langle \bar{\alpha}_2 \rangle = \alpha_2$  etc. We now introduce the drift velocity. This velocity is defined to be the velocity of a given phase relative to the flux  $\bar{q}$ . Without loss of generality we now assume that the dispersed phase is associated with  $k = 2$ , and we define the drift velocity according to

$$\bar{v}_{2q}^{x\rho} = \bar{\mathbf{v}}_2^{x\rho} \cdot \mathbf{i} - \bar{q} \quad (4.6.3)$$

In the case where  $\bar{v}_{2q}^{x\rho} \equiv 0$  it is readily found that  $\bar{\mathbf{v}}_1^{x\rho} \cdot \mathbf{i} = \bar{\mathbf{v}}_2^{x\rho} \cdot \mathbf{i}$  which implies a state of perfect mixing. In an experimental setup we generally do not know the velocities of each of the phases. However we generally do know the volume flow rate of each of the phases and in particular we know  $q_2 = \langle \bar{\alpha}_2 \bar{\mathbf{v}}_2^{x\rho} \cdot \mathbf{i} \rangle = U_{2SL}$ . Thus, rather than working with equation (4.6.3) directly, we first multiply it by  $\bar{\alpha}_2$  and then take the area-average of the whole equation. Proceeding as outlined, we readily obtain

$$u_2 = \frac{\langle \bar{\alpha}_2 \bar{q} \rangle}{\alpha_2} + \frac{\langle \bar{\alpha}_2 \bar{v}_{2q}^{x\rho} \rangle}{\alpha_2} \quad (4.6.4)$$

The velocity  $u_2$  is defined via  $u_2 = \langle \bar{\alpha}_2 \bar{\mathbf{v}}_2^{x\rho} \cdot \mathbf{i} \rangle / \alpha_2$ , in line with the weighted area-averages introduced in section 4.4. At this point it is useful to introduce the distribution parameter  $C_0$ , defined according to

$$C_0 = \frac{\langle \bar{\alpha}_2 \bar{q} \rangle}{\alpha_2 q}$$

Using the above expression together with (4.6.4) we find

$$u_2 = C_0 q + u_{2d} \quad (4.6.5)$$

in which we have introduced the weighted mean drift velocity  $u_{2d} = \frac{\langle \bar{\alpha}_2 \bar{v}_{2q}^{x\rho} \rangle}{\bar{\alpha}_2}$ . Before proceeding, let us discuss the physical meaning of the distribution parameter  $C_0$ . Recall that the starting point of the above analysis was a desire to quantify the average velocity of a dispersed phase relative to that of the continuous phase. It was remarked that this relative velocity could be the result of both velocity profile and concentration profile variations across the pipe cross section. It is precisely this effect which is captured by  $C_0$ : the distribution parameter is a measure of how strongly  $\bar{\alpha}_2$  varied across the cross section of the pipe. Only in the case of a perfectly mixed flow in which  $\bar{\alpha}_2$  is constant across the whole cross section of the pipe, it is found that  $C_0 = 1$  in all other cases  $C_0 > 1$ .

Mass conservation
$\frac{\partial}{\partial t} (\alpha_1 \rho_1) + \frac{\partial}{\partial x} (\alpha_1 \rho_1 u_1) = 0$
$\frac{\partial}{\partial t} (\alpha_2 \rho_2) + \frac{\partial}{\partial x} (\alpha_2 \rho_2 u_2) = 0$
Momentum Conservation
$\frac{\partial}{\partial t} (\alpha_1 \rho_1 u_1 + \alpha_2 \rho_2 u_2) + \frac{\partial}{\partial x} (\alpha_1 \rho_1 u_1^2 + \alpha_2 \rho_2 u_2^2) = - \frac{\partial p}{\partial x} - g(\rho_1 \alpha_1 + \rho_2 \alpha_2) \sin \beta - \frac{4}{D} \tau$
Closure Relations
$u_2 = C_0 q + u_{2d}$
$u_{2d} = u_{2d}(\alpha, u_m, \dots)$ and $C_0 = C_0(\alpha, u_m, \dots)$
$\tau = \frac{1}{8} \rho_m u_m^2 f_m$

**Table 4.2:** Summary of the drift-flux equations.

If we assume that the drift velocity  $u_{2d} \ll u_2$  it follows from (4.6.5) that

$$\alpha_2 \simeq \frac{1}{C_0} \frac{U_{2SL}}{U_{1SL} + U_{2SL}}$$

where we have used  $u_2 = q_2/\alpha_2 = U_{2SL}/\alpha_2$ . In the case of a homogeneously mixed flow, the dispersed phase volume fraction would be given by the second fraction in the above equation. Clearly, the influence of radial concentration variations is taken care of by the factor  $1/C_0$ . Hence, if the dispersed phase is concentrated in the region of the flow where the velocities are highest (resulting in  $C_0 > 1$ ), the measured area-averaged concentration of the dispersed phase is significantly lower than that found in the case of a homogeneously mixed flow.

So far, closure relations for the drift velocity  $u_{2d}$  and numerical values for the distribution parameter  $C_0$  have not been discussed in detail. Not surprisingly, both the drift velocity and the distribution parameter are dependent on flow details associated with a given parameter set (such as flow regime and dispersed-phase volume fraction). Some specific closure relations will be discussed in the following section.

## 4.7 Area-averaged model for dispersed flow

The drift flux model as introduced in the previous section has some of the characteristics of a mixture model (only one "equivalent" momentum equation is employed). However, since the model does not consistently employ mixture quantities (like mixture densities or mixture velocities) it is not truly a model for a two-phase mixture. Such a model will be introduced here. Let us briefly return to the flow regime map shown in figure

3.2.3. There we see that for sufficiently large values of the superficial liquid velocity (typically exceeding  $1\text{m/s}$ ) the gas phase will be dispersed into the liquid phase when the volume fraction of gas is sufficiently small. A similar situation is observed in the case of liquid-liquid flow but there a dispersed-flow situation is easier to obtain due to the strongly reduced buoyancy forces. However, even in this case, buoyancy forces can not be neglected entirely as is shown in figure 4.7.1. There we see that even when one of the liquids is fully dispersed, this does not necessarily mean that a spatially homogeneous mixture exists.

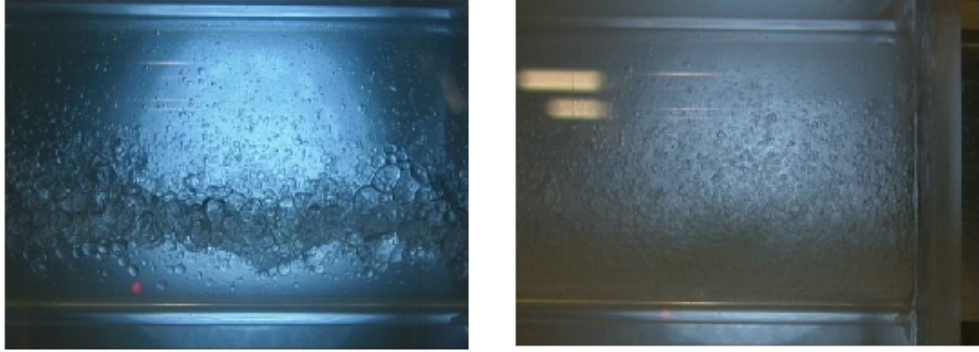


Figure 4.7.1: Examples of oil-water flow. On the left-hand side we see stratified oil-water flow with both oil and water drops dispersed in the continuous phase. On the right-hand side the flow is dispersed, oil-continuous (pictures by H.K. Kvandal).

When modelling a fully-mixed two-fluid system, it is tempting to treat this mixture as a single-phase system with some sort of averaged physical properties. To some extend this is indeed possible as will be shown below. The equations will reduce to one conservation equation for mass and one conservation equation for momentum. However, like in the drift-flux model, extra equations are required that take into account the effects associated with the difference in velocity between the phases, the so-called slip.

In order to obtain the mixture conservation equations we return to section 4.4 in which the general conservation equations in one-dimensional form were derived. First we consider the mass conservation equations. Adding the conservation equations for each phase as given in (4.4.4), we obtain

$$\frac{\partial}{\partial t} (\rho_m) + \frac{\partial}{\partial x} (\rho_m u_m) = 0 \quad (4.7.1)$$

In order to arrive at (4.7.1) we have used the jump condition (4.4.9) and we have defined the mixture density via

$$\rho_m = \sum_k \alpha_k \rho_k$$

and the mixture velocity via

$$u_m = \frac{1}{\rho_m} \sum_k \alpha_k \rho_k u_k$$

The momentum equation for the mixture is obtained by adding the momentum equations for each phase as given by (4.4.8). In order to proceed we first assume that the profile coefficients  $c_{kv}$  are equal to unity. On adding the momentum equations we obtain

$$\frac{\partial}{\partial t} (\rho_m u_m) + \frac{\partial}{\partial x} (\rho_m u_m^2) = \frac{\partial}{\partial x} (T_m + T^{\text{Re}} + T^D) + \frac{4}{D} T_w - \rho_m g_m + m_i^{(n)} \quad (4.7.2)$$

in which  $T_m = \sum_k \alpha_k T_k$  and  $T^{\text{Re}} = \sum_k \alpha_k T_k^{\text{Re}}$ . We note that an additional stress term  $T^D = -\sum_k \alpha_k \rho_k u_{km}^2$  is obtained in which

$$u_{km} = u_k - u_m. \quad (4.7.3)$$

denotes the diffusion velocity. The term  $T^D$  is called the diffusion stress and is the result of the mixture velocity being employed in the convective term on the left hand side of the momentum equation. The remaining terms on the right hand side of the momentum equation are the perimeter-averaged wall shear stress  $T_w = \frac{1}{\pi D} \int_{\partial A} \sum_k \bar{\alpha}_k \bar{T}_k : \mathbf{nids}$  and the gravitational force acting on the mixture  $g_m = \frac{1}{\rho_m} \sum_k \alpha_k \rho_k g_k$ . In addition we have the interface momentum source, denoted by  $m_i^{(n)}$ , resulting from the application of the jump condition (4.4.12). Finally, with the stress tensor of the usual form  $\mathbf{T} = -p \mathbf{I} + \mathbf{D}$  it follows that mixture stress  $T_m$  can be written like

$$T_m = \sum_k \alpha_k \left( -p_k + 2\mu_k \frac{\partial u_k}{\partial x} \right) = -p_m + \mu_m \frac{\partial u_m}{\partial x}$$

in which we have defined the mixture pressure  $p_m = \sum_k \alpha_k p_k$ . The mixture viscosity is defined via  $\mu_m = 2 \sum_k \alpha_k \mu_k \frac{\partial u_k}{\partial x} \times \left( \frac{\partial u_m}{\partial x} \right)^{-1}$  and is clearly a quantity that needs to be modelled. We will come back to this in section 6.3. The turbulent stresses also have to be modelled and the simplest approach, based on a Boussinesq-like argument commonly used in homogeneous turbulence modelling, is to write

$$T^{\text{Re}} = \mu_t \frac{\partial u_m}{\partial x}$$

in which  $\mu_t$  denotes a turbulent viscosity associated with the mixture. The presence of particles can both enhance and dampen turbulence (Brennen, 2005) so that  $\mu_t$  will, in general, be a function of the particle size and the particle concentration.

Before we proceed with a discussion of the additional closure relations, let us briefly return to the end of section 4.5. There we discussed the validity of terms in the equations containing higher-order spatial derivatives. The reason for giving these terms special attention was related to the fact that terms can only be retained in the equations if they are consistent with the inherent limitations of the model equations. We argued that terms containing second (or higher) derivatives describe physical processes on length scales that are small compared with the typical pipe diameter. This is not consistent with the limitations imposed by the area-averaging procedure which removes all information on length scales of the order of a pipe diameter. Hence, it was argued that all the terms involving second (or higher) derivatives could be neglected. A similar reasoning with respect to the terms in (4.7.2) shows that stress terms  $\mu_m \frac{\partial u_m}{\partial x}$  and  $\mu_t \frac{\partial u_m}{\partial x}$  as well as the interface momentum source term  $m_i^{(n)}$  should be neglected in the drift-flux equations. This does not mean, however, that the need to model the mixture viscosity is removed. Namely, the wall shear stress term  $T_w$  still requires a model for the mixture viscosity as will become evident below.

In formulating the momentum equation of the mixture, the diffusion velocity  $u_{km}$  was introduced. This implies that the diffusion velocity has to be related to the mixture velocity  $u_m$  in order to obtain a closed system of equations. To obtain the additional closure relations we first introduce the relative velocity between the phases denoted by  $u_r = u_2 - u_1$ . It is easy to show that the relative and diffusion velocities are related via  $u_{1m} = -\frac{\alpha_2 \rho_2}{\rho_m} u_r$  and  $u_{2m} = \frac{\alpha_1 \rho_1}{\rho_m} u_r$  from which it follows immediately that

$$\alpha_1 \rho_1 u_{1m} + \alpha_2 \rho_2 u_{2m} = 0 \quad (4.7.4)$$

At this point it is convenient to assume (without loss of generality) that phase  $k = 2$  is the dispersed phase and it is natural to ask how the diffusion velocity  $u_{2m}$  can be related to the drift velocity  $u_{2d}$  as introduced in equation (4.6.5). It is not hard to show that the following relation holds

$$u_{2m} = \frac{\rho_1}{\rho_m C_0 - \rho_1(C_0 - 1)} [u_{2d} + (C_0 - 1) \times u_m] \quad (4.7.5)$$

For the special case in which the mixture is homogeneous, we have  $C_0 = 1$  and it follows that  $u_{2m} = \frac{\rho_1}{\rho_m} u_{2d}$ . Once a closure relation for the drift velocity is established, the diffusion velocities  $u_{km}$  are found from (4.7.4) and (4.7.5). This implies that the diffusion stress  $T^D$  can be evaluated once the phase fraction  $\alpha_1$  or  $\alpha_2$  is known. This information is not supplied by the mass conservation equation (4.7.1) so that an additional equation is required for the dispersed phase fraction. The additional equation is called the diffusion equation and it is obtained directly from the mass conservation equation for phase 2 which is assumed to be the dispersed phase. Using (4.4.4) and (4.7.3) we get

$$\frac{\partial}{\partial t} (\alpha_2 \rho_2) + \frac{\partial}{\partial x} (\alpha_2 \rho_2 u_m) = \Gamma_2 - \frac{\partial}{\partial x} (\alpha_2 \rho_2 u_{2m})$$

A summary of the of the conservation equations and closure relations that formulate the mixture model is given in table 4.3.

Mass conservation
$\frac{\partial}{\partial t} (\rho_m) + \frac{\partial}{\partial x} (\rho_m u_m) = 0$
Momentum Conservation
$\frac{\partial}{\partial t} (\rho_m u_m) + \frac{\partial}{\partial x} (\rho_m u_m^2) = -\frac{\partial p_m}{\partial x} + \frac{\partial T^D}{\partial x} + \frac{4}{D} T_w + \rho_m g_m$
Diffusion Equation
$\frac{\partial}{\partial t} (\alpha_2 \rho_2) + \frac{\partial}{\partial x} (\alpha_2 \rho_2 u_m) = \Gamma_2 - \frac{\partial}{\partial x} (\alpha_2 \rho_2 u_{2m})$
Constitutive equations and closure relations
$u_{2m} = \frac{\rho_1}{\rho_m C_0 - \rho_1(C_0 - 1)} [u_{2d} + (C_0 - 1) \times u_m]$ and $\alpha_1 \rho_1 u_{1m} + \alpha_2 \rho_2 u_{2m} = 0$
$T^D = -\sum_k \alpha_k \rho_k u_{km}^2$
$u_{2d} = u_{2d}(\alpha_2, g_m, u_m, \dots)$ , $\Gamma_2 = \Gamma_2(\alpha_2, g_m, u_m, \dots)$ and $C_0 = C_0(\alpha_2, g_m, u_m, \dots)$
$T_w = \frac{1}{8} \rho_m u_m^2 f_m$

**Table 4.3:** Summary of the mixture equations.

For a flow without mass exchange we have  $\Gamma_2 \equiv 0$  so that closure relations for the drift velocity and the distribution parameter are required. Let us start with the distribution parameter. Experiments show that the numerical value of the distribution parameter  $C_0$  lies in the range between 1.0 and 1.5 and a value of 1.2 is often used. A thorough analysis of experimental results related to dispersed gas-liquid flows leads Ishii & Hibiki (2006) to the expression

$$C_0 = 1.2 - 0.2 \sqrt{\rho_G / \rho_L}$$

In low-pressure systems where  $\rho_G \ll \rho_L$  it follows that a good approximation of the distribution parameter is given by  $C_0 \simeq 1.2$ . In the case of annular flow the distribution parameter is found to be close to unity. Shi *et al* (2005) propose similar values for the distribution parameter for the case of oil-water flow.

The final closure required by the mixture and the drift flux model is an expression for the drift velocity. In general we expect the drift velocity to be influenced by main parameters of the problem as well as the flow regime. For example, for the case of fully-dispersed, vertical flow we may, as a first approximation, write

$$u_{2d} = U_\infty \times (1 - \alpha_2)^n$$

in which  $U_\infty$  denotes the terminal velocity of a particle in an infinite medium (for details refer to section 6.2). The term  $(1 - \alpha_2)^n$  indicates that the terminal velocity is reduced by the presence of other dispersed-phase particles. In section 6.2 particle drift in a suspension of other particles is discussed and there the value of the exponent  $n$  is discussed in some detail (typically,  $n \simeq 2$ ). In the case of slug flow, a commonly-used expression for the drift velocity is

$$u_{2d} = 0.35 \left( \frac{g\Delta\rho D}{\rho_1} \right)^{1/2}$$

while for the case of churn-turbulent bubbly flow the drift velocity can be described by

$$u_{2d} = 1.53 \left( \frac{\sigma g \Delta \rho}{\rho_1^2} \right)^{1/4}$$

Ishi & Hibiki (2006) present an extensive discussion of different closure relations for both the distribution parameter and the drift velocity in particular in relation to different flow regimes. Shi *et al* (2005) discuss expressions for the distribution coefficient and the drift velocity for the cases of gas-liquid and oil-water flow.

## 4.8 The Control Volume Method

The equations as summarized in Table 4.1 have followed rigorously from the Navier-Stokes equations. Namely, starting with the local instant formulations for mass and momentum conservation, we formulated the general conservation equations for a two-fluid mixture which were subsequently reduced to a set of one-dimensional conservation equations by taking the cross sectional average in a pipe-like geometry. The rigorous derivation has the advantage of highlighting the approximations which belie the derivation of the equations. The drawback is, however, that the derivation of the equations is rather laborious. Therefore, in many practical applications one uses a different method to arrive at the same equations as those summarized in Table 4.1. This method is called the control volume method.

The control volume method takes as a starting point the general conservation equation for a quantity  $\rho\Psi$  associated with the fluid (cf. section 2.2). The total amount of  $\rho\Psi$  that is enclosed by a surface  $S$  is then  $\int_V \rho\Psi dV$  where  $V$  is the volume bounded by  $S$ . The total rate of change of  $\rho\Psi$  is the result of surface and volume sources that are denoted by  $\Sigma$ . Mathematically, this can be written like

$$\frac{d}{dt} \int_V \rho\Psi dV = \Sigma$$

We now use Reynolds transport theorem (1) together with the divergence theorem to reformulate the integral on the left-hand-side, giving

$$\int_V \frac{\partial}{\partial t}(\rho\Psi)dV + \int_S \rho\Psi \mathbf{v} \cdot \mathbf{n} dS = \Sigma \quad (4.8.1)$$

The integral equation as given above is the starting point of the control volume method. As an example of how this method can be used, we study the case of stratified gas-liquid flow in a pipe where we assume that the axis of the pipe is aligned with the  $x$ -axis. Let us first consider the liquid phase. In order to derive the relevant equations we consider a control volume bounded by the pipe wall  $S_w$ , the two surfaces  $A_L(x, t)$  and  $A_L(x + \Delta x, t)$  and the interfacial surface element  $A_I$ , see figure 4.8.1. Taking the distance  $\Delta x$  separating the surfaces  $A_L(x, t)$  and  $A_L(x + \Delta x, t)$  sufficiently small, we may approximate the volume integrals in (4.8.1) via

$$\int_V \frac{\partial}{\partial t}(\rho_L\Psi)dV \simeq \Delta x \int_{A_L(x,t)} \frac{\partial}{\partial t}(\rho_L\Psi)dS$$

while the surface integral yields

$$\int_S \rho_L \Psi \mathbf{v} \cdot \mathbf{n} dS = \int_{A_L(x+\Delta x,t)} \rho_L \Psi v_n dS - \int_{A_L(x,t)} \rho_L \Psi v_n dS + \int_{A_I} \rho_L \Psi \mathbf{v} \cdot \mathbf{n} dS$$

where  $v_n = \mathbf{v} \cdot \mathbf{n}|_{A_L(x+\Delta x)}$ . Note that there is no contribution from the pipe wall in the surface integral since  $\mathbf{v} \cdot \mathbf{n}|_{S_w} = 0$ . The interfacial surface element  $A_I \simeq s_I \Delta x$  where  $s_I$  denotes the interfacial cord length (see figure 4.5.2). The last of the above integrals can thus be approximated via  $\int_{A_I} \rho_L \Psi \mathbf{v} \cdot \mathbf{n} dS \simeq s_I \Delta x \rho_L \Psi_I v_I$  with  $\Psi_I = \Psi|_{A_I}$  and  $v_I = \mathbf{v} \cdot \mathbf{n}|_{A_I}$ . A direct application of Leibnitz's rule (see exercise 4.5) yields

$$\int_{A_L(x,t)} \frac{\partial}{\partial t}(\rho_L\Psi)dS + \rho_L \Psi_I s_I v_I = \frac{\partial}{\partial t} \int_{A_L(x,t)} \rho_L \Psi dS \quad (4.8.2)$$

so that the generic conservation euqation (4.8.1) can be approximated by

$$\Delta x \frac{\partial}{\partial t} \int_{A_L(x,t)} \rho_L \Psi dS + \int_{A_L(x+\Delta x,t)} \rho_L \Psi v_n dS - \int_{A_L(x,t)} \rho_L \Psi v_n dS \simeq \Sigma \quad (4.8.3)$$

Let us now apply the above equation to the case of mass conservation, that is, we take  $\Psi = 1$  and  $\Sigma = 0$  (that is, no mass sources). Taking the result, dividing by  $\Delta x$  and taking the limit  $\Delta x \rightarrow 0$  we find immediately that

$$\frac{\partial}{\partial t} (A_L \rho_L) + \frac{\partial}{\partial x} (A_L \rho_L v_L) = 0$$

in which  $v_L$  denotes the mean velocity in the liquid phase defined according to  $A_L v_L = \int_{A_L} v_n dS$ . An analogous expression is obtained for mass conservation in the gas phase. In order to obtain the momentum conservation equations we take  $\Psi = v_n$  and we set  $\Sigma$  equal to the total force acting on the control volume. Let us focus once again on the liquid phase. Defining the distribution coefficient according to  $c_{Lv} = \frac{1}{A_L v_L^2} \int_{A_L} v_n^2 dS$ , it follows that for sufficiently small  $\Delta x$  equation (4.8.3) reduces to

$$\Delta x \left[ \frac{\partial}{\partial t} (A_L \rho_L v_L) + \frac{\partial}{\partial x} (c_{Lv} A_L \rho_L v_L^2) \right] = \Sigma \quad (4.8.4)$$

The forces acting on the control volume in the liquid phase are

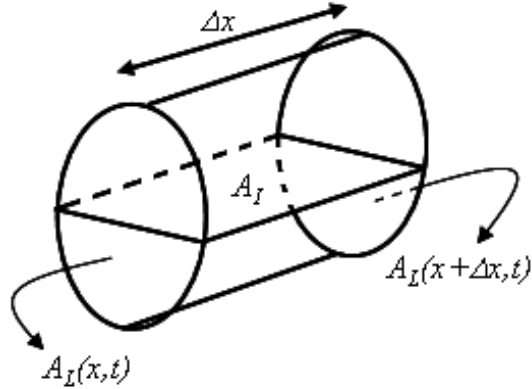


Figure 4.8.1: Schematic diagram of a control volume.

1. Forces due to wall and interfacial shear stresses,
2. Viscous Forces, and,
3. Pressure Forces

and hence  $\Sigma = F_{shear} + F_{viscous} + F_{pressure}$ . The shear forces give a contribution to the total force equal to

$$F_{shear} = \Delta x (-\tau_w s_w + \tau_{LI} s_I) \quad (4.8.5)$$

with  $\tau_{Lw}$  and  $\tau_{LI}$  denoting the wall and interfacial shear stresses respectively and  $s_w$ ,  $s_I$  are as defined in figure 4.5.2 (note that we have assumed that the gas phase moves faster than the liquid phase such that the interfacial shear contributes positively to the shear forces acting on the liquid phase). The viscous forces are related to axial velocity gradients and can be found by considering the contributions from the deviatoric stress tensor  $\mathbf{D}$  on the area elements  $A_L(x, t)$  and  $A_L(x + \Delta x, t)$ . It is not hard to show that one obtains

$$F_{viscous} = 2A_L \mu_L \frac{\partial u_L}{\partial x} \Big|_x - 2A_L \mu_L \frac{\partial u_L}{\partial x} \Big|_{x+\Delta x}$$

which in the limit  $\Delta x \rightarrow 0$  reduces to

$$F_{viscous} = -2 \frac{\partial}{\partial x} \left[ A_L \mu_L \frac{\partial u_L}{\partial x} \right] \Delta x \quad (4.8.6)$$

With reference to figure 4.8.2 it follows that the contribution due to pressure forces on the control volume is equal to

$$F_{pressure} = p_{LI} \delta A_L + \int_{A_L(x)} [p_{LI} + \rho_L g(h - y)] dS - \int_{A_L(x+\Delta x)} [p_{LI} + \rho_L g(h - y)] dS$$

Using Leibnitz's rule (c.f. exercise 4.3) and taking the limit  $\Delta x \rightarrow 0$  it follows that

$$F_{pressure} = -\Delta x \left( A_L \rho_L g \frac{\partial h}{\partial x} + A_L \frac{\partial p_{LI}}{\partial x} \right) \quad (4.8.7)$$

Combining (4.8.4)-(4.8.7) we obtain the momentum conservation equation for the liquid phase in the case of a horizontal pipe (c.f. table 4.1). A similar procedure yields the momentum conservation equation for the gas phase.

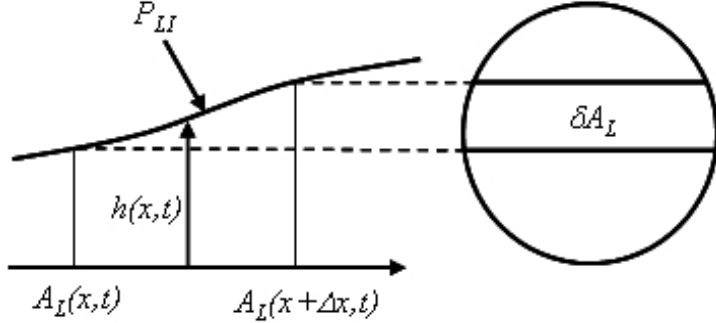


Figure 4.8.2: Schematic diagram used in deriving the pressure force.

The boundary condition at the interface is all that remains to be specified. Employing continuity of normal and tangential forces we find immediately that the interfacial conditions as given in equations (4.5.10) and (4.5.11).

It is evident that the conservation equations for mass and momentum can be derived readily using the control volume method. However, one has to be careful in ensuring that all relevant terms are included.

## 4.9 Exercises

**Exercise 4.1** Proof the validity of the transport equation (4.2.6). Hint: multiply all terms in this equation by a test function  $\phi$ , integrate over all space and time and manipulate the terms such that and space integral over the domain  $\Omega_k$  is obtained. Subsequently use Reynolds transport theorem (1) and the fact that  $\phi(t \rightarrow \pm\infty) = 0$

**Exercise 4.2** Prove the product rule (4.2.8). Hint: multiply the left-hand-side of the equation by a test function  $\phi$  and integrate over a domain  $\Omega$ . Manipulate the integrals using Green's theorem and subsequently use property (4.2.3) and (4.2.2) to obtain the required result.

**Exercise 4.3** Show that  $-\frac{\partial}{\partial x}(A_L p_L) + p_{LI} \frac{\partial A_L}{\partial x} = -A_L \frac{\partial p_{LI}}{\partial x} - \rho_L g A_L \cos \beta \frac{\partial h}{\partial x}$ . Hint: start with the expression for hydrostatic pressure, viz.  $\tilde{p}_L(x, y, t) = p_{LI}(x, t) + \rho_L(h(x, t) - y)g \cos \beta$ , and compute  $A_L p_L = \int_{A_L} \tilde{p}_L da$ . Subsequently use the Leibnitz-rule to obtain the desired result.

**Exercise 4.4** Consider a stratified flow in a pipe. Show that by assuming  $\mathbf{n}_1 \cdot \mathbf{i} \ll 1$ , the tangential component of the momentum jump condition yields the condition for continuity of stress at the interface  $\tau_{LI} = \tau_{GI}$ . Hint: start with the decomposition of the stress vector  $\overline{\mathbf{D} \cdot \mathbf{n}_k}$  into a normal and tangential component to the interface. Subsequently, employ the tangential stress condition definition (4.4.13) and the definition of the mean interfacial shear stress  $\tau_{kI} = \pm \overline{\mathbf{D} : \mathbf{n}_k \mathbf{i}}$  to obtain the required result.

**Exercise 4.5** Proof the validity of (4.8.2). Hint: use the fact that  $v_I = \frac{\partial h}{\partial t}$  where  $h$  denotes the height of the interface above the bottom of the pipe. Further show that  $\frac{\partial A_L}{\partial t} = \frac{\partial A_L}{\partial h} \frac{\partial h}{\partial t} = s_I \frac{\partial h}{\partial t}$ . Finally, use Leibnitz's rule to obtain the required result.

**Exercise 4.6** Let  $\mathcal{L}$  denote the length scale associated surface tension effects. Using exercise 2.1, show that  $\sigma\bar{C} \sim \sigma D/\mathcal{L}^2$ . By balancing the pressure gradient terms and the hydro-static terms in the momentum equations, show that  $p_{kI} \sim \mathcal{L}\rho_k g$  in which  $k = L, G$ . Hence show that  $\mathcal{L} \sim D/\sqrt[3]{Bo}$  in which the Bond number is defined as  $Bo = \Delta\rho g D^2/\sigma$ . Show that for air-water flow in a 10cm pipe,  $Bo \sim 10^4$  and finally show that the capillary length scale  $\mathcal{L} \ll D$ .

**Exercise 4.7** Show that the following relations hold between the diffusion velocities  $v_{km}$  and the relative velocity  $v_r$ :  $v_{1m} = -\frac{a_2\rho_2}{\rho_m}v_r$  and  $v_{2m} = \frac{a_1\rho_2}{\rho_m}v_r$

## 5 Fully developed stratified Flow

### 5.1 Introduction

Stratified flow is the flow regime that occurs when the velocity of each of the phases is relatively low. The reason is that inertia forces are not large enough to generate large waves which may lead to instabilities marking the onset of the intermittent flow regimes (elongated bubble flow or slug flow). In addition, at low velocities the dispersion of one phase into the second phase will not occur because the flow may be laminar or because turbulent forces are too weak to overcome buoyancy forces. This then means that a number of complex physical processes will not be present when the phase velocities are low enough. Hence, stratified flow is relatively easy to model even though complex closure relations are required. In this chapter we will focus on models for fully-developed stratified flow.

### 5.2 Stratified, laminar flow between two parallel plates

The problem that will be considered in this section is shown schematically in Figure 5.2.1. Two immiscible fluids with different but constant densities and viscosities flow between two infinite parallel plates which are situated between  $z = -h_1$  and  $z = h_2$ . A necessary condition for the flow to be stable is  $\rho_1 > \rho_2$  but note that this condition is not sufficient for stability since shear-induced instabilities may occur (these so called, Kelvin-Helmholtz instabilities, will be investigated later). The first issue we will consider is the position of the interface separating the two fluids. If the channel is sufficiently long we may assume that at some point, a long distance from the inlet, the flow will reach an equilibrium situation. This equilibrium situation is dictated by a balance between shear forces in the lower and upper liquid. The question we now want to answer is, given the volume flows of the lower and upper fluid, at what height does the fluid interface position itself? For simplicity we select the origin of the coordinate system at the interface at  $z = 0$  but we have to remember that, in general, we do not know where the interface is.

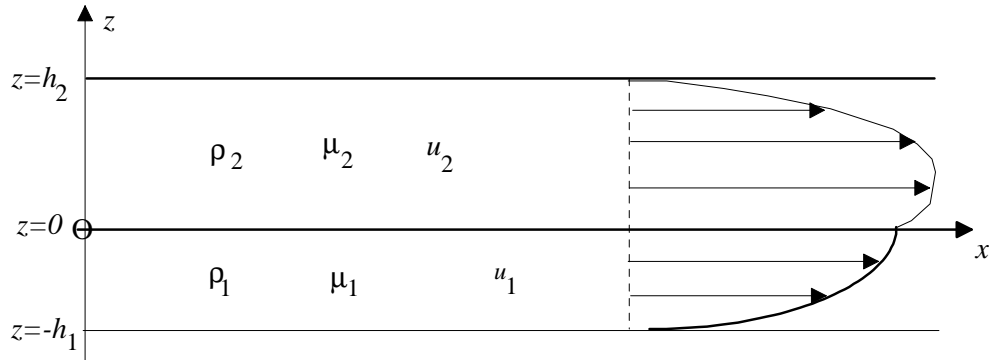


Figure 5.2.1: Laminar flow between parallel plates.

Our assumption that there exists a state of steady, fully developed flow implies that the fluid is flowing only in a direction parallel to the bounding plates. This means  $\mathbf{v}_k = (u_k(x, y, z), 0, 0)$ ,  $k = 1, 2$ . Given the fact that densities are assumed to be constant, it follows that the mass conservation equation reduces to  $\nabla \cdot \mathbf{v}_i = 0$  which, together with the unidirectional flow assumption yields immediately  $u_k = u_k(z)$ . The momentum equation in each phase is given by (2.2.6). Assuming a steady state, the time-derivative term in (2.2.6) vanishes while the non-linear convective term is identically zero due to the unidirectional flow assumption. The momentum equation in each of the phases reduces then to the simple form

$$\nabla \cdot \mathbf{T}_k - \rho_k \mathbf{g} = 0, \quad \text{for } k = 1, 2 \quad (5.2.1)$$

Applying the constitutive relation (2.2.7) and using the velocity field as specified above, it follows that the momentum equation in each of the phases reduces to

$$-\frac{\partial p_k}{\partial x} + \mu_k \frac{\partial^2 u_k}{\partial z^2} = 0 \quad \text{and} \quad -\frac{\partial p_k}{\partial z} - \rho_k g = 0 \quad \text{for } k = 1, 2 \quad (5.2.2)$$

The jump conditions at the interface  $z = 0$  require (c.f. exercise 2.1)

$$p_1(x, 0) = p_2(x, 0) \quad \text{and} \quad \mu_1 \frac{\partial u_1}{\partial z} = \mu_2 \frac{\partial u_2}{\partial z} \quad (5.2.3)$$

Integrating the hydrostatic equation in (5.2.2) and using the first of the jump conditions as given in (5.2.3), it immediately follows that  $p_k(x, z) = -\rho_k g z + P(x)$  in which  $P(x)$  is some unknown function denoting the interfacial pressure. Using the expression obtained for  $p_k(x, z)$  in the first equation in (5.2.2) it follows immediately that the velocities  $u_k$  are of the form

$$u_k(z) = -\frac{\Theta}{2\mu_k} z^2 + a_k z + b_k, \quad k = 1, 2 \quad (5.2.4)$$

in which  $a_k$  and  $b_k$  are, as yet, unknown constants and we have defined  $\Theta = -\frac{dP}{dx}$ . Four closure relations are required in order to be able to determine the unknown constants in the above equation. These relations are;

1. the no-slip boundary conditions on the solid boundaries,  $u_1(z = -h_1) = u_2(z = h_2) = 0$ ,
2. the condition of continuity of velocity at the interface,  $u_1(z = 0) = u_2(z = 0)$  and
3. the continuity of stress condition. as obtained from the jump condition, specified in (5.2.3).

Using these closure relations it follows after some algebra that the unknown constants are given by  $a_k = \frac{\Theta}{2\mu_k} \mathcal{H}$  and  $b_k = \frac{\Theta}{2} \mathcal{B}$  for  $k = 1, 2$  in which  $\mathcal{H} = \frac{\mu_1 h_2^2 - \mu_2 h_1^2}{\mu_1 h_2 + \mu_2 h_1}$  and  $\mathcal{B} = \frac{h_1 h_2 (h_1 + h_2)}{\mu_1 h_2 + \mu_2 h_1}$ . The shear stress, defined via  $\tau_k(y) = \mu_k \frac{du_k}{dy}$ , is easily shown to exhibit the same linear behaviour in each phase, namely  $\tau_1(z) = \tau_2(z) = \frac{1}{2}\Theta(\mathcal{H} - 2z)$ . The interfacial shear (shear stress at  $z = 0$ ) is then given by

$$\tau_I = \frac{\Theta}{2} \mathcal{H} \quad (5.2.5)$$

Before we proceed with finding the position of the interface we recall the concept of superficial velocity as introduced in chapter 3. The superficial velocity for a given phase is defined as the ratio of the volume flow of that phase divided by the total available flow area. For the problem under consideration we define  $Q_i$  to be the volume flow of phase  $i$  per unit width so that the superficial velocities become  $U_{iSL} = Q_i/(h_1 + h_2)$ . We now average the fluid velocity of each phase over the area available to that phase, denoting the resulting velocity by  $\bar{u}_k$ . It follows readily that the superficial and the average velocities are related via  $h_1 \bar{u}_1 = (h_1 + h_2) U_{1SL}$  and  $h_2 \bar{u}_2 = (h_1 + h_2) U_{2SL}$  while the average velocities are easily computed using (5.2.4). The resulting expressions are for the velocities in both phases proportional to the pressure gradient  $\Theta$ . Eliminating the pressure gradient between the expressions for the mean velocities gives a single equation

relating the mean velocities to the viscosities and liquid heights in each phase. Finally, we use the expressions for the superficial velocities to eliminate the average velocities and after some algebra we obtain

$$\frac{U_{1SL}}{U_{2SL}} - \frac{\mu_2 h_1}{\mu_1 h_2} \frac{6\mu_1 \mathcal{B} - 3h_1 \mathcal{H} - 2h_1^2}{6\mu_2 \mathcal{B} + 3h_2 \mathcal{H} - 2h_2^2} = 0 \quad (5.2.6)$$

The above equation is an example of what is known as the holdup equation in the multiphase flow literature. It is called a holdup equation since it is an equation that gives the equilibrium liquid height (essentially the liquid fraction) in terms of physical parameters defining the problem. The holdup equation as given above is easily shown to reduce to a fourth-order polynomial of the height ratio  $h_1/h_2$ . It is interesting to note that even for the relatively simple problem of laminar flow between two infinite, parallel plates, the problem of finding the equilibrium height of the interface involves finding the roots of a rather complex algebraic equation.

Let us now consider some special cases to illustrate roots of equation (5.2.6). For the case in which an equal amount of two immiscible fluids with identical physical properties is inserted between the plates, it is left as an exercise (see Exercise 5.1) to show that interface separating the two fluids is situated at equal distances from the plates. Approximate solutions to the holdup equation can be found for the cases in which  $\mu_1 \ll \mu_2$  or  $\mu_1 \gg \mu_2$ . Let us first consider the case with  $\mu_2 \ll \mu_1$ . Before we do the mathematics, let us use physical arguments to indicate what should happen. Let us assume that roughly the same amount of each phase is inserted between the plates which means that the superficial velocity of each phase is roughly the same. However, the mean velocity is going to be quite different in each phase since we have to maintain a balance of shear stresses at the interface separating the two fluids. With  $\mu_2 \ll \mu_1$  it follows from the shear stress relation in (5.2.3) that  $\frac{\partial u_1}{\partial z} \ll \frac{\partial u_2}{\partial z}$  and this can only be achieved when  $\max(u_2) \gg \max(u_1)$ . This in turn implies that  $\bar{u}_2 \gg \bar{u}_1$ . Using the definition of the superficial velocity we find that

$$\frac{\bar{u}_1}{\bar{u}_2} = \frac{U_{1SL}}{U_{2SL}} \times \frac{1 + h_2/h_1}{1 + h_1/h_2} \ll 1$$

which can only be achieved when  $h_1 \gg h_2$ . Hence, we find that the interface moves towards the upper solid plate. Clearly, the balance of shear stresses at the interface implies that the least-viscous fluid starts to move faster. Maintaining mass balance requires subsequently an associated reduction of the flow area.

Let us now do the mathematics. We have seen that the upper layer becomes thinner as the viscosity of the upper layer decreases. This suggests searching for solutions of (5.2.6) which have the form  $h_2 = Ah_1(\mu_2/\mu_1)^p$  in which  $A$  is some constant and we anticipate  $p \ll 1$  (implying that topological changes are weakly dependent on viscosity changes). Substituting this form for  $h_2$  into (5.2.6) we obtain to leading order

$$\frac{U_{1SL}}{U_{2SL}} = \frac{4}{A^3} \left( \frac{\mu_2}{\mu_1} \right)^{1-3p} + O \left[ \left( \frac{\mu_2}{\mu_1} \right)^p, \left( \frac{\mu_2}{\mu_1} \right)^{1-2p} \right]$$

The left-hand-side of the above equation is of order  $O(1)$  which means that the right-hand-side must also be  $O(1)$ . The only way in which this can be achieved is by choosing  $p = 1/3$  and the constant  $A$  is immediately seen to be given by  $A = (4U_{2SL}/U_{1SL})^{1/3}$ . Therefore, in the limit  $\mu_2 \ll \mu_1$  the solution of the holdup equation (5.2.6) is approximated by

$$h_2 = h_1 \left( 4 \frac{\mu_2 U_{2SL}}{\mu_1 U_{1SL}} \right)^{1/3} + o \left( \frac{\mu_2}{\mu_1} \right)^{1/3} \quad (5.2.7)$$

In the case where the upper fluid is much more viscous than the lower fluid we expect, in direct analogy with the previous case, that the lower fluid moves faster than the upper fluid and that the interface separating the two fluids moves towards the lower solid plate. An analysis very similar to the one given above shows that in the limit  $\mu_2 \gg \mu_1$  the solution of the holdup equation (5.2.6) is indeed approximated by

$$h_1 = h_2 \left( \frac{\mu_1 U_{1SL}}{\mu_2 U_{2SL}} \right)^{1/3} + o\left(\frac{\mu_1}{\mu_2}\right)^{1/3}$$

### 5.2.1 Stratified, laminar flow: hydraulic model

Let us now approach the problem of laminar flow between two infinite, parallel plates in a way similar to that outlined for the case on laminar, single phase flow in section 2.4.1. There we showed that a hydraulic approach (that is, working only with averaged velocities) would yield the correct pressure drop provided the correct friction factor was supplied. The following question now arises: can we use the hydraulic approach for the 2-phase problem considered here and if so, which friction factors have to be supplied in order to obtain the same results as the exact holdup calculations given above? As before, we start with formulating a simple force balance in each of the two fluid layers where the driving force is again the pressure gradient. Let us first concentrate on the lower fluid layer. When the flow is fully developed, this pressure gradient must be balanced by a shear stress on the lower solid boundary (denoted by  $\tau_1$ ) and by a shear stress on the interface separating the two fluids (denoted by  $\tau_i$ ). If we assume that the fluid in the upper layer flows with a larger velocity than the fluid in the lower layer, it follows that the upper fluid drags along the lower fluid. This means that the interfacial shear stress acts to accelerate the lower fluid while the wall shear stress acts as a break. A force balance (per unit width) in the lower layer reads thus

$$-h_1 \frac{dP}{dx} = \tau_1 - \tau_i \quad (5.2.8)$$

where  $P(x)$  denotes the pressure at the level of the interface  $z = 0$ . A similar reasoning for the force balance in the upper layer yields immediately

$$-h_2 \frac{dP}{dx} = \tau_2 + \tau_i \quad (5.2.9)$$

where  $\tau_2$  denotes the wall shear stress exerted by the upper plate on the fluid. Note that since we have assumed that the lower fluid moves slower than the upper fluid, the interfacial shear acts to slow down the upper fluid layer.

In order to proceed we need closure relations, both for the wall shear stresses and for the interfacial shear stress. Using results from our analysis as given earlier in this section, we have enough information to find exact expressions for the wall and interfacial shear stresses. However, rather than using known information about the velocity profile to compute shear stresses, we take an approach which is common in problems where no information about the velocity profile is available (which, indeed, is the case in most practical problems). Recall (see section 2.4.1) that for the case of single phase flow between two infinite, parallel plates, the wall shear stress was expressed in terms of the mean velocity via  $\tau = \frac{1}{8} \rho \bar{u}^2 f$  where friction factor  $f = 48/\text{Re}$  and the Reynolds number based on the thickness of the fluid layer. This then suggests that we can write  $\tau_1 = \frac{1}{8} \rho_1 \bar{u}_1^2 f_1$  in which  $f_1 = 48/\text{Re}_1$  with  $\text{Re}_1 = \rho_1 h_1 \bar{u}_1 / \mu_1$ . Similarly, for the wall shear stress in the upper layer we have  $\tau_2 = \frac{1}{8} \rho_2 \bar{u}_2^2 f_2$  in which  $f_2 = 48/\text{Re}_2$  with  $\text{Re}_2 = \rho_2 h_2 \bar{u}_2 / \mu_2$ .

Next we turn to the interfacial shear stress. Interfacial shear results from the fact that fluids move with different velocities on either side of the interface. Since shearing

forces are roughly proportional to the square of the velocity we may assume that for the interfacial shear we have  $\tau_i \propto (\bar{u}_2 - \bar{u}_1)^2$ . To complete the expression for the interfacial shear we need to decide which density and which friction factor to use. In our force balance equations we have assumed that the upper fluid moves faster than the lower fluid. In the extreme case where the lower fluid is almost stationary we would expect the interface to behave like a solid plate giving  $\tau_i \sim \tau_H$ . This would then suggest taking  $\tau_i = \frac{1}{8}\rho_2(\bar{u}_2 - \bar{u}_1)^2 f_2$ . It turns out that this is not entirely correct and we will, at this stage, allow ourselves some extra freedom by taking  $\tau_i = \frac{1}{8}\rho_2(\bar{u}_2 - \bar{u}_1)^2 f_i$  with  $f_i = \theta \times f_2$  where the constant  $\theta$  has yet to be decided.

We will next derive and analyse the holdup equation resulting from the hydraulic model. This means that we eliminate the pressure gradient between the momentum equations (5.2.8) and (5.2.9) and apply the closure relations for the wall and interfacial shear stresses as discussed above. When, in addition we replace the mean velocities by the expressions for the superficial velocities, we find that the holdup equation based on the hydraulic flow model becomes

$$\frac{U_{1SL}}{U_{2SL}} - \frac{\mu_2}{\mu_1} \left( \frac{h_1}{h_2} \right)^3 \left[ 1 + \theta \left( 1 + \frac{h_2}{h_1} \right) \left( 1 - \frac{h_2}{h_1} \frac{U_{1SL}}{U_{2SL}} \right)^2 \right] = 0 \quad (5.2.10)$$

As before, the holdup equation gives us the equilibrium position of the interface separating the two fluids. We now have a holdup equation based on a hydraulic model, equation (5.2.10), and a holdup based on an exact analysis, equation (5.2.6). When comparing the functional forms of these two equations, it is not immediately obvious that these equations may predict similar equilibrium positions. Let us therefore study the roots of (5.2.10). To start with we consider the case in which  $\mu_2 \ll \mu_1$  where, as before, we expect a root where  $h_2 \ll h_1$ . Hence we consider a root of the form  $h_2 = Bh_1(\mu_2/\mu_1)^r$  where the constant  $B$  and the exponent  $r$  are to be determined. Substituting this expression into (5.2.10) we find without much difficulty that the correct leading-order behaviour is obtained when we take  $r = 1/3$  and  $B = ([1+\theta]U_{2SL}/U_{1SL})^{1/3}$ . A comparison with the exact solution (5.2.7) reveals that the asymptotic behaviour is the same for the exact and the hydraulic model, provided we take  $\theta = 3$ . What we have shown here is that the roots of the holdup equations obtained from the exact and the hydraulic problems are identical in the limit  $\mu_2 \ll \mu_1$  provided we take the interfacial shear stress three times larger than the wall shear stress in the least viscous fluid.

What does the exact solution tell us about the ratio between interfacial and wall shear stresses? Using the velocity profiles as given in (5.2.4) it is easy to show that according to the exact analysis, the interfacial and wall shear stresses in the least viscous phase are identical in the limit  $\mu_2 \ll \mu_1$ . Now we have a dilemma: the roots of the hydraulic holdup equation (that is, the equilibrium height of the gas-liquid interface) can be matched to the roots of the exact holdup equation only when we take the interfacial shear stress to be larger (three times larger!) than what the exact result indicates it should be. This means that we either have to accept that the equilibrium height as predicted by the hydraulic model is wrong or that the ratio of interfacial and wall shear is wrong - it is not possible to have both correct in a hydraulic model. This result reveals a number of interesting points. For a start we see that we have to pay a price for the simplifications introduced through the hydraulic model: it is simply not possible to obtain the same results with the hydraulic and the complete model. A second thing to note is the fact that the interfacial shear plays a rather special (and important) role in the hydraulic model. It turns out that obtaining good closure relations for the interfacial shear is one of the most difficult problems when modelling stratified flows.

### 5.3 Stratified, laminar flow in a circular pipe

The laminar, stratified flow problem in a circular pipe requires the solution of the momentum equation in each phase as specified in equation (5.2.1) combined with the

boundary conditions (5.2.2) and the no-slip condition at the interface. If we assume that there is only flow in the direction along the axis of the pipe then, as before,  $\mathbf{v}_k = (u_k, 0, 0), k = 1, 2$  where we take fluid 1 to be the denser fluid. In a circular pipe we can, however, no longer assume that  $u_k = u_k(y)$  as was possible for the case of flow between infinite parallel plates. Due to the presence of the pipe walls, the velocity field changes significantly over the cross section of the pipe so that  $u_k = u_k(y, z)$ . The problem to be solved for the case of a pipe becomes therefore

$$-\frac{\partial p_k}{\partial x} + \mu_k \nabla^2 u_k = 0 \quad \text{and} \quad -\frac{\partial p_k}{\partial y} - \rho_k g = 0 \quad \text{for } k = 1, 2$$

where the Laplace operator  $\nabla^2 = \partial^2/\partial y^2 + \partial^2/\partial z^2$ . The jump conditions at the interface  $z = h$  require, as before

$$p_1(x, h) = p_2(x, h) \quad \text{and} \quad \mu_1 \frac{\partial u_1}{\partial z} = \mu_2 \frac{\partial u_2}{\partial z}$$

while the no-slip conditions at the solid pipe walls also need to be satisfied. Note that the position of the interface is, in general, unknown. When the volume flow rate of each phase is specified, the position of the interface has to be determined as part of the solution of the problem. A typical example of the solution of this problem, is shown in figure 5.3.1 (this solution is obtained numerically using a finite-element technique). Here we show velocity contours for the case in which the lower fluid has the physical properties of water while the upper fluid is 5 times more viscous. The diameter of the pipe in the simulations is taken to be 0.3m. In line with our observations from laminar flow between parallel plates, we see that the largest velocities occur in the least viscous fluid.

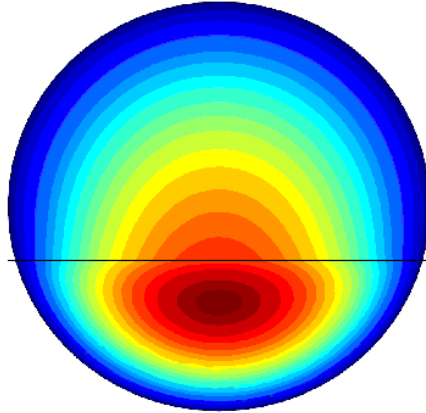


Figure 5.3.1: Velocity contours for the case of laminar, stratified flow in a pipe.

As may be expected by observing the velocity contours, the interfacial shear stress  $\mu_1 \frac{\partial u_1}{\partial z}$  is not constant along the interface. In figure 5.3.2 we have plotted the interfacial shear as a function of the interfacial arc length. We observe that the interfacial shear is largest in magnitude on the vertical symmetry axis while it decreases in the direction of the wall. In a simulation in which the least viscous fluid is on the top, a similar variation would have been observed with the exception that the shear stress curve would have been convex rather than concave.

Using a bipolar coordinate system, the problem as specified above can be solved analytically using standard separation of variable techniques (Biberg & Halvorsen, 2000). One of the interesting results from this analysis is the fact that a remarkably simple

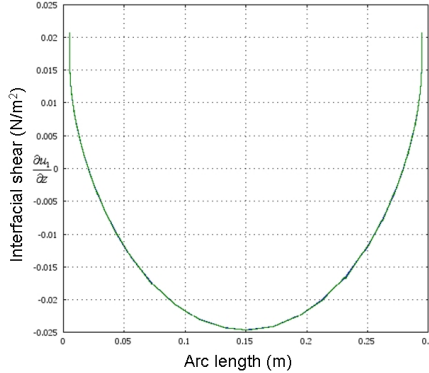


Figure 5.3.2: The interfacial shear plotted as a function of the interfacial arclength.

expression for the mean interfacial shear stress can be obtained. Namely, it can be shown that for horizontal flow, the mean interfacial shear stress can be written like

$$\bar{\tau}_I = \frac{\Theta}{2} \frac{\mu_1 \mathcal{A}_2 - \mu_2 \mathcal{A}_1}{\mu_2 s_1 + \mu_1 s_2} \quad (5.3.1)$$

in which  $\Theta = -\frac{dP}{dx}$ ,  $s_1$  and  $s_2$  denote the wall section wetted by the respective phases and

$$\mathcal{A}_k = h_k(s_I + s_k) - 2A_k, \quad k = 1, 2$$

with  $h_k$  denoting the maximum vertical distance between the interface and the pipe wall,  $s_I$  the interfacial perimeter and  $A_k$  the cross sectional area occupied by the respective phases (see also figure 4.5.2). Note the similarity between the expression for the mean interfacial shear stress for the circular pipe in equation (5.3.1) and the equivalent expression for the case of channel flow in equation (5.2.5).

We have seen that the interfacial shear stress varies significantly along the interfacial perimeter and it is therefore also expected that the wall shear stress shows similar variations. In figure 5.3.3 we have plotted the wall shear stress as a function of the arc length along the perimeter of the pipe (the origin being taken at the bottom of the pipe). We see that over most of the perimeter the wall shear stress is relatively constant. However, a large change occurs when the arclength is approximately 0.2. This point coincides with the point at which the interface separating the two fluids intersects the pipe wall. For the case shown here (the most viscous fluid occupies the larger part of the cross section of the pipe), Biberg & Halvorsen (2000) have shown that the shear stress at the intersection point tends to infinity.

When the most viscous fluid occupies the smaller part of the cross section, it turns out that the shear stress in the intersection point is identically zero. The wall shear stresses on either side of the intersection points do not vanish which means that there is a discontinuity in the wall shear stress as the interface is crossed! Even though the wall shear stress may be infinite at the intersection point, Biberg & Halvorsen show that the mean value of the wall shear stress remains always finite (as is, of course, expected).

## 5.4 Stratified pipe flow: one dimensional models

In the previous sections we have seen that in the special case of laminar, stratified flow, the problem of finding the velocity field and the interfacial position can be solved analytically. When the flow becomes turbulent in either or both of the phases, analytical solutions are no longer known and hence it becomes necessary to consider simplified

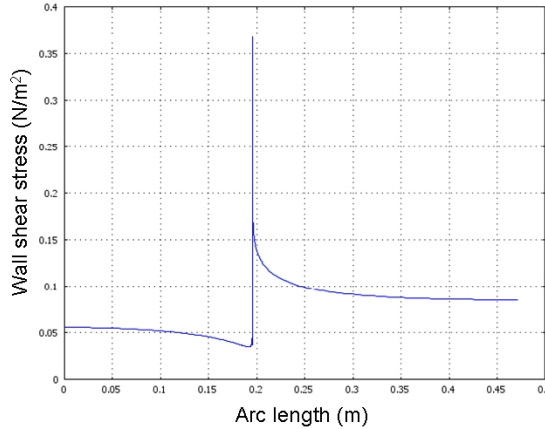


Figure 5.3.3: The wall shear stress for two-phase flow in a circular pipe, plotted as a function of the arc length.

hydraulic models. Recall that in these hydraulic models, all details of the flow field in the directions perpendicular to the main flow direction are neglected: the only velocity of interest is the mean velocity in the flow direction. Assuming as before, fully developed stratified flow, it follows that mass conservation in each phase takes the form

$$m_k = \rho_k A_k u_k \text{ with } k = L, G$$

with  $m_k$  denoting the mass flow,  $u_k$  the mean velocity and  $A_k$  the cross sectional area occupied by phase  $k$ , see figure 4.5.2. Without loss of generality we have assumed that the heavy phase is the liquid phase while the lighter phase is the gas phase. We can now return to the equations derived earlier in section 4.5 for the area-averaged two-fluid model for stratified flow. Under the assumptions of steady state (that is  $\frac{\partial \cdot}{\partial t} = 0$ ) and fully developed flow (that is  $\frac{\partial \cdot}{\partial x} = 0$ ), the momentum equations given in table 4.1 reduce to the desired steady state force balances in each phase, namely

$$-A_L \frac{\partial p_{LI}}{\partial x} - \rho_L g A_L \sin \beta - \tau_{Lw} s_L + \tau_{LI} s_I = 0 \quad (5.4.1)$$

$$-A_G \frac{\partial p_{GI}}{\partial x} - \rho_G g A_G \sin \beta - \tau_{Gw} s_G - \tau_{GI} s_I = 0 \quad (5.4.2)$$

together with the interfacial boundary conditions

$$p_{LI} = p_{GI}$$

and

$$\tau_{LI} = \tau_{GI} = \tau_I$$

Using the interfacial pressure conditions, the pressure gradient terms in the momentum equations can be eliminated between the two momentum balances. Using in addition the interfacial shear condition we obtain what is known as the holdup equation

$$\mathcal{H}(u_L, u_G, A_L, A_G) \equiv \frac{1}{A_L} \tau_{Lw} s_L - \frac{1}{A_G} \tau_{Gw} s_G - \left( \frac{1}{A_L} + \frac{1}{A_G} \right) \tau_I s_I + \Delta \rho g \sin \beta = 0 \quad (5.4.3)$$

in which  $\Delta\rho = \rho_L - \rho_G$ . In section 5.2 we already met to the holdup equation, there for the case of laminar flow between two infinite plates. The holdup equation obtained here, although of a different form, has the same physical meaning: it is essentially an algebraic equation which determines the equilibrium position of the gas-liquid interface. However, some additional information is required before the holdup equation is in a form where the equilibrium position can be determined. Namely, we have, as yet, not specified explicit expressions for the wall shear stress in each phase and neither has the interfacial shear stress been specified. Here, we arrive at one of the main challenges in area of multiphase flow modelling. Namely, by working with hydraulic models in which all cross sectional information about the velocity field is removed, we have also lost all information about velocity gradients which govern wall and interfacial stresses. Indeed, in the hydraulic model, only the mean velocities in each phase appear and hence the shear stresses have to be related to the mean velocities. We have seen that in the case of single phase flow (section 2.4) it is relatively simple to obtain precisely these relations. For two-phase flow these relations are unfortunately not so easy to obtain. We proceed as outlined in section 5.2.1, namely, by applying the single-phase methodology to the multiphase problem. Thus, the wall stresses are written in the familiar form

$$\tau_{Lw} = \frac{1}{8}\rho_L u_L^2 f_L \quad (5.4.4a)$$

$$\tau_{Gw} = \frac{1}{8}\rho_G u_G^2 f_G \quad (5.4.4b)$$

in which the friction factors  $f_L$  and  $f_G$  are as yet unknown. These friction factors are often of the form

$$f_k = \frac{C_k}{\text{Re}_k^n} \text{ with } k = L, G \quad (5.4.5)$$

The Reynolds number for each phase is defined via

$$\text{Re}_k = \frac{\rho_k u_k D_{H,K}}{\mu_k}$$

in which the hydraulic diameters are given by

$$D_{H,L} = \frac{4A_L}{s_L} \text{ and } D_{H,G} = \frac{4A_G}{s_G + s_I}$$

For laminar flow we take  $C_k = 64$  and  $n = 1$  and for turbulent flow the values  $C_k = 0.2$  and  $n = 0.2$  are often used. Note the analogy between the friction factors defined here and the friction factors as applied in single-phase flow as presented in section 2.4. In cases where the pipe wall roughness is important, the Colebrook or Haaland friction factors are applied. In that case, the Reynolds number is computed as outlined above. Before we proceed with a discussion on how to model the interfacial shear stress, it is worthwhile to discuss the rather bold step of using single-phase friction factors in a multiphase system. Namely, all we have done to take into account the fact that we are dealing with a multiphase system, is to use a hydraulic diameter in the definition of the Reynolds number while the parameter  $C_k$  is held constant. How valid is this approach? It turns out that the variation in the friction factor resulting from the pipe being only partly filled is not completely taken care of by employing the hydraulic diameter in the Reynolds number. This implies that the parameter  $C_k$  may be anticipated to be a function of the liquid height in the pipe. For the case where liquid partly fills a circular pipe and where the flow in the liquid phase is laminar, the pressure gradient in the liquid phase has been established numerically. The gas-liquid interface was assumed

to be flat and subjected to a constant interfacial shear stress. Employing the friction factor as outlined above together with the numerically computed pressure gradient, it is possible to determine  $C_L(h/D)$ . The result is shown in 5.4.1 where we observe that the parameter  $C_L$  is less than 64 for all liquid filling fractions. In the case of turbulent flow, the friction factor is less strongly dependent on the Reynolds number and hence we anticipate a weaker dependence of  $C_k$  on the liquid holdup than that found for laminar flow.

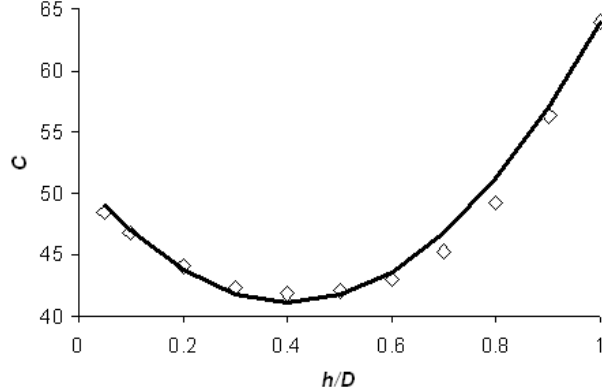


Figure 5.4.1: The parameter  $C_L$  as a function of the dimensionless liquid depth  $h/D$ . The drawn line has the equation  $C_L(h/D) = 64 \times (h/D)^2 + 51.5 \times (1 - h/D)$  while the symbols are numerical results by Russel *et al* (1974).

The determination of the wall and interfacial friction factors is not entirely trivial. Namely, since we can not measure the shear stresses directly we have to employ indirect measurements to obtain this information. The procedure is generally as follows. In multiphase flow experiments the pressure gradient and the mean (time-averaged) liquid holdup is measured which supplies us with two measurements while we have three unknowns ( $\tau_{Lw}$ ,  $\tau_{Gw}$  and  $\tau_I$ ). This means that extra information has to be supplied. An extensive analysis by Espedal (1998) shows that the gas wall shear stress as computed by (5.4.4b) and (5.4.5) gives a reasonable estimate of the measured wall shear stress. This means that  $\tau_{Gw}$  can be assumed to be known and  $\tau_{Lw}$  and  $\tau_I$  can subsequently be determined by using the experimental data together with equations (5.4.1) and (5.4.2). An example of the measured liquid wall friction factors as a function of the liquid Reynolds number is shown in figure 5.4.2. Also shown are computed friction factors based on Haaland's equation (see table 2.3) and on Blasius-type equations (5.4.5). We observe that the match between measured and computed friction factors is far from perfect.

For the interfacial shear stress we write

$$\tau_I = \frac{1}{8} \rho_G (u_G - u_L) |u_G - u_L| f_I$$

Many different expressions for the interfacial friction factor  $f_I$  have been proposed and in appendix B a number of the published friction factors are listed. This, in itself, is an indication of the fact that complex physical processes govern the dynamics at the gas-liquid interface. Namely, the gas-liquid interface is generally not smooth and the physical properties of each phase clearly influence wave amplitudes, wave lengths, entrainment of drops or bubbles and turbulent intensities. It will seem clear that all this complex physical behaviour is unlikely to be captured within one single closure relation, thereby explaining why so many expressions for the interfacial friction factor are in use. One often-used expression for the interfacial shear stress due to Cohen & Hanratty (1968) is the simple relation

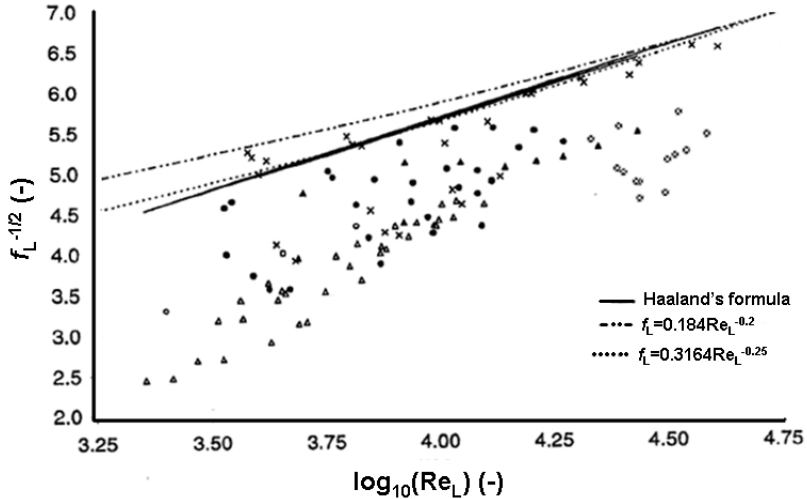


Figure 5.4.2: A comparison of selected liquid wall friction factors with experimental data (Espedal, 1998)

$$f_I = \max(0.056, f_G)$$

The effect of interfacial waves is obviously not captured by the friction factor given above. These effects can be included by using Colebrook or Haaland-type friction factors (see section 2.4) in which the interfacial roughness is somehow related to the interfacial shear stress. Using the Colebrook formula we get

$$\frac{1}{\sqrt{f_I}} = -2 \log \left( \frac{\epsilon_I}{3.7 D_{H,G}} + \frac{2.51}{\text{Re}_G \sqrt{f_I}} \right)$$

in which  $\epsilon_I$  denotes the interfacial roughness. Rosant (1994) proposes the following estimate of the interfacial roughness parameter

$$\epsilon_I = \begin{cases} 1238 H_L & 0 < H_L < 0.1 \\ 123.8 \frac{\tau_I}{\rho_L g} & 0.1 < H_L < 1 \end{cases}$$

in which  $H_L = A_L/A$  denotes the liquid holdup.

The benefit of the friction factors as given above is their simplicity. A drawback is, however, that they represent an over-simplification of the physics in a stratified flow system. At this point it is important to retrace our steps. The closure relations for the shear stress require friction factors and these were obtained by drawing links between the single-phase and the two-phase flow systems. This immediately leads to the implicit assumption that the shear stress in the gas phase is independent of the shear stress in the liquid phase: we have formulated closure relations in each phase by pretending that the neighbouring phase in some way can be neglected. This is not the case! Indeed, in the previous section we have seen that the mean interfacial shear and wall shear stresses are related. Biberg (1998) has shown that there is a coupling between wall shear stress in both the gas and the liquid phase on one hand, and the interfacial shear on the other hand. For example, Biberg (1998) shows that the friction factor for the gas phase can be written like

$$\frac{1}{\sqrt{f_G}} = -1.8 \log \left( \frac{6.9}{\text{Re}_G} + \left( \frac{\epsilon_I}{3.7 D_{H,G}} \right)^{1.11} \right) - 2 \log \left( 1 + \frac{s_I}{s_G} \right) \left( \text{sign} \left( \frac{\tau_I}{\tau_G} \right) \sqrt{\left| \frac{\tau_I}{\tau_G} \right|} - 1 \right)$$

Here we clearly see that the friction factor is composed of two parts: the single phase part consisting of the familiar Haaland expression and a correction due to the presence of the interface. The disadvantage with this expression is that it is highly implicit owing to the appearance of the wall gas shear stress on both sides of the equation.

The solution of the holdup equation (5.4.3) is often obtained in the following manner. The volume flow rates of both phases  $Q_k$ ,  $k = G; L$ , are assumed known and the insitu velocities are then written like  $u_k = Q_k/A_k$ . With the insitu velocities in this form, the holdup equation (5.4.3) contains only unknowns that can be related to the flow geometry (see Appendix A for the geometric relations). In order to determine the roots of the holdup equation, numerical root-finding routines (like the bi-section or the Newton-Raphson method) have to be employed.

## 5.5 Solutions of the holdup equation and the Lockhart-Martinelli parameter

It was mentioned in the previous section that the holdup equation (5.4.3) is essentially a non-linear equation for the position of the gas-liquid interface. A slightly simplified type of this equation in dimensionless form, yields a convenient graphical representation of solutions of the holdup equation. In order to obtain this result, let us apply the closure relations (5.4.4) and (5.4.5) as specified in the previous section. In addition we make the approximation  $\tau_I = \theta \times \tau_{Gw}$ . For  $\theta = 1$  this approximation implies that the gas-liquid interface behaves like a smooth solid wall. the case  $\theta > 1$  may be interpreted as being representative for a rough (wavy) gas-liquid interface. We now introduce the dimensionless parameters

$$\tilde{D}_L = \frac{D_{H,L}}{D}, \quad \tilde{s}_L = \frac{s_L}{D}, \quad \tilde{A}_L = \frac{A_L}{D^2}, \quad \tilde{u}_L = \frac{u_L}{U_{SL}}, \quad \text{etc.}$$

in which  $U_{SL}$  denotes the superficial liquid velocity. Writing (5.4.3) in terms of these dimensionless variables it is easy to show that the holdup equation in dimensionless form becomes

$$X^2 \left[ \tilde{u}_L^2 \left( \tilde{u}_L \tilde{D}_L \right)^{-n} \frac{\tilde{s}_L}{\tilde{A}_L} \right] - \tilde{u}_G^2 \left( \tilde{u}_G \tilde{D}_G \right)^{-n} \left( \frac{\tilde{s}_G}{\tilde{A}_G} + \theta \frac{\tilde{s}_I}{\tilde{A}_L} + \theta \frac{\tilde{s}_I}{\tilde{A}_G} \right) + 4Y = 0 \quad (5.5.1)$$

The parameter  $X$  in the above equation is known as the Lockhart-Martinelli parameter and is defined according to

$$X^2 = \frac{\frac{C_L}{2D} \left( \frac{U_{SL} D \rho_L}{\mu_L} \right)^{-n} \rho_L U_{SL}^2}{\frac{C_G}{2D} \left( \frac{U_{SG} D \rho_G}{\mu_G} \right)^{-n} \rho_G U_{SG}^2} = \frac{\frac{dp}{dx} \Big|_{SL}}{\frac{dp}{dx} \Big|_{SG}}$$

while the gravitational parameter  $Y$  is defined via

$$Y = \frac{\Delta \rho g \sin \beta}{\frac{C_G}{2D} \left( \frac{U_{SG} D \rho_G}{\mu_G} \right)^{-n} \rho_G U_{SG}^2} = \frac{\Delta \rho g \sin \beta}{\frac{dp}{dx} \Big|_{SG}}$$

The expressions  $\frac{dp}{dx} \Big|_{SL}$  and  $\frac{dp}{dx} \Big|_{SG}$  represent pressure gradients for the cases in which only liquid or gas flows in the pipe. All the dimensionless quantities in equation (5.5.1) can be written in terms of the dimensionless liquid height  $\tilde{h} = h/D$ . For example, if we let  $\chi = 2\tilde{h} - 1$  then

$$\tilde{A}_L = \frac{1}{4} \left( \pi - \arccos \chi + \chi \sqrt{1 - \chi^2} \right)$$

$$\tilde{s}_L = \pi - \arccos \chi$$

$$\tilde{s}_I = \sqrt{1 - \chi^2}$$

$$\tilde{u}_L = \frac{\tilde{A}}{\tilde{A}_L}, \text{ etc.}$$

This implies that the dimensionless holdup equation is of the form

$$X^2 F(\tilde{h}) - G(\tilde{h}, \theta) + 4Y = 0 \quad (5.5.2)$$

This now means that for given values of  $X$  and  $Y$  we have to find the root of the algebraic equation (5.5.2) - the root corresponds to the dimensionless liquid height  $\tilde{h}$  at which pressure gradients in the gas and liquid phase are equal. The big advantage of this formulation is that we do not need information about the position of the interface in order to calculate  $X$  or  $Y$ . Namely, all the information about the (unknown) interface position is contained within the two algebraic functions  $F(\tilde{h})$  and  $G(\tilde{h}, \theta)$ .

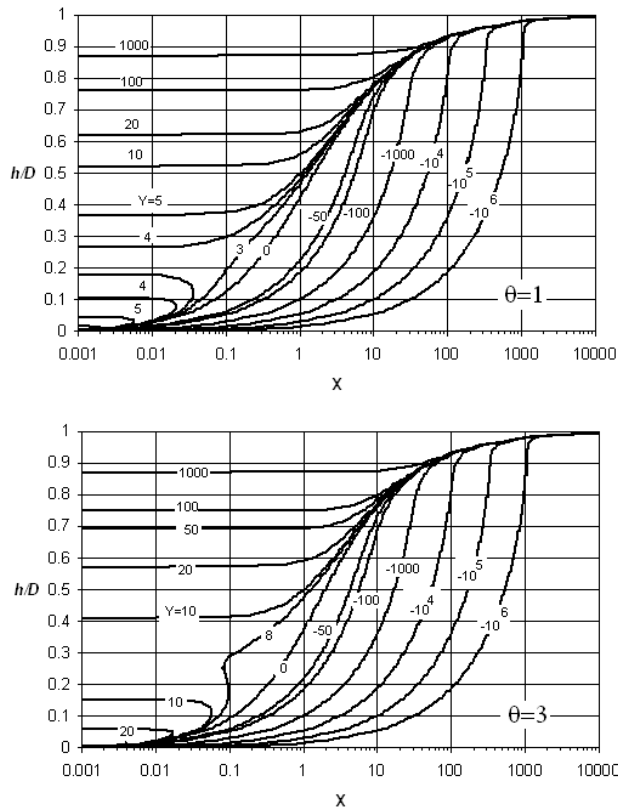


Figure 5.5.1: Equilibrium liquid heights as obtained from the dimensionless hold-up equation (5.5.2) for the values of  $X$  and  $Y$  as indicated in the plots. Liquid heights are computed for  $\theta = 1$  in the upper plot while  $\theta = 3$  is used in the lower plot.

Figure 5.5.1 shows curves of the dimensionless liquid height as a function of  $X$  for the values of  $Y$  as indicated in the plot for the cases with  $\theta = 1$  and  $\theta = 3$ . With reference to Figure 5.5.1 we note that for increasing values of  $Y$  (that is, increasing pipe inclination) the dimensionless liquid height increases. This is, of course, as expected since for positive inclinations the gravitational force acts to slow down the liquid phase more than the gas phase. When the liquid volume flow is constant (that is  $U_{SL}$  is constant) mass conservation implies that a reduced velocity must imply an increased liquid holdup.

We note that for small positive pipe inclinations (relatively small positive values of  $Y$ ), the holdup equation yields multiple values of the dimensionless liquid height for a given value of  $X$ . When  $X$  is sufficiently small, equation (5.5.2) has three distinct roots which suggests that three distinct equilibria can be found for upwardly inclined pipe flows. A stability analysis of the three equilibria by Landman (1991) suggests that the upper root (the root corresponding to the highest liquid holdup) is unstable while the lower root represents a stable solution. The intermediate root can be stable or unstable but is often deemed to be unphysical due to the fact that the liquid height decreases for increasing liquid flow rates. Ullmann *et al* (2003) have shown that multiple holdup solutions also exist experimentally in a liquid-liquid system while Langsholt & Holm (2007) have studied the consequences of multiple holdup solutions in gas-liquid systems. The presence of multiple roots has interesting consequences for the transport of gas-liquid systems in which  $U_{SG} \gg U_{SL}$ . Namely, experiments indicate that for a given pipe inclination there exists a critical value of the superficial gas velocity,  $U_{SG}^*$  say. When  $U_{SG} > U_{SG}^*$  it is found that the root with the lowest holdup is selected while for  $U_{SG} < U_{SG}^*$  the high holdup root is chosen. This means that for relatively small changes in the superficial gas velocity, large changes in the holdup may be observed. Experimental measurements of this behaviour are shown in figure 5.5.2. There we observe the discontinuous change in the liquid holdup as a function of the superficial gas velocity as predicted by the holdup equation.

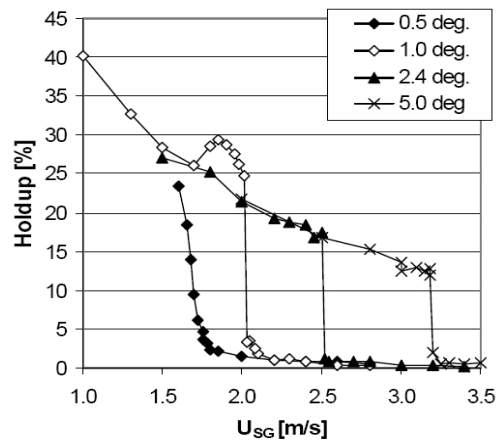


Figure 5.5.2: The influence of the inclination of the pipe on the transition from the low hold-up to the high hold-up solution, Langsholt & Holm (2007). In the experiments the superficial liquid velocity is held constant at  $U_{SL} = 0.001\text{ms}^{-1}$ .

## 5.6 Stratified, turbulent flow between two parallel plates

In section 5.4 we have met one of the large challenges in modelling stratified flows using one-dimensional models. Namely, the need for closure relations due to the fact that all information about the velocity profile has been removed through the averaging process. We have seen that the interfacial shear stress is a particularly difficult closure relation with more than 20 published expressions for this relation (appendix B lists a number of the interfacial friction factors which have been proposed). How can we overcome this difficulty which is inherently linked to the one-dimensional models, while still retaining a one-dimensional frame work (which has obvious advantages with respect to computational speed)? One approach is to use information from configurations in which details of the flow field are known analytically and try to draw an analogy between these configurations and the system we are interested in. Take, for example, figure 5.6.1 in which the measured velocity profiles in a stratified gas-liquid flow are shown. We

see that the profile in the liquid phase resembles that of a Couette flow (see exercise 5.5) while that in the gas phase is not unlike a turbulent velocity profile. It is therefore natural to start with single-phase analogies in order to describe the turbulent profiles in a stratified, two-phase flow case.

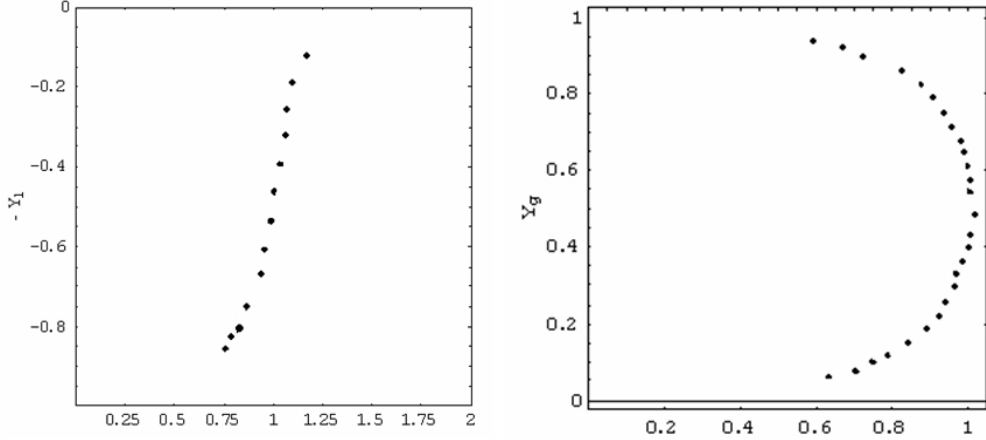


Figure 5.6.1: Velocity profile in the liquid layer (left) and gas layer (right) for the case: smooth gas-liquid interface (data from Akai et al 1980).

Biberg (2005, 2007) has shown how this can be done for the case of stratified turbulent flow between two infinite plates and this approach will be followed closely in this section. The basic idea is to find an approximate expression of the turbulent diffusion coefficient  $\mathcal{K}$  that is valid for each layer in the stratified flow. Once we have found  $\mathcal{K}$  we use the  $x$ -component of the turbulent momentum equation to compute the velocity profile in direct analogy with the procedure in single phase flow as outlined in section 2.5.

The system to be studied here is precisely the system as shown in figure 5.2.1, but in this case the flows in both layers are assumed to be turbulent. In the case of a turbulent, stratified flow between two infinite plates we essentially have two wall-bounded flows separated by an interface. This implies that it is not necessary to consider the lower and upper layers separately since results obtained for one layer can be applied directly to the other layer by means of a simple coordinate transformation. Henceforth we therefore only consider the upper layer. As in the case of single phase turbulent flow, we start the stratified flow model development by assuming that the Prandtl mixing length model can be applied in each layer. This means that we assume that turbulent diffusion can be modelled via a mixing-length model of the form (2.5.8), namely  $\mathcal{K} = \mathbb{L}\mathbb{U}$ . In order for this model to be successful we have to find a mixing length  $\mathbb{L}$  and a turbulent velocity scale  $\mathbb{U}$  that are representative for a stratified flow system.

Let us start with the mixing length. In section 2.5 we have seen that the mixing length is modified by the ratio of wall and turbulent shear stresses. For the mixing length in the upper-layer, near the solid wall we have in direct analogy with equation (2.5.14)

$$\mathbb{L} = \kappa h_2 (1 - \hat{z}) \sqrt{\left| \frac{\tau_t}{\tau_w} \right|} \quad (5.6.1)$$

in which  $\hat{z} = z/h_2$ . If we assume that the velocity profile near the interface is logarithmic, it follows that near the interface we have a mixing length of the form

$$\mathbb{L} = \kappa h_2 \hat{z} \sqrt{\left| \frac{\tau_t}{\tau_i} \right|}$$

in which  $\tau_i$  denotes the interfacial shear stress. Although it may seem rather extreme to assume that the profile near the (often rough) interface is logarithmic, this is in fact not unrealistic. Indeed, it is found that even for very rough walls (walls with a roughness extending beyond the viscous sub-layer), the velocity in the wall region still exhibits a logarithmic profile. However, the interface is no solid wall and hence we can not assume that the size of turbulent eddies decrease uniformly as the interface is approached. We assume, instead, that there is a finite mixing length associated with the largest turbulent eddies near the interface. This mixing length is denoted by  $l_i$ . We see that the assumption of a logarithmic velocity profile near the interface and the solid wall leads to a generalised mixing length of the form

$$\mathbb{L} = \mathcal{L}\mathcal{F}$$

in which the shear stress ratio  $\mathcal{F}(\hat{z} \rightarrow 1) = \sqrt{|\tau_t/\tau_w|}$  and  $\mathcal{F}(z \rightarrow 0) = \sqrt{|\tau_t/\tau_i|}$  and  $\mathcal{L}$  denotes the length scale of turbulent structures. We do not have detailed information about the variation of  $\mathcal{L}$  over the height of the upper layer but we know from (5.6.1) that  $\mathcal{L}|_{\hat{z}=1} = 0$  and  $d\mathcal{L}/dz|_{\hat{z}=1} = -\kappa h_2$ . In addition we have stipulated  $\mathcal{L}|_{\hat{z}=0} = l_i$ . It is reasonable to assume that the mixing length varies continuously over the cross section so we apply a simple quadratic interpolation using the boundary values as specified, to give

$$\mathcal{L} = \kappa h_2 [\zeta + (1 - 2\zeta)\hat{z} + (\zeta - 1)\hat{z}^2]$$

in which  $\zeta = l_i/\kappa h_2$ . Since  $l_i$  is an unknown parameter, we can regard  $\zeta$  as a free tuning parameter for this model. It may be anticipated that  $\zeta$  is in someway related to the roughness (wave height) on the interface but at the moment this is only a hypothesis. We next turn our attention to the turbulent velocity scale  $\mathbb{U}$  in the mixing-length model. To start with, we use the velocity scale as obtained in the single-phase bounded flow case (see section 2.5), namely

$$\mathbb{U} \equiv \sqrt{\frac{|\tau_t|}{\rho}} = \mathcal{F}^{-1}\mathcal{U} \quad (5.6.2)$$

With the turbulent velocity scale  $\mathbb{U}$  as defined above, the turbulent diffusion  $\mathcal{K}$  reduces to (2.5.8) as required since  $\mathcal{K} = \mathbb{U}\mathbb{L} = \mathcal{L}\mathcal{U}$ . Using the properties of the shear ratio function  $\mathcal{F}$  near the solid boundary and the interface, it follows that  $\mathcal{U} \rightarrow \frac{|\tau_t|}{\rho u_*}$  as  $\hat{z} \rightarrow 1$  while  $\mathcal{U} \rightarrow \frac{|\tau_t|}{\rho u_{*,i}}$  as  $\hat{z} \rightarrow 0$  in which we have defined the interfacial friction velocity via  $u_{*,i} = \sqrt{|\tau_i|/\rho}$ . These relations provide us with two boundary conditions for the turbulent velocity, namely  $\mathcal{U}|_{\hat{z}=0} = u_{*,i}$  and  $\mathcal{U}|_{\hat{z}=1} = u_*$ . Which additional information do we have about the turbulent velocity scale  $\mathcal{U}$ ? Let us briefly return to the case of single-phase turbulent flow (section 2.5.3). There it was shown, see equation (2.5.10), that the turbulent shear stress varies linearly over the cross section of the flow. In a stratified flow situation, this result still holds, so that the shear stress distribution in the upper layer can be written like  $\tau_t = \tau_i - (\tau_i + \tau_w)\hat{z}$  in which  $\tau_w$  denotes the wall shear stress at the upper solid boundary. If we introduce the ratio  $R = \tau_i/\tau_w$  then this result can be written like

$$\tau_t = \text{sgn}(\tau_w)\rho u_*^2 [R(1 - \hat{z}) - \hat{z}] \quad (5.6.3)$$

It is tempting to use this result directly in (5.6.2) order to give us the velocity scale  $\mathcal{U}$ . However, this is not possible since the turbulent shear stress in the above equation

vanishes at  $\hat{z}_0 = R/(1+R)$ . In the case where  $R > 0$  the point of vanishing shear stress would lie within the domain of the flow which would yield  $\mathcal{U}(\hat{z}_0) = 0$  and hence  $\mathcal{K} = 0$ . This is simply not allowed (the turbulent diffusion is expected to vanish as a solid wall is approached but at no other point within the domain of the flow). However, even though we can not use (5.6.3) directly to obtain  $\mathcal{U}$ , we can use the limiting behaviour of this function near the interface and the solid wall in order to provide us with information about the asymptotic behaviour of  $\mathcal{U}$  in these regions. From (5.6.3) we obtain

$$\frac{d\tau_t}{dz} = \rho u_*^2 (R + 1) = -\tau_i (1 + 1/R)$$

Using the above result together with the expressions for the limiting behaviour of  $\mathcal{U}$  in the limits  $\hat{z} \rightarrow 0, 1$  we obtain the additional boundary conditions  $d\mathcal{U}/d\hat{z}|_{\hat{z}=0} = -u_{*,i}(1+1/R)$  and  $d\mathcal{U}/d\hat{z}|_{\hat{z}=1} = u_*(1+R)$ . Since the first derivative is constant at the boundaries  $\hat{z} = 0, 1$  it follows finally that  $d^2\mathcal{U}/d\hat{z}^2|_{\hat{z}=0} = d^2\mathcal{U}/d\hat{z}^2|_{\hat{z}=1} = 0$ . Biberg (2005, 2007) has chosen to use a rational function to interpolate between the 6 boundary conditions to yield

$$\mathcal{U} = \frac{u_* (\hat{z}^3 + |R|^{5/2} (1 - \hat{z})^3)}{R^2(1 - \hat{z})^2 + R(1 - \hat{z})\hat{z} + \hat{z}^2}$$

With both the mixing length and the turbulent velocity scale known in the upper layer, we know the turbulent diffusion coefficient  $\mathcal{K}$  and hence the velocity profile can be found by integrating the equation

$$\frac{d\bar{u}}{dz} = \frac{1}{\rho\mathcal{K}}\tau_t$$

between the interface and the upper solid boundary. It turns out that with  $\mathbb{L}$  and  $\mathbb{U}$  as specified above, this integration can be performed analytically such that an explicit expression for the velocity profile in the upper layer can be obtained.

The analysis given above can be repeated for the lower layer such that also there the velocity profile is known. At the moment, it appears that the complete description of the velocity profile in the upper and lower layer requires the determination of 4 parameters: the shear ratio  $R$  in the upper and lower layers,  $R_U$  and  $R_L$  say, and the mixing length associated with the interface in both layers,  $l_{i,U}$  and  $l_{i,L}$  say (or  $\zeta_U$  and  $\zeta_L$ ). However, so far the boundary conditions at the interface have not been used, so the number of unknown parameters is less than 4. First of all, continuity of shear stress at the interface implies that  $\tau_{i,U} = \tau_{i,L} = \tau_i$  and hence the shear-ratio parameters in the upper and lower layer are related via  $R_U = \frac{\tau_{w,L}}{\tau_{w,U}}R_L$ . We next employ the no-slip condition at the interface. It can be shown that this condition can be used to determine the interfacial shear stress  $\tau_i$  explicitly (see Biberg, 2007). With this information in place, the shear ratios in both layers can be determined and the free parameters in the model are therefore the mixing lengths associated with the interface, that is  $\zeta_U$  and  $\zeta_L$ . Biberg (2005, 2007) has compared model predictions with a number of experimental measurements. Some of these results are shown in figure 5.6.2. In figures 5.6.2 (a,b) we see the measured and computed velocity profiles (measured data from Akay et al, 1980) in the gas phase for the gas Reynolds numbers  $Re_G = 3690$  and  $10500$  respectively. The values of the tuning parameters in figures **a** and **b** are  $\zeta_U = 0$  and  $\zeta_U = 0.075$  respectively, while the computed values of the shear ratio parameters  $R_U = 1.01$  and  $R_U = 1.81$  respectively.

We note that the value of  $\zeta_U$  increases with increasing gas velocity. This is as expected since, as speculated above, the value of  $\zeta_U$  is related to the mixing length at the interface which, in turn, is expected to be coupled to interfacial wave motion. In figures **c** and **d** the measured and computed profiles in the liquid phase when the gas Reynolds numbers

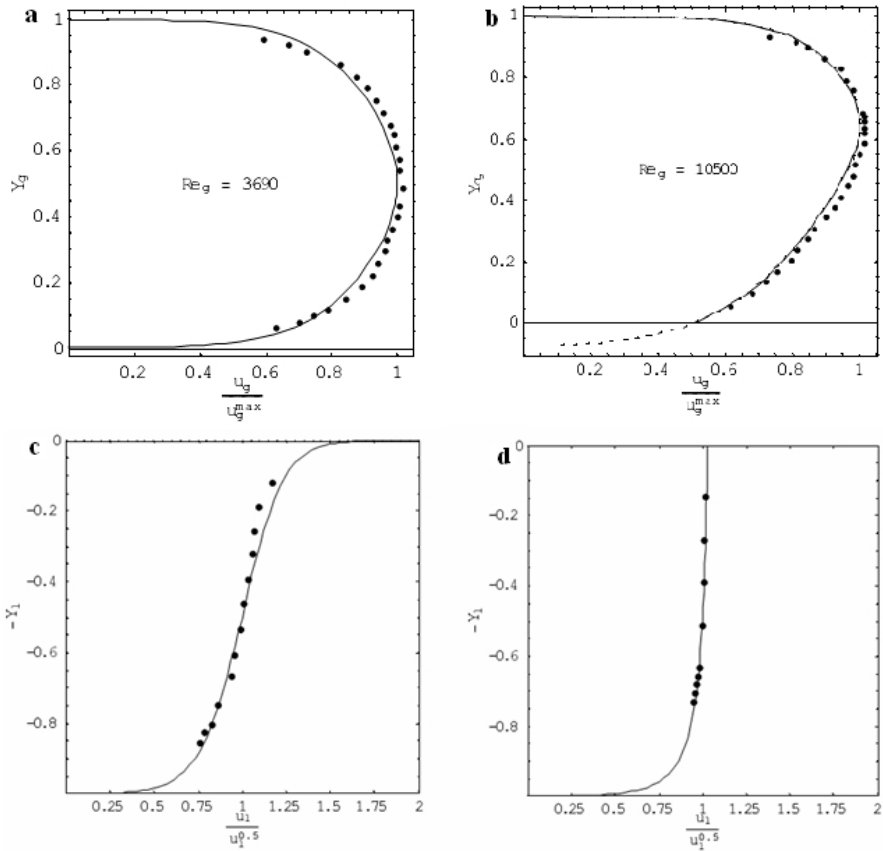


Figure 5.6.2: Measured and computed velocity profiles in the gas (a,b) and liquid (c,d) phases. The values of the tuning parameters are (a)  $\zeta = 0$ ,  $R = 1.01$ ; (b)  $\zeta = 0.075$ ,  $R = 1.81$ ; (c)  $\zeta = 0$ ,  $R = 0.839$  and (d)  $\zeta = 4$ ,  $R = 0.691$ .

are  $\text{Re}_G = 2340$  and  $13200$  respectively. The values of the tuning parameters in figures **c** and **d** are  $\zeta_L = 0$  and  $\zeta_L = 4$  respectively, with the computed shear ratio parameters given by  $R_L = 0.839$  and  $R_L = 0.691$  respectively. Once again we see that the value of  $\zeta_L$  increases with increasing gas velocity. A significant flattening of the velocity profile is obtained when  $\zeta_L$  is increased, indicating an increased momentum transfer from the interface into the bulk of the liquid phase.

The approach outlined in this section shows that it is possible to apply the mixing-length concept to the case of stratified gas-liquid flow in a channel. Extending this approach to the case of stratified flow in a pipe is the topic of ongoing research.

## 5.7 Exercises

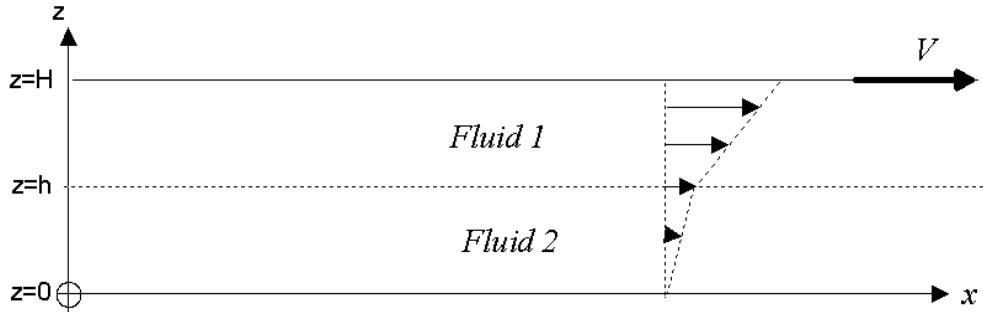
**Exercise 5.1** Show that  $h_1/h_2 = 1$  is a root of the holdup equation 5.2.6 for the case where  $\mu_1 = \mu_2$  and  $U_{1SL} = U_{2SL}$ .

**Exercise 5.2** For a horizontal circular pipe with diameter  $D$ , partly filled with liquid, show that the hydraulic diameter in the liquid phase can be written like  $D_{H,L} = 2s_L^2/3D$  in the limit where the liquid level goes to zero. Hint, use the geometric relations given in appendix A.

**Exercise 5.3** Use the Moody chart as shown in figure 2.6.1 to indicate for which range of Reynolds numbers the approximation  $X \approx \sqrt{\frac{\rho_L}{\rho_G} \frac{U_{SL}}{U_{SG}}}$  of the Lockhart-Martinelli parameter is valid. Show subsequently that we can write  $X \approx \sqrt{\frac{\rho_G}{\rho_L} \frac{m_L}{m_G}}$  in which  $m_k$  denotes the mass flow of phase  $k$ .

**Exercise 5.4** A pipe with a diameter of 0.2 m is used to transport gas and liquid. The superficial velocity of the liquid phase is equal to  $U_{SL} = 2 \text{ m s}^{-1}$  while for the gas phase we have  $U_{SG} = 10 \text{ m s}^{-1}$ . Assume  $\rho_L = 800 \text{ kg m}^{-3}$ ,  $\rho_G = 50 \text{ kg m}^{-3}$ ,  $\mu_L = 2 \times 10^{-3} \text{ kg m}^{-1} \text{s}^{-1}$  and  $\mu_G = 4 \times 10^{-5} \text{ kg m}^{-1} \text{s}^{-1}$ . Determine the Lockhart-Martinelli parameter and use Figure 5.5.1 to find the height of the liquid in the pipe for the cases with  $\theta = 0^\circ$  and  $\theta = 3^\circ$ . Repeat the exercise for the case in which the pipe has a negative inclination of  $3^\circ$ .

**Exercise 5.5** Consider two immiscible fluids with constant densities  $\rho_2 > \rho_1$  and viscosities  $\mu_1, \mu_2$ . The fluids are placed between two infinite parallel plates located at  $y = 0$  and  $y = H$ , the upper plate moving with a constant velocity  $(V, 0, 0)$  as shown below. This wall-driven flow is an example of what is known as a Couette flow.



The heavy fluid is located in the layer between  $0 < y < h$  while the light fluid is located in the layer  $h < y < H$ . Assuming one-dimensional flow and a flat interface, state the interfacial boundary conditions. Show that the interfacial velocity  $v_i$  is given by

$$v_i = V \frac{\mu_1 / (H - h)}{\mu_2 / h + \mu_1 / (H - h)}$$

Draw velocity profiles for the cases  $\frac{\mu_1}{\mu_2} < 1$ ,  $\frac{\mu_1}{\mu_2} = 1$ ,  $\frac{\mu_1}{\mu_2} > 1$ .

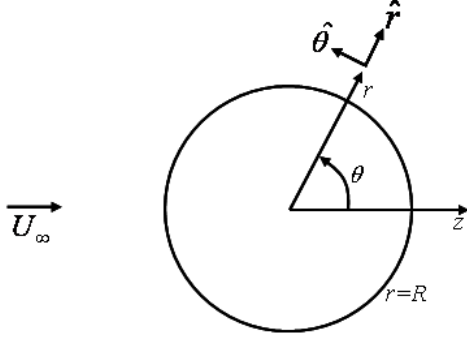


Figure 6.2.1: Schematic diagram of a spherical particle moving in an infinite fluid

## 6 Dispersed Flow

### 6.1 Introduction

In section 4.7 the model equations for a fully dispersed flow were introduced. As always, closure relations have to be supplied in order to obtain the same number of equations as unknowns. The closure relations generally relate parameters computed in the model to physical effects which have been removed through the averaging procedure. For example, in the mixture model we found that the closure relation for the drift velocity required information about particle motion through a suspension of other particles. In the mixture model we do not track individual particles but we still require information which can only be obtained by studying individual particles.

In this chapter we consistently start by looking at systems in which the particle concentration is dilute. This means that the particle concentration is so low that particle-particle interactions can be neglected. The benefit of this is that it is possible to obtain a number of important analytical results. Starting with these results obtained in the dilute limit we then use experimental data to extrapolate into the region in which particle-particle interactions can no longer be neglected. In this chapter only isothermal and steady state conditions are considered. A more extensive exposition of dispersed flows can be found in Crowe *et al* (1998) or Brennen (2005).

### 6.2 The motion of a spherical particle in an infinite fluid

In this section we consider the motion of a spherical particle which moves through an infinite fluid. Given the fluid and particle properties (density and viscosity), we are interested to find the velocity of the particle. In a frame of reference fixed to the centre of the particle, the problem to be considered is as shown schematically in Figure 6.2.1. We assume that the particle, with a constant diameter equal to  $2R$ , moves with a steady velocity  $\mathbf{u}_{\text{particle}} = (0, 0, -U_{\infty})$ . In a frame of reference fixed to the centre of the particle, the particle sees an oncoming stream with uniform velocity  $\mathbf{u} = (0, 0, U_{\infty})$ . In order to be able to solve the equations governing the motion of the fluid around the particle we assume that the flow is steady ( $\partial_t = 0$ ) and that the particle Reynolds number  $\text{Re}_p = \frac{2RU_{\infty}\rho_f}{\mu_f}$  is small. This last assumption corresponds to the so-called Stokes flow limit in which viscous forces dominate inertia forces. In addition, the fluid surrounding the particle is taken to be incompressible so that the equations governing the fluid motion become (cf. section 2.2)

$$\nabla \cdot \mathbf{u} = 0 \tag{6.2.1}$$

and

$$\nabla \hat{p} = \mu_f \nabla^2 \mathbf{u} \quad (6.2.2)$$

The body force is included in the pressure via  $\hat{p} = p + \rho \mathbf{g} \cdot \mathbf{x}$ . We now introduce a spherical polar coordinate system  $(r, \theta, \phi)$  and assume symmetry with respect to the azimuthal angle  $\phi$ , hence  $\partial_\phi = 0$  and  $u_\phi = 0$ . With these assumptions, equations (6.2.1) and (6.2.2) in spherical polar coordinates become (cf. Batchelor, 1967)

$$\frac{1}{r^2} \frac{\partial}{\partial r} (r^2 u_r) + \frac{1}{r \sin \theta} \frac{\partial}{\partial \theta} (\sin \theta u_\theta) = 0 \quad (6.2.3a)$$

$$\frac{\partial \hat{p}}{\partial r} = \frac{\mu_f}{r^2} \left[ \frac{\partial}{\partial r} \left( r^2 \frac{\partial u_r}{\partial r} \right) + \frac{1}{\sin \theta} \frac{\partial}{\partial \theta} \left( \sin \theta \frac{\partial u_r}{\partial \theta} \right) - 2u_r - \frac{2}{\sin \theta} \frac{\partial}{\partial \theta} (u_\theta \sin \theta) \right] \quad (6.2.3b)$$

$$\frac{1}{r} \frac{\partial \hat{p}}{\partial \theta} = \frac{\mu_f}{r^2} \left[ \frac{\partial}{\partial r} \left( r^2 \frac{\partial u_\theta}{\partial r} \right) + \frac{1}{\sin \theta} \frac{\partial}{\partial \theta} \left( \sin \theta \frac{\partial u_\theta}{\partial \theta} \right) + 2 \frac{\partial u_r}{\partial \theta} - \frac{u_\theta}{\sin^2 \theta} \right] \quad (6.2.3c)$$

The condition far away from the particle, namely  $\mathbf{u} \rightarrow \mathbf{U}_\infty$  as  $r \rightarrow \infty$ , implies that  $u_r \rightarrow U_\infty \cos \theta$  and  $u_\theta \rightarrow -U_\infty \sin \theta$  as well as  $u_\phi = 0$ . These conditions suggest looking for solutions of equations (6.2.3) that are of the form  $u_r = U_\infty f(r) \cos \theta$  and  $u_\theta = U_\infty g(r) \sin \theta$ . Substituting these specific expressions into (6.2.3b) or (6.2.3c) it is found that the pressure is in the form  $\hat{p}(r, \theta) = P_0 + \mu_f U_\infty P(r) \cos \theta$ . On substituting the proposed expressions for  $u_r$ ,  $u_\theta$  and  $\hat{p}$  into the conservation equations, we obtain

$$\begin{aligned} \frac{r}{2} f' + f + g &= 0 \\ P' &= \frac{1}{r^2} (r^2 f')' - \frac{4}{r^2} f - \frac{4}{r^2} g \\ P &= \frac{2}{r} g + \frac{2}{r} f - \frac{1}{r} (r^2 g')' \end{aligned}$$

in which a dash denotes a derivative with respect to  $r$ . The functions  $P(r)$  and  $g(r)$  can be eliminated from the above equations to yield one differential equation for  $f(r)$ , namely

$$\frac{r^4}{8} f^{(iv)} + r^3 f''' + r^2 f'' - r f' = 0 \quad (6.2.4)$$

The solution of this differential equation is found by taking  $f = r^m$  which on substituting into (6.2.4) yields the characteristic equation

$$m [m^3 + 2m^2 - 5m - 6] = 0$$

with roots  $m = 2, 0, -1, -3$ . The general solution is thus of the form

$$f(r) = A + \frac{B}{r} + \frac{C}{r^3} + Dr^2 \quad (6.2.5a)$$

$$g(r) = -A - \frac{B}{2r} + \frac{C}{r^3} - 2Dr^2 \quad (6.2.5b)$$

$$P(r) = \frac{B}{r^2} + 10Dr \quad (6.2.5c)$$

The boundary conditions at infinity give immediately that  $A = 1$  and  $D = 0$ . The remaining constants  $B$  and  $C$  are found by imposing boundary conditions at the surface of the particle where three distinct cases need be considered: a solid particle, a gas

bubble and a liquid particle. For the case of a solid particle the boundary conditions are the usual no-slip conditions, namely

$$u_r|_{r=R} = u_\theta|_{r=R} = 0$$

This implies  $f(R) = g(R) = 0$  which yields immediately  $B = -\frac{3}{2}R$  and  $C = \frac{1}{2}R^3$ . For the case of a gas bubble the two conditions at the surface are different from those at the surface of a solid particle. Firstly, a gas-liquid interface can not sustain tangential stresses implying that the tangential stress at the surface of the bubble must vanish. The tangential stress is given by

$$\tau_{r\theta} = \mu \left[ r \frac{\partial}{\partial r} \left( \frac{u_\theta}{r} \right) + \frac{1}{r} \frac{\partial u_r}{\partial \theta} \right] = -3\mu_f \frac{C}{r^4} \sin \theta U_\infty \quad (6.2.6)$$

from which it follows immediately that the vanishing stress at  $r = R$  is only obtained when  $C = 0$ . The additional condition to be satisfied at the gas-liquid interface is that the normal velocity component at the interface must vanish. Thus  $u_r|_{r=R} = 0$  which yields  $B = -R$ . The case of a fluid particle in which the internal motion of the fluid in the particle has to be included is left as an exercise (see exercise 6.1). In table 6.1 the coefficients  $B$  and  $C$  are summarized for the different fluid particles.

Particle Type	$B$	$C$	Drag Coefficient
Solid Particle	$-\frac{3}{2}R$	$\frac{1}{2}R^3$	$\frac{24}{Re_p}$
Gas Bubble	$-R$	0	$\frac{16}{Re_p}$
Fluid Particle	$-\frac{R}{2} \frac{2+3\mu'}{1+\mu'}$	$\frac{R^3}{2} \frac{\mu'}{1+\mu'}$	$\frac{24}{Re_p} \frac{2+3\mu'}{3+3\mu'}$

**Table 6.1:** Values of the coefficients  $B$  and  $C$  in equations (6.2.5) for different types of particles with  $\mu' = \mu_p/\mu_f$ . The last column shows the drag coefficient for the different particles.

A quantity frequently of interest in dispersed flows is the so-called drag force on a particle. This is the force which the surrounding medium exerts on the particle moving through medium. The drag force in the  $x$ -direction is given by

$$F_D = \int_{A_p} (\mathbf{T} \cdot \mathbf{n}) \cdot \mathbf{i} ds, \quad (6.2.7)$$

with  $\mathbf{T}$  denoting the stress tensor as defined in (2.2.7). Using the fact that the normal to the spherical surface is in the  $\hat{\mathbf{r}}$ -direction and  $\mathbf{i} = \cos \theta \hat{\mathbf{r}} - \sin \theta \hat{\theta}$  (see figure 6.2.1), we obtain

$$(\mathbf{T} \cdot \mathbf{n}) \cdot \mathbf{i} = -\hat{p} \cos \theta + \tau_{rr} \cos \theta - \tau_{r\theta} \sin \theta$$

in which the shear stress  $\tau_{r\theta}$  is as given in (6.2.6) and the normal stress is given by

$$\tau_{rr} = 2\mu_f \frac{\partial u_r}{\partial r} = -2\mu_f U_\infty \left( \frac{B}{r^2} + \frac{C}{r^4} \right) \cos \theta.$$

Carrying out the surface integration we obtain the drag force

$$F_D = -4B\pi\mu_f U_\infty \quad (6.2.8)$$

For the special case of a solid particle the drag force becomes equal to  $F_D = 6\pi R\mu_f U_\infty$  which is known as the Stokes drag law. From the drag force we obtain the drag coefficient  $C_D$  which is defined via

$$C_D = \frac{F_D}{\frac{1}{2}\pi R^2 \rho U_\infty^2} \quad (6.2.9)$$

which, on using (6.2.8) can be written as  $C_D = -\frac{16B}{R} \times \text{Re}_p$ . In Table 6.1 the drag coefficients for the different particles are listed.

By equating the force which gravity exerts on a particle to the drag force as given in (6.2.8) it is possible to compute the terminal settling velocity of a small particle in an infinite fluid. The gravitational force on a particle is given by  $F_G = -\frac{4}{3}\pi R^3(\rho_g - \rho_f)g$  (assuming gravity acts in the negative  $\mathbf{k}$  direction, cf. Figure 6.2.1), which, on using the expression for the drag force yields the terminal settling equal to

$$U_\infty = \frac{R^3}{3B} \frac{(\rho_p - \rho_f)g}{\mu_f} \quad (6.2.10)$$

It is important to remember the restriction on which the analysis in this section is based. Namely, in order to be able to neglect inertia forces it was required that  $\text{Re}_p \ll 1$ . When we now consider the concrete example of a rain drop falling through air we find that  $U_\infty \simeq 3 \times 10^8 R^2 \text{ m s}^{-1}$ . The condition  $\text{Re}_p \ll 1$  is then satisfied when the rain drop has a diameter less than 0.1 mm!

The analysis so far in this section is based on the assumption that the inertia term  $(\mathbf{u} \cdot \nabla)\mathbf{u}$  is small compared with the viscous term  $\mu_f \nabla^2 \mathbf{u}$  in the momentum equation. We have seen that, subject to this assumption, a linear problem is obtained which can be solved without too much difficulty. If we were to plot the stream lines based on the solution given in (6.2.5) we would observe that these stream lines are symmetric with respect to the plane defined by  $\theta = \pi/2$  (stream lines ahead of the particle follow the same path as those behind the particle). However, experiments show that fore-aft symmetry already breaks down when  $\text{Re}_p \simeq 0.5$  which means that the expression for Stokes drag ceases to be valid when  $\text{Re}_p \gtrsim 0.5$ . In cases where the flow field is only slightly perturbed as compared with the Stokes flow case, work by Oseen (1910) and Proudman & Pearson (1957) showed that the drag coefficient can be written like

$$C_D = \frac{24}{\text{Re}_p} \left[ 1 + \frac{3}{16} \text{Re}_p \right]$$

The range of validity of the above expression is only slightly larger than the Stokes drag approximation. Namely, already for Reynolds numbers exceeding 0.7 it is found that the Oseen approximation of the drag coefficient exceeds the values observed in experiments, see figure 6.2.2. A good approximation of the drag coefficient for Reynolds numbers in the range  $1 < \text{Re}_p < 10^3$  is given by the relation

$$C_D = \frac{24}{\text{Re}_p} \left[ 1 + \frac{1}{6} \text{Re}_p^{2/3} \right]. \quad (6.2.11)$$

For Reynolds numbers in the range  $10^3 < \text{Re}_p < 10^5$  one can assume that the drag coefficient is approximately constant and equal to  $C_D = 0.44$ .

### Sedimentation velocity of a suspension of particles

The drag coefficients given earlier in this section are valid for the case in which a single particle moves through an unbounded fluid. However, in multiphase systems, there are usually many particles present and it is reasonable to expect that particle-particle

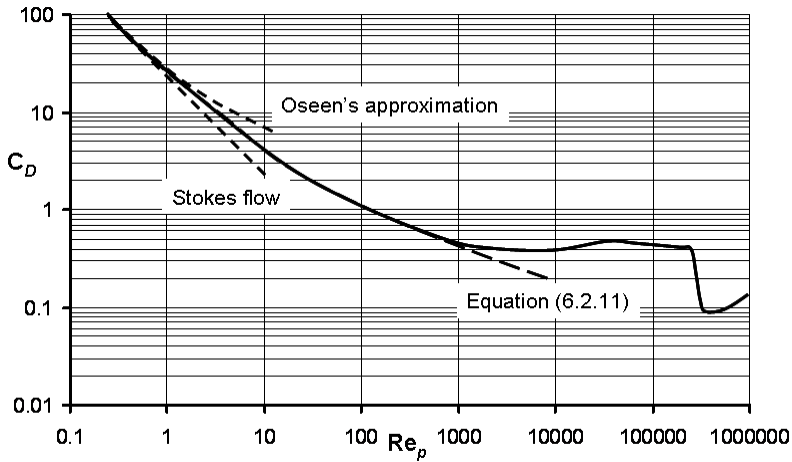


Figure 6.2.2: The drag coefficient  $C_D$  for a smooth sphere as a function of the particle Reynolds number.

interactions will influence the drag coefficient. It is therefore of interest to know how the drag coefficient will be influenced by such particle-particle interactions? To answer this question, imagine the situation in which there is a large cloud of equal-sized particles sedimenting in a liquid. Imagine that there is one particle which is slightly larger than the surrounding particles. Due to its larger mass, this larger particle will have a larger terminal velocity than the other particles (this was shown earlier in this section) and hence it wants to move faster than the others. However, since there are slower-moving particles surrounding it, the larger particle will often find its path blocked by these slower particles. This then implies that the larger particle will not reach the terminal velocity which it could reach if it was moving alone in an unbounded fluid. We come to the conclusion that due to particle-particle interactions, the apparent drag on the larger particle has increased.

For the case of a solid particle falling steadily through a fluid under the action of gravity, the drag force is equal to the gravitational force. Using the gravitational force in equation (6.2.9) we find that the terminal settling velocity can be written in the form

$$U_{\infty,0} = \mathcal{V} \frac{1}{\sqrt{C_{D,0}}}$$

in which  $\mathcal{V} = \sqrt{\frac{8}{3} \frac{R \Delta \rho}{\rho} g}$  and the subscript 0 on the drag coefficient indicates that this is the drag coefficient obtained for a single particle in an unbounded flow. In the case where a cloud of particles falls under the action of gravity though the same fluid, the physical properties of the fluid immediately surrounding the particle are not changed. Therefore it is reasonable to suggest that the terminal velocity in this system can be written like

$$U_{\infty,\phi} = \mathcal{V} \frac{1}{\sqrt{C_{D,\phi}}}$$

where the subscript  $\phi$  indicates properties in a suspension of particles where the volume fraction of particles is equal to  $\phi$ . It follows immediately that

$$\frac{U_{\infty,\phi}}{U_{\infty,0}} = \sqrt{\frac{C_{D,0}}{C_{D,\phi}}} \quad (6.2.12)$$

If we now assume that the drag coefficient  $C_{D,\phi}$  is a regular function of the volume fraction  $\phi$  then a simple expansion of  $C_{D,\phi}$  about  $\phi = 0$  yields  $C_{D,\phi} = C_{D,0} + \phi \frac{dC_{D,\phi}}{d\phi} \Big|_{\phi=0} + O(\phi^2)$ . Substituting this into the above equation we find that in the case where the volume fraction of particles is small, that is  $\phi \ll 1$ , the terminal velocity in a suspension can be written like

$$U_{\infty,\phi} = U_{\infty,0} (1 - n\phi)$$

in which  $n = \frac{1}{2C_{D,0}} \frac{dC_{D,\phi}}{d\phi} \Big|_{\phi=0}$ . Batchelor (1972) has shown theoretically that  $n = 6.5$  for a suspension of mono-sized particles in the low-Reynolds number regime, while for a suspension with a slightly dispersed particle size, Batchelor & Wen (1982) obtain  $n = 5.5$ . Experimental work place the coefficient  $n$  in the range  $4.65 < n < 7.5$  (Di Felice, 1999). For higher Reynolds numbers or systems in which particle-particle interactions can not be neglected, one has to rely on experimental data in order to obtain information about terminal settling velocity. In a classic series of experiments Richardson & Zaki (1954) have investigated how the concentration of suspended particles influences the terminal velocity. They show that data from all their experiments can be written in the form

$$\frac{U_{\infty,\phi}}{U_{\infty,0}} = (1 - \phi)^n \quad (6.2.13)$$

in which the exponent  $n$  is now no longer a constant but a function of the flow regime. For systems where the particle size is small compared with the diameter of the pipe in which the experiments were performed, it is found that the exponent  $n$  is given by the equation

$$\frac{A - n}{n - B} = C \times Re^{3/4} \quad (6.2.14)$$

in which  $A = 4.7$ ,  $B = 2.35$  and  $C = 0.175$ . Similar experiments have been performed more recently by Di Felice (1999) in a system with a lower particle concentration than that used by Richardson & Zaki. There it is found that the constants take one slightly different values, namely,  $A = 6.5$ ,  $B = 3$  and  $C = 0.1$ . Note that both the low and the high Reynolds number limits yield higher values of  $n$  in the Di Felice data set as compared with data set of Richardson & Zaki. Figure 6.2.3 shows how the exponent  $n$  varies as a function of the Reynolds number for both the Richardson & Zaki data set and the Di Felice data set.

We note that by combining equations (6.2.12) and (6.2.13) we can write the drag coefficient for particles in a suspension like

$$C_{D,\phi} = C_{D,0} \times (1 - \phi)^{-2n}$$

Clearly, the drag coefficient for particles in a suspension increases relative to the drag for a single particle in an unbounded fluid. The exponent  $n$  can be found from equation (6.2.14). Here we should keep in mind that the De Felice correlation (with  $A = 6.5$ ,  $B = 3$  and  $C = 0.1$ ) was obtained for particle volume fractions in the range  $0 < \phi < 0.05$  while the Richardson & Zaki correlation ( $A = 4.7$ ,  $B = 2.35$  and  $C = 0.175$ ) was obtained for  $0.2 < \phi < 0.6$ .

An alternative approach to determine the drag coefficient in particulate flows, is to assume that a given, sedimenting particle moves in a pseudo fluid. The density and viscosity of this pseudo fluid will then determine the terminal velocity of the particle under consideration. Let us start with the terminal velocity of a particle in the low-Reynolds number regime. If that particle is moving through a pseudo fluid with density

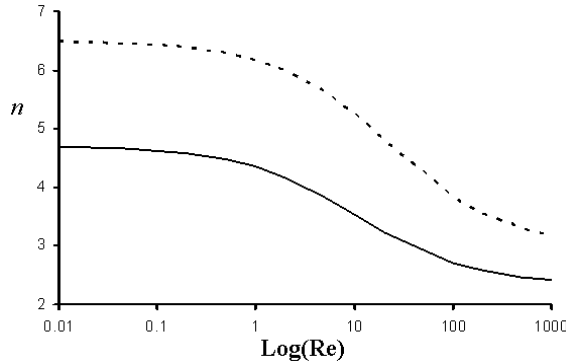


Figure 6.2.3: The exponent  $n$  as a function of the Reynolds number. The dashed curve marks the data by Di Felice (1999) while the drawn curve is based on the data by Richardson & Zaki (1954).

and viscosity given by  $\hat{\rho}$  and  $\hat{\mu}$ , then in direct analogy with (6.2.10) we find that the terminal velocity is equal to

$$\hat{U}_\infty = \frac{R^3}{3B} \frac{(\rho_p - \hat{\rho})g}{\hat{\mu}} = U_\infty \times \frac{\mu_f}{\hat{\mu}} \frac{\rho_p - \hat{\rho}}{\rho_p - \rho_f}$$

We now assume that the density of the pseudo fluid is simply given by the homogeneous mixture density. The volume fraction of particles in the fluid is equal to  $\phi$  and hence the mixture density is equal to  $\hat{\rho} = \phi\rho_p + (1-\phi)\rho_f$ . In the next section it will be shown that the mixture viscosity is equal to  $\hat{\mu} = \mu_f \times (1 + \frac{5}{2}\phi)$  in the limit where  $\phi \ll 1$ . Substituting these expressions for the mixture density and mixture viscosity into the above equation, we obtain

$$\hat{U}_\infty = U_\infty \frac{1 - \phi}{1 + \frac{5}{2}\phi} = U_\infty \left(1 - \frac{7}{2}\phi + O(\phi^2)\right)$$

We observe that the above expression corresponds to a Taylor expansion of (6.2.13) where the exponent is given by  $n = 3.5$ . Note that this value for  $n$  is smaller than the theoretical values determined by Batchelor ( $n = 5$  for a poly-disperse system and  $n = 6$  for a mono-disperse system) and the experimental values of Di Felice and Richardson & Zaki (with  $n = 6.5$  and  $n = 4.7$  respectively). However, Ishii & Zuber (1979) have shown that with an appropriate expression for the mixture viscosity in the non-dilute limit, the pseudo-fluid approach gives quite reasonable estimates of the terminal velocity in poly-disperse systems.

### 6.3 The effective viscosity of a dilute suspension

In multiphase flows, we often have to deal with the motion of gas bubbles, liquid drops or solid particles embedded in a fluid matrix. In the previous section we have considered the motion of such discrete particles relative to the fluid in which they are embedded. We now turn our attention to finding out how the presence of embedded fluid particles alter the physical properties of the fluid matrix. If the particles are homogeneously distributed, it is an easy task to compute the mixture density of the fluid/particle mixture. Namely, given the volume fraction of particles,  $\phi$  say, we find the mixture density via  $\rho_{mixture} = \phi\rho_p + (1-\phi)\rho_f$ .

What about the mixture viscosity? The naive approach would be to use a direct analogy with the mixture density and compute the mixture viscosity via  $\mu_{mixture} = \phi\mu_p + (1-\phi)\mu_f$ .

$\phi)\mu_f$ . Clearly in the case of a solid particle where  $\mu_p \rightarrow \infty$  we have a problem since even for infinitesimal particle concentrations, the influence of the particles in the mixture viscosity would be unphysically large. In the case where the particle viscosity is much less than the viscosity of the fluid matrix (e.g. gas bubbles embedded in a viscous fluid), the naive approach would suggest that the mixture viscosity is always less than the fluid viscosity. This is not in line with experimental observations. It turns out that the naive approach does not provide us with the correct answer for the mixture viscosity, neither in the limit of solid particles, nor in the limit of gas bubbles. So what is the correct answer?

In a classical paper in 1906, Einstein derived an expression for the mixture viscosity of a fluid in which a dilute suspension of small particles is embedded. The assumption of a dilute suspension is important in the analysis. Namely, it is assumed that the distance between individual particles is such that the disturbance of the flow as a result of the presence of each particle is not felt by any of the neighbouring particles. The motion of the fluid in which the particles are embedded can be approximated by summing three components: a uniform translation, a uniform rotation and a straining motion. Particles in the fluid translate and rotate with the fluid so it is only the straining component which is influenced by the presence of particles. The pure straining motion we will consider is that generated by two large plates positioned parallel to the  $x - y$  plane and moving with a velocity equal to  $\xi z$ , see figure 6.3.1. We are now interested in finding the velocity field between the diverging plates with and without a spherical particle present.

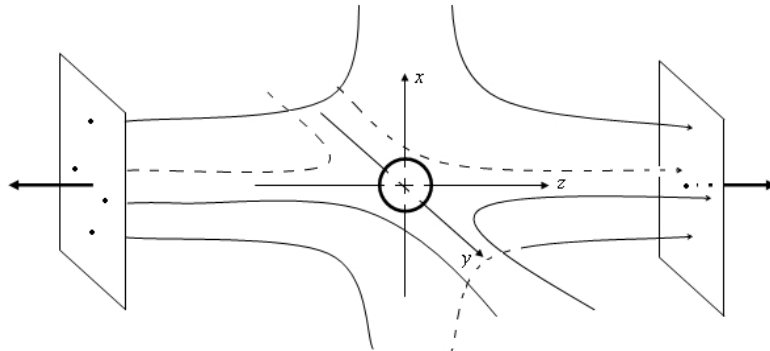


Figure 6.3.1: A uniform extensional flow generated by flat plates moving with a constant velocity along the  $z$ -axis

As in the previous section, we assume steady-state, creeping flow. This implies that the Reynolds number is small and hence that the nonlinear inertia term in the Navier-Stokes equation may be neglected. This then means that we once again have to solve equations (6.2.1) and (6.2.2). It is again convenient to use a spherical coordinate system  $(r, \theta, \phi)$  where there is no  $\phi$ -dependency in any of the terms because of symmetry with respect to rotation about the  $z$ -axis. With reference to figures 6.3.1 and 6.2.1 we may anticipate that  $u_\theta \sim \sin 2\theta$  since symmetry requires that this velocity component vanishes at  $\theta = 0, \pi/2, \pi$  and  $3\pi/2$ . This result, together with the mass conservation equation yields immediately that the angle-dependency of the radial velocity component must be of the form  $u_r \sim 3 \cos^2 \theta - 1$ . These angle dependencies, together with the velocity of the plates which generate the straining motion, lead us to consider velocity components of the forms

$$\begin{aligned} u_r &= \xi(3 \cos^2 \theta - 1)f(r) \\ u_\theta &= \xi \sin 2\theta g(r) \end{aligned}$$

Substituting these velocity components into the  $r$ - or  $\theta$ -components of the momentum equation yields immediately that the pressure needs to be of the form

$$\hat{p}(r, \theta) = P_0 + \mu_f \xi (3 \cos^2 \theta - 1) P(r)$$

Solving the equations is now directly analogous to the procedure outlined in the previous section. Namely, first we substitute the above expressions for the velocity components and the pressure into the mass and the momentum equations. This gives rise to three linear, coupled ODE's from which one fourth-order ODE can be obtained. The characteristic equation for the function  $f(r)$  is now found to be given by

$$(m-1)(m+2)(m+4)(m-3) = 0 \quad (6.3.1)$$

which yields that the function  $f(r)$  is of the general form

$$f(r) = Ar + Br^3 + \frac{C}{r} + \frac{D}{r^4}$$

At large values of  $r$  we expect the radial velocity to be determined by the large plates which generate the straining motion and this implies that  $A = \frac{1}{2}$  and  $B = 0$  since at  $\theta = 0$  we expect  $u_r \rightarrow \xi r$  as  $r \rightarrow \infty$ . It is now not hard to show that the velocity components and the pressure have the following functional forms

$$u_r = \frac{1}{2} \xi r (3 \cos^2 \theta - 1) \left[ 1 + \frac{2C}{r^3} + \frac{2D}{r^5} \right] \quad (6.3.2a)$$

$$u_\theta = -\frac{3}{4} \xi r \sin 2\theta \left[ 1 - \frac{4D}{3r^5} \right] \quad (6.3.2b)$$

$$\hat{p}(r, \theta) = P_0 + \mu_f \xi (3 \cos^2 \theta - 1) \frac{2C}{r^3} \quad (6.3.2c)$$

The remaining constants  $C$  and  $D$  are determined by specifying boundary conditions at the surface of the particle. For a solid particle, in which case we demand  $u_r = u_\theta = 0$  at the particle surface  $r = R$ , it is easy to show that  $C = -\frac{5}{4}R^3$  and  $D = \frac{3}{4}R^5$ . However, we are not only interested in the effective viscosity of a solid-particle suspension. Indeed, the case in which internal circulation in a suspended particle is possible, is also of significant interest.

Let us therefore consider the flow field inside the particle resulting from the external straining motion. In complete analogy with the analysis related to the external motion, we now consider velocity components and the pressure inside the particle to be of the form

$$\begin{aligned} \tilde{u}_r &= \xi (3 \cos^2 \theta - 1) \tilde{f}(r) \\ \tilde{u}_\theta &= \xi \sin 2\theta \tilde{g}(r) \\ \tilde{p}(r, \theta) &= \mu_p \xi (3 \cos^2 \theta - 1) \tilde{P}(r) \end{aligned}$$

where  $\mu_p$  denotes the viscosity of the fluid inside the particle. Substituting these expressions into the mass and momentum conservation equations yields once again three linear, coupled ordinary differential equations. The characteristic equation for the function  $f(r)$  is identical to (6.3.1). Continuity at  $r = 0$  requires now that the coefficients related to the negative powers are identically zero so that the velocity components related to the internal motion are of the form

$$\begin{aligned}\tilde{u}_r &= \xi r (3 \cos^2 \theta - 1) [\tilde{A} + \tilde{B} r^2] \\ \tilde{u}_\theta &= -\frac{1}{2} \xi r \sin 2\theta [3\tilde{A} + 5\tilde{B} r^2]\end{aligned}$$

Once again, the remaining unknown constants  $\tilde{A}$  and  $\tilde{B}$  are determined by the boundary conditions at the particle surface. In total we have four unknowns ( $C$ ,  $D$ ,  $\tilde{A}$  and  $\tilde{B}$ ) which implies that four conditions are required in order to be able to determine each unknown. What are these four conditions? To start with, we have assumed that the fluids are incompressible which implies that the particle can not change volume as a result of the straining motion. We have assumed that the particle remains spherical so that volume conservation implies

$$\tilde{u}_r = 0 \text{ and } u_r = 0 \text{ at } r = R$$

Continuity of tangential velocity at the particle interface requires

$$\tilde{u}_\theta = u_\theta \text{ at } r = R$$

and, finally, continuity of interfacial shear stress at the particle interface demands

$$\tilde{\tau}_{r\theta} = \tau_{r\theta} \text{ at } r = R$$

It turns out that the effective viscosity is closely related to the coefficient  $C$ . Application of the boundary conditions at the particle surface as specified above, yields without much difficulty that

$$C = -\frac{R^3}{4} \frac{2 + 5\mathcal{M}}{1 + \mathcal{M}} \quad (6.3.3)$$

in which  $\mathcal{M} = \mu_p/\mu_f$ .

We are now at the point where we can return to the central question which we try to answer in this section: what is the effective viscosity of a dilute suspension of particles? Suppose we had some way of measuring the force required to move the plates that generate the straining motion. This force would be slightly increased by the presence of the particle. Hence, if we, in some way, could relate the modified force to some effective viscosity we would have the result we are seeking. However, rather than considering the modification of the force on the plates as a result of the particle, it turns out to be more convenient to consider the rate work being done on a large spherical surface surrounding the particle.

The rate of work done on a given surface  $S$  in a continuum is given by

$$\dot{W} = \int_S \mathbf{T} \cdot \mathbf{n} \cdot \mathbf{v}_0 dS$$

in which  $\mathbf{n}$  denotes a unit normal to the surface  $S$  and  $\mathbf{v}_0$  is the velocity resulting from the pure straining motion. For the surface  $S$  we take a sphere, concentric with the particle and with a radius  $R_S \gg R$ . We now take the tensor  $\mathbf{T}$  to be the stress tensor in the fluid where the particle is present, hence  $\mathbf{T} = \mathbf{T}_0 + \mathbf{T}'$ . Here  $\mathbf{T}_0 = -P_0 \mathbf{I} + 2\mu_f \mathbf{E}_0$  denotes the stress tensor in the case of pure straining motion without the particle present (obtained from (6.3.2) with  $C = D = 0$ ) and  $\mathbf{T}'$  denotes the deviation of  $\mathbf{T}$  due to the presence of the particle (the terms in  $\mathbf{T}'$  all involve the coefficients  $C$  and  $D$ ). If the fluid containing the particle was replaced by a homogeneous fluid with viscosity  $\mu^*$  then

the corresponding stress tensor would be  $\mathbf{T}^* = -P_0\mathbf{I} + 2\mu^*\mathbf{E}_0$ . The work done on the surface  $S$  for this fluid would be

$$W^* = \int_S \mathbf{T}^* \cdot \mathbf{n} \cdot \mathbf{v}_0 dS$$

The question we now have to answer is the following: which viscosity  $\mu^*$  is required in order to obtain  $W^* = \dot{W}$ ? Substituting for  $\mathbf{T}$  and  $\mathbf{T}^*$  in the work-integrals, it is not hard to show that

$$2(\mu^* - \mu_f) \int_S \mathbf{E}_0 \cdot \hat{\mathbf{r}} \cdot \mathbf{v}_0 dS = \int_S \mathbf{T}' \cdot \hat{\mathbf{r}} \cdot \mathbf{v}_0 dS \quad (6.3.4)$$

The relation between the rate of strain tensor and the deviatoric stress tensor is given by  $2\mu\mathbf{E} = \mathbf{D}$  and the components of the rate of strain tensor are as follows:  $e_{rr} = \frac{\partial u_r}{\partial r}$ ,  $e_{r\theta} = \frac{r}{2} \frac{\partial}{\partial r} \left( \frac{u_\theta}{r} \right) + \frac{1}{2r} \frac{\partial u_r}{\partial \theta}$  and  $e_{\theta\theta} = \frac{1}{r} \frac{\partial u_\theta}{\partial \theta} + \frac{u_r}{r}$ . Using the velocity components given in (6.3.2) with  $C = D = 0$  we can now calculate  $\mathbf{E}_0$ . Likewise, using (6.3.2) with  $C, D \neq 0$  the tensor  $\mathbf{T}'$  can be determined. Evaluating the surface integrals in (6.3.4), it is not hard to show that the final result can be written like

$$\frac{\mu^*}{\mu_f} = 1 - \frac{2C}{R_S^3} + O(R_S^{-5})$$

Using the above result together with (6.3.3), we finally obtain

$$\mu^* = \mu_f \left[ 1 + \phi \frac{1 + 2.5\mathcal{M}}{1 + \mathcal{M}} + O(\phi^2) \right] \quad (6.3.5)$$

where  $\phi = (R/R_S)^3$  denotes the fraction of the volume occupied by the particle. In the limit where the particle viscosity becomes much larger than that of the surrounding fluid (that is  $\mathcal{M} \gg 1$ ), the effective viscosity becomes  $\mu^* = \mu_f [1 + \frac{5}{2}\phi + O(\phi^2)]$  which is the result first derived by Einstein in 1906. When the particle viscosity is much less than that of the surrounding fluid (the case of a bubbly flow), the effective viscosity becomes  $\mu^* = \mu_f [1 + \phi + O(\phi^2)]$ . The expression for the effective viscosity as given in (6.3.5) is valid for the case when particle-particle interactions are negligible. In practice this means that  $\phi \lesssim 0.02$  which means that (6.3.5) is of limited use in all but the most dilute systems of dispersed particles.

An analysis similar to that performed above can be carried out for the case on non-spherical (spheroidal) particles. Landau & Lifshitz (1987) show that the first-order estimate of the effective viscosity for spheroidal particles can be written like

$$\mu^* = \mu_f [1 + A\phi + O(\phi^2)]$$

in which the coefficient  $A$  is strongly dependent on the ratio of the semi-axes on the spheroid. In figure 6.3.2 we have plotted the parameter  $A$  as a function of  $\frac{a}{b}$  where  $a$  and  $b = c$  are the semi-axes of the spheroid. We observe that the effective viscosity is smallest for spheres while it increases both for oblate and prolate spheroids.

### The effective viscosity of emulsions

If a mixture of oil and water flows in a pipe, we have seen in figure 3.3.4 that the measured pressure drop may increase significantly as the water fraction increases beyond a value of 0.2. If we assume that the oil and water in the pipe flows as a homogeneous mixture, we can use the pressure gradient to deduce a mixture viscosity. An analysis of this type

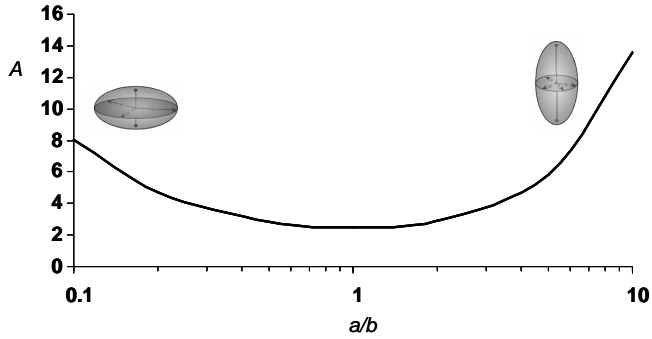


Figure 6.3.2: The value of the parameter  $A$  as a function of the ratio of the semi-axes  $a/b$  of a spheroidal particle

shows how the mixture viscosity increases by almost a factor 10 when the dispersed water fraction increases from 0 to 0.4. It will be clear that equation (6.3.5) can not be used to predict this increase in the mixture viscosity and models which are valid for larger volume fractions of the dispersed phase are needed.

Before we can discuss different models for the effective viscosity of systems containing a significant fraction of a dispersed phase, we need to have some understanding of the physical processes that may influence the viscosity. It will be clear that the viscosity ratio  $\mathcal{M} = \mu_p/\mu_f$  will be an important parameter but it is reasonable to expect that the particle radius  $R$ , the shear rate  $\dot{\gamma}$  and the surface tension coefficient  $\sigma$  also play a role. A standard application of dimensional analyses shows, that for sufficiently large particles which constitute the dispersed phase in a neutrally-buoyant system at steady state, the effective viscosity is a function of 4 parameters, namely

$$\mu^* = \mu_f \times f(\phi, \mathcal{M}, \text{Re}_{\dot{\gamma}}, Ca)$$

where we have introduced the Reynolds number  $\text{Re}_{\dot{\gamma}} = \rho_f R^2 \dot{\gamma} / \mu_f$  and the capillary number  $Ca = \mu_f \dot{\gamma} R / \sigma$ . Let us now look at the role which each of the four parameters play in the function  $f(\phi, \mathcal{M}, \text{Re}_{\dot{\gamma}}, Ca)$ . Referring to the previous section, it is intuitive that the concentration of the dispersed phase is a very important parameter. Namely, there it was seen that the mobility of the dispersed phase particles reduces significantly when the particle concentration increases. We therefore expect the ease with which we can deform a fluid containing a certain concentration of dispersed phase particles, to be reduced when the particle concentration increases. The particle concentration can not, of course, be increased indefinitely. Long before the volume fraction of the particles reaches unity, particles will be in mutual contact. For rigid spheres with equal diameters, it turns out that the particle volume fraction can not exceed the value 0.64. This, so called, maximum packing fraction is larger when particles are deformable or when particles of different sizes are present. As the concentration of the dispersed phase approaches the maximum packing fraction  $\phi_m$ , we expect to observe special effects. In the case where the dispersed phase consists of solid particles, we expect the fluid in which the particles are dispersed to become increasingly stiff as  $\phi \rightarrow \phi_m$ , suggesting that the viscosity should become very large. Alternatively, when the dispersed phase consists of bubbles or drops, a dispersed phase fraction close to  $\phi_m$  will lead to increasingly strong bubble-bubble or droplet-droplet interactions and therefore clearly the possibility that drops or bubbles will coalesce.

It turns out that it is important to distinguish between *stable* and *unstable* emulsions. Stable emulsions refer to systems in which the size distribution of the dispersed phase

is unaffected by the shearing action of the fluid motion and the dispersed phase concentration. This is the case when the dispersed phase consists of solid particles or when the particles are so small that they behave as if they were solid. On the other hand, in unstable emulsions, the mean particle size may change as a result of the shearing motion (due to coalescence or break-up events). When the capillary number is small, surface tension forces dominate shearing forces and hence deformation or break-up of the dispersed phase particles will not occur. Hence, a stable emulsion in the case of non-solid particles occurs only when  $Ca \rightarrow 0$ .

In the limit of creeping flow, inertia effects are small (that is  $Re_\gamma \ll 1$ ), and hence we are in the regime which was studied earlier in this section. If in addition  $Ca \rightarrow 0$  we have seen that in the case of dilute suspensions, equation (6.3.5) tells us how the effective viscosity varies as a function of  $\phi$  and  $\mathcal{M}$ .

Let us start with the case in which the emulsion consists of solid particles in a creeping flow, that is  $Ca = 0$  and  $Re_\gamma \ll 1$ . By taking into account long-range hydro-dynamic interactions, Batchelor (1977) has shown that for the case of solid spherical particles, a second-order estimate of the effective viscosity is given by

$$\mu^* = \mu_f [1 + 2.5\phi + 7.6\phi^2 + O(\phi^3)]$$

While this expression has an increased range of validity as compared with the Einstein approximation, it is still limited to the case where  $\phi \ll \phi_m$ .

In order to obtain an estimate of the effective viscosity in the case where the dispersed phase concentration is large, that is  $\phi = O(\phi_m)$ , we can once again use the concept of a pseudo-fluid (sometimes also referred to as the effective medium theory). Recall, that this was used earlier when considering sedimentation in a system with a large concentration of particles (see section 6.2). Using the concept of a pseudo-fluid we may assume that for a given dispersed phase concentration  $\phi$ , the fluid surrounding a given particle has some given effective viscosity, equal to  $\mu^*(\phi)$ . When the dispersed phase concentration is now increased to  $\phi + \Delta\phi$  we use the result from the dilute limit by computing a new effective viscosity equal to

$$\mu^*(\phi) + \Delta\mu^* = \mu^*(\phi) [1 + A \times \Delta\phi]$$

In the limit where  $\phi \rightarrow 0$  we know that the constant  $A = 2.5$  but for higher volume fractions of the dispersed phase this is not necessarily the case and therefore we let  $A$  be a free parameter for the moment. We have to take some care in calculating  $\Delta\phi$  since the volume fraction of the dispersed phase can not be increased *ad infinitum*. Clearly,  $\phi$  can never increase beyond unity and for realistic systems there will be a maximum packing fraction  $\phi_m$  which defines an upper limit for the dispersed phase fraction. Hence, as the maximum packing fraction is approached, the "available volume" to which new particles can be added is equal to  $V_a = V \times (\phi_m - \phi)$  (here  $V$  denotes the total volume of the fluid to which particles are added). The volume of the dispersed phase is equal to  $V_d = V \times \phi$  so that  $\Delta\phi = \delta V_d / V_a$ , and hence

$$\mu^*(\phi) + \Delta\mu^* = \mu^*(\phi) \left[ 1 + A \times \frac{\delta V_d}{V_a} \right] = \mu^*(\phi) \left[ 1 + A \times \frac{\delta\phi}{\phi_m - \phi} \right]$$

Taking the limit  $\delta\phi \rightarrow 0$  and solving the resulting differential equation we obtain

$$\mu^* = B \times \left( 1 - \frac{\phi}{\phi_m} \right)^{-A} \tag{6.3.6}$$

in which  $B$  is an integration constant. We demand that in the limit  $\phi \rightarrow 0$  we should regain the familiar Einstein result  $\mu^* = \mu_f [1 + 2.5\phi]$ . This determines the constants,

namely  $A = 2.5\phi_m$  and  $B = \mu_f$ . The result given above was first derived by Krieger & Dougherty (1959). Experiments with a mono-disperse, dense suspension of particles in a rheometer (generating Couette flow) show that the Krieger-Dougherty model closely follows experimental results when one allows  $\phi_m$  to be used as a tuning parameter (see figure 6.3.3).

A number of different expressions have been proposed which describe the effective viscosity of stable emulsions as a function of the volume fraction of the dispersed phase. In table 6.2 we list some of the expressions which are commonly used. All of the expressions in table 6.2 exhibit the behaviour as predicted by Einstein's equation in the limit  $\phi \rightarrow 0$ .

$\mu^*/\mu_f$	Reference
$\left(1 + \frac{2.5\phi}{2(1-\phi/\phi_m)}\right)^2$	Eilers (1941)
$\exp\left(\frac{2.5\phi}{1-0.609\phi}\right)$	Vand (1948)
$\left(1 - \frac{\phi}{\phi_m}\right)^{-2.5\phi_m}$	Krieger & Dougherty (1959)
$1 + \frac{10(1-\lambda^7)}{4-25\lambda^3+42\lambda^5-25\lambda^7+4\lambda^{10}}\phi$	Choi & Schowalter (1975)

**Table 6.2:** Some commonly-used expressions for the effective viscosity for the case of stable emulsions. In the last of the above expressions we have used  $\lambda = \phi^{1/3}$ .

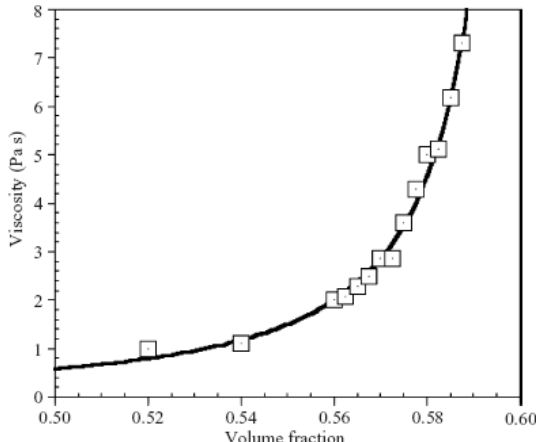


Figure 6.3.3: The measured effective viscosity as a function of the particle volume fraction  $\phi$  (Huang & Bonn, 2007). The maximum packing fraction  $\phi_m = 0.608$  is used to fit the data.

So far we have looked at the case of a stable emulsion that has the characteristic that the particle size distribution is unaffected by the shearing motion and possible particle-particle interactions. Consider now the case where two immiscible liquids, like oil and water, flow simultaneously in a pipe. When the volume fraction of water is small (typically less than 0.2) it is found that for sufficiently large velocities, the water is transported in the form of dispersed droplets in the oil phase (see figure 3.3.2). As the water fraction increases, the volume fraction of water droplets increases. Hence, droplet-droplet interactions will become more and more common and it is reasonable to expect that some of these interactions will lead to coalescence events: larger drops will be formed. A nice example of this behaviour is shown in figure 6.3.4 where we observed that the mean diameter increased dramatically when the volume fraction of water increases beyond 0.3. This is clearly an unstable emulsion and one has to be careful in applying the emulsion viscosity models as discussed above. How do then we proceed?

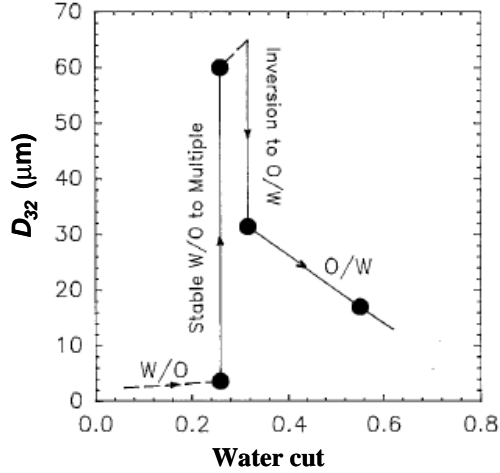


Figure 6.3.4: The Sauter mean diameter ( $D_{32}$ ) as a function of the water concentration (Pal, 1993).

When dealing with drops or bubbles as the dispersed phase, it is clear that internal circulation may occur and hence equation (6.3.5) should be used in the pseudo-fluid modelling approach of the effective viscosity. The procedure is exactly the same as that outlined above for the case of solid particles and it is not hard to show that the following result is obtained

$$\frac{\mu^*}{\mu_f} \times \left( \frac{\mu^*/\mu_f + 2.5\mathcal{M}}{1 + 2.5\mathcal{M}} \right)^{3/2} = \left( 1 - \frac{\phi}{\phi_m} \right)^{-5/2} \quad (6.3.7)$$

The parameter  $\phi_m$  is now the maximum packing fraction for the case of an unstable emulsion. We expect that  $\phi_m$  decreases in systems where it is easy for drops to coalesce. Hence, in systems with small drops or in systems where the dispersed phase is stabilised through the action of surfactants, we expect  $\phi_m$  to be relatively large. An analysis by Pal (2000) suggest that in this case  $\phi_m \simeq 0.74$ . In systems where coalescence events are frequent (typically when drops are large) it is found that the maximum packing fraction decreases to  $\phi_m \simeq 0.5$ . The liquid-liquid system related to the data shown in figure 6.3.4 is a typical example of a very unstable emulsion. There we see that mean drop sizes increase significantly already when  $\phi \simeq 0.3$ . This then suggests that for this system the maximum packing fraction is even less than 0.5.

#### 6.4 The formation of drops and bubbles in turbulent flows

In the previous sections we have seen how dispersed-phase particles move through a fluid and how their presence influences the macroscopic properties of the fluid in which they are dispersed. If the dispersed phase particles are solid then it is clear that their size is pre-determined and invariant under normal flow conditions. However, if the dispersed phase consists of bubbles or drops, we have to consider the possibility that the particles will deform and break apart as a result of the forces exerted on the particles by the surrounding fluid. This is in particular the case when the carrying phase is in violent turbulent motion, see figure 6.4.1. A natural question to ask is: which forces are responsible for a possible break-up of the dispersed phase? If this break-up is due to shearing action of the carrying fluid, then the particle dimension has to be small compared to typical length scales associated with the shearing. In a turbulent flow, the main shearing action occurs on the Kolmogorov scales (see section 2.5.1), and these

are small compared with typical bubble or drop sizes. This then suggests that the shearing forces are not the main mechanism for particle break-up in a turbulent flow.

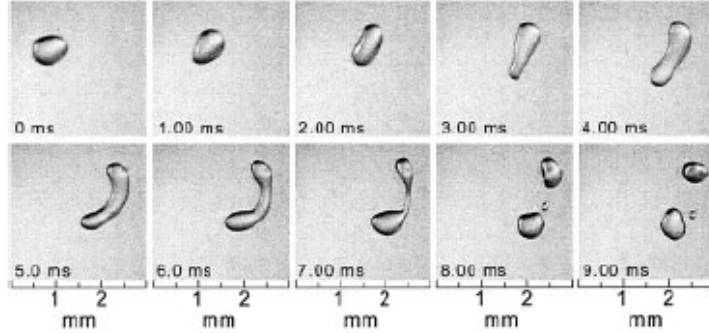


Figure 6.4.1: Break-up of a liquid drop in a turbulent water-dodecane flow (Andersson & Andersson, 2006)

Kolmogorov (1949) and Hinze (1955), independently, suggested that the dynamic pressure force associated with turbulent fluctuations is the governing mechanism leading to particle breakup. The force which holds the dispersed phase particle together is clearly the surface tension force given by  $\sigma/R$  with  $R$  denoting the radius of the particle. It follows that if there is some maximum particle diameter  $d_{\max}$  then this diameter will be determined by some critical ratio between the (deforming) dynamic pressure force and the (restoring) surface tension force. The dynamic pressure force is proportional to  $\rho_f V^2$  where  $V$  is some velocity representative of dynamic pressure fluctuations on a length scale  $d_{\max}$ . Hence, the critical ratio of deforming and restoring forces is given by the critical Weber number

$$We_{crit} = \frac{\rho_f V^2}{\sigma/d_{\max}} \quad (6.4.1)$$

When the density of the dispersed phase and the continuous phase are similar we may assume that the velocity of dispersed phase particle is close to that of the continuous phase. In that case we may take  $V \sim U$  where the turbulent velocity scale  $U$  is the velocity scale associated turbulent eddies with a size approximately equal to  $d_{\max}$ . Namely, we expect the strongest interaction when turbulent eddies and dispersed phase particles have a similar size. Larger eddies will just transport the particle rather than break it while smaller eddies do not have the energy to stretch and break it.

When the density of the dispersed phase is much higher than that of the continuous phase (liquid drops in gas flow), we can no longer assume that  $V \sim U$  due to particle inertia effects. By considering the particle motion on the scale of a turbulent eddy, Levich (1962) shows the velocity of the particle relative to that of the eddy, is strongly dependent on the size of the particle. The maximum relative velocity can be shown to be related to the eddy velocity via  $V \sim U \left( \frac{\rho_d}{\rho_f} \right)^{1/3}$ . When the density of the dispersed phase is much less than that of the continuous phase (gas bubble in liquid flow) the dispersed phase particle has negligible inertia and hence it will follow the eddy. However, dynamic pressure effects inside the particle will be significant and Levich shows that in this case  $V \sim U \left( \frac{\rho_d}{\rho_f} \right)^{1/6}$ . Now, provided  $d_{\max} \gg \lambda$  where  $\lambda$  denotes the Kolmogorov micro scale, we can use Kolmogorov's relation (2.5.2) to obtain

$$U^2 = C_1 (\varepsilon d_{\max})^{2/3} \quad (6.4.2)$$

It can be shown that the constant  $C_1 \simeq 2$  for the case of isotropic, homogeneous turbulence. If there is indeed one specific critical Weber number which determines the

maximum particle size, then (6.4.1) and (6.4.2) can be used to determine the maximum stable particle diameter via

$$d_{\max} = C \times \varepsilon^{-2/5} \left( \frac{\sigma}{\rho_f} \right)^{3/5} \left( \frac{\rho_f}{\rho_d} \right)^{3n/5} \quad (6.4.3)$$

in which  $C = (\frac{1}{2}W_{crit})^{3/5}$  is a constant which is yet to be determined. The exponent  $n$  is dependent on the relative density of the dispersed and the continuous phase: for liquid-liquid flows the density ratio in (6.4.2) is approximately unity and we can take  $n = 0$ ; for the case of liquid drops in a gas stream where  $\rho_f \ll \rho_d$  we take  $n = \frac{1}{3}$  and finally, for gas bubbles in a liquid stream where  $\rho_f \gg \rho_d$  we take  $n = \frac{1}{6}$ .

By comparing maximum drop sizes as predicted by (6.4.3) with experimental data in a liquid-liquid system, Hinze (1955) determined the value of the constant be  $C = 0.725$ . Using this value of  $C$  to determine the critical Weber number, it is found that  $We_{crit} \simeq 1.18$ . It was later shown by Sevik & Park (1973) that this value of the critical Weber number corresponds well with the value predicted theoretically when one assumes that the droplet break-up in a liquid-liquid system is caused by the excitation of the lowest resonance frequency of the drop as a result turbulent fluctuations. In a gas-liquid system (gas bubbles in a liquid matrix), the critical Weber number was found to be  $We_{crit} \simeq 2.48$ .

The rate of dissipation of turbulent energy  $\varepsilon$ , which is needed in (6.4.3), is readily obtained from our knowledge of the pressure gradient. Namely, the rate of dissipation of turbulent energy must be equal to the total energy input. For the case of pipe flow, the energy input per unit time and per unit mass is equal to  $-\frac{1}{\rho} \bar{U} \frac{dp}{dx}$  and the pressure gradient is found using equation (2.6.2), so that we obtain

$$\varepsilon = \frac{\bar{U}^3 f}{2D} \quad (6.4.4)$$

It is now interesting to know how well the relatively simple model proposed by Hinze and Levich predicts actual drop or bubble sizes in turbulent pipe flow. Extensive studies by Kalabelas (1978) and Simmons & Azzopardi (2001) among others, show that in experiments where the dispersed phase concentration is low, the Hinze–Levich model predicts the maximum drop size surprisingly well. Hesketh et al (1987) and Razzaque et al (2003) show that the same conclusion holds for the case of bubbly flow.

Experiments by Simmons & Azzopardi (2001) show that the maximum drop size in non-dilute systems is generally under-predicted by the Hinze model. It is natural to ask if the pseudo-fluid concept can be applied here to modify the Hinze model such that it becomes valid for non-dilute systems. It turns out that this is not the case. The reason is that the influence of the dispersed phase on the dissipation rate of turbulent energy is not captured by equation (6.4.4). Namely, experimental evidence suggests that the turbulent intensities in dispersed-phase flow can both increase and decrease as a result of the presence of the dispersed phase. The particle size appears to have a defining influence on the turbulent intensity: small particles (significantly smaller than the main turbulent structures) reduce the turbulent intensity while large particles may enhance turbulence (Brennen, 2005). Hence, the turbulent energy dissipation rate  $\varepsilon$  is a function of the particle size distribution and this functional dependence is not present in (6.4.4). Extensions of the Hinze model for dense suspensions have been proposed by, for example, Brauner (2001). The region of validity of these extensions is, however, unclear at present. In a dense suspension, coalescence and break-up events imply that the particle size of the dispersed phase is a dynamic quantity. Hence, rather than assuming that there exists some average particle size (Brauner's approach) one could introduce an additional conservation equation for the interfacial area concentration. This conservation equation requires models for coalescence and break-up events. A detailed outline of this approach is given by Ishii & Hibiki (2006).

As is clear from figure 6.4.1, break-up events generally lead to the formation of large and small particles. We expect therefore that emulsions in pipe flow consists of particles of many different sizes. Extensive pipe flow experiments by Karabelas (1978) and Angelli & Hewitt (2000b) in liquid-liquid systems, show that particle sizes can be described using a Rosin-Rammler distribution, given by the relation

$$1 - V_{cum} = \exp\left(-\left(\frac{d}{d_{95}}\right)^n\right) \quad (6.4.5)$$

In the above equation,  $V_{cum}$  denotes the cumulative volume fraction of drops that have a diameter equal to  $d$ . The diameter  $d_{95}$  denotes the particle size for which 95% of the particles are smaller than  $d_{95}$  and  $n$  is an experimentally-determined parameter. Experimental data puts the parameter  $n$  in the range  $2.5 \lesssim n \lesssim 3$  for liquid-liquid flows. Simons & Azzopardi (2001) and Razzaque et al (2003) show that for liquid-liquid and gas-liquid systems, dispersed phase particle sizes can also be modelled using log-normal distributions.

## 6.5 The cross-sectional distribution of a dispersed phase

When one phase is completely dispersed in the second phase, it is not necessarily the case that the dispersed phase concentration is constant over the whole of the cross section of the pipe. A clear example of such a situation is shown in figure 4.7.1. In the picture we see a dispersed, oil-continuous system where the concentration of water drops is large at the bottom of the pipe while at the top of the pipe there are very few drops. The one-dimensional area-averaged models as derived in sections 4.4 and 4.8 can, obviously not be used to predict cross-sectional variations in the dispersed phase fraxctions. However, with the building blocks which we have established in chapter 4 and the current chapter, it is possible to develop a model that can explain the spatial distribution of the drops as seen in figure 4.7.1.

As a starting point we take the conservation equations for a two-fluid mixture as derived in section 4.3 and we use these to obtain a multi-dimensional dispersed-flow model. The path to the multi-dimensional model is very similar to that take in section 4.7 to derived the one-dimensional dispersed flow model. Proceeding as outlined, we add the mass conservation equations (4.3.13) and use mass conservation at the interface (4.3.9) to obtain the mass conservation equation for the mixture, namely

$$\frac{\partial}{\partial t} (\bar{\rho}_m) + \nabla \cdot (\bar{\rho}_m \bar{\mathbf{v}}_m) = 0 \quad (6.5.1)$$

Here we have defined the mixture density via

$$\bar{\rho}_m = \sum_k \bar{\alpha}_k \bar{\rho}_k^x$$

and the mixture velocity via

$$\bar{\mathbf{v}}_m = \frac{1}{\bar{\rho}_m} \sum_k \bar{\alpha}_k \bar{\rho}_k^x \bar{\mathbf{v}}_k^{x\rho}$$

The momentum conservation equation for the mixture is obtained by adding the conservation equation for each phase as given in (4.3.15) and employing the interface condition (4.3.10), to give

$$\frac{\partial}{\partial t} (\bar{\rho}_m \bar{\mathbf{v}}_m) + \nabla \cdot (\bar{\rho}_m \bar{\mathbf{v}}_m \bar{\mathbf{v}}_m) = \nabla \cdot \left( \bar{\mathbf{T}}_m + \bar{\mathbf{T}}^{\text{Re}} + \bar{\mathbf{T}}^D \right) - \bar{\rho}_m \bar{\mathbf{g}}_m + \mathbf{m}_i \quad (6.5.2)$$

We have introduced the mixture shear stress tensors  $\bar{\mathbf{T}}_m = \sum_k \bar{\alpha}_k \bar{\mathbf{T}}_k$ , the mixture Reynolds stress tensor  $\bar{\mathbf{T}}^{\text{Re}} = \sum_k \bar{\alpha}_k \bar{\mathbf{T}}_k^{\text{Re}}$  and mixture diffusion stress tensor  $\bar{\mathbf{T}}^D = -\sum_k \bar{\alpha}_k \bar{\rho}_k^x \bar{\mathbf{v}}_{km} \bar{\mathbf{v}}_{km}$  in which the diffusion velocity is defined via  $\bar{\mathbf{v}}_{km} = \bar{\mathbf{v}}_k^{x\rho} - \bar{\mathbf{v}}_m$ . Finally,  $\bar{\mathbf{g}}_m = \frac{1}{\bar{\rho}_m} \sum_k \bar{\alpha}_k \bar{\rho}_k \bar{\mathbf{g}}_k^{x\rho}$  the weighted gravitational force acting on the mixture. As in case of the one-dimensional dispersed-flow model, one additional conservation equation is required since we have three independent variables: the mixture density, the mixture velocity and the diffusion velocity. This additional conservation equation (termed the diffusion equation) is obtained from the mass conservation equation for phase 2, namely

$$\frac{\partial}{\partial t} (\bar{\alpha}_2 \bar{\rho}_2) + \nabla \cdot (\bar{\alpha}_2 \bar{\rho}_2^x \bar{\mathbf{v}}_m) = \bar{\Gamma}_2 - \nabla \cdot (\bar{\alpha}_2 \bar{\rho}_2^x \bar{\mathbf{v}}_{2m}) \quad (6.5.3)$$

With the relevant equations in place we now return to the problem we want to study, that is a dispersed flow where the dispersed phase is not homogeneously distributed over the cross-section of the pipe. We assume that the axis of the pipe is aligned with the  $x$ -axis and that the flow under consideration is stationary ( $\partial_t = 0$ ) and fully developed ( $\partial_x = 0$ ). For fully developed flow it is natural to assume that the velocity field is of the form  $\bar{\mathbf{v}}_m = (\bar{v}_{mx}(y, z), 0, 0)$ . With this assumption and the requirement that the flow be stationary, it follows immediately that the mass conservation equation (6.5.1) is identically satisfied. Under the given assumptions it follows that both terms on the left-hand-side of the momentum equation (6.5.2) vanish. Hence, the momentum equation reduces to a statement that the pressure gradient is constant along the axis of the pipe (note the similarity between the current problem and the problem studied in sections 2.4 and 5.2).

We next turn our attention to the diffusion equation (6.5.3). Subject to the assumptions as stated above, it is clear that both terms on the left hand side of this equation vanish. When we assume, in addition, that there is no transfer of mass between the phases (that is  $\bar{\Gamma}_2 \equiv 0$ ) we are left with the equation

$$\nabla \cdot (\bar{\alpha}_2 \bar{\rho}_2^x \bar{\mathbf{v}}_{2m}) = 0 \quad (6.5.4)$$

The diffusion velocity  $\bar{\mathbf{v}}_{km}$  is an unknown quantity and it has to be modelled, based on our physical understanding of the problem. So what are the physical processes governing the motion of the dispersed phase in the pipe? Clearly the action of gravity will induce a buoyancy force which will try to move the heaviest phase to the lower part of the pipe. If there are no forces counter-acting the gravity force, we may expect a complete segregation of the phases to occur. This would happen in the case where the axial flow velocity in the pipe is zero. However, in the case where there is sufficiently fast axial transport, gravitational settling of the dispersed phase would be counteracted by turbulent re-dispersion. Since turbulent forces are diffusive, turbulence tries to re-distribute the dispersed phase in the direction of decreasing dispersed phase concentrations. These considerations suggest the following closure model for the drift velocity

$$\bar{\mathbf{v}}_{2d} = \mathbf{v}_S - \frac{\mathcal{D}_2}{\bar{\alpha}_2} \nabla \bar{\alpha}_2 \quad (6.5.5)$$

in which  $\mathbf{v}_S$  denotes the sedimentation velocity of the dispersed particle and  $\mathcal{D}_2$  denotes the turbulent diffusion coefficient. Using definitions from section 4.3, it is easy to show that the diffusion velocity and the drift velocity are related via  $\bar{\mathbf{v}}_{2d} = \frac{\bar{\rho}_m}{\bar{\rho}_1^x} \bar{\mathbf{v}}_{2m}$ .

The sedimentation velocity of a particle in the presence of other particles was studied in section 6.2. With reference to equation (6.2.13) we find that

$$\mathbf{v}_S = \mathbf{v}_0 \times (1 - \bar{\alpha}_2)^n$$

in which  $\mathbf{v}_0$  denotes the sedimentation velocity in a fluid without other particles present. For the problem under consideration where gravity is the dominant force leading to particle sedimentation, it follows that  $\mathbf{v}_0 = (0, 0, v_{0z})$ .

When we now consider the individual components of the drift velocity  $\bar{\mathbf{v}}_{2d}$  we find immediately that the  $x$ -component is identically zero (remember that we have assumed fully-developed flow). Hence, (6.5.4) together with (6.5.5) leads to a two-dimensional Poisson equation in the  $y-z$  plane for the dispersed phase fraction  $\bar{\alpha}_2$ . This equation has to be solved numerically since it is a nonlinear equation in  $\bar{\alpha}_2$  (through the sedimentation velocity). However, an approximate solution may be obtained by assuming that, at leading order, the distribution of the dispersed phase is governed by the action of gravity forces. This implies that a vertical stratification of the dispersed phase fraction may be expected, meaning that  $\bar{\alpha}_2 = \bar{\alpha}_2(z)$ . For relatively low axial velocities and regions away from the solid boundaries this is anticipated to be a relatively good approximation. Under this assumption equation (6.5.4) becomes

$$\frac{\partial}{\partial z} \left[ \bar{\alpha}_2 \bar{\rho}_2^x \frac{\bar{\rho}_1^x}{\bar{\rho}_m} \left( v_{0z}(1 - \bar{\alpha}_2)^n - \frac{\mathcal{D}_2}{\bar{\alpha}_2} \frac{\partial \bar{\alpha}_2}{\partial z} \right) \right] = 0 \quad (6.5.6)$$

Integrating this equation once yields after some minor rearrangements

$$v_{0z}(1 - \bar{\alpha}_2)^n - \frac{\mathcal{D}_2}{\bar{\alpha}_2} \frac{\partial \bar{\alpha}_2}{\partial z} = \frac{C}{\bar{\alpha}_2} \frac{\bar{\rho}_m}{\bar{\rho}_1^x \bar{\rho}_2^x}$$

in which  $C$  is some integration constant. On the left hand side of the equation given above we recognize the flux of dispersed-phase particles passing through any horizontal plane in the cross section of the pipe. In a fully developed flow we expect this flux to be zero which fixes the integration constant, namely  $C = 0$ . This implies that the concentration of the dispersed phase in the cross section of the pipe satisfies

$$v_{0z}(1 - \bar{\alpha}_2)^n - \frac{\mathcal{D}_2}{\bar{\alpha}_2} \frac{\partial \bar{\alpha}_2}{\partial z} = 0 \quad (6.5.7)$$

Once the necessary closure relations are known, the solution of this ordinary differential equation is easily computed numerically. The closure relation for the sedimentation velocity was discussed in section 6.2 where it was also shown that the exponent  $n \simeq 5$ . The particle diffusion coefficient  $\mathcal{D}_2$  has to be modelled. Mols & Oliemans (1998) suggest using  $\mathcal{D}_2 = \gamma \mathcal{D}_f$  where the fluid diffusivity  $\mathcal{D}_f$  is approximated via  $\mathcal{D}_f \approx (0.7u^*)^2 \mathcal{T}$  with  $\mathcal{T} \approx 0.1D/u^*$  denoting the integral fluid time scale (the time scale related to the largest turbulent structures in a pipe with diameter  $D$ ). The correction factor  $\gamma < 1$  accounts for the fact that the particle diffusivity is smaller than the fluid diffusivity owing to particle inertia effects. The solution of (6.5.7) requires one additional integration constant which we determine as follows. We know the volume fractions of the different phases entering the pipe and with knowledge of the distribution parameter  $C_0$  (see section 4.6), we clearly know the area-averaged volume fraction of the dispersed phase. Hence, we have to solve (6.5.7) subject to the condition that  $\int_A \bar{\alpha}_2 dy dz$  is known. In figure 6.5.1 we show measured and computed dispersed phase fractions in horizontal, oil-water pipe flow where the computed values are based on equation (6.5.7) with  $C_0 = 1$ . It is clear that the simple model is able to predict the vertical distribution of the dispersed phase fraction reasonably well.

So far we have dealt with the case in which one phase is fully dispersed into the other phase. However, the model as outlined above can equally well be used in situations as depicted in figure 3.3.3(c). There we see stratified oil-water flow with dispersed oil drops in the water phase and dispersed water drops in the oil phase. In order to use (6.5.7) for this situation it is, however, required that we know the dispersed phase concentration at the interface separating the oil-continuous from the water-continuous

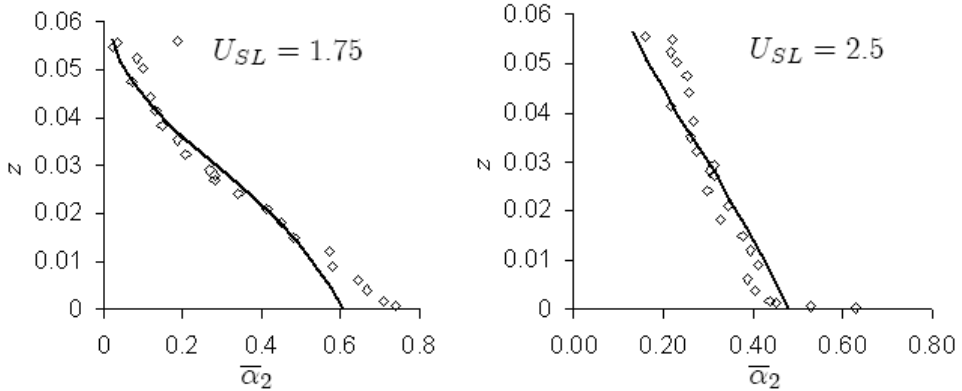


Figure 6.5.1: Measured and computed dispersed phase fractions in oil-water flow as a function of the vertical position. The water cut is 0.3 and the pipe diameter is 56.3mm. The superficial mixture velocities are as indicated in the plots.

region. While this is obviously not a quantity that is easily determined, it turns out that the inversion water cut may be used as a first approximation of the dispersed phase concentration at the water-continuous side of the interface. Amundsen *et al* (2009) have shown that measured concentration profiles in stratified oil-water flow can be predicted with reasonable accuracy with this type of modelling approach, see figure 6.5.2.

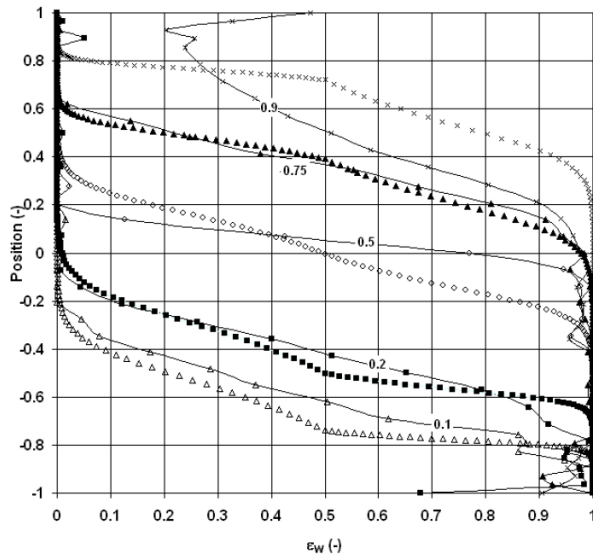


Figure 6.5.2: A plot of the water fraction as a function of the dimensionless height in the pipe for the case where  $U_{mix} = 1$  m/s. Drawn lines represent measurements, symbols represent computed results. The watercut is indicated in the plot.

## 6.6 Exercises

**Exercise 6.1** Here we consider the motion of a spherical liquid particle moving steadily in an infinite fluid. In this case we have to solve the equations of fluid motion (6.2.1) and (6.2.2) on the inside and on the outside of the particle. The general solution for the external motion is discussed in section 3.3. Assume that the viscosity of the fluid inside the particle is given by  $\mu_p$ . For the internal motion assume the functional forms

$\bar{u}_r = U_\infty \bar{f}(r) \cos \theta$ ,  $\bar{u}_\theta = U_\infty \bar{g}(r) \sin \theta$  and  $\bar{p}(r, \theta) = \bar{P}_0 + \mu_p U_\infty \bar{P}(r) \cos \theta$ . Derive the differential equation for  $\bar{f}$  and show subsequently that the general solution is of the form

$$\bar{f}(r) = \bar{A} + \frac{\bar{B}}{r} + \frac{\bar{C}}{r^3} + \bar{D}r^2$$

Continuity in the limit  $r \rightarrow 0$  evidently requires that  $\bar{B} = \bar{C} = 0$ . The two remaining unknowns are found by considering the boundary conditions at the interface of the particle. These conditions are: continuity of velocity  $\bar{u}_r|_{r=R} = u_r|_{r=R} = 0$  and  $\bar{u}_\theta|_{r=R} = u_\theta|_{r=R}$  and continuity of interfacial shear, viz.  $\bar{\tau}_{r\theta}|_{r=R} = \tau_{r\theta}|_{r=R}$  where the shear stress is as defined in (6.2.6). With these conditions the constants  $A$ ,  $B$ ,  $\bar{A}$  and  $\bar{B}$  can be determined. Show subsequently that the drag coefficient in this case is given by

$$C_D = \frac{24}{Re_p} \frac{2 + 3\mu'}{3 + 3\mu'}$$

in which  $\mu' = \mu_p/\mu_f$ .

**Exercise 6.2** Using the concept of a pseudo-fluid, show that in the case where internal circulation in a dispersed phase particle is possible, the effective viscosity in the non-dilute limit can be written like (6.3.7).

**Exercise 6.3** Using the definitions for the drift velocity  $\bar{\mathbf{v}}_{2d} = \bar{\mathbf{v}}_2^{x\rho} - \sum_k \bar{\alpha}_k \bar{\mathbf{v}}_k^{x\rho}$  and the diffusion velocity  $\bar{\mathbf{v}}_m = \frac{1}{\bar{\rho}_m} \sum_k \bar{\alpha}_k \bar{\rho}_k^x \bar{\mathbf{v}}_k^{x\rho}$ , show that the following relation holds  $\bar{\mathbf{v}}_{2d} = \frac{\bar{\rho}_m}{\bar{\rho}_1^x} \bar{\mathbf{v}}_{2m}$

## 7 Slug Flow

### 7.1 Introduction

In the previous chapters we have discussed the flow regimes where the phases are either completely segregated (stratified flow) or completely dispersed. There is a flow regime in which these two states are present at the same time although separated in space: slug flow. Slug flow is the flow regime in which regions of stratified flow are separated by regions in which the whole of the pipe cross section is filled with an aerated liquid plug. The flow regime diagram for horizontal pipes (see figure 9.1.1) shows that the slug flow regime is situated between the stratified and the dispersed flow regime so that slug flow can be regarded as a type of transitional flow regime. It is interesting to point out that this transitional flow regime is not always present. In multiphase flow experiments with hydrocarbon fluids at high pressure conditions, the slug flow regime may disappear almost completely.

The formation of slugs consists of an exceeding rapid chain of events. Prior to slug formation, gas is freely flowing above the liquid. If an interfacial wave with an amplitude sufficiently large to reach the top of the pipe is formed, the gas suddenly finds its path blocked by a bridge of liquid, see figure 7.1.1. This liquid bridge moves with a velocity much lower than the gas velocity and as a result, gas-inertia effects lead to large stagnation pressure on the back side of the liquid bridge. This, in turn, leads to a rapid acceleration of the liquid blockage. As the liquid blockage accelerates, it collects fluid from the liquid layer ahead of it since this layer moves slower. The liquid blockage increases in size and eventually it starts moving with a steady velocity: a liquid slug is formed.

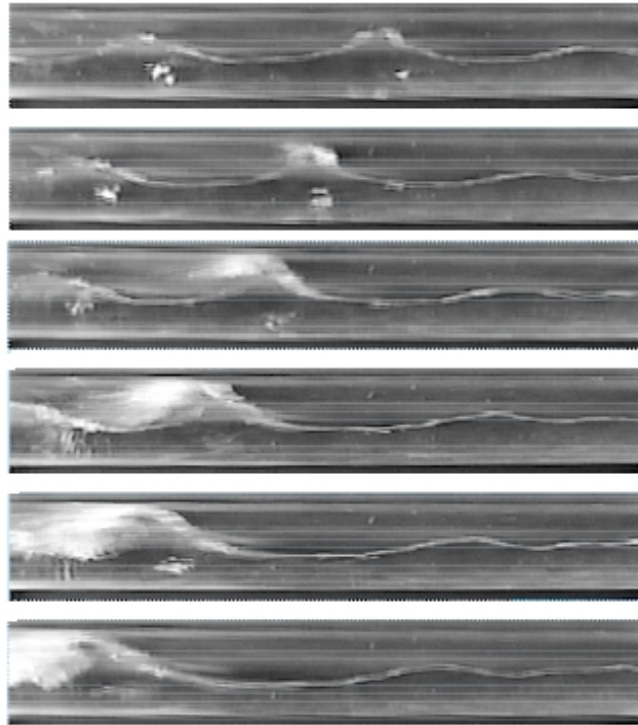


Figure 7.1.1: Video images of slug formation (Woods & Hanratty, 1999). The flow is from right to left.

Generating slug flow experimentally is not very hard but despite this fact a lot remains unknown about the basic features of slug flow. Apparently simple questions such as,

what is the typical length of a slug?, what is the typical length of the separated region between two slugs?, what is the frequency with which slugs are formed?, can not be answered with a large degree of generality or certainty at the present time. This indicates that slug flow is probably the most complicated flow regime from an experimental as well as modelling point of view.

One of the reasons for our lack of understanding of slug flow is the fact that controlled slug flow experiments are hard to perform. A fundamental reason for this fact will be discussed in section 8.3 where it will be shown that flow regime transitions may be associated with a change in the mathematical character of the governing equations. While the equations for stratified gas-liquid flow are hyperbolic in nature (meaning that information travels along well-defined characteristic curves in the  $x-t$  plane), there are indications that the equations for slug flow are elliptic in nature (upstream and downstream events may influence the flow characteristics at a given point). The possible elliptic nature of slug flow has experimental implications as well. For example, it is found that controlling the mass flow rate of the gas phase is surprisingly hard due to the large pressure fluctuations associated with the formation of slugs. Without proper control of the liquid and gas mass flow rates, slug statistics may differ between experiments which are performed under apparently identical conditions. These inherent experimental uncertainties together with our lack of understanding regarding basic physics, have contributed to the fact that there exist a plethora of so-called correlations for different slug-related closure relations. The danger with most of these correlations, as can not be pointed out often enough, is that their range of validity is often unknown and in most cases restricted to the system in which they were obtained.

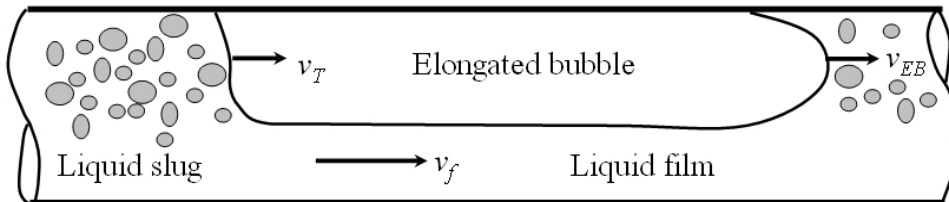


Figure 7.1.2: Schematic diagram of a slug unit

With reference to figure 7.1.2, we now introduce some common terminology related to slug flow. Slug flow consists of discrete liquid plugs which are separated by large, elongated gas bubbles. The region occupied by the gas bubble is often referred to as the bubble region or the film region, referring to the liquid film which lies underneath the bubble. A slug unit refers to one slug combined with the film region. The front of the elongated bubble travels with a velocity  $v_{EB}$  while the slug front travels with a velocity equal to  $v_T$ . For stable slugs to exist we obviously require  $v_{EB} = v_T$ . Usually, the bubble front velocity is significantly larger than the fluid velocity in the film  $v_f$ . This results in a very complicated flow structure at the slug front: for large front velocities the slug front has the characteristics of a continuously breaking wave. The breaking wave structure of the slug front leads to the fact that a slug can entrain a large amount of gas.

## 7.2 The motion of elongated bubbles

As a starting point in modelling slug flow we first consider the motion of the elongated gas bubbles that separate different slugs. Most of the gas is transported in these large gas bubbles so that understanding their behaviour is an important part of slug flow modelling. The velocity of the elongated bubble is commonly written like

$$v_T = C_0 v_S + u_d \quad (7.2.1)$$

in which  $u_d = C_\infty \sqrt{g'D}$  is called the drift velocity of the bubble in a fluid at rest and  $C_\infty$  is called the drift coefficient. In addition  $g' = g\Delta\rho/\rho_L$ . The cross sectional average of the velocity of the liquid in the slug is denoted by  $v_S$  and  $C_0$  denotes the distribution coefficient. The parameter  $C_0$  is not necessarily a constant and it may depend on  $v_S$  through relevant dimensionless parameters in the problem (such as, for example, the Reynolds or the Froude number) implying that the slug front velocity may be a nonlinear function of  $v_S$ .

For the case of bubble motion in a horizontal, large diameter pipe, experimental evidence suggests that the drift velocity is equal to  $u_d = 0.54\sqrt{g'D}$  (Zukoski, 1966). An elegant model supporting this experimental result was presented by Benjamin (1968). Here we will present Benjamin's model for the case  $\rho_G \ll \rho_L$  such that  $\Delta\rho/\rho_L \simeq 1$ . We start by considering a circular pipe with a diameter  $D$ , initially filled with a frictionless fluid which is at rest. At some time  $t = 0$  the fluid is allowed to pour out of the end of the pipe which results in a pocket of gas travelling upstream, see Figure 7.2.1. After the pocket of gas has travelled a certain distance upstream, fluid is injected into the pipe at just the right rate in order to stop the gas bubble from moving further upstream. For simplicity, inertia effects associated with the gas phase are neglected here and the questions we would like to answer are:

- (i) which velocity  $v_1$  is required in order to keep the gas bubble stationary, and
- (ii) what is the height of the liquid film underneath the gas bubble at this velocity.

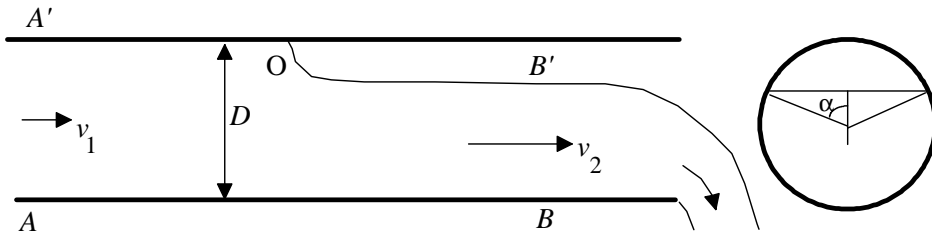


Figure 7.2.1: Diagram of an elongated gas bubble in a pipe

The cross sectional area occupied by the fluid downstream from the bubble front is equal to

$$A_2 = \frac{1}{4}D^2 \left( \pi - \alpha + \frac{1}{2} \sin 2\alpha \right)$$

with  $\alpha$  as defined in Figure 7.2.1. Conservation of mass requires obviously that

$$A_1 v_1 = A_2 v_2$$

in which  $A_1 = \frac{\pi}{4}D^2$  denotes the cross sectional area of the pipe.

Let us next consider momentum conservation for the system with the stationary gas bubble. In section 2.2 we saw that in the case of stationary flow where viscous effects can be neglected, the momentum equation reduces to Bernoulli's equation

$$\frac{1}{2}\rho v^2 + p + \rho gy = C = \text{constant} \quad (7.2.2)$$

It is now important to realise that this equation is valid along any streamline within the fluid. The point  $O$  in Figure 7.2.1 is a stagnation point and the pressure on the

free surface is constant, equal to the atmospheric pressure  $p_a$ . Applying (7.2.2) at  $O$  yields the value of the constant in (7.2.2), namely  $C = \rho g D + p_a$ . Applying Bernoulli's equation along the free surface far down stream from the stagnation point yields

$$v_2^2 = gD(1 - \cos \alpha) \quad (7.2.3)$$

Application of (7.2.2) at a point on the upper boundary, far upstream from the stagnation point also yields

$$p_1 - p_a = -\frac{1}{2}\rho v_1^2 \quad (7.2.4)$$

We next apply the conservation equation for the  $x$ -momentum component. We use the form of the conservation equation as given in (4.8.1) with  $\Psi = v_x$  and the surface  $S$  being the surface which passes through the points  $A', A, B, B'$  and  $O$  in Figure 7.2.1. Since we assume steady state, the time-derivative term in (4.8.1) vanishes so that the integral conservation equation reduces to

$$\int_S \rho v_x \mathbf{v} \cdot \mathbf{n} dS = F_{pressure} \quad (7.2.5)$$

with  $F_{pressure}$  denoting the pressure force acting on the control volume. The velocity normal to the solid boundaries and normal to the free surface is identically zero, implying that the surface integral in (7.2.5) reduces to

$$\int_S \rho v_x \mathbf{v} \cdot \mathbf{n} dS = \int_{A'A} \rho v_x \mathbf{v} \cdot \mathbf{n} dS + \int_{B'B} \rho v_x \mathbf{v} \cdot \mathbf{n} dS = -\rho v_1^2 A_1 + \rho v_2^2 A_2 \quad (7.2.6)$$

The total pressure force acting in the  $x$ -direction on the control volume bounded by  $A'ABB'O$  is given by

$$F_{pressure} = -p_a(A_1 - A_2) + \int_{A'A} [p_1 + \rho g(D - y)] dS - \int_{B'B} [p_2 + \rho g(h - y)] dS \quad (7.2.7)$$

The integrals in the above equation are easily evaluated (see exercise 7.1). When we now combine (7.2.5), (7.2.6) and (7.2.7) we obtain a relation between the velocities  $v_1$ ,  $v_2$  and the pressure  $p_1 - p_a$ . Combing this result together with (7.2.3) and (7.2.4) we finally obtain the following algebraic equation in  $\alpha$

$$\xi^2(1 - \cos \alpha) + \xi \cos \alpha - \frac{2}{3\pi} \sin^3 \alpha = 0$$

in which  $\xi = \frac{1}{\pi}(\alpha - \frac{1}{2}\sin 2\alpha)$ . The above equation may be shown to have only one physically acceptable root, namely  $\alpha = 82.8^\circ$ . Computing the velocities  $v_1$  and  $v_2$  we find:  $v_1 = 0.542\sqrt{gD}$  and  $v_2 = 0.935\sqrt{gD}$ .

We have assumed that the gas-liquid interface far downstream from the bubble front is flat. This is not necessarily true and in principle it is possible to have stationary waves on the gas-liquid interface. Computing the Froude number far downstream from the bubble nose we find  $Fr = v_2/\sqrt{gh} \approx 1.25$ . Since the Froude number is larger than unity it follows that the flow below the bubble is super-critical (that is, fluid velocity exceeds the maximum wave velocity) implying that any wave will be washed downstream. Hence, stationary waves can not exist.

The velocity  $v_1$  is what we defined earlier as the drift velocity of the elongated bubble. Namely, if we had taken  $v_1 = 0$  we would have found that the large bubble drifted away from the entrance of the pipe with a velocity  $u_d$ . We see that our analysis gives the

constant  $C_\infty$  the value 0.542 in the case where the liquid velocity  $v_S = 0$ . In the case of a slowly-moving liquid it is found that the approximation  $C_\infty = 0.54$  holds. However, as  $v_S$  starts to increase, it is observed that the nose of the elongated bubble moves away from the top of the pipe to a position approximately  $\frac{2}{3}$  from the bottom, see Figure 7.2.2. The fluid velocity at which the nose of the bubble separates from the top of the pipe appears to be linked to a fairly abrupt reduction in the drift velocity to approximately zero.

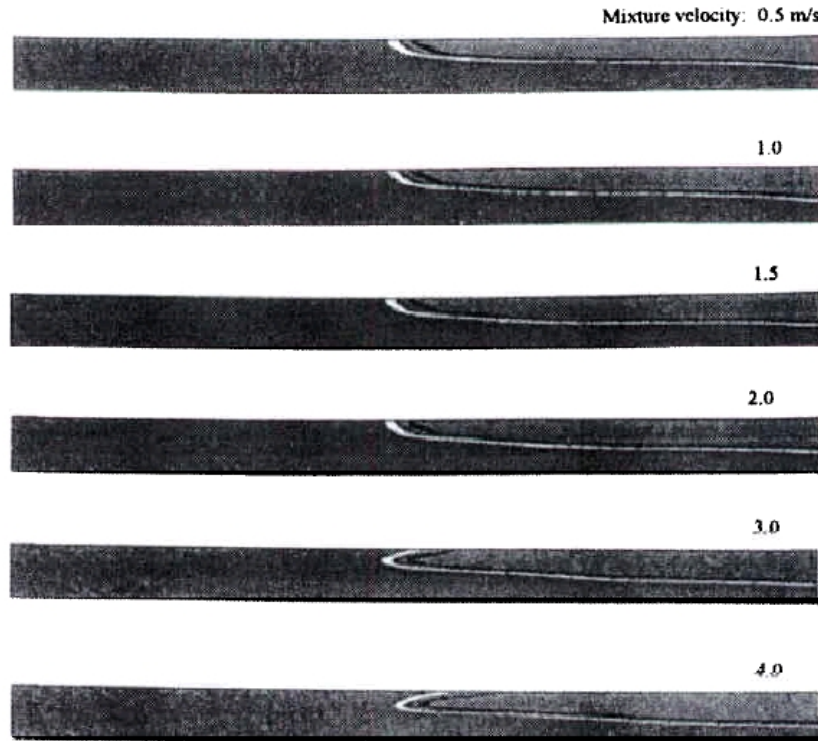


Figure 7.2.2: Elongated bubble shapes for different mixture velocities (Pan,1996)

### 7.2.1 Closure relations for the distribution and drift coefficients

Through extensive experimental work, values for the distribution coefficient  $C_0$  and the drift coefficient  $C_\infty$  have been determined for a wide range of conditions as reviewed by Fabre & Liné (1992). The constants  $C_0$  and  $C_\infty$  are found to be dependent on the inclination of the pipe, the diameter of the pipe and on the viscosity of the fluid. Below, the values of the constants are listed as a function of the viscosity parameter  $N_f = D^{3/2}g^{1/2}\rho_L/\mu_L = \text{Re}/\text{Fr}$  and the Bond (or Eötvös) number  $Bo = \rho_L g' D / \sigma$ .

#### The distribution and drift coefficients for (near-) horizontal flows

In the case of horizontal, inviscid flow it is shown above that  $C_\infty = 0.542$ . Experiments in small tubes provide information about the influence of surface tension on the drift velocity. Weber (1981) shows that data from these experiments is well correlated by

$$C_\infty = 0.54 - 1.76 Bo^{-0.56}$$

Extensive experiments by Bendiksen (1984) have shown how the coefficients  $C_0$  and  $C_\infty$  depend on the pipe inclination  $\theta$ . The results are valid for the limit where inertia forces

dominate the viscous forces (that is  $N_f \rightarrow \infty$ ) and can be summarized as follows. For the distribution coefficient  $C_0$  we have

$$C_0 = \begin{cases} 1.05 + 0.15 \sin \theta & \text{for } Fr < 3.5 \\ 1.20 & \text{for } Fr > 3.5 \end{cases}$$

while for the drift coefficient  $C_\infty$  we have

$$C_\infty = \begin{cases} 0.35 \sin \theta + 0.54 \cos \theta & \text{for } Fr < 3.5 \\ 0.35 \sin \theta & \text{for } Fr > 3.5 \end{cases}$$

where the Froude number is defined by  $Fr = v_S / \sqrt{gD}$ . In section 7.5 it will be shown that  $v_S \simeq U_{mix}$  when it is assumed that the slip between the liquid and the dispersed gas in the slug is small (see equation 7.5.4). Hence, in the evaluation of the distribution and drift coefficients the cross-sectional average of the liquid velocity  $v_S$  is usually replaced by  $U_{mix}$ .

### The influence of viscosity on the distribution coefficient

From the work by Collins *et al* (1978) we know that for laminar, vertical flow, the distribution coefficient is  $C_0 = 2.27$ . The experiments by Bendiksen (1984) have shown that for sufficiently large Froude numbers, the distribution coefficient is equal to  $C_0 = 1.2$ . The experiments of Bendiksen were performed in an air-water system which implies that the Reynolds number is large. This then indicates that the distribution coefficient  $C_0$  decreases from a value of 2.27 for low Reynolds number flows to a value of 1.2 for high Reynolds number flows. In Figure 7.2.3 the variation of the distribution coefficient as a function of the Reynolds number is shown. The limiting value of  $C_0$  for high and low Reynolds numbers are evident.

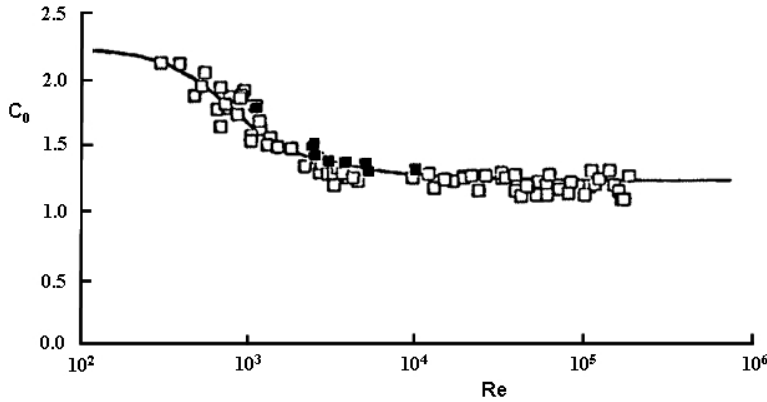


Figure 7.2.3: Variation of distribution coefficient  $C_0$  as a function of the Reynolds number (Fabre & Liné, 1992)

### The distribution and drift coefficients for vertical flow

Analytical work by Dumitrescu (1943) yields  $C_\infty = 0.351$  while Collins (1978) shows that

$$C_0 = \begin{cases} 2.27 & \text{for laminar flow} \\ \frac{\log Re + 0.309}{\log Re - 0.743} & \text{for turbulent flow} \end{cases}$$

Bendiksen (1985) has extended the work by Dumitrescu and Collins by including the influence of surface tension on the constants  $C_0$  and  $C_\infty$ . In addition, Wallis (1969) has

given an expression for the drift velocity in the limit where viscous forces dominate the inertia forces. The results can be summarized as follows

$$\begin{aligned}
C_0 &= 2.29 \left( 1 - \frac{20}{Bo} [1 - e^{-0.0125Bo}] \right) && \text{for laminar flow} \\
C_0 &= \frac{\log Re + 0.309}{\log Re - 0.743} \left( 1 - \frac{2}{Bo} [3 - e^{-0.025Bo} \log Re] \right) && \text{for turbulent flow} \\
C_\infty &= 0.344 \frac{1 - 0.96 \exp(-0.0165Bo)}{(1 - 0.52 \exp(-0.0165Bo))^{3/2}} \sqrt{1 + \frac{20}{Bo} \left( 1 - \frac{6.8}{Bo} \right)} && \text{for } N_f \rightarrow \infty \\
C_\infty &= 0.01N_f && \text{for } Bo \rightarrow \infty
\end{aligned}$$

### 7.3 The slug front

A slug front can, at least visually, be regarded as a continuously breaking waves which propagates over a liquid film which moves at a lower velocity. At the slug front, a large amount of gas may be entrained, clearly shown in figure 3.2.2. This entrainment process constitutes one of the most challenging problems in the area of multiphase flow since we have to deal with the complex interaction between turbulence and dispersed phases. With our current (limited) level of understanding of the entrainment physics there is limited hope of modelling the entrainment process in any detail. However, some features associated with the slug front may be modelled while other features may be understood qualitatively by analysing detailed experiments. Here we will consider both the pressure jump at the slug front and the entrainment process in some detail.

#### 7.3.1 Pressure jump at the slug front

Consider figure 7.3.1 in which a time trace of a differential pressure cell is shown over a time interval in which a slug front passes. At the instance at which the slug front passes we observe a large jump in the pressure drop after which an almost linear increase in the pressure is observed. The large pressure jump at the slug front passes is reminiscent of shock front passing by, suggesting that the slug front may be treated as a propagating discontinuity.

In section 2.3 a general conservation equation was derived specifically for dealing with surfaces which represent a discontinuity. With a slight modification, this conservation equation can be applied directly to the slug-front problem. When we briefly return to section 2.3 we recall that the conservation equation (2.3.3) was derived on the (implicit) assumption that the area occupied by phase 1 was equal to the area occupied by phase 2 on both sides of the surface  $\Sigma$ . However, if this is not the case then this change in area has to be included in the jump condition. It is easy to show that a generalised form of (2.3.3) which includes the influence of a non-constant area across the interface  $\Sigma$  leads to a conservation of the form

$$[\int_{\Lambda} (\rho\Psi(\mathbf{v} - \mathbf{v}_i) - \mathbf{J}) \cdot \mathbf{n}_1 ds] = \int_{\Lambda} \mathbf{m}_i ds$$

As before, the notation  $[\theta] = \theta_+ - \theta_-$  is used to denote the jump of a quantity  $\theta$  across the interface  $\Sigma$  which marks the boundary of the discontinuity. Consider now the situation depicted in figure 7.3.2. The surface  $\Lambda$  denotes a cross section of the pipe on either side of the discontinuity. In order to obtain the mass and momentum conservation equations across the jump we use the specific choices of  $\Psi$  and  $\mathbf{J}$  as specified in Table 2.1. Thus, for mass conservation we take  $\Psi = 1$  and  $\mathbf{J} = 0$ . In addition we take in each phase

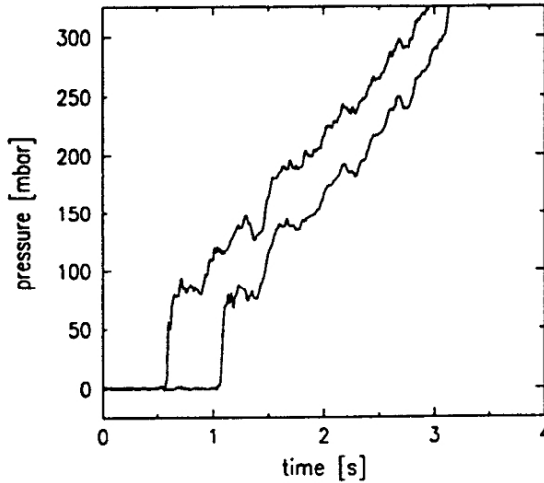


Figure 7.3.1: Time series showing pressure variation at the passing of a slug front (from Nydal, 1991)

$\mathbf{v} = (u, 0, 0)$  while the velocity of the propagating front (the discontinuity!) is given by  $\mathbf{v}_i = (v_T, 0, 0)$ . Finally, the unit normal  $\mathbf{n}_1 = (1, 0, 0)$  pointing outwards from the slug front. Assuming the velocity  $u$  to be constant over the cross section of the pipe we find that the mass conservation equations for the gas and the liquid phases become

$$[\rho_k A_k (u_k - v_T)]_-^+ = 0 \quad (7.3.1)$$

in which  $k = L, G$ . Since mass is neither created nor destroyed at the front of the slug, we have taken  $\mathbf{m}_i = 0$  in the mass conservation equation in order to arrive at the above result.

We next turn our attention to the jump conditions for the momentum equations. With reference to Table 2.1 we find that we have to take  $\Psi = \mathbf{v} = (u, 0, 0)$  and  $\mathbf{J} = \mathbf{T}$ . It is not immediately obvious that we can take the interfacial momentum source to be zero at the slug front. Namely, there is a strong vortex motion at the front of the slug which may suggest that we should take  $\mathbf{m}_i > 0$ . However, since we do not have measurements which enable us to estimate the strength of this source we assume that  $\mathbf{m}_i = 0$ , also for the momentum jump condition. Momentum conservation at the slug front becomes then

$$[\rho_k A_k (u_k - v_T) u_k]_-^+ = [F_k]_-^+ \quad (7.3.2)$$

in which  $F_k = \int_{A_k} T_{11,k} da$  denotes the force exerted on the slug front by phase  $k$ . With reference to Figure 7.3.2 we choose

$$\begin{aligned} \rho_{L+} &= \rho_L, & \rho_{L-} &= \rho_L, & \rho_{G+} &= \rho_G, & \rho_{G-} &= \rho_G \\ A_{L+} &= A_f, & A_{L-} &= H_s A, & A_{G+} &= A_g, & A_{G-} &= (1 - H_s) A, \\ u_{L+} &= v_f & u_{L-} &= v_S & u_{G+} &= v_g & u_{G-} &= v_B \end{aligned} \quad (7.3.3)$$

in which  $H_s$  denotes the liquid holdup in the slug and  $v_B, v_S$  denote the bubble and liquid velocities respectively in the slug. Note that we assume that the pressure jump over the slug front is so small that compressibility effects can be neglected, meaning that densities are constant over the slug front. Using the variables as specified in (7.3.3) we find that combining the jump conditions (7.3.1) and (7.3.2) yields

$$\rho_L A_f (v_T - v_f) (v_f - v_S) = F_{L+} - F_{L-} \quad (7.3.4a)$$

$$\rho_G A_g (v_T - v_g) (v_g - v_B) = F_{G+} - F_{G-} \quad (7.3.4b)$$

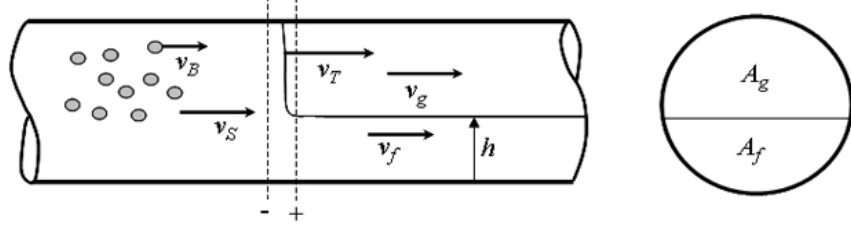


Figure 7.3.2: Schematic diagram of slug front.

We next consider the force  $F_k$  which phase  $k$  exerts on the slug front. With the stress tensor as given in equation (2.2.7) it follows that  $T_{11,k} = -p_k + 2\mu_k \frac{\partial u_k}{\partial x}$ . We assume that the velocity gradient term in the stress tensor is much smaller than the pressure term such that we can make the approximation  $T_{11,k} \approx -p_k$  (this assumption will be justified below). The pressures downstream and upstream from the front are given by

$$p(y)_- = p_- - \rho_s g y \quad (7.3.5a)$$

$$p(y)_+ = \begin{cases} p_+ - \rho_L g y & \text{for } 0 \leq y \leq h \\ p_+ - \rho_L g h - \rho_G g(y-h) & \text{for } h \leq y \leq D \end{cases} \quad (7.3.5b)$$

in which  $\rho_s = (1 - H_s)\rho_G + H_s\rho_L$  denotes the mixture density in the slug. Using the variables and pressures as defined above we can compute the forces on the slug front in the liquid and gas phases upstream and downstream from the slug front (see exercise 7.4). Using these forces in the jump conditions (7.3.4) and solving subsequently for  $p_+$  and  $p_-$  we find the pressure jump over the slug front to be given by

$$[p]_+^+ = \frac{A_f}{A} (\kappa_L + \eta_L) + \frac{A_g}{A} (\kappa_G + \eta_G) \quad (7.3.6)$$

in which

$$\begin{aligned} \kappa_L &= \rho_L (v_f - v_T) (v_f - v_S) & \kappa_G &= \rho_G (v_g - v_T) (v_g - v_B) \\ \eta_L &= g \left( \rho_L \xi_f - \rho_s \xi_A \frac{H_s A}{A_f} \right) & \eta_G &= g \left( \rho_L h + \rho_G (\xi_g - h) - \rho_s \xi_A \frac{(1-H_s)A}{A_g} \right) \end{aligned} \quad (7.3.7)$$

and  $\xi_k = \frac{1}{A_k} \int_{A_k} y da$ . The pressure jump over the slug front as given in (7.3.6) contains contributions due to inertia forces and hydrostatic forces. For slug flow in small-diameter pipes, inertia forces dominate the hydrostatic forces so that  $\frac{\eta_L}{\kappa_L} \ll 1$  and  $\frac{\eta_L}{\kappa_G} \ll 1$ . When in addition  $\rho_L \gg \rho_G$  we have  $\kappa_L \gg \kappa_G$  so that (7.3.6) simplifies to

$$[p]_+^+ \approx H_f \kappa_L = H_f \rho_L (v_f - v_T) (v_f - v_S)$$

which is the expression given by Duckler & Hubbart (1975) for the pressure jump over a slug front. In Figure 7.3.3 we have plotted the measured pressure drop over the slug front (based on measured data from Nydal, 1991) versus the computed pressure drop based on equation (7.3.6). We see that the predictions based on the shock model agree well with the measured data.

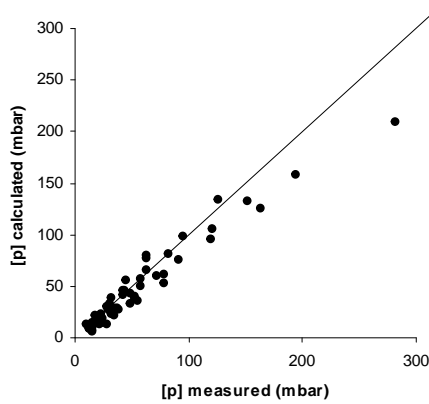


Figure 7.3.3: A comparison of measured and computed values of the pressure jump over a slug front. The measured data are obtained from Nydal (1991).

### 7.3.2 Slug body holdup and gas entrainment

In a slug unit (see figure 7.1.2) the relative volumes of gas and liquid can assumed to be constant. This means that as the amount of gas entrained into the liquid phase increases, the amount of gas which resides in the large gas bubble in between the slugs, must decrease. Under certain conditions so much gas can be entrained into the liquid phase that the large gas bubble completely disappears. If this happens the flow regime changes from slug flow to bubbly flow (see figure 9.1.1). It will be clear that being able to estimate the amount of gas entrained into the liquid slug is of significant importance. Due to buoyancy forces gas bubbles will migrate to the top of the pipe and separate bubbles may merge (coalesce). If this happens, pockets of gas appear in the upper part of the slug (clearly visible in the upper picture shown in figure 7.3.4). The pockets of gas will leave the tail of the slug by entering the large gas bubble following the slug tail. This process of gas entrainment and the slug front and gas release at the slug tail determines how much gas (in the form of bubbles) resides in the slug. Clearly, the liquid holdup (or liquid fraction) in the slug attains a given value if the entrainment and release rates of gas are in equilibrium.



Figure 7.3.4: Gas entrainment at the front of a hydraulic jump in a pipe (Julshamn, 2006). In both pictures the pipe diameter is 70mm. The upper picture shows entrainment in an air-water system, while the lower picture shows entrainment in an air-exxsol system

If the gas bubbles entrained at the front are so small that buoyancy forces are small compared with the dispersive turbulent forces, the gas bubbles will not experience a

significant up-drift. If this happens, a large fraction of the dispersed bubbles will leave the slug, not by entering the large gas bubble but, instead, by entering the liquid in the film region. The dispersed bubbles in the liquid film may then enter the next slug. If this is the case, a positive entrainment rate at the slug front means that an increasing amount of gas is dispersed into the liquid. This process removes gas from the large gas bubble, eventually leading to a transition to dispersed (bubbly) flow when all the gas in the large bubble has been dispersed into the liquid.

The details of the entrainment process of gas at the slug front are poorly understood. Systematic experiments measuring the gas entrainment rate as a function of the fluid properties have been performed for propagating liquid fronts (Nydal, 1991 and Manolis, 1995) and hydraulic jumps (Julshamn, 2006). These experiments indicate that the entrainment rate is not significantly influenced by either the liquid density, the viscosity or gas-liquid surface tension. The entrainment rate increases with increasing gas density while its dependence on the pipe diameter is still a matter of discussion. The dimensionless entrainment rate  $Q_g/Q_l$  for a propagating liquid front as well as a stationary hydraulic jump correlates well with the Froude number  $Fr = \bar{v}_f / \sqrt{g' h_f}$  in which  $\bar{v}_f$  denotes the relative velocity of the liquid film upstream from the jump,  $g' = g\Delta\rho/\rho_L$  and  $h_f$  denotes the maximum depth of the film, see figure 7.3.5. From the figure we see that experiments indicate that no entrainment occurs when  $Fr \lesssim 1.3$ .

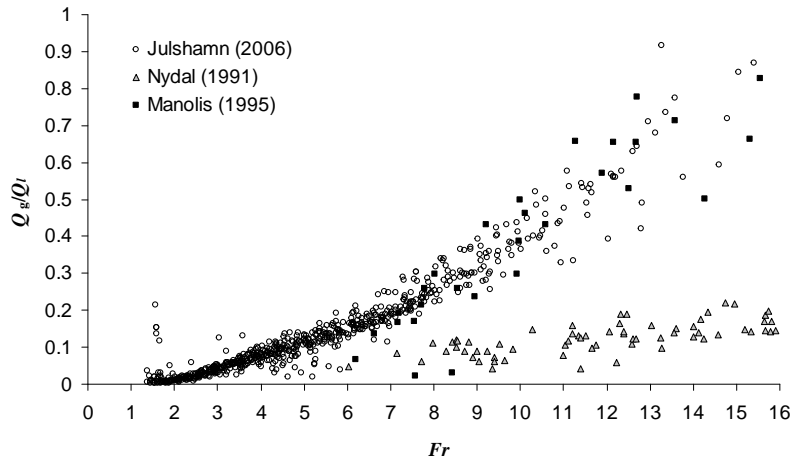


Figure 7.3.5: A plot of the dimensionless gas entrainment rate  $Q_g/Q_l$  as a function of the Froude number. A best fit of the Manolis (1995) and Julshamn (2006) data yields  $Q_l/Q_g = 10^{-3} \times (3.2Fr^2 + 7.8Fr - 8.2)$  while the Nydal data gives  $Q_l/Q_g = 0.011 \times (Fr - 1.5)$

The amount of gas in a slug can be determined by measuring the average density of the gas-liquid mixture in the slug (an example of such a measurement is given in figure 3.4.1). With the gas and liquid densities known, the fraction of gas in the slug can be inferred. A typical result of such measurements is shown in figure 7.3.6. Here we observe that the liquid volume fraction in the slug decreases with increasing mixture velocity, that is, the amount of entrained gas increases with increasing mixture velocity. As discussed above, the gas entrainment rate at the slug front may be only slightly dependent on physical parameters of the fluids. Even so it is not unlikely that the liquid holdup in the slug is dependent on these parameters since the holdup is determined by the relative velocity of the gas and the liquid in the slug. Hence, figure 7.3.6 depicts only one part of a complex physical process.

Quite a few, so-called, correlations exist, which relate the measured liquid volume fraction to relevant experimental parameters. For example, the data shown in figure 7.3.6 was

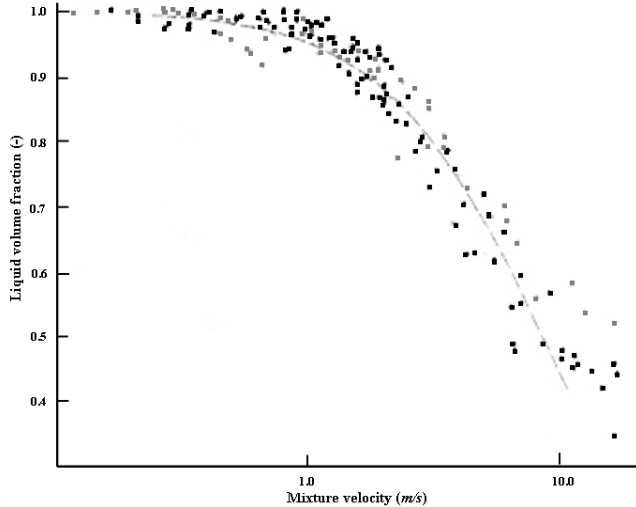


Figure 7.3.6: The measured liquid volume fraction in a slug as a function of the mixture velocity  $U_{mix} = U_{SL} + U_{SG}$  (Gregory et al, 1978).

correlated by Gregory et al (1978) via

$$H_s = \left( 1 + \left( \frac{U_{mix}}{U} \right)^{1.39} \right)^{-1} \quad (7.3.8)$$

in which  $H_s$  denotes the liquid holdup in the slug and the velocity scale  $U = 8.66\text{ms}^{-1}$ . While the relation given above is certainly valid for the system in which the data is obtained, it is unlikely to have a general validity. One reason for this lack of general validity is related to the fact that velocity scale  $U$  in the above correlation is taken to be a constant, independent of physical properties, pipe dimensions and flow variables. Earlier we have already seen that the liquid holdup in a slug is probably dependent on surface tension (and therefore bubble size) and therefore we could speculate that  $H_s = H_s(\sigma, \mu, D, \dots)$ . Proceeding along this path, Ooi (2001) has performed an extensive analysis of the liquid holdup in slugs using data from high-pressure systems with hydrocarbon fluids. She found that the liquid holdup could be expressed in the following way

$$H_s = 1 - 0.474 \times Ca^{0.88} Re^{0.2} \left( \frac{\rho_G}{\rho_L} \right)^{0.1} \left( \frac{\mu_G}{\mu_L} \right)^{0.3} \quad (7.3.9)$$

in which we have defined the Capillary number  $Ca = U_{mix}\mu_L/\sigma$  and the Reynolds number  $Re = \rho_L U_{mix} D / \mu_L$ . When we consider the Gregory correlation (7.3.8) for the case  $U_{mix}/U \ll 1$  we may approximate it via  $H_s \simeq 1 - C_1 U_{mix}^{1.39}$  and in a similar way, (7.3.9) can be written like  $H_s = 1 - C_2 U_{mix}^{1.08}$ . While the exponent on the mixture velocity is different, we observe the same general trend in both relations: the liquid holdup in the slug decreases when the mixture velocity increases.

Experimental measurements by Nydal (1991) and Ferscheinder (1983) show that the distribution of dispersed gas in the slug is highly non-uniform both in the radial and in the axial direction (see also figure 7.3.4) We can now employ a modelling approach as outlined in section 6.5 to show how void fraction variation in the axial direction can be explained. We start by assuming that the volume flow of gas entering the slug front,  $Q_g$  say, is known. In a frame of reference where the slug front is stationary, the volume flux of gas passing any cross section in the slug is equal to

$$Q_g = A(v_T - v_B)(1 - \bar{H}_s) \quad (7.3.10)$$

in which  $A$  denotes the cross section of the pipe,  $v_B$  denotes the velocity of gas bubbles in the liquid slug and  $\tilde{H}_s(x)$  denotes the insitu holdup. The insitu holdup is related to the average holdup via

$$H_s = \frac{1}{L_s} \int_0^{L_s} \tilde{H}_s(x) dx$$

in which  $L_s$  denotes the length of the liquid slug. In analogy with the propagation velocity of the slug front, the velocity of the dispersed gas phase is commonly written like

$$v_B = C_1 U_{mix} + v_{drift} \quad (7.3.11)$$

where the distribution coefficient  $C_1$  has values in the range 1.0 -1.2. In vertical flow, the drift velocity is likely to be dominated by buoyancy forces but in horizontal flow we may argue that turbulent dispersion is the main transport mechanism. In line with the modelling approach in section 6.5 we therefore take

$$v_{drift} = \Gamma \frac{d\tilde{H}_s}{dx} \quad (7.3.12)$$

in which  $\Gamma$  is a diffusion coefficient. Combining equations (7.3.10)-(7.3.12) we obtain an ordinary differential equation that provides an approximation of the axial variation of the holdup in the slug, namely

$$\Gamma \frac{d\tilde{H}_s}{dx} = v_T - C_1 U_{mix} - \frac{Q_g}{A(1 - \tilde{H}_s)} \quad (7.3.13)$$

The closure relation for  $v_T$  is discussed in the previous section while an expression for  $Q_g$  has been discussed earlier in this section (see figure 7.3.5). The diffusion coefficient  $\Gamma$  can be modelled by assuming that the large vortex motion at the front of the slug is the main dispersive mechanism. The velocity scale of the vortex is proportional to the difference between the slug propagation velocity and the film velocity and hence we can postulate a diffusion coefficient of the form  $\Gamma = \gamma(v_T - v_f)D$  in which  $\gamma$  is some constant. In order to solve (7.3.13) we require the value of the holdup at the slug front as well as a value for the diffusion constant  $\gamma$ . These parameters are not known (and likely to depend on fluid properties) but a comparison with the measured holdup data by Nydal (1991) give an indication of their magnitude. Namely, by taking  $\gamma = 5$  and allowing  $\tilde{H}_s(0)$  to vary with  $U_{mix}$  it is found that the computed mean holdup can be matched with relation (7.3.8) while the holdup profiles show a fair qualitative match with the measured trends. In figure 7.3.7 we show computed holdup profiles based on computations with a unit slug model (see section 7.5) for the case of an air-water system in a 31mm horizontal pipe.

Currently, our understanding of the detailed physical processes governing gas entrainment are limited and therefore there is no model which accurately predicts the liquid holdup of a slug. As a result, predictions of the liquid holdup in a slug are often based on correlations which are derived from curve fits through experimental data points. Some models have been developed and in appendix C a number of often-used expressions for the liquid holdup in a slug are listed.

## 7.4 Slug statistics

Gas expansion effects associated with pressure losses along the pipe will inevitably cause an increase in the mixture velocity. It is therefore legitimate to ask whether or not

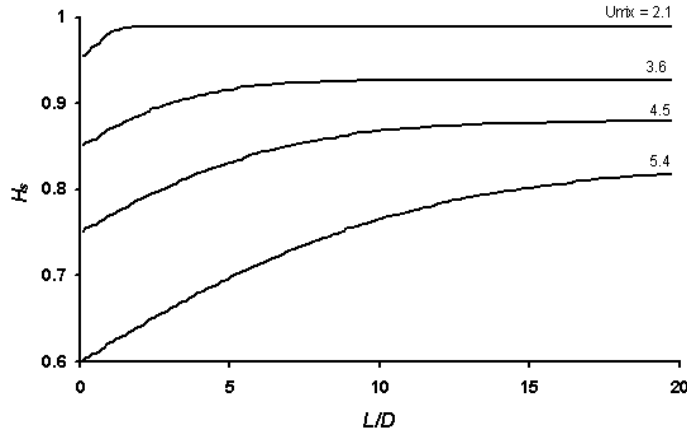


Figure 7.3.7: A plot of the axial holdup profile for mixture velocities as indicated in the plot. In all case  $U_{SL} = 0.6\text{m/s}$ . The position  $L/D = 0$  corresponds to the slug front.

fully-developed slug flow can exist and if it does, what do we mean by it? The most obvious answer would be to demand that at some distance sufficiently far from the pipe inlet, meaningful averaged properties of an ensemble of slugs are independent of the measurement position. In figure 7.4.1 we show experimental measurements of this kind. We clearly see that both the length distribution and the mean slug length slowly change as one moves downstream from the inlet. From these measurements we clearly see that slug flow is a slowly-developing flow regime. Experiments by Nydal *et al* (1992) have shown that "developing slugs" have fundamentally different characteristics than developed slugs. The developing slugs are typically shorter and more aerated than the developed slugs and may take many hundreds of pipe diameters to evolve into developed slugs. As the developing slugs evolve into developed slugs, the mean slug length increases while the standard deviation of the size distribution becomes less.. This feature is illustrated in figure 7.4.1. Contrary to what is observed with slugs, it is found that the size distribution of the elongated bubbles flattens as one moves down stream, see figure 7.4.1.

Experiments indicate that for inclined flow, the slug length is only weakly dependent on variations in the liquid or gas flow rates or, indeed, the water cut. The main parameter which appears to influence the slug length is the pipe inclination. For inclinations exceeding 20 degrees, the slug length are typically in the range  $l_s \sim 8 - 20D$  (cf. figure 7.4.1). For inclinations below 20 degrees, the slug length increases rapidly, reaching values in the range  $l_s \sim 15 - 40D$  for horizontal pipes.

Let us next turn our attention to the slug frequency,  $f_S$ , which we define to be the number of slugs passing a fixed observer per unit time. If the propagation speed of the slugs  $v_T$ , as well as the unit slug length  $l_u$ , is known, then the slug frequency can be determined via

$$f_S = \frac{v_T}{l_u} = G(U_{SL}, U_{SG}, g, D, \theta)$$

where the function  $G$  is found by considering experimental data. The dimensionless slug frequency is defined by  $\mathcal{F} = f_S D / U_{mix}$ . Relation (7.2.1) and the fact that  $v_S \simeq U_{mix}$  is the motivation for using the mixture velocity in the definition of the dimensionless frequency. We note that besides the inclination only two independent dimensionless group can be constructed from the arguments of the function  $G$ , namely the Froude number  $Fr = U_{SL}/\sqrt{gD}$  and the velocity ratio  $\mathcal{U} = U_{SL}/U_{SG}$ . Hence,

$$\mathcal{F} = \mathcal{G}(Fr, \mathcal{U}, \theta)$$

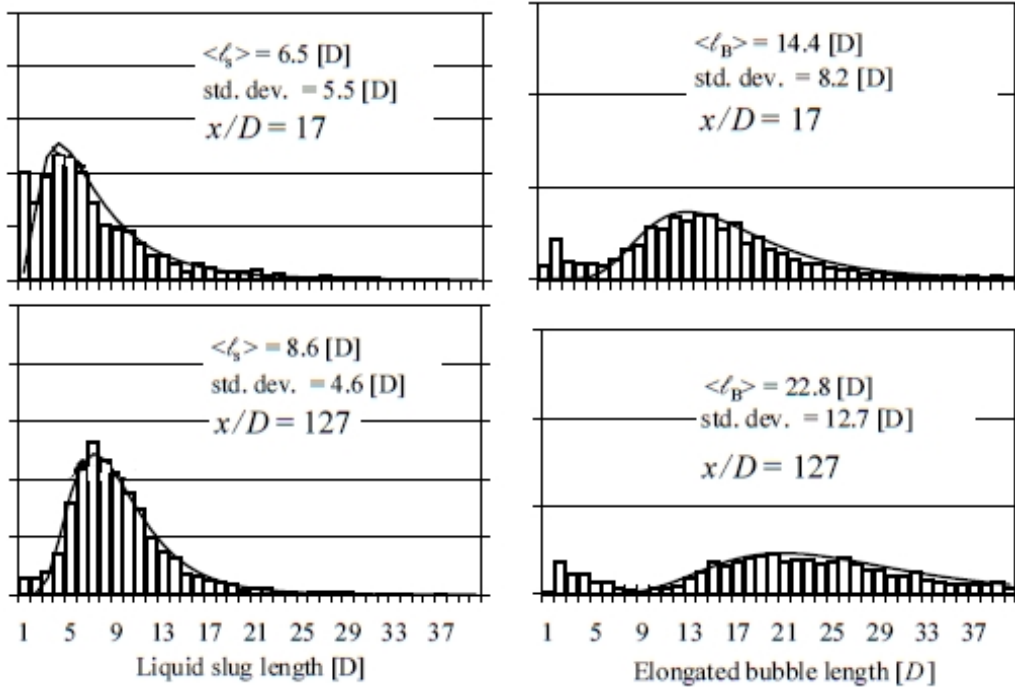


Figure 7.4.1: The evolution of the slug length and elongated bubble lengths as a function of the distance from the inlet of the pipe as indicated in the plot.  $D = 0.054\text{m}$ ,  $U_{SL} = 0.01\text{m/s}$ ,  $U_{SG} = 0.41\text{m/s}$  and pipe inclination is  $10^\circ$  (Van Hout *et al.*, 2003).

By using experimental data (Heywood & Richardson, 1979, Langsholt *et al.*, 2002, Van Hout *et al.*, 2003 and Woods *et al.*, 2006) we are now in a position to determine the functional form of  $\mathcal{G}(Fr, \mathcal{U}, \theta)$ . A least-squares analysis of available data yields

$$\mathcal{F} = 0.0545 \times f(Fr) \times g(\theta) \quad (7.4.1)$$

in which  $f(Fr) = 1.0 + 0.11 \times Fr + 0.0073 \times Fr^2$  and  $g(\theta) = 1.0 + 22.2 \times \theta - 4.4 \times \theta^2$ .

In figure 7.4.2 we have plotted the measured dimensionless slug frequency versus the computed dimensionless frequency for data points in the range  $0 \leq \theta \leq \pi/2$ . We note that there is a large difference between slug frequencies in horizontal and inclined flows: the slug frequencies for horizontal flow tend to be at least one order of magnitude smaller than those for inclined flow. Slug flow is very sensitive to small variations in the inlet conditions which may explain some of the scatter observed in figure 7.4.2. In addition there are indications that the slug frequency may also dependent on the pipe length (Shea *et al.*, 2004). This is probably particularly important when one operates on the boundary between stratified and slug flow. In that case very long slugs have been observed. Some alternative correlations that have been proposed for the slug frequency are listed appendix D.

We have seen on a number of occasions that there is a fundamental difference in slug characteristics when we go from horizontal to inclined flow. Even for relatively small inclinations (1-2 degrees, say) it is found that experimental results deviate significantly from those obtained in horizontal systems. Slug flow with relatively well-defined slug lengths is much easier to obtain when the pipe is inclined than when the pipe is horizontal. Clearly, the gravitational force has a strong influence on the flow features.

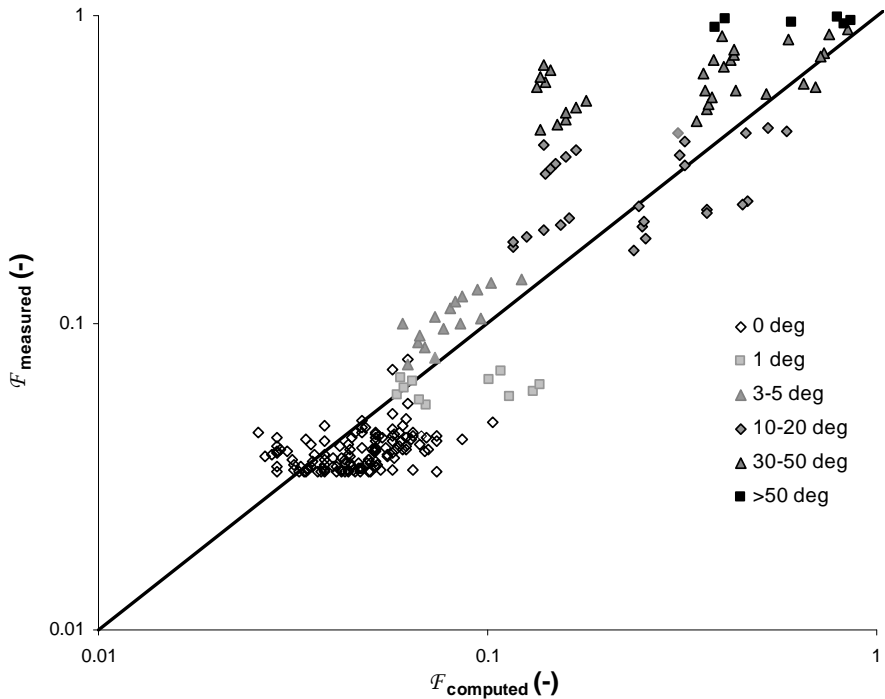


Figure 7.4.2: A plot of the measured dimensionless frequency as a function of the computed frequency using equation (7.4.1).

## 7.5 The unit slug model

In the previous sections we have considered separate models for the advancing bubble and the slug front. We have seen that the pressure drop at the slug front requires information about properties in both the liquid slug and the liquid film. With respect to the liquid film we have seen that the holdup in the liquid film, the film velocity and the gas velocity in the bubble are parameters that have to be described. This implies that an integral part of slug modelling, is a proper model of the liquid film region which lies underneath the elongated bubble. In figure 7.5.1 some measured shape profiles of the liquid film are shown. These measurements reveal that the film has a clear nose region (where the liquid holdup decreases rapidly) and a well-defined tail.

The film region together with the liquid slug constitute what referred to as a *slug unit*. Clearly, modelling slug flow requires a unified model for the slug unit. Let us start with the liquid film. Figure 7.5.1 shows that the long, flat tail of the film is the dominant part of the film region. As a good first approximation, we may therefore take the film to have a constant thickness. With this approximation, the slug unit will then consist of an aerated liquid slug with length  $l_s$  and a flat liquid film with a length  $l_f$ . The slug unit has a total length equal to  $l_u = l_f + l_s$ , see figure 7.5.2.

It will be evident that a unified model for the slug unit is build by considering mass and momentum balances in the film and the liquid slug regions. Let us start by considering mass conservation. The total mass flow into the pipe of each phase must be equal to the total mass flow of each phase in the slug unit. A slug unit passes a fixed observer in a time equal to  $t_u = l_u/v_T$  and likewise  $t_f = l_f/v_T$  and  $t_s = l_s/v_T$ . Mass conservation of the liquid phase requires therefore that

$$\rho_L U_{SLA} = \frac{1}{t_u} (\rho_L v_S A H_s t_s + \rho_L v_f A H_f t_f)$$

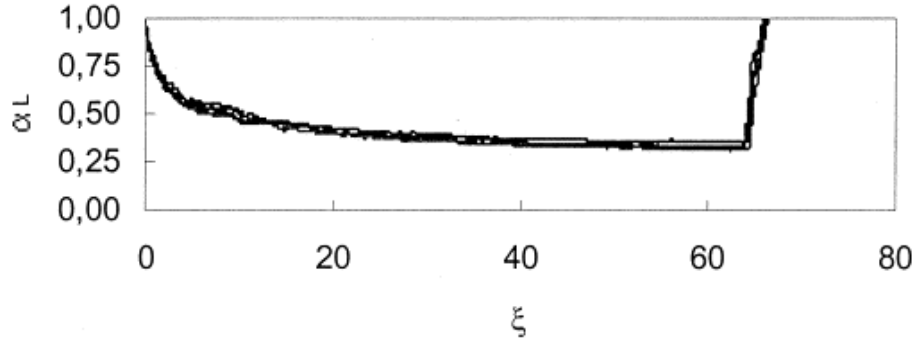


Figure 7.5.1: Experimental measurement of the shape of the liquid film region (Fagundes Netto *et al*, 1999)

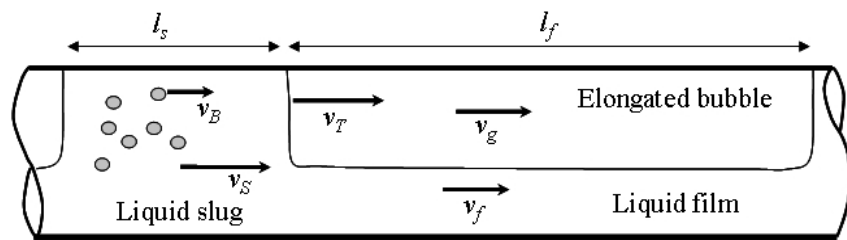


Figure 7.5.2: Schematic diagram of slug unit

in which  $H_s$  and  $H_f$  denote the liquid holdup in the slug and film regions respectively. Simplifying the above equation and replacing time scales by length scales gives

$$U_{SL} = \frac{l_s}{l_u} v_s H_s + \frac{l_f}{l_u} v_f H_f \quad (7.5.1)$$

Similarly, mass conservation for the gas phase yields

$$U_{SG} = \frac{l_s}{l_u} v_B (1 - H_s) + \frac{l_f}{l_u} v_g (1 - H_f) \quad (7.5.2)$$

In addition to mass conservation of the slug unit we have mass conservation at the front of the propagating slug as described by the jump conditions. Using the jump condition (7.3.1) we find immediately that mass conservation for the liquid and the gas phase at the slug front yields respectively

$$H_f(v_T - v_f) = H_s(v_T - v_s) \quad (7.5.3a)$$

$$(1 - H_f)(v_T - v_g) = (1 - H_s)(v_T - v_B) \quad (7.5.3b)$$

The jump conditions at the slug front can be used to eliminate  $v_f$  and  $v_g$  from (7.5.1) and (7.5.2) and it is easy to show that by adding the the mass conservation equations for the gas and liquid phases, one obtains the interesting result

$$U_{SL} + U_{SG} = v_s H_s + v_B (1 - H_s) \quad (7.5.4)$$

We next turn our attention to the liquid film region. The unit slug model clearly requires a means to determine the height of the liquid film. In order to obtain this information

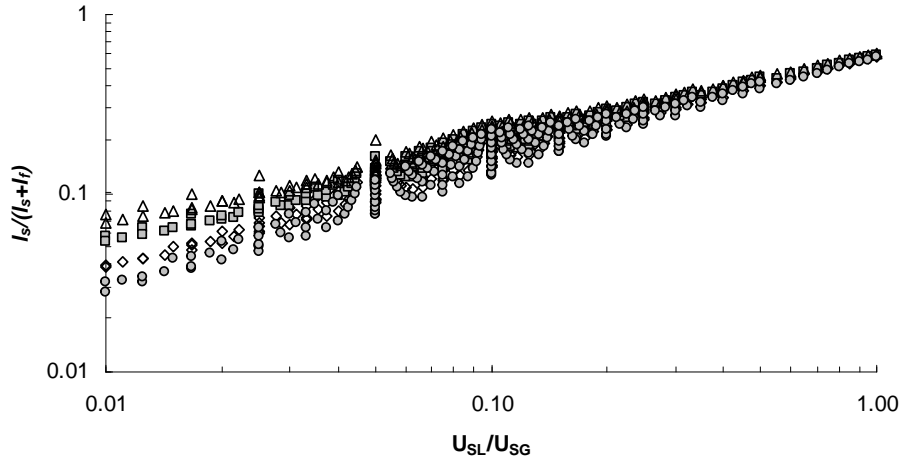


Figure 7.5.3: The computed slug length to slug unit length ratio  $l_s/(l_s + l_u)$  plotted as a function of the velocity ratio  $U_{SL}/U_{SG}$ . The different symbols correspond to the density ratios  $\rho_L/\rho_G = 10, 25, 100, 400$  (the triangles corresponding to the lowest density ratio).

we use the equations for fully-developed stratified flow as outlined in section 5.4. There it was shown that the holdup equation (5.4.3), written like

$$\mathcal{H}(v_f, v_g, H_f) = 0$$

yields the required liquid height. It turns out that with the height of the liquid film in place, we have completed the model for the unit slug for the case where the film region has a constant film thickness. Namely, the additional parameters we require in order to close the model are all obtained from experimental observations as discussed in previous sections: the slug translational velocity  $v_T$  is discussed in section 7.2; the liquid holdup  $H_s$  and the dispersed bubble velocity  $v_B$  in the liquid slug are discussed in section 7.3 and Appendix C; the slug unit length is discussed in section 7.4. With all the experimental closure relations in place, the solution procedure is now as follows. With the bubble velocity  $v_B$  known (approximated by equation (7.3.11) without the diffusion term), the liquid velocity in the slug  $v_s$  is obtained from equation (7.5.4), after which the liquid and gas velocities in the film region can be related to the holdup in the film region via the jump conditions (7.5.3). The holdup equation can now be solved after which the mass conservation equation for the gas or the liquid phase can be used to determine the ratio  $l_s/l_u$ .

Figure 7.3.5 shows the computed ratio  $l_s/l_u$  as a function of the velocity ratio  $U_{SL}/U_{SG}$  for different gas-liquid density ratio's in the case of a horizontal pipe (simulations show the length ratio to be rather insensitive to diameter variations). Although there is a degree of scatter in the plot we see a very clear trend: the ratio  $l_s/l_u$  increases monotonically with the velocity ratio  $U_{SL}/U_{SG}$ . This is entirely in line with expectations. Namely, we first note that as the ratio  $l_s/l_u$  approaches unity, the liquid film length becomes short compared with the slug length. In this limit we may expect a transition to dispersed flow, in line with the flow regime chart shown in figure 9.1.1. For low values of the velocity ratio we observe low values of the length ratio  $l_s/l_u$  indicating slug flow with long liquid films separating the slugs. It is entirely plausible that slug flow in this case degenerates into stratified flow: the fact that we have assumed slug flow to exist does not mean that the slugs are stable or that slugs would have been generated in the first place. The results obtained here are qualitatively in line with experimental observations.

However, the predicted slug length in the square slug model is over-estimated compared with experimental observations (Heywood & Richardson, 1979). The reason for this is that in the square slug model the amount of liquid in the film is under-estimated as may be clear from figure 7.5.1.

In the previous section it was observed that slug lengths are typically found to be in the range  $l_s \sim 8 - 20D$ . It is natural to ask how this experimentally observed slug length compares with the slug lengths computed using the unit slug model. The unit slug model has provided us with the length ratio  $l_s/l_u$  and this, in combination slug frequency information given in the previous section, allows us to determine the slug length. We proceed as follows. A least-squares analysis reveals that a best-fit to the data shown in figure 7.3.5 is given by

$$\frac{l_s}{l_s + l_f} = 0.67 \left( \frac{U_{SL}}{U_{SG}} \right)^{0.57}$$

Combining this result with equation (7.4.1) for the case  $\theta = 0$ , it is easy to show that

$$\frac{l_s}{D} = 12.3 \times \left( \frac{U_{SL}}{U_{SG}} \right)^{0.57} \frac{v_T}{f(Fr)U_{SL}} \quad (7.5.5)$$

With reference to figure 9.1.1 we find that in the case of slug flow, we typically have  $O(0.1) \lesssim U_{SL}/U_{SG} \lesssim O(1)$  and  $Fr \sim O(1)$ . Hence, the above equation predicts slug lengths in the range  $10 \lesssim l_s/D \lesssim 40$ , broadly in line with experimental observations.

In order to compute the pressure loss over one slug unit we proceed as follows. The total pressure loss over one slug unit consists of three contributions: pressure loss over the liquid slug, the pressure loss over the film and the pressure loss at the slug front. Hence

$$\Delta p_{slug\ unit} = - \left. \frac{dp}{dx} \right|_{slug} \times l_s - \left. \frac{dp}{dx} \right|_{film} \times l_f + \Delta p_{front}$$

The pressure gradient in the liquid slug is determined by assuming that the gas-liquid mixture in the slug has well-defined mixture properties. Hence

$$- \left. \frac{dp}{dx} \right|_{slug} = \frac{1}{2D} \rho_s v_s^2 f_s + \rho_s g \sin \beta$$

in which  $\rho_s$  denotes the mixture density in the slug, the liquid velocity in the slug  $v_s$  is obtained from (7.5.4) and the friction factor  $f_s$  is computed using the Reynolds number  $Re_s = \rho_s D v_s / \mu_L$ . Note, rather than using a mixture viscosity we choose to use the liquid viscosity in the Reynolds number. In the liquid film region we compute the pressure gradient by using the momentum equations for stratified flow given in (5.4.1) and (5.4.2). Hence,

$$- \left. \frac{dp}{dx} \right|_{film} = \tau_{Lw} \frac{s_L}{A} + \tau_{Gw} \frac{s_G}{A} + [\rho_L H_f + \rho_G (1 - H_f)] g \sin \beta$$

Finally, the pressure loss at the slug front  $\Delta p_{front}$  was determined in section 7.3 and is given in equation (7.3.6). The above equations can be combined to give the pressure drop over a slug unit in the form

$$\Delta p_{slug\ unit} = \frac{1}{2D} \rho_s v_s^2 f_s l_s + \left( \tau_{Lw} \frac{s_L}{A} + \tau_{Gw} \frac{s_G}{A} \right) l_f + \rho_u g \sin \beta l_u + \Delta p_{front} \quad (7.5.6)$$

In the above equation  $\rho_u = (1 - H_u) \rho_G + H_u \rho_L$  denotes the average density of the slug unit and the mean slug unit holdup is defined via  $H_u = (H_s l_s + H_f l_f) / l_u$ .

So far we have assumed that the liquid film is flat while in reality (see figure 7.5.1) the film has a clear nose and a long (more or less flat) tail. Taitel & Barnea (1990) have shown how the shape of the liquid film can be modelled. This model is essentially based on the two-fluid equations for stratified gas liquid flow as formulated in table 4.1. The mass and momentum equations are formulated in a frame of reference moving with the front of the propagating slug. The momentum equations are subsequently used to formulate a generalised holdup equation in which effects of fluid inertia on the film profile are incorporated. In the case of relatively short liquid films, the influence of the non-uniform film thickness may significantly influence the pressure drop in the film. For long liquid films the approximations made in this section will yield adequate pressure drop estimates.

## 7.6 Exercises

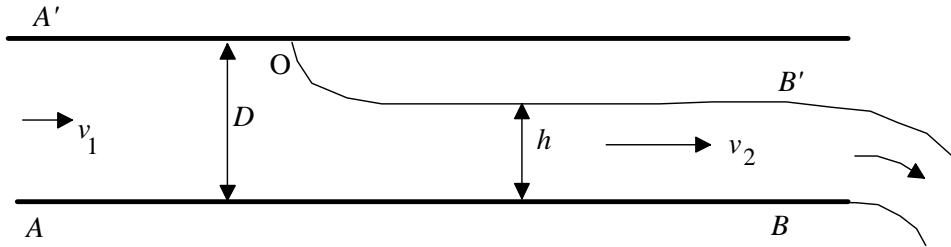
**Exercise 7.1** With reference to figure 7.2.1, show that the first of the pressure integrals in equation (7.2.7) becomes

$$\int_{A'A} [p_1 + \rho g (D - y)] dS = \frac{1}{4} \pi D^2 \left( p_1 + \frac{1}{2} \rho g D \right)$$

**Exercise 7.2** At the interface separating the gas and the liquid in cross section  $B'B$ , the pressure is atmospheric. Show that the second pressure integral in equation (7.2.7) becomes

$$\int_{B'B} [p_2 + \rho g (h - y)] dS = \frac{1}{2} \rho g D \left( A_2 \cos \alpha + \frac{1}{6} D^2 \sin^3 \alpha \right) + p_a A_2$$

**Exercise 7.3** The aim of this exercise is to solve a simplified version of the problem discussed in section 7.2. Here we consider the case of a large bubble moving upstream between two infinite parallel plates, see figure below.



Assume as before that the velocity  $v_1$  is adjusted such that the point  $O$  becomes a stagnation point. Show that the application of Bernoulli's theorem yields

$$v_2^2 = 2g(D - h) \quad (1)$$

and  $p_1 - p_a = -\frac{1}{2}\rho v_1^2$ , with  $p_a$  denoting the atmospheric pressure. Show that the total pressure force acting on the control volume

$$F_{pressure} = -\frac{1}{2} \rho v_1^2 D + \frac{1}{2} \rho g (D^2 - h^2)$$

Combining the above results and using mass conservation, show that on application of equation (7.2.5) one obtains

$$v_2^2 = \frac{gD(D^2 - h^2)}{2hD - h^2} \quad (2)$$

Show finally that the polynomial defined by equations (1) and (2) has only one physically realistic root, given by  $h = \frac{D}{2}$ .

**Exercise 7.4** With reference to figure 7.3.2 and the upstream/downstream variables as defined in equation (7.3.3) and the pressures as defined in equation (7.3.5), show that the forces  $F_k = \int_{A_k} T_{11,k} da \approx - \int_{A_k} p_k da$  in the liquid and the gas phase, upstream and downstream from the shock can be written like

$$\begin{aligned} F_{L+} &= -(p_+ - \rho_L g \xi_f) A_f \\ F_{L-} &= -(p_- - \rho_s g \xi_A) (1 - \alpha) A \\ F_{G+} &= -(p_+ - \rho_L g h - \rho_G g [\xi_g - h]) A_g \\ F_{G-} &= -(p_- - \rho_s g \xi_A) \alpha A \end{aligned}$$

in which  $\xi_k = \frac{1}{A_k} \int_{A_K} y ds$ .

## 8 Interfacial waves

### 8.1 Introduction

One of the special features of multiphase flow is the fact that the appearance of the flow may alter drastically when either the liquid or the gas volume flow rate is changed. This is exemplified in figure 3.2.1 where the flow regimes in a gas-liquid system are shown. It will be evident that all flow regime transitions are related to highly nonlinear gas-liquid interactions, characterised by a dramatic change in the interfacial structure separating the gas and the liquid phases. Due to the inherent nonlinearity of the regime transitions, modelling any of the transitions is difficult. However, the transition from stratified smooth to stratified wavy flow can be modelled using standard linear wave theory. In this chapter linear waves such as those shown in figure 8.1.1 will be studied within the frameworks of potential theory and the two-fluid equations. In addition it will be investigated under which conditions the two-fluid equations are well-posed. As will be shown, interfacial waves may become linearly unstable. The requirement for stable interfacial waves is shown to be closely related to the question of well-posedness.



Figure 8.1.1: Small-amplitude interfacial waves in gas-liquid pipe flow (picture by P. Andersson, IFE)

It is tempting to relate unstable interfacial waves (or loss of well-posedness) to the appearance of slug flow. Unfortunately it turns out that this is a step too far. Unstable interfacial waves lead to the formation of large-amplitude roll waves but not quite slug formation. An example of a large-amplitude roll wave is shown in figure 1.0.1. It is clear that a significant amount of wave-overturning occurs and modelling this system, and hence the transition to slug flow, will require a model for gas entrainment to be coupled to nonlinear wave models. This modelling step has yet to be taken.

### 8.2 Stability of stratified, frictionless shear flow

As a starting point we take the momentum conservation equation (2.2.9). In order to reduce the complexity of this equation we first consider the limit of vanishing viscosity which is achieved by leaving out the term containing the highest derivative in (2.2.9). The physicist Feynman refers to a fluid with this property as "dry water" in order to stress the point that by leaving out viscosity, an essential property of the fluid is neglected. A flow in which viscous effects are neglected, is called inviscid. Having neglected viscous effects, we next turn our attention to the nonlinear convective term, that is  $(\mathbf{v} \cdot \nabla)\mathbf{v}$ . Using an identity from vector analysis, it follows that this term can be written like  $(\mathbf{v} \cdot \nabla)\mathbf{v} = \boldsymbol{\Omega} \times \mathbf{v} + \frac{1}{2}\nabla(\mathbf{v} \cdot \mathbf{v})$  in which we have introduced a quantity called the vorticity  $\boldsymbol{\Omega} = \nabla \times \mathbf{v}$ . Vorticity is related to the local angular rate of rotation of the fluid and a flow field is called irrotational if its vorticity vanishes everywhere. It is not hard to show that an inviscid flow which is irrotational in the whole domain at some time  $t$ , will remain irrotational for all subsequent times (for more details see Batchelor, 1967). If

we assume the velocity field  $\mathbf{v}$  to be irrotational we may introduce a velocity potential  $\phi(x, y, z, t)$  which is related to the fluid velocity via

$$\mathbf{v} = \nabla\phi \quad (8.2.1)$$

Having neglected the viscous term and subject to the assumption of an irrotational velocity field, it follows now that the momentum equation (2.2.9) can be written like

$$\nabla \left( \frac{\partial \phi}{\partial t} + \frac{1}{2}\mathbf{v} \cdot \mathbf{v} + \frac{1}{\rho}p - \mathbf{g} \cdot \mathbf{x} \right) = 0$$

which integrates immediately to

$$\frac{\partial \phi}{\partial t} + \frac{1}{2}\mathbf{v} \cdot \mathbf{v} + \frac{1}{\rho}p - \mathbf{g} \cdot \mathbf{x} = A(t) \quad (8.2.2)$$

in which  $A(t)$  is an integration constant. In the special case where the flow is steady we have  $\partial\phi/\partial t = 0$  and the above equation reduces to the famous Bernoulli equation

$$\frac{1}{2}\mathbf{v} \cdot \mathbf{v} + \frac{1}{\rho}p - \mathbf{g} \cdot \mathbf{x} = \text{constant}$$

Bernoulli's equation is nothing more than a statement of conservation of energy along a streamline: the sum of potential and kinetic energy along a streamline is constant. An application of Bernoulli's equation will be given in the next chapter but here we are interested in interfacial waves and hence we will be dealing with (8.2.2) in this section. Using (8.2.1) it follows that the mass conservation equation (2.2.8) becomes

$$\nabla^2\phi = 0 \quad (8.2.3)$$

showing that in the case of inviscid, irrotational flow, mass conservation reduces to solving a potential equation for the velocity potential  $\phi$ .

The boundary conditions for an inviscid flow are as follows. Since the fluid is assumed to be frictionless, the fluid velocity tangential to a solid wall will not be influenced by the presence of the wall. However, the fluid velocity normal to a wall must be zero. Thus, using (8.2.1) and the fact that  $\mathbf{v} \cdot \mathbf{n} = 0$  on any solid boundary, it follows that

$$\left. \frac{\partial \phi}{\partial n} \right|_{\text{solid wall}} = 0 \quad (8.2.4)$$

At a fluid interface, the jump conditions as specified in section 2.3 have to be applied. With no exchange of mass at the interface it follows that the normal interfacial velocity must equal the normal velocity of liquid particles immediately adjacent to the interface. This in turn implies that the normal velocities must be continuous over the interface, giving

$$\left. \frac{\partial \phi_1}{\partial n} \right|_{\text{interface}} = \left. \frac{\partial \phi_2}{\partial n} \right|_{\text{interface}} \quad (8.2.5)$$

in which the subscripts 1 and 2 refer to fluids on either side of the interface. When the interface is a material surface, the jump conditions related to momentum conservation are given by (2.3.7). Since the deviatoric part of the stress tensor vanishes in the limit of vanishing viscosity, it follows that the second equation in (2.3.7) (continuity of shear stress) is automatically satisfied, while the continuity of normal stress reduces to

$$[p] = \mathcal{C}\sigma$$

Using the integrated momentum equation (8.2.2) together with the jump condition, the interfacial boundary condition becomes

$$[p] = -\rho_1 \frac{\partial \phi_1}{\partial t} + \rho_2 \frac{\partial \phi_2}{\partial t} - \frac{1}{2} \rho_1 (\nabla \phi_1)^2 + \frac{1}{2} \rho_2 (\nabla \phi_2)^2 + (\rho_1 - \rho_2) \mathbf{g} \cdot \mathbf{x}_i - \Theta = \mathcal{C}\sigma \quad (8.2.6)$$

in which  $\Theta$  denotes some constant which is to be determined. The Laplace equation (8.2.3) together with the no-flux condition (8.2.4) on solid walls and (8.2.5), (8.2.6) at interfacial boundaries, completely defines the potential flow problem.

We are now in a position to consider the specific case of two frictionless fluids flowing between two parallel, infinite plates. The geometry is as shown in Figure 8.2.1 and we assume that the position of the undisturbed interface is at located at  $z = h$ .

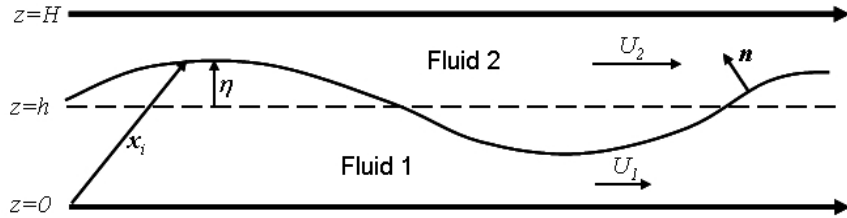


Figure 8.2.1: Geometry of flow between infinite parallel plates

The fluids 1 and 2 flow with constant, uniform velocities  $U_1$  and  $U_2$  in the positive  $x$ -direction. The velocity potential in each layer can thus be written  $\phi_i(x, z, t) = U_i x + \tilde{\phi}_i(x, z, t)$  in which  $\tilde{\phi}_i(x, z, t)$  presents a perturbation of the flow field relative to the uniform flow  $U_i$ . The perturbations in the flow field are the result of waves at the interface between the fluids and the properties of these waves are of interest: which wavelengths develop, can waves grow in amplitude, etc. The amplitude of the waves is denoted by  $\eta(x, t)$  and these amplitudes are assumed to be small such that all nonlinear effects (such as products of  $\tilde{\phi}_i$  or  $\eta$ ) can be neglected. The properties of the waves can be studied by considering each Fourier-component separately (see Whitham, 1974) and this is achieved by taking  $\tilde{\phi}_i = \Phi_i(z) e^{i(kx - \omega t)}$  and  $\eta = \eta_0 e^{i(kx - \omega t)}$ .

We now use the technique of separation of variables to solving the potential equation (8.2.3) for each fluid layer. Thus, (8.2.3) together with the condition of no vertical flow on the lower and upper wall gives

$$\begin{aligned} \Phi_1(z) &= A \cosh kz \\ \Phi_2(z) &= B [\cosh kz - \sinh kz \tanh kH] \end{aligned}$$

The unit normal to the perturbed interface (see exercise 2.6) may be approximated by  $\mathbf{n} = \left( -\frac{\partial \eta}{\partial x}, 1 \right)$  so that the velocity normal to the interface is equal to  $\frac{\partial \phi_i}{\partial n} = -U_i \frac{\partial \eta}{\partial x} + \frac{\partial \tilde{\phi}_i}{\partial z}$  when neglecting products of perturbed quantities. When we now apply the mass conservation condition (8.2.5) at  $z = h$  while using the expressions for  $\Phi_1$  and  $\Phi_2$  as given above as given above to obtain

$$i(U_2 - U_1)\eta_0 = -A \sinh kh + B [\sinh kh - \cosh kh \tanh kH] \quad (8.2.7)$$

Next we apply the normal stress condition (8.2.6) and first consider the case in which the flow is steady, that is,  $\eta = \tilde{\phi}_i \equiv 0$ . Under these conditions the position vector for the (flat) interface is given by  $\mathbf{x} = (x, h)$  and equation (8.2.6) reduces to

$$-\frac{1}{2}\rho_1 U_1^2 + \frac{1}{2}\rho_2 U_2^2 - (\rho_1 - \rho_2) gh = \Theta$$

which determines the constant  $\Theta$ . In the case where the flow field and the interface are perturbed, the normal stress condition (8.2.6) becomes

$$-\rho_1 \frac{\partial \tilde{\phi}_1}{\partial t} + \rho_2 \frac{\partial \tilde{\phi}_2}{\partial t} - \rho_1 U_1 \frac{\partial \tilde{\phi}_1}{\partial x} + \rho_2 U_2 \frac{\partial \tilde{\phi}_2}{\partial x} - (\rho_1 - \rho_2) g\eta = -\sigma \frac{\partial^2 \eta}{\partial x^2} \quad (8.2.8)$$

in which, as before, we have neglected products of perturbed quantities. Substituting the Fourier forms into the above equation yields

$$i\rho_1 A(\omega - kU_1) \cosh kh - i\rho_2(B\omega - kU_2)(\cosh kh - \sinh kh \tanh kH) = (\Delta\rho g + \sigma k^2)\eta_0 \quad (8.2.9)$$

Since the position of the interface  $\eta$  has entered the problem we need an additional equation for the interface position. For problems in which interfacial waves do not break we have no entrainment and therefore no exchange of mass between the two layers. For this case, the jump condition established in section 2.3 tells us that the interfacial velocity must be equal to the fluid velocity. It is left as an exercise to show that this yields

$$\frac{\partial \eta}{\partial t} + U_1 \frac{\partial \eta}{\partial x} = \left. \frac{\partial \tilde{\phi}_1}{\partial z} \right|_{z=h} \quad (8.2.10)$$

Substituting the Fourier forms into the above equation, we obtain

$$-i\omega\eta_0 + U_1\eta_0 = Ak \sinh kh \quad (8.2.11)$$

Between equations (8.2.7), (8.2.9) and (8.2.11) it is now possible to eliminate the constants  $A$ ,  $B$  and  $\eta_0$  which yields after some manipulations

$$(\sigma k^3 + k\Delta\rho g) \tanh kH - \rho_1(kU_1 - \omega)^2 - \frac{\tanh kh}{\tanh k(H-h)} \rho_2(kU_2 - \omega)^2 = 0 \quad (8.2.12)$$

The above equations is an example of what is called a dispersion relation. This relation links the angular frequency of the waves to the wave number via  $\omega = \omega(k)$ : waves with a given wavenumber have only specific frequencies associated with them.

Of particular interest in relation to stratified shear flows is the question of stability: are the waves on the interface stable or is it possible that interfacial waves become unstable with increasing amplitudes? Linear stability, that is, the stability of waves with infinitesimal amplitudes, can be studied by considering the dispersion relation (8.2.12). The condition for stable linear waves is that the angular frequency  $\omega$  is real for all wave numbers  $k$ . We note that (8.2.12) constitutes a quadratic equation for  $\omega$  and the condition for real  $\omega$  (and thus stable waves) is simply that the discriminant must be positive. It is not hard to show that this yields

$$(U_1 - U_2)^2 \leq \left( \frac{\tanh kh}{\rho_1} + \frac{\tanh k(H-h)}{\rho_2} \right) \left( \sigma k + \frac{\Delta\rho g}{k} \right) \quad (8.2.13)$$

We see that for a given wave number, stable interfacial waves only exist for a certain range of gas and liquid velocities. If the stability criterion given in (8.2.13) is not satisfied, interfacial waves are unstable and their amplitude will grow. According to our analysis, the amplitude of the interfacial waves will grow exponentially with time. However, since we have assumed that wave amplitudes are small (in order to be able to neglect all the nonlinear terms) it will be evident that results from the linear theory are valid only for short times after the onset of wave growth. In principle, the wave amplitudes may grow so large that they reach the upper solid boundary of the flow channel. If this would happen we would have the two-dimensional equivalent of the formation of a liquid slug: the complete blockage of the flow area by a liquid plug. When the interfacial waves become unstable, the imaginary part of the angular frequency determines the growth rates of the interfacial waves. As an example of the growth rate of the interfacial waves we have plotted  $\text{Im}(\omega)$  as a function of the scaled wavelength  $\lambda/H$  in figure 8.2.2. The parameters for this particular case are as follows:  $H = 5 \text{ cm}$ ,  $h = 3 \text{ cm}$ ,  $\rho_1 = 1000 \text{ kg m}^{-3}$ ,  $\rho_2 = 1.3 \text{ kg m}^{-3}$ ,  $U_1 = 7.5 \text{ m s}^{-1}$ ,  $\sigma = 0.07 \text{ N m}^{-1}$  and the values of  $U_2$  are as indicated in the plot. As the stability boundary (near  $U_2 \simeq 1.63 \text{ m s}^{-1}$ ) is approached we see that the growth rate of the interfacial waves decreases. Figure 8.2.2 shows clearly that there is a most unstable wavelength, that is, the wavelength of the wave which has the largest growth rate. In this particular example the most unstable wave has a wavelength equal to approximately one third of the height of the flow channel.

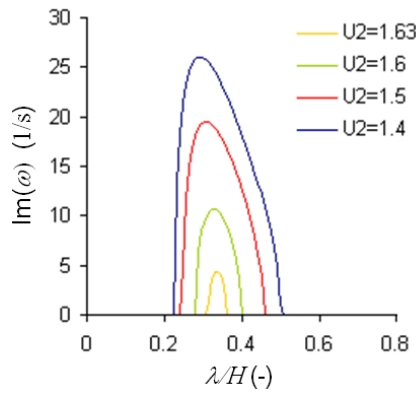


Figure 8.2.2: Growth rates of unstable interfacial waves.

So far we have considered the case of inviscid flow between infinite, parallel plates. A study of this system is worthwhile since a number of basic properties related to the stability of shear flows are relatively easy to obtain. However, the infinite, parallel plate geometry is not the geometry which is of most practical interest. Hence, we next consider stratified, inviscid flow in a circular pipe of which the symmetry axis points along the  $x$ -axis (see figures 4.5.1 and 4.5.2). The basic equations for this geometry are already specified. Namely, in the inviscid limit, mass conservation means that in each phase the velocity potential satisfies the Laplace equation (8.2.2). Since we are now dealing with a three-dimensional problem we choose to write the mass conservation equation like

$$\nabla_{\perp}^2 \phi + \frac{\partial^2 \phi}{\partial x^2} = 0$$

in which  $\nabla_{\perp}^2 = \partial^2/\partial y^2 + \partial^2/\partial z^2$ . As before, we write the velocity potential in each phase like  $\phi_i(x, y, z, t) = U_i x + \tilde{\phi}_i(x, y, z, t)$ . We now take the following steps. The mass conservation equation in each phase is first integrated over the cross section occupied by the relevant phase. Subsequently we use the divergence theorem and apply the

boundary condition on the solid walls, equation (8.2.4), and on the interface, equation (8.2.10). Going through these steps one obtains the following expression for the mass conservation equation

$$\pm s_I \left( \frac{\partial \eta}{\partial t} + U_k \frac{\partial \eta}{\partial x} \right) + \int_{A_k} \frac{\partial^2 \tilde{\phi}_k}{\partial x^2} = 0, \quad k = 1, 2$$

in which  $s_I$  denotes the length of the interfacial perimeter (see figure 4.5.2) and we have assumed that the interfacial wave height is uniform across the interface, that is  $\eta = \eta(x, t)$ . For  $k = 1$  we take the positive sign in the above equation. The next step we take in the analysis can be justified by performing a formal perturbation expansion based on the assumption that the interfacial waves have a wavelength which is long compared to the pipe diameter. Performing such an expansion, it can be shown (for details, see Peregrine, 1968) that a consistent, leading-order approximation of the above equation is given by

$$\pm s_I \left( \frac{\partial \eta}{\partial t} + U_k \frac{\partial \eta}{\partial x} \right) + A_k \frac{\partial^2 \tilde{\phi}_k}{\partial x^2} = 0, \quad k = 1, 2 \quad (8.2.14)$$

We can now use this result in the interfacial condition (8.2.8) and eliminate the velocity potentials  $\tilde{\phi}_k$  from the interface condition. Proceeding as indicated, it is easy to show that the following evolution equation for  $\eta$  is obtained

$$a \frac{\partial^2 \eta}{\partial t^2} + 2b \frac{\partial^2 \eta}{\partial x \partial t} + c \frac{\partial^2 \eta}{\partial x^2} = 0 \quad (8.2.15)$$

in which  $a = \frac{\rho_1}{A_1} + \frac{\rho_2}{A_2}$ ,  $b = \frac{\rho_1 U_1}{A_1} + \frac{\rho_2 U_2}{A_2}$  and  $c = \frac{\rho_1 U_1^2}{A_1} + \frac{\rho_2 U_2^2}{A_2} - \frac{\Delta \rho g}{s_I}$ . The simplification which leads to the mass conservation equation (8.2.14) is based on a long-wavelength assumption and therefore we have neglected the surface tension term which is present in the interface condition (8.2.8). In order to study traveling-wave solutions we again consider the Fourier components  $\eta = \eta_0 e^{i(kx - \omega t)}$  and it follows immediately that (8.2.15) yields the dispersion relation  $a\omega^2 - 2bk\omega + ck^2 = 0$ . Stable interfacial waves are obtained when  $\omega$  is real and it is not hard to show that this implies

$$(U_2 - U_1)^2 \leq \left( \frac{A_1}{\rho_1} + \frac{A_2}{\rho_2} \right) \frac{\Delta \rho g}{s_I} \quad (8.2.16)$$

It is interesting to note the similarity between the stability condition based on the two-dimensional analysis as given by (8.2.13) and the three-dimensional analysis as given above. Namely, by taking the long-wavelength limit of condition (8.2.13) (that is, letting  $k \rightarrow 0$ ) we find that the two stability conditions are identical when we take  $h \rightarrow A_1/s_I$  and  $H - h \rightarrow A_2/s_I$ . This means that if we regard  $A_1/s_I$  as an indication of the mean height of phase 1 below the interface (and likewise for phase 2), we find a direct link between the stability conditions for the two-dimensional and three-dimensional cases. Before we leave this section it is important to point out one major short coming of the frictionless flow analysis given in this section. In the entire analysis it has been assumed that the position of the interface  $h$  is known. In general this is not the case and we have seen earlier (for example section 5.2) that the interfacial position follows from a balance of shearing forces at the interface. In potential flow where all shear-stress effects are eliminated the interfacial height is essentially an undetermined parameter.

### 8.3 Well-posedness of two-fluid equations

In Section 4.5 the equations governing a stratified gas-liquid flow were derived and summed up in Table 4.1. We will now analyze the solution properties of these equations

without explicitly solving the equations. To this end we will apply the method of characteristics (for an in-depth discussion of this method we refer to Whitham, 1974). We begin by defining what constitutes a *well-posed* problem. A well-posed problem is a problem that has

- (i) A solution which is unique, and:
- (ii) A solution which depends continuously on the initial data.

With point (ii) we mean that small changes in the initial data (such as inlet conditions) should result in small changes in the solution properties of the equations. A problem is called *ill-posed* if it is not well-posed.

With the exception of a few special cases, it turns out to be very difficult to proof that a non-linear partial differential equation (PDE) has a solution which is unique. It is, however, not uncommon to assume that equations that have a sound physical basis, have a solution that is unique, even though this can not (yet) be proved formally. Here we also follow this path: the equations listed in Table 4.1 are thus assumed to have a solution that is unique. Having a solution does not mean, however, that the solution depends continuously in the initial data. This last property can be investigated using the method of characteristics.

Consider a set of  $n$  quasi-linear PDE's of the form

$$\mathbf{A} \frac{\partial}{\partial t} \Psi + \mathbf{B} \frac{\partial}{\partial x} \Psi = \mathbf{c} \quad (8.3.1)$$

in which the non-singular coefficient matrices  $\mathbf{A}(\Psi)$  and  $\mathbf{B}(\Psi)$  are of order  $n \times n$  and neither the coefficient matrices nor the column vector  $\mathbf{c}(\Psi)$  contain derivatives of  $\Psi$ . Assume now that at all points on some curve  $C_0$  in the  $x$ - $t$  plane values for  $\Psi$  are specified, see Figure 8.3.1.

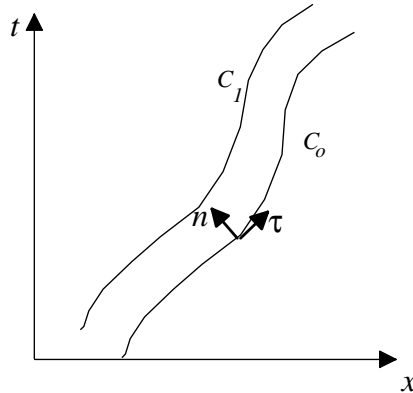


Figure 8.3.1: Characteristic curves in the  $x$ - $t$  plane.

Using a Taylor series expansion, new values of  $\Psi$  in the neighbourhood of the curve  $C_0$  can be found provided the first derivative of  $\Psi$  with respect to  $x$  and  $t$  can be computed. It is convenient to introduce the variables  $n(x, t)$  and  $\tau(x, t)$  which denote directions normal and tangential respectively to the curve  $C_0$ . In terms of the variables  $n$  and  $\tau$ , equation (8.3.1) becomes

$$\left[ \mathbf{A} \frac{\partial n}{\partial t} + \mathbf{B} \frac{\partial n}{\partial x} \right] \frac{\partial}{\partial n} \Psi = \mathbf{c} - \left[ \mathbf{A} \frac{\partial \tau}{\partial t} + \mathbf{B} \frac{\partial \tau}{\partial x} \right] \frac{\partial}{\partial \tau} \Psi \quad (8.3.2)$$

Since  $\Psi$  is known along the curve  $C_0$  it follows that the right-hand-side of equation (8.3.2) is known. Thus, provided the coefficient matrix

$$\mathbf{A} \frac{\partial n}{\partial t} + \mathbf{B} \frac{\partial n}{\partial x} \quad (8.3.3)$$

is non-singular, the change of  $\Psi$  in the direction normal to the curve  $C_0$  can be determined uniquely. This then implies that starting from the data given on  $C_0$  we can determine new data on a curve  $C_1$  which lies in the neighbourhood of  $C_0$ . Proceeding in this manner, values of  $\Psi$  in the whole  $x-t$  plane can be determined. This is the typical situation for a *boundary value problem*: the solution of a problem defined on a given domain is determined by the values specified on the boundary of that domain. A classical example of a boundary value problem is the problem of steady-state heat conduction. If the temperature on the boundary of a given domain is specified, then the temperature at any point within the domain is determined by solving the steady-state heat conduction equation  $\nabla^2 T = 0$  subject to the given boundary conditions.

Let us return to the quasi-linear PDE and consider the special situation which occurs when the coefficient matrix given in (8.3.3) is singular. If this is the case, it is clear that the solution of  $\Psi$  in the neighbourhood of the curve  $C_0$  can not be obtained from values on  $C_0$ . What is happening here? Is information only defined on this special curve  $C_0$  and nowhere else in the  $x-t$  plane? It turns out that there are many curves  $C_0, C_1, C_2, \dots$  but information flows *along* these curves and the values of  $\Psi$  along these curves are determined by the initial conditions  $\Psi(x, t = 0)$ . The curves  $C_0, C_1, C_2$  are called a *characteristic curves* and the dependence of the solution on the initial data reduces to finding the characteristic curves. Once the characteristic curves are specified and the initial conditions are known, the solution of (8.3.1) in the whole  $x-t$  plane can be determined. The characteristic curves are found by considering the equation

$$\det [\mathbf{A}\lambda - \mathbf{B}] = 0 \quad (8.3.4)$$

Information propagates along the characteristics with a characteristic velocity equal to  $\frac{dx}{dt} = \frac{\partial n}{\partial t} / \frac{\partial n}{\partial x} = -\lambda$  and the slopes of the characteristics in the  $x-t$  plane are equal to  $-\frac{1}{\lambda}$ . It is then evident that one of the conditions for the existence of well-defined characteristic curves is that the characteristic values (or eigenvalues)  $\lambda$  are real. Namely, if the eigenvalues are real then, evidently, curves with well-defined directions in the  $x-t$  plane and with well-defined characteristic velocities exist. The second condition required for the existence of well-defined characteristic curves, is that it should be possible to devise a time-stepping scheme that allows the propagation of information in time. This clearly demands that (8.3.1) can be solved for  $\frac{\partial}{\partial t} \Psi$  which implies that  $\mathbf{A}$  should be non-singular.

On the basis of these observations, a general classification of the system of equations given by (8.3.1) can be given:

- (i) If all  $\lambda$  are real and  $\mathbf{A}$  is invertible, then the system of equations is called *hyperbolic*. In this case information propagates along well-defined curves in  $x-t$  space and the solution of the system of equations is determined by initial conditions  $\Psi(x, t = 0)$ ;
- (ii) If the characteristic values  $\lambda$  are complex then the system of equations is called *elliptic* and the solution of (8.3.1) is determined uniquely from data given along some curve  $C_0$ .

For a one-dimensional set of transport equations, as for example the equations given in Table 4.1, ellipticity implies loss of causality (future events will influence the solution at the current time). Loss of causality therefore necessarily implies that the problem is ill-posed. Thus, in order to determine whether or not the two-fluid equations for separated flow constitute a well-posed system of equations, it is necessary to determine whether or not the system of equations is elliptic or not. It is interesting to note that

the change from a hyperbolic to an elliptic system of equations is not only a change in the mathematical nature of the problem. Namely, in the next section it will be shown that the change from a hyperbolic to an elliptic system of equations is closely related to interfacial instabilities. These interfacial instabilities may, in turn, be related to the onset of slug flow. Controlled experiments with slug flow are surprisingly hard to perform precisely because of the elliptic nature of the problem: the generation of a slug at any point in a pipe may influence the flow structure both upstream and down stream from the point at which the slug is generated!

Let us return to the equations listed in Table 4.1. Assuming constant densities in the gas and the liquid phases, the mass conservation equations can be written like

$$\frac{\partial A_L}{\partial t} + u_L \frac{\partial A_L}{\partial x} + A_L \frac{\partial u_L}{\partial x} = 0 \quad (8.3.5a)$$

$$-\frac{\partial A_G}{\partial t} - u_G \frac{\partial A_G}{\partial x} + A_G \frac{\partial u_G}{\partial x} = 0 \quad (8.3.5b)$$

where we have used the fact that  $A_L + A_G = \text{constant}$ . We next consider the two momentum conservation equations in Table 4.1. First we divide each of the momentum equations by the cross sectional area on which they are defined and we subtract the resulting equations from each other on order to eliminate the pressure gradient. Note that the interfacial jump conditions defining the interfacial pressure condition and the interfacial shear stress condition have to be used here. In order to simplify the analysis we neglect the axial momentum diffusion terms as well as surface tension effects for the moment (these terms would introduce second- and third-order derivatives into the resulting equation. and the influence of these terms in non-trivial as will be shown in exercise 8.1). It is not hard to show that with the mentioned simplifications, the resulting equation reads

$$\begin{aligned} \rho_L \frac{\partial u_L}{\partial t} - \rho_G \frac{\partial u_G}{\partial t} + \left( \frac{\rho_L u_L}{A_L} + \frac{\rho_G u_G}{A_G} \right) \frac{\partial A_L}{\partial t} + 2c_L \rho_L u_L \frac{\partial u_L}{\partial x} - \\ 2c_G \rho_G u_G \frac{\partial u_G}{\partial x} + \left( \frac{c_L \rho_L u_L^2}{A_L} + \frac{c_G \rho_G u_G^2}{A_G} + \frac{\Delta \rho g \cos \beta}{s_I} \right) \frac{\partial A_L}{\partial x} = \mathcal{H} \end{aligned} \quad (8.3.6)$$

in which  $\Delta \rho = \rho_L - \rho_G$ , the interfacial perimeter  $s_I = dA_L/dh$  and the holdup function  $\mathcal{H}$  is as defined in equation (5.4.3). Note that for the case in which a fully developed ( $\frac{\partial \cdot}{\partial x} = 0$ ), steady state ( $\frac{\partial \cdot}{\partial t} = 0$ ) is reached, equation (8.3.6) reduces to  $\mathcal{H} \equiv 0$  which is the holdup equation studied in section (5.4).

We will now investigate under which conditions the equations (8.3.5)-(8.3.6) define a hyperbolic system. Defining the vector  $\Psi = (A_L, u_L, u_G)^T$ , we can immediately write these three equations in the form of (8.3.1) by taking

$$\begin{aligned} \mathbf{A} &= \begin{bmatrix} 1 & 0 & 0 \\ -1 & 0 & 0 \\ \frac{\rho_L u_L}{A_L} + \frac{\rho_G u_G}{A_G} & \rho_L & -\rho_G \end{bmatrix} \text{ and} \\ \mathbf{B} &= \begin{bmatrix} u_L & A_L & 0 \\ -u_G & 0 & A_G \\ \frac{c_L \rho_L u_L^2}{A_L} + \frac{c_G \rho_G u_G^2}{A_G} + \frac{\Delta \rho g \cos \beta}{s_I} & 2c_L \rho_L u_L & -2c_G \rho_G u_G \end{bmatrix} \end{aligned}$$

We note first of all that  $\mathbf{A}$  is non-singular. It is now easily shown that the characteristic equation  $\det(\mathbf{A} - \lambda \mathbf{B}) = 0$  yields a quadratic equation for the eigenvalues  $\lambda$ . The eigenvalues are real (and hence the set of equations is hyperbolic) provided the discriminant is positive. Without much difficulty is can now be shown that the system of equations is hyperbolic provided

$$(c_G u_G - c_L u_L)^2 \leq \left( \frac{A_L}{\rho_L} + \frac{A_G}{\rho_G} \right) \left( c_L(c_L - 1) \frac{\rho_L u_L^2}{A_L} + c_G(c_G - 1) \frac{\rho_G u_G^2}{A_G} + \frac{\Delta \rho g \cos \beta}{s_I} \right) \quad (8.3.7)$$

The analysis leads to the conclusion that the equations describing stratified gas-liquid flow in a pipe are conditionally well-posed when surface tension and axial diffusion effects are neglected. Louaked *et al* (2003) have shown that under condition (8.3.7) with equality excluded, the solution of equations (8.3.5)-(8.3.6) is unique for sufficiently small times. Taking the profile coefficients equal to unity we note that the condition for well-posedness as given above is identical to the inviscid stability condition (8.2.16). This is the first indication that hyperbolicity is related to stability of interfacial waves. The profile coefficients  $c_L$  and  $c_G$  play an interesting role in the equation (8.3.7). It is common to take  $c_L = c_G = 1$  which eliminates the inertia terms on the right hand side of the stability condition. The profile coefficients are difficult to measure experimentally and also surprisingly difficult to determine computationally. However, the velocity is not entirely constant over the cross section of the pipe so that the coefficients must be larger than unity. For the case of stratified gas-liquid flow, there are indications that the profile coefficient for the gas phase is similar to that for single phase turbulent flow, that is  $c_G \simeq 1.1$ . For the liquid phase it is believed that the coefficients is smaller,  $c_L \simeq 1.02 - 1.05$ . It is clear that the magnitudes of the Froude numbers

$$Fr_k = c_k(c_k - 1) \frac{s_I}{A_k} \frac{\rho_k u_k^2}{\Delta \rho g \cos \beta}, \quad k = L, G$$

determine to what extend the inertia terms can be neglected. Interestingly, we see that Froude number is strongly influenced both by the velocity in each phase as well as by the system pressure. Namely, when  $u_k$  is sufficiently large or when the density difference  $\Delta \rho = \rho_L - \rho_G$  is sufficiently small, we can not assume that both Froude numbers are small. We observe an interesting pressure-dependence of the region in which the equations are hyperbolic or elliptic since it is the system pressure which governs the magnitude of  $\Delta \rho$ . In figure 8.3.2 we have plotted the curves specified by equation (8.3.7) for the case of air-water flow in a 5cm horizontal pipe. The influence of the inertia terms on the boundary separating the hyperbolic from the elliptic regions is clearly visible.

In this section we have studied the general properties of the stratified flow equations as given in Table 4.1. We have seen that the equations are well-posed only under specific conditions. In exercise 8.1 we show that the inclusion of surface tension effects leads to a system of equations which is unconditionally well-posed and the same can be shown when axial momentum diffusivity effects are included. Note that both the effects of surface tension and axial diffusivity are described by terms which contain higher-order derivatives. This suggests that the problem of well-posedness is governed by physical effects which operate on short length scales (typically length scales much less than the pipe diameter). This is an important observation since the equations we are dealing with are essentially based on the so-called long-wave-length (or shallow-water) assumption. This assumption means that all relevant flow phenomena occur on length scales which are long compared with the typical thickness of the liquid layer. However, we have seen that the question of well-posedness is related to length scales much less than a typical pipe diameter (and thus much less than the thickness of the liquid layer). We conclude that the two-fluid model has the unfortunate property that important properties of the equations are related to length scales on which the equations are stricktly-speaking no longer valid. Holmås *et al* (2008) have shown how artificial diffusion terms can be applied in order to remove short-wavelength instabilities while retaining the correct long-wavelength behaviour.

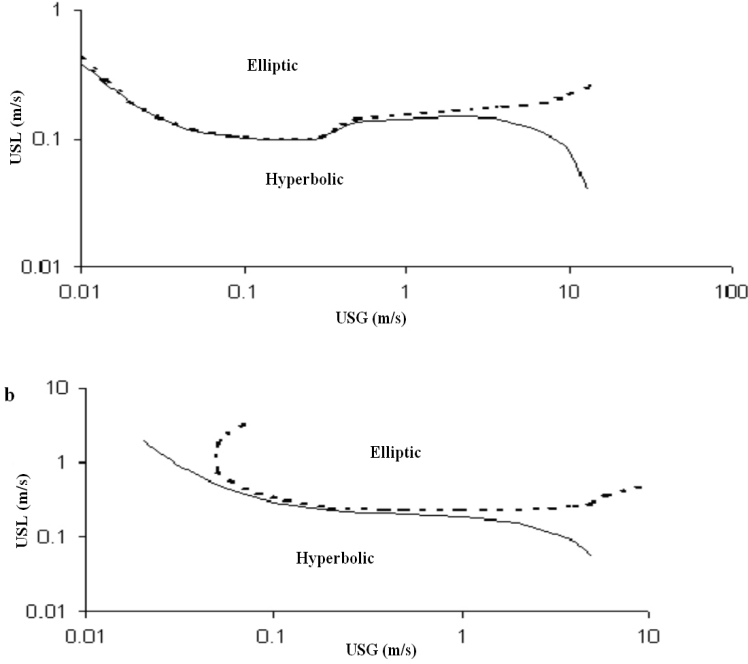


Figure 8.3.2: Lines indicating the boundary between the hyperbolic and elliptic regions. The drawn line is the curve as predicted for the case  $c_L = c_G = 1$  while the dotted line is the curve as predicted for the case with  $c_L = c_G = 1.1$ . In figure (a) the pressure is atmospheric while in figure (b) the system pressure is 10bar.

The question now arises to what extent well-posedness can be related to possible changes in flow regime. We have already seen that there is a link between well-posedness and stability of interfacial waves in the inviscid limit. A natural question to ask is to what extent waves generated on the gas-liquid interface can become unstable and grow to become precursors of slugs? To answer (part of) this question we next consider waves exhibited by the two-fluid equations.

#### 8.4 Linear stability of interfacial waves

So far we have studied waves in a frictionless system as well as the conditions required to obtain a well-posed system of equations. We now proceed to study linear wave solutions permitted by the two-fluid model. To that end we will start with the conservation equations (8.3.5) and (8.3.6) and we will consider growth rates of interfacial waves as predicted by these equations. We start with the assumption that the conservation equations permit a steady state solution of the form

$$A_L = \bar{A}_L, \quad A_G = \bar{A}_G, \quad u_L = \bar{u}_L \text{ and } u_G = \bar{u}_G \quad (8.4.1)$$

with the barred quantities denoting constants. We note that the mass conservation equations (8.3.5) are identically satisfied when we insert the steady state solution. The combined momentum equation (8.3.6) is satisfied provided we satisfy the holdup equation (see section 5.4)

$$\mathcal{H}(\bar{u}_L, \bar{u}_G, \bar{A}_L, \bar{A}_G) = 0 \quad (8.4.2)$$

In order to study wave solutions of equations (8.3.5) and (8.3.6) we consider the following perturbations relative to the steady state solution (8.4.1)

$$A_L(x, t) = \bar{A}_L + \tilde{A}_L(x, t), \quad u_L(x, t) = \bar{u}_L + \tilde{u}_L(x, t) \text{ and } u_G(x, t) = \bar{u}_G + \tilde{u}_G(x, t) \quad (8.4.3)$$

The magnitude of perturbations relative to the steady state values are assumed to be small, that is  $\left| \frac{\tilde{A}_L(x, t)}{\bar{A}_L} \right| \ll 1, \left| \frac{\tilde{u}_L(x, t)}{\bar{u}_L} \right| \ll 1$  etc.

In figure 8.1.1 typical small-amplitude interfacial waves are shown and it is this type of system to which the analysis in this section can be applied. We now substitute the expressions (8.4.3) into the conservation equations (8.3.5) and (8.3.6) and we neglect all terms which consist of products of perturbed quantities. The following set of linear equations is now obtained

$$\frac{\partial \tilde{A}_L}{\partial t} + \bar{u}_L \frac{\partial \tilde{A}_L}{\partial x} + \bar{A}_L \frac{\partial \tilde{u}_L}{\partial x} = 0 \quad (8.4.4a)$$

$$-\frac{\partial \tilde{A}_L}{\partial t} - \bar{u}_G \frac{\partial \tilde{A}_L}{\partial x} + \bar{A}_G \frac{\partial \tilde{u}_G}{\partial x} = 0 \quad (8.4.4b)$$

$$\begin{aligned} \rho_L \frac{\partial \tilde{u}_L}{\partial t} - \rho_G \frac{\partial \tilde{u}_G}{\partial t} + c_L \rho_L \bar{u}_L \frac{\partial \tilde{u}_L}{\partial x} - c_G \rho_G \bar{u}_G \frac{\partial \tilde{u}_G}{\partial x} + \\ \Delta \rho g \cos \beta \frac{1}{s_I} \frac{\partial \tilde{A}_L}{\partial x} = \tilde{\mathcal{H}} \end{aligned} \quad (8.4.4c)$$

in which  $\tilde{\mathcal{H}}$  is given by

$$\tilde{\mathcal{H}} = \tilde{u}_L \frac{\partial \bar{\mathcal{H}}}{\partial u_L} + \tilde{u}_G \frac{\partial \bar{\mathcal{H}}}{\partial u_G} + \tilde{A}_L \frac{\partial \bar{\mathcal{H}}}{\partial A_L} \quad (8.4.5)$$

In the above equation we have used the short-hand notation  $\frac{\partial \bar{\mathcal{H}}}{\partial u_L} = \left. \frac{\partial \mathcal{H}}{\partial u_L} \right|_{\bar{u}_L, \bar{u}_G, \bar{A}_L}$  etc. Using equations (8.4.4a) and (8.4.4b) it is possible to eliminate the velocities  $\tilde{u}_L$  and  $\tilde{u}_G$  from (8.4.4c) which then yields a linear differential equation in terms of  $\tilde{A}_L$  only. In order to study the properties of the waves as described by this equation it again is sufficient to consider each Fourier component separately and this is achieved by writing  $\tilde{A}_L = A_o e^{i(kx - \omega t)}$ . Substituting this from for  $\tilde{A}_L$  into the differential equation we obtain, once again, a dispersion relation. For the case under consideration, the dispersion relation has the form

$$\bar{c}\omega^2 - (i\bar{e} + k\bar{b})\omega + \bar{a}k^2 + ik\bar{d} = 0 \quad (8.4.6)$$

in which

$$\begin{aligned} \bar{a} &= \frac{c_L \rho_L \bar{u}_L^2}{\bar{A}_L} + \frac{c_G \rho_G \bar{u}_G^2}{\bar{A}_G} - \frac{\Delta \rho g \cos \beta}{s_I} \\ \bar{b} &= (c_L + 1) \frac{\rho_L \bar{u}_L}{\bar{A}_L} + (c_G + 1) \frac{\rho_G \bar{u}_G}{\bar{A}_G} \\ \bar{c} &= \frac{\rho_L}{\bar{A}_L} + \frac{\rho_G}{\bar{A}_G} \\ \bar{d} &= \frac{\bar{u}_L}{\bar{A}_L} \frac{\partial \bar{\mathcal{H}}}{\partial u_L} - \frac{\bar{u}_G}{\bar{A}_G} \frac{\partial \bar{\mathcal{H}}}{\partial u_G} - \frac{\partial \bar{\mathcal{H}}}{\partial A_L} \\ \bar{e} &= \frac{1}{\bar{A}_L} \frac{\partial \bar{\mathcal{H}}}{\partial u_L} - \frac{1}{\bar{A}_G} \frac{\partial \bar{\mathcal{H}}}{\partial u_G} \end{aligned}$$

Note that equation (8.4.6) is a quadratic equation for  $\omega$  which can readily be solved to give

$$\omega_{\pm} = \frac{1}{2c} \left( i\bar{e} + k\bar{b} \pm \sqrt{(i\bar{e} + k\bar{b})^2 - 4\bar{c}k(\bar{a}k + i\bar{d})} \right) \quad (8.4.7)$$

It is evident that interfacial waves are stable only when  $\omega_{\pm}$  is real or when  $\text{Im}(\omega_{\pm}) < 0$ . The stability condition  $\text{Im}(\omega_{\pm}) < 0$  is often referred to as the Viscous Kelvin Helmholtz (VKH) stability condition. In order to gain insight into the stability of interfacial waves we first consider the stability condition in the short-wavelength limit, that is  $k \gg 1$ . In this limit we can make the approximations  $\bar{d} \ll \bar{a}k$  and  $\bar{e} \ll \bar{b}k$  so that the discriminant of (8.4.7) reduces to  $\bar{b}^2 - 4\bar{a}\bar{c}$ . It is easy to show that stable interfacial waves are only obtained when this discriminant is positive so that the stability condition reads

$$\bar{b}^2 - 4\bar{a}\bar{c} \geq 0 \quad (8.4.8)$$

Substituting for  $\bar{a}, \bar{b}$  and  $\bar{c}$  we find after some manipulations that the condition for stability as given above becomes identical to (8.3.7). We conclude that the condition for obtaining a hyperbolic system of equations is identical to the condition for stable interfacial waves in the short-wavelength limit. Evidently, maintaining a hyperbolic (and thus a well-posed problem) is intimately related to stability of short-wavelength disturbances. The stability condition (8.4.8) or (8.3.7) is often referred to as the Inviscid Kelvin Helmholtz (IKH) stability condition. This name may suggest that the stability boundary as predicted by the VKH condition will approach the IKH stability boundary when the viscosity is reduced sufficiently. It may come as a surprise that this is not the case! In fact, the opposite is observed: the IKH and VKH stability boundaries become closer for increasing viscosities of the liquid phase. This counter-intuitive result is demonstrated in figure 8.4.1.

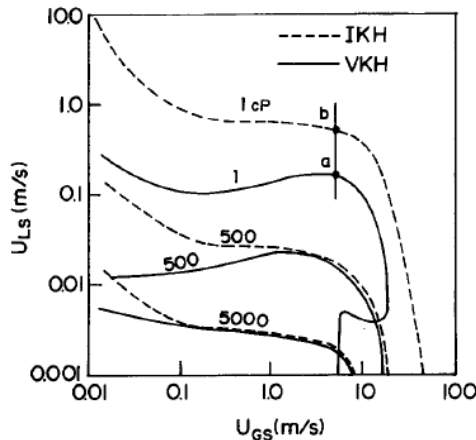


Figure 8.4.1: The effect of viscosity of the VKH and IKH stability boundaries. From Barnea & Taitel (1993). Liquid viscosities are indicated in the plot. Calculated results are based on air and water in a 5cm horizontal pipe at atmospheric conditions.

A detailed analysis of wave growth characteristics shows that waves become unstable when the VKH stability boundary is crossed but that the growth rate of the instabilities is finite for all wavelengths as long as one is below the IKH stability boundary. Once the IKH stability boundary is crossed, the growth rate of instabilities becomes unbounded: as the wavelength tends to zero, the growth rate tends to infinity.

We have seen that interfacial waves can become unstable and it is now clearly of interest to investigate the nature of these unstable waves. Recall that the amplitude of the unstable waves will grow in time proportional to  $e^{\text{Im}(\omega)t}$  so that it is natural to plot  $\text{Im}(\omega)$  as a function of  $\frac{\lambda}{D}$  where  $\omega$  is computed using (8.4.7).

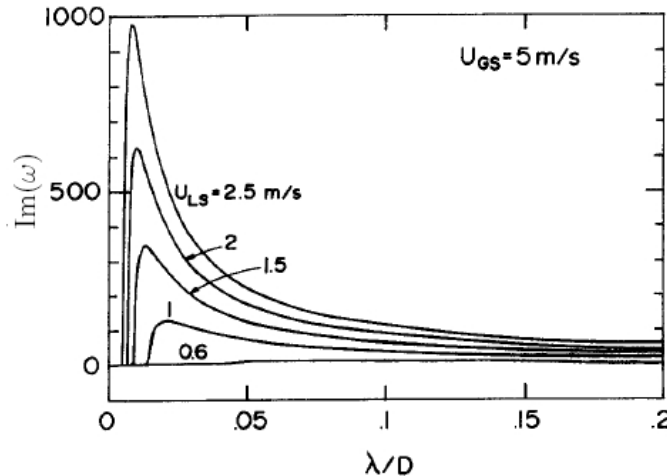


Figure 8.4.2: Plot of  $\text{Im}(\omega)$  as a function of  $\frac{\lambda}{D}$  for different values of  $U_{SL}$  (from Barnea & Taitel, 1993)

In Figure 8.4.2 we show such a plot for the case of an air-water system at atmospheric conditions in a 5 cm pipe. First of all we note that there is a "most unstable" wavelength, namely, a wavelength at which the growth rate is maximum. The wavelength of this most unstable wave is short since it occurs at  $\frac{\lambda}{D} \simeq 0.02$ . It turns out that it is the inclusion of surface tension effects which leads to this most unstable wave. Namely, if surface tension effects had been neglected, we would have found that  $\text{Im}(\omega) \rightarrow \infty$  in the limit  $\frac{\lambda}{D} \rightarrow 0$ . This observation is intimately coupled to the ill-posedness of the two-fluid equations and is a reflection of the fact that there are no mechanisms for energy dissipation on small length scales in the two-fluid model as described by (8.3.5)-(8.3.6). In Holmås *et al* (2008a) this problem is discussed in detail and there it is shown that the ill-posedness of the two-fluid model can be remedied by including artificial diffusion terms. By choosing the diffusion coefficients appropriately it is found that (unphysical) short-wavelength features are suppressed while features with long wavelengths ( $\lambda \gg D$ ) are unaffected by the diffusion terms.



Figure 8.4.3: Roll waves in two-phase pipe flow (picture by P. Andersson, IFE).

We have seen that well-posedness of the two-fluid equations and stability of the interfacial waves are linked. However, is there a connection between the transition from stable to unstable interfacial waves and the transition stratified to slug flow? Here we have to be careful since interfacial waves that become so large that slugs are formed, are outside the reach of the linear stability analysis. Recall that the stability analysis was performed on the assumption that a steady state exists and that perturbations relative

to this steady state are small, and in particular for the wave height  $|\tilde{h}(x, t)/\bar{h}| \ll 1$ . It turns out that the transition to unstable waves as predicted by the VKH stability line is not related to the transition from stratified to slug flow. In fact, the transition to unstable waves can be linked to the appearance of roll waves (see Holmås *et al*, 2008b). Roll waves are finite-amplitude waves with long tails and steep fronts. The wavelength of roll waves is typically larger than the mean liquid depth, see figure 8.4.3.

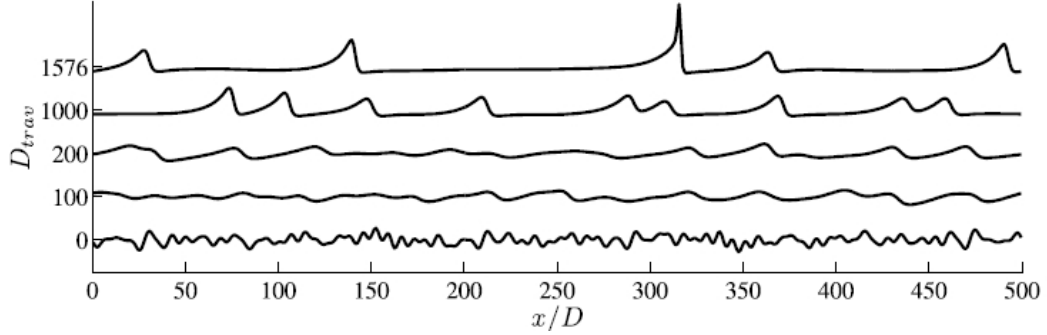


Figure 8.4.4: Hold-up profiles for simulated gas-liquid pipe flow (Holmås *et al*, 2008a). On the vertical axis the distance travelled (in number of pipe diameters) is indicated.

Simulations performed by Holmås *et al* (2008b) indicate that merging roll waves can lead to the appearance of large-amplitude waves. Since the propagation speed of the waves increases with amplitude, it is found that the large waves overtake waves with smaller amplitudes, "gobbling-up" the smaller amplitude wave in the process, see figure 8.4.4 . This process leads to a wave with increasing amplitude. At some point the amplitude has increased so much that the crest of the wave may be sucked up to the top of the pipe. This then may lead to the formation of a slug but only when the conditions are such that a stable slug can exist.

## 8.5 Exercises

**Exercise 8.1** In this exercise we consider the influence of surface tension on the eigenvalues of the quasi-linear system of equations. We start with the momentum equations as in table 4.1 and we remove the interfacial pressure in the same way as the procedure leading to (8.3.6). When surface tension effects are not neglected, show that the pressure condition at the gas-liquid interface yields an additional term equal to  $\sigma \partial^3 h / \partial x^3$ . Neglect the momentum diffusion terms ( $\mu_L^e = \mu_G^e = \mathbf{0}$ ) and set the profile coefficients equal to  $\mathbf{c}_L = c_G = 1$ . In order to obtain a system of equations such as (8.3.1) (a system containing only first-order derivatives) define  $Q = \frac{\partial h}{\partial x}$  and  $R = \frac{\partial Q}{\partial x}$ . Introduce the vector  $\Psi = (h, u_L, u_G, Q, R)^T$  and show that the matrices  $\mathbf{A}$  and  $\mathbf{B}$  become

$$\mathbf{A} = \begin{bmatrix} 1 & 0 & 0 & 0 & 0 \\ 1 & 0 & 0 & 0 & 0 \\ 0 & \rho_L & -\rho_G & 0 & 0 \\ 0 & 0 & 0 & 0 & 0 \\ 0 & 0 & 0 & 0 & 0 \end{bmatrix} \quad \text{and} \quad \mathbf{B} = \begin{bmatrix} 0 & H_L & 0 & 0 & 0 \\ 0 & 0 & -H_G & 0 & 0 \\ 0 & \rho_L u_L & -\rho_G u_G & 0 & -\sigma \\ 1 & 0 & 0 & 0 & 0 \\ 0 & 0 & 0 & 1 & 0 \end{bmatrix}$$

in which  $H_L = A_L/s_I$  and  $H_G = A_G/s_I$ . Show that the eigenvalue problem  $\det(\mathbf{A} - \lambda \mathbf{B})$  has the characteristic equation  $\lambda^5 \sigma H_L H_G = 0$ . What is the implication of this characteristic equation with respect well-posedness of the equations which include surface tension effects (hint, it is in addition important to determine  $\det(\mathbf{A})$  ).

**Exercise 8.2** Consider a layer of shallow water of infinite horizontal extent. The height of the water layer is denoted by  $h(x, t)$  and the velocity in the positive  $x$ -direction is

denoted by  $v(x, t)$ . On neglecting wall shear stresses and horizontal pressure gradients, show using the control volume method (ref. 4.8), that mass and momentum conservation equations are of the form

$$\frac{\partial h}{\partial t} + \frac{\partial}{\partial x} (hv) = 0$$

$$\rho \frac{\partial v}{\partial t} + \rho v \frac{\partial v}{\partial x} + \rho g \frac{\partial h}{\partial x} = 0$$

Compute the characteristics and hence show that the system of equations given above is hyperbolic. Write down the linearised equations by starting with steady state values  $\bar{h}$  and  $\bar{v}$ , and considering perturbations of the form  $h(x, t) = \bar{h} + \tilde{h}(x, t)$  and  $v(x, t) = \bar{v} + \tilde{v}(x, t)$ . In order to study the properties of interfacial waves we take  $\tilde{h}(x, t) = h_o e^{i(kx - \omega t)}$  and likewise for  $\tilde{v}$ . By substituting these forms of  $\tilde{h}$  and  $\tilde{v}$  into the linearised equations, show that the following dispersion relations is obtained

$$(k\bar{v} - \omega)^2 = k^2 g \bar{h}$$

Is it possible to have unstable surface waves?

**Exercise 8.3** Start with the conservation equations in Table 4.1. Take the profile coefficients  $c_L = c_G = 1$  and assume that axial diffusion terms can be neglected. Eliminate the pressure gradient between the two momentum equations (like in (8.3.6)) but do not neglect the surface tension term in the interfacial pressure condition. Show that a new term equal to  $\sigma \partial^3 h / \partial x^3$  is obtained in the reduced momentum equation.

**Exercise 8.4** Show that for the case of an inviscid flow shearing flow, the jump condition (2.3.4) can be written like.

$$\frac{\partial \eta}{\partial t} + U_1 \frac{\partial \eta}{\partial x} = \left. \frac{\partial \tilde{\phi}_1}{\partial z} \right|_{z=h}$$

## 9 Flow Regime Transitions

### 9.1 Introduction

One of the special features of multiphase flow is the fact that the structure of the flow may alter drastically when either the liquid or the gas volume flow rates is changed. In Figure 9.1.1 an example is shown of what is known as a *flow regime map*. This particular flow regime map composed by Mandhane *et al* (1974) shows the different flow patterns that may be observed in horizontal gas/liquid flow. While the flow regime map shown in figure 9.1.1 has its limitations (flow regime transitions are not only determined by superficial velocities), it gives a nice qualitative overview of changes in the flow structure that may occur when the volume flow of liquid or gas entering the pipe is changed.

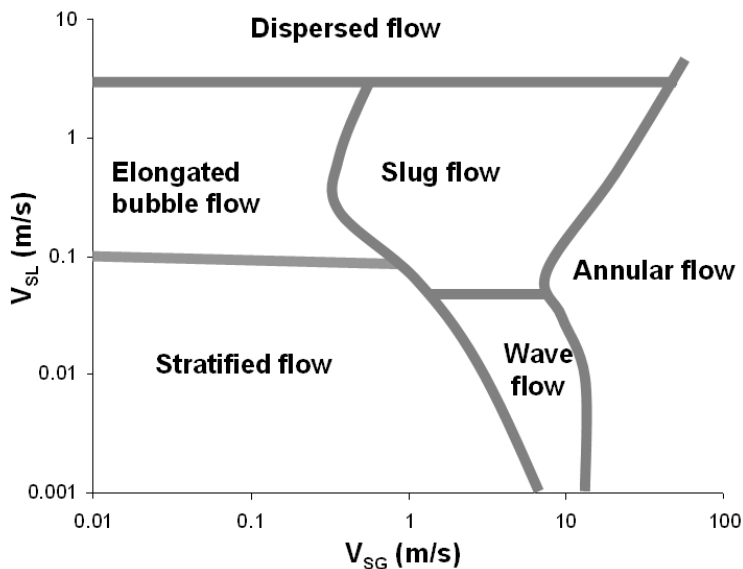


Figure 9.1.1: The flow regime map as proposed by Mandhane *et al* (1974).

As an example, consider the case in which the superficial gas velocity is held constant at a low value ( $< 1 \text{ m s}^{-1}$ ). For small values of the superficial liquid velocity figure 9.1.1 shows that we are in the stratified flow region: a film of liquid runs along the bottom of the pipe. Keeping the superficial gas velocity constant but increasing the superficial liquid velocity, figure 9.1.1 shows that at some point we will enter a new flow regime which is characterized by intermittency. What happens physically is that the liquid level rises with increasing superficial liquid velocities. This rise in liquid level leaves a progressively smaller flow area for the gas phase which implies increasing gas velocities. Due to shear stresses at the gas-liquid interface, waves will develop at the interface and at some point the wave heights become so large that one of the wave crests will reach the top of the pipe. Once this happens, liquid slugs may form. It will be clear that the transition from stratified to intermittent flow may be due to hydrodynamic instabilities that form at the gas-liquid interface. These instabilities were studied in the previous chapter but it turns out linear wave theory is not able to predict the transition from stratified to slug flow due to the importance of nonlinear effects. This implies that more heuristic arguments are used to obtain the final transition closure. The flow regime transitions as given below are formulated by Taitel & Dukler (1976). As we will see, these criteria are partly based on physical reasoning and partly based on experimental observations in small diameter pipes with air and water. As such care has to be taken when applying these criteria to other systems.

## 9.2 The transition criteria for (near) horizontal flow

The transition for *stratified smooth to stratified wavy flow* is based on a model for wave growth developed by Jeffreys (1926). Jeffreys shows that waves will grow when the energy due to external forcing exceeds the rate of dissipation of energy in the liquid phase.

$$c(u_G - c)^2 > \frac{1}{s} \times \frac{4\mu_L \Delta \rho g \cos \beta}{\rho_L \rho_G} \quad (9.2.1)$$

Under the assumption that the gas velocity is large compared with the wave velocity, it can be shown that the transition condition can be written like

$$u_G > \frac{1}{\sqrt{s}} \times \left[ \frac{4\mu_L \Delta \rho g \cos \beta}{\rho_L \rho_G u_L} \right]^{1/2} \quad (9.2.2)$$

The parameter  $s$  is a heuristic constant called the "sheltering coefficient" and is typically in the range 0.01 – 0.03. Taitel & Dukler use  $s = 0.01$ .

The transition from *stratified to slug (intermittent) flow* is based on wave stability arguments. As a starting point we take the stability condition (8.2.16) with phase 1 denoting the liquid phase and phase 2 denoting the gas phase. A slight generalisation of (8.2.16) tells us that the flow is unstable when

$$u_G - u_L > C \times \left[ \left( \frac{A_G}{\rho_G} + \frac{A_L}{\rho_L} \right) \frac{\Delta \rho g \cos \beta}{s_I} \right]^{1/2} \quad (9.2.3)$$

We have seen in the previous chapter that this stability condition in the case with  $C = 1$  may be associated with the appearance or roll waves, not slug flow. Hence, a modification of equation (9.2.3) is required in order to capture the transition to slug flow. We proceed as follows. For high liquid levels, the area available to the gas phase is small. Hence, even relatively small-amplitude waves may reduce the flow area of the gas significantly. The reduction in flow area leads to an increase in the gas velocity above the wave crest (due to mass conservation) which, in turn, leads to a reduction in the dynamic pressure above the crest. It is argued that this reduction in the pressure leads to the wave crest being "sucked-up" to the top of the pipe. This Bernoulli effect is incorporated in the stability condition given in (9.2.3) by choosing the parameter like  $C = 1 - h/D$ . The liquid height  $h$  is obtained by solving the holdup equation or it may be approximated using the dimensionless holdup equation and the Martinelli parameter is described in section 5.5. In the limit where  $u_G \gg u_L$  and  $\rho_G \ll \rho_L$  (9.2.3) reduces to the transition criteria for stratified to slug flow as formulated by Taitel & Dukler (1976). When there is not sufficient liquid in the pipe, it will not be possible to generate sufficiently large waves which generate a slug even though the the gas velocity exceeds the critical value for the transition to slug flow as given above. In this case it is argued that a transition from *stratified to annular flow* occurs. Thus, annular flow is achieved when the gas velocity exceeds the critical value as specified in (9.2.3) while at the same time the liquid holdup satisfies

$$\frac{h}{D} \leq 0.35 \quad (9.2.4)$$

The liquid height is, once again found by solving the holdup equation.

When considering the transition from *slug flow to dispersed bubble flow* it is necessary to consider the relative size of the dynamic forces due to turbulent fluctuations and bouyancy forces acting on the Taylor bubble in the slug. When the turbulent fluctuations exceed bouyancy forces it may be argued that the large Taylor bubble is broken up into

smaller bubbles, indicating the transition to dispersed bubbly flow. Taitel & Dukler show that happens when

$$u_L > \left[ \frac{4A_G(\rho_L - \rho_G)g \cos \beta}{s_I \rho_L f_L} \right]^{1/2}$$

where  $f_L$  denotes the liquid friction factor. The flow regime boundaries as predicted by the equations outlined above yield a flow regime map as given in the figure below. The Froude number on the vertical axis in the figure is defined via  $F = \sqrt{\frac{\rho_G}{\Delta \rho}} \frac{U_{SG}}{\sqrt{gD} \cos \beta}$ .

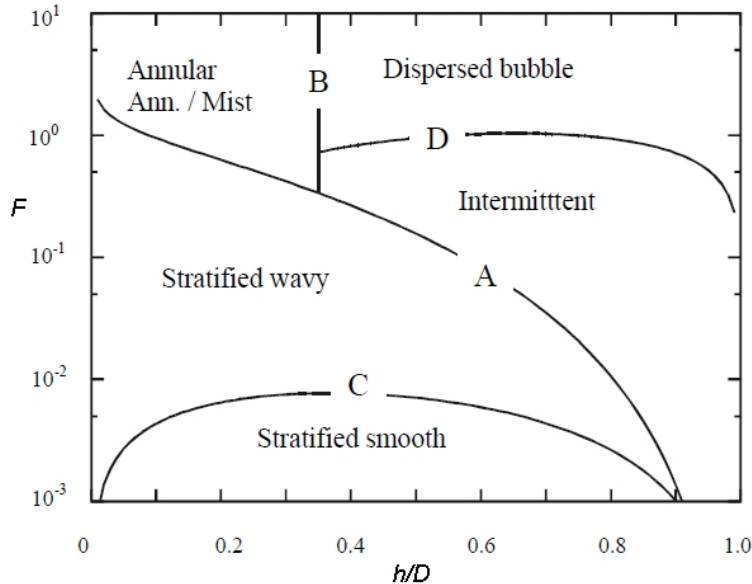


Figure 9.2.1: Flow regime map based on dimensionless liquid height and Froude number.

### 9.3 The transition criteria for vertical flow

We have seen (figure 3.2.3) that the flow pattern map changes dramatically when the pipe inclination increases from horizontal to vertical. A whole new flow regime (churn flow) is present in the case of vertical flow. Clearly, separate criteria for flow regime transitions are required. Here we present the often-used criteria as formulated by Taitel *et al* (1980). For vertical flow we start with the case where the flow is liquid dominated and where we may assume that gas is dispersed in the liquid phase. The gas velocity is in the case is given by

$$u_G = u_L + u_{drift}$$

When the volume fraction of the gas phase is equal to  $\phi$  then  $\phi u_G = U_{SG}$  and  $(1-\phi)u_L = U_{SL}$ . Using these results in the above equation we obtain

$$U_{SL} = \frac{1-\phi}{\phi} U_{SG} - (1-\phi) \times u_{drift}$$

If we now can find an expression for the drift velocity as well as for the volume fraction  $\phi$  at which the transition from dispersed bubble flow to slug flow occurs, the above equation

will boundary in the flow regime map. Experiments show that bubble collisions (and thereby bubble coalescence events) increase rapidly when  $\phi \simeq 0.25$  when liquid velocities are low. The bubble rise velocity for medium sized bubbles is found experimentally (Harmathy, 1960) to be

$$u_{drift} = 1.53 \left[ \frac{g(\rho_L - \rho_G)\sigma}{\rho_L^2} \right]^{1/4}$$

Hence, the transition boundary between *dispersed bubble flow* and *slug flow* at low liquid velocities is given by the equation

$$U_{SL} = 3U_{SG} - 1.15 \left[ \frac{g(\rho_L - \rho_G)\sigma}{\rho_L^2} \right]^{1/4}$$

At high liquid velocities it is found that the volume fraction at which bubble coalescence events become important, increases to  $\phi \simeq 0.52$ . The reason for this increase being that bubbles are much smaller due to the action of turbulent forces and, as a consequence, coalescence becomes more difficult. At these large liquid velocities, the drift velocity becomes insignificant so that the transition between dispersed bubble flow and slug flow at low liquid velocities is given by

$$U_{SL} = 0.92U_{SG}$$

The boundary between high and low liquid velocities is determined by the balance between the maximum bubble size as a result of turbulent fluctuations,  $d_{max}$  say, and the critical bubble size above which no spherical bubbles can exist,  $d_{crit}$  say. In section 6.4 it was shown how  $d_{max}$  can be found while experimental evidence yields

$$d_{crit} = \left[ \frac{0.4\sigma}{(\rho_L - \rho_G)g} \right]^{1/2}$$

Taking  $d_{max} = d_{crit}$ , Taitel *et al* (1980) show that the boundary between high and low liquid velocities is given by

$$U_{SL} + U_{SG} = 4.0 \times \frac{D^{0.429}(\sigma/\rho_L)^{0.089}}{(\mu_L/\rho_L)^{0.072}} \left[ \frac{g(\rho_L - \rho_G)}{\rho_L} \right]^{0.446}$$

The transition boundary between *slug flow* and *churn flow* is based on heuristic arguments related to the stability of liquid slugs in vertical flow. Experiments show that short slugs are unstable, falling back to merge with the slug coming from below (this is essentially a description of churn flow). Due to this process, the liquid slug length as well as the Taylor bubble size will increase steadily. At some point the slug length has increased so much in size that a stable liquid film can exist between two consecutive slugs. It is argued that this is achieved when the Taylor bubbles are so far apart that they will no longer be influenced by each other's wake. Taitel *et al* (1980) introduce the concept of the entrance length and argue that over the distance of the entrance length, unstable churn-like flow will turn into stable slug flow. It is shown that the entrance length  $L_E$  is related to the volume flow rate of gas and liquid via

$$\frac{L_E}{D} = 40.6 \left( \frac{U_{SL} + U_{SG}}{\sqrt{gD}} + 0.22 \right)$$

With the entrance length as a free parameter, the above relation indicates the final transition boundary.

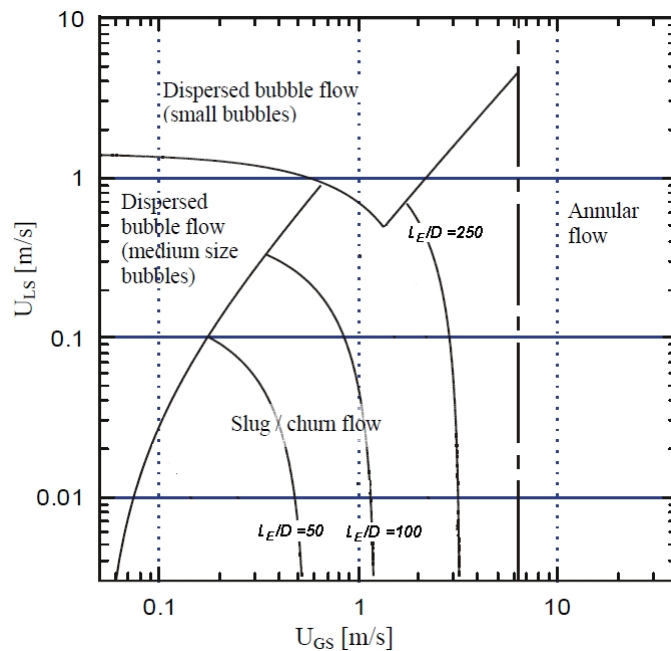


Figure 9.3.1: Flow regim transition boundaries for vertical gas-liquid flow.

## 10 High-inclination multiphase flow

### 10.1 Introduction

To be written

### 10.2 Upward flow

Manera et al IJMF 2006 experiments vertical flow.  
Mayor et al Chem Eng Sci 2008

### 10.3 Downward flow

Ishii et al IJMF 30 2004, p779

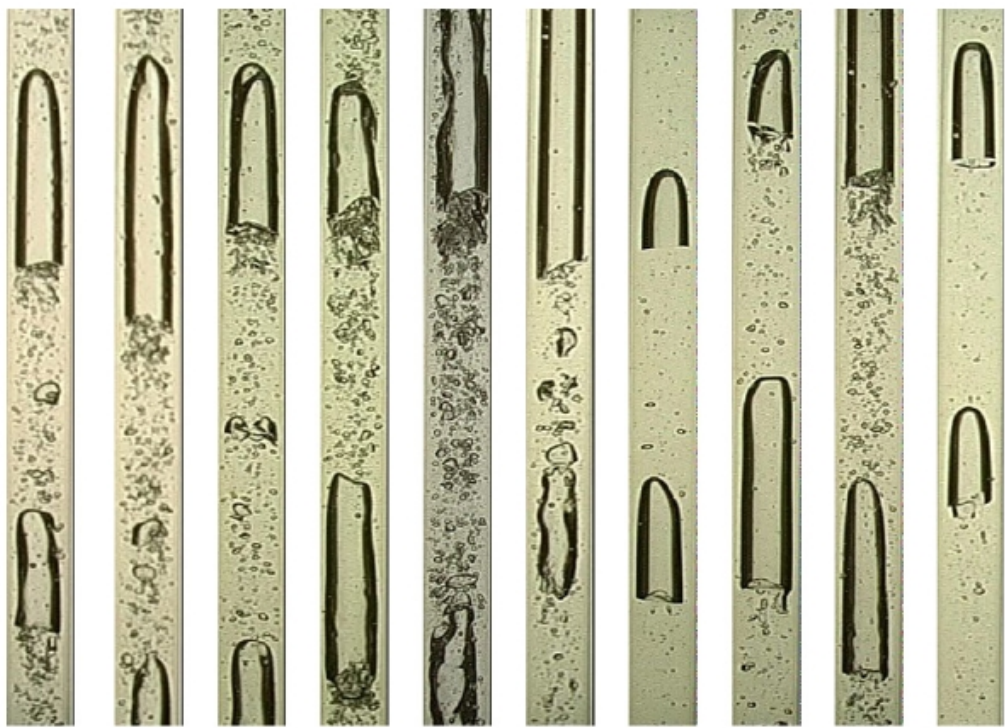


Figure 10.2.1: Mayor et al Chem Engng Sci 63 (2008)

## Appendix A

### Geometrical Relations

In stratified multiphase pipe flow one often has to find expression for the cross sectional areas, interfacial perimeters etc. given the position of the interface in a circular pipe. Relevant geometrical expression are listed here. We consider the cross section of a pipe as show in figure 10.3.1. The pipe has a diameter equal to  $D$ . Using some elementary trigonometry gives us with the following relations for:

The interfacial perimeter:

$$s_I = D \sin \delta$$

The interfacial height above the pipe bottom:

$$h = \frac{1}{2}D(1 - \cos \delta)$$

The perimeter wetted by the liquid phase:

$$s_L = D\delta$$

The perimeter wetted by the gas phase:

$$s_G = D(\pi - \delta)$$

The cross-sectional area of the liquid phase:

$$A_L = \frac{1}{4}D^2(\delta - \sin \delta \cos \delta)$$

The cross-sectional area of the gas phase:

$$A_G = \frac{1}{4}D^2(\pi - \delta + \sin \delta \cos \delta)$$

In a number of cases the geometrical quantity  $A'_L = \frac{d}{dh}A_L$  appears. Using the definitions given above it is easily shown that  $A'_L = D \sin \delta = s_I$ .

The liquid holdup can be expressed in terms of the wetted half-angle  $\delta$ , via

$$H_L = \frac{A_L}{A} = \frac{1}{\pi}(\delta - \sin \delta \cos \delta)$$

When solving the holdup equation, it is found that we have to know the wetted half-angle  $\delta$  in terms of the liquid holdup, that is  $\delta = \delta(H_L)$ . While the equation above can

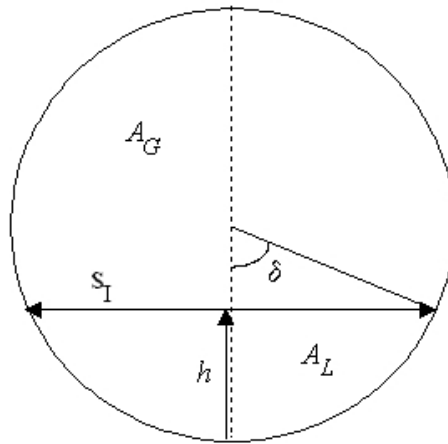


Figure 10.3.1: Stratified flow geometry in circular pipe.

easily be solved numerically, an explicit approximation is provided by the expression

$$\begin{aligned}\delta &= \pi H_L + \left(\frac{3\pi}{2}\right)^{1/3} \left[ 1 - 2H_L + H_L^{1/3} - (1 - H_L)^{1/3} \right] \\ &\quad - \frac{1}{200} H_L (1 - H_L) (1 - 2H_L) (5 - 8H_L + 8H_L^2)\end{aligned}$$

which is accurate to within  $\pm 5 \times 10^{-5}$  radians for  $0 \leq H_L \leq 1$  as shown by Biberg (1999).

## Appendix B

### Some commonly-used interfacial friction factors

In section 5.4 three examples of interfacial friction factors are mentioned. However, in the multiphase flow literature, a much larger number of different interfacial friction factors has been published. While it is difficult to provide a complete list of all the interfacial friction factors which are in use, the list below gives an indication of the wide variety of friction factors which have been proposed by different researchers. Espedal (1998) and Khor (1998) have both listed interfacial friction factors proposed by various researchers. A number of the proposed friction factors are given below. Note that we have consistently used Darcy-type friction factors.

The simplest expression for the interfacial friction factor is to assume that it is simply a constant, thus

$$f_i = C_0$$

Shoham and Taitel (1984) have suggested taking  $C_0 = 0.0568$ . A number of researchers have proposed an interfacial friction factor of the form

$$f_i = C_1 + C_2 \times \text{Re}_L$$

in which  $C_1$  and  $C_2$  are constants and the Reynolds number is computed via  $\text{Re}_L = Q_L \rho_L / \mu_L$  with  $Q_L$  denoting the volume flow per unit width of the channel. Different values of the constants have been proposed, some of these are listed in the table below

$C_1$	$C_2$	Reference
0.0524	$0.92 \times 10^{-5}$	Linehan (1968)
0.022	$10.4 \times 10^{-5}$	Tsiklauri <i>et al</i> (1979)
0.084	$0.56 \times 10^{-5}$	Kim <i>et al</i> (1985)

An interfacial friction factor which is directly related to the gas-wall friction factor via

$$f_i = C_3 \times f_G$$

has also been proposed. Taitel & Dukler (1976) simply choose  $C_3 = 1$  but there are indications that this choice leads to an under-prediction of the interfacial shear. For this reason, Kawaji *et al* (1987) proposed using  $C_3 = 3$  while Spedding *et al* (1990) used  $C_3 = 4$ . In both these cases, the gas friction factor was based on a Reynolds number computed using the superficial gas velocity. An analysis of data from large diameter pipes (Crowley & Rothe, 1988) shows that agreement between measurements and theory can generally be obtained when  $1 < C_3 < 10$ . However, when the liquid phase becomes very viscous such that laminar flow is obtained in the liquid phase, the interfacial friction factor decreases dramatically as a result of the reduction in the interfacial roughness. Spedding *et al* (1990) suggest that in that case  $C_3 = 0.6$ .

Models in which the parameter  $C_3$  is a function of the liquid holdup  $H_L$  have also been suggested. Stratified air-water experiments lead Crouzier (1978) to suggest

$$C_3 = 1 + 204H_L^{1.42}$$

while oil-water experiments lead Mouly (1979) to suggest

$$C_3 = 2.6 + 87.2H_L^{2.3}$$

It is clear that the structure of the gas-liquid interface will change when the relative velocity of the gas and the liquid increases. For low relative velocities, the interface will be fairly smooth. However, as the relative velocity increases the interface becomes increasingly rough due to the appearance of waves (both short-wavelength capillary waves and longer-wavelength, roll waves will be present). Obviously, the rougher the interface, the larger the interfacial shear stress. It is natural to expect that the interfacial friction factor reflects this change in the interfacial structure. The interfacial friction factor as proposed by Andreussi & Persen (1987) incorporates changes in the interfacial roughness by modifying constant  $C_3$  according to

$$C_3 = \begin{cases} 1 & \text{for } Fr_G < 0.36 \\ 1 + 29.7(Fr_G - 0.36)^{0.67}H_L^{0.2} & \text{for } Fr_G > 0.36 \end{cases}$$

in which the gas Froude number is defined via  $Fr_G = U_{SG}\sqrt{\frac{\rho_G s_I}{(\rho_L - \rho_G)A_{GG}g\cos\theta}}$ . Andritsos & Hanratty (1987) have proposed a similar relation in which also  $C_3 = C_3(H_L, U_{SG})$ . Interfacial roughness effects have also been used more explicitly in calculating the interfacial friction factor. For example, Hamersma & Hart (1987) suggest that the apparent interfacial roughness, denoted by  $k_i$ , can be related to the mean liquid height via

$$k_i = 2.3h_L$$

This value of the roughness is subsequently used in the Colebrook friction factor (see Table 2.3). Similar approaches in which the interfacial roughness has been evaluated by alternative (more elaborate) means have been proposed by for example Bendiksen *et al* (1989), Hart *et al* (1989) and Srichai (1994).

Common for all of the interfacial friction factors which are mentioned here, is that they contain specific constants which are obtained by testing against (often limited) data sets. An alternative approach is therefore, to use all the data which is available to obtain a correlation based on dimensionless groups which are assumed to be relevant. At the start of chapter 3 we showed that dimensional analysis in multiphase flow has had limited success due to the large number of dimensionless groups which can be constructed. Even so, Xiao (1990) has obtained the following correlation based on analysis of data in a data bank for stratified flow

$$f_i = 0.212 \times N_G^{0.23} N_L^{0.202} N_D^{-0.46} N_\mu^{0.076}$$

in which the dimensionless groups are defined as follows  $N_G = u_G \sqrt[4]{\frac{\rho_G}{g\sigma}}$ ,  $N_L = u_L \sqrt[4]{\frac{\rho_L}{g\sigma}}$ ,  $N_D = D \sqrt{\frac{\rho_L g}{\sigma}}$  and  $N_\mu = \mu_L \sqrt[4]{\frac{g}{\rho_L \sigma^3}}$ . The success of this type of approach is clearly dependent on the range of the data in the data bank which is used and on how successful one is in selecting relevant dimensionless groups.

## Appendix C

### Closure relations for slug body holdup

Closure relations for the liquid holdup in the slug body can roughly be divided into two groups: those which are purely based on curve fitting based on a given set of data and those in which physical modelling is applied. The relations proposed by Gregory *et al* (1978), Malnes (1982), Ferschneider (1983), Abdul-Majeed (1999) and Ooi (2002) are all examples of the curve-fitting approach. The correlation for the slug bold holdup  $H_L$  proposed by Gregory et al (1978) is given by

$$H_L = \left( 1 + \left( \frac{U_{mix}}{U_1} \right)^{1.39} \right)^{-1}$$

in which the velocity scale  $U_1 = 8.66\text{ms}^{-1}$  and  $U_{mix} = U_{Sl} + U_{SG}$ . The data was based on experiments in air-light oil experiments in 25.8 and 52.1mm pipes. On the basis of the same data set, Malnes (1982) proposed the following relation

$$H_L = \frac{1}{1 + U_{mix}/U_2}$$

in which  $U_2 = 83 \left( \frac{g\sigma}{\rho_L} \right)^{1/4}$ . Ferschneider (1983) conducted experiments in a 146mm pipe with a condensate/natural gas system at 15 bars. On the basis of these experiments he proposed the relation

$$H_L = \left( 1 + \frac{U_{mix}^2}{(\Delta\rho/\rho_L)gD} \frac{Bo^\beta}{C_2} \right)^{-2}$$

in which the Bond number  $Bo = \Delta\rho g D^2 / \sigma$  with  $\Delta\rho = \rho_L - \rho_G$ . The parameters  $\beta$  and  $C_2$  are not specified. Based on an analysis of 423 data points Abdul-Majeed (1999) proposed the following relation

$$H_L = (1.009 - C_{AM} U_{mix}) \times A(\theta)$$

in which  $C_{AM} = 0.006 + 1.3377\mu_G/\mu_L$  and  $A(\theta) = \max(1, 1 - \sin\theta)$ . Abdul-Majeed explicitly noted the weak dependence of the slug body holdup on both pipe diameter and surface tension. Ooi (2002) performed an analysis of 180 data points derived from hydrocarbon/natural gas and air/water experiments with performed at pressures in the range from 1-90bar and in horizontal pipes with diameters equal to 0.0779m and 0.29m. The correlation which fitted best to the data set is given by

$$H_L = 1 - 0.474 \times Ca^{0.88} Re^{0.2} \left( \frac{\rho_G}{\rho_L} \right)^{0.1} \left( \frac{\mu_G}{\mu_L} \right)^{0.3}$$

in which the Capillary number  $Ca = V_{mix}\mu_L/\sigma$  and the Reynolds number  $Re = \rho_L V_{mix} D / \mu_L$ .

An attempt to model some of the basic physics governing gas entrainment was presented by Andreussi & Bendiksen (1989). By demanding mass balance for the liquid phase and equating the net loss rate of bubbles at the tail of the slug to the net production rate at the slug front, the following relation for slug body holdup was derived

$$H_L = \begin{cases} 0 & \text{if } V_{mix} \leq U_{crit} \\ \frac{U_{mix} - U_{crit}}{(U_{mix} + U_{MO})^n} & \text{if } V_{mix} > U_{crit} \end{cases}$$

In here,  $U_{crit}$  denotes the limiting velocity below which the liquid film is continuously merged into the slug without swirl motion and so no bubbles are entrained. The limiting velocity is given by  $U_{crit} = 2.6 \left(1 - 2 \left(\frac{D_{ref}}{D}\right)^2\right) \sqrt{gD}$  where  $D_{ref} = 0.025\text{m}$ . In addition  $U_{MO} = 1200(1 - \frac{1}{3} \sin \theta) Bo^{-3/4} \sqrt{\Delta\rho/\rho_L g D} + 5v_T$  (with  $v_T$  denoting the translational velocity of the slug, see section 7.2.1 ) and the exponent  $n = 1 - 3\rho_G/\rho_L$ . Chen *et al* (1997) developed a model which is based on the notion that the turbulent kinetic energy of the fluid entering the slug front should be related to the surface energy of the bubbles that are entrained at the slug front. The following relation for the liquid holdup in the slug body was derived

$$\frac{(1 - H_L)^{3-n}}{H_L} = 12.65 \frac{Y_M}{Bo^{1/2}}$$

in which  $Y_M = \Delta\rho g \times \left[ \frac{2C_L}{D} \left( \frac{\rho_L D U_{mix}}{\mu_L} \right)^{-0.2} \rho_L U_{mix}^2 \right]^{-1}$  with  $C_L = 0.046$ .

## Appendix D

### Correlations for the slug frequency

Quite a few relations have been proposed that relate the slug frequency to different parameters that are perceived to be relevant. In many cases the relations that are obtained are curve fits where no attempt has been made to obtain a dimensionally-correct relation. This means that the extrapolation properties of these realtions is uncertain.

Gregory & Scott (1969) performed experiments in a 19mm horizontal pipe with carbon dioxide and water as the working fluids. The data yields a correlation for the slug frequency  $f_s$  of the form

$$f_s = 0.0226 \left[ \frac{U_{SL}}{gD} \left( \frac{19.75}{U_{mix}} + U_{mix} \right) \right]^{1.2}$$

Experiments with air and water in a 42mm horizontal pipe lead Heywood & Richardson (1979) to the following expression for the slug frequency

$$f_s = 0.0434 \left( \frac{U_{SL}}{U_{mix}} \left[ \frac{2.02}{D} + \frac{U_{mix}^2}{gD} \right] \right)^{1.02}$$

The experiments of both Gregory & Scott and Heywood & Richardson showed a minimum in the observed slug frequency when plotting the frequency as a function of the mixture velocity. Zabaras (1990) reports the Shell slug frequency correlation which is of the form

$$f_s = \sqrt{\frac{g}{D}} \left( A + B \left[ (Fr_L + Fr_G)^{0.1} - 1.17 Fr_L^{0.064} \right] \right)^2$$

in which  $Fr_k = U_{Sk}/\sqrt{gD}$  with  $k = L, G$ ,  $A = 0.048 Fr_L^{0.81}$  and  $B = 0.73 Fr_L^{2.34}$ . This correlation is based on the Heywood and Richardson (1979) data set containing data with only one pipe diameter. The diameter dependence as predicted by this correlation is thus uncertain. Hill & Wood (1990) present a relation in which the steady state liquid holdup  $H_L$  and the in-situ slip velocity  $v_G - v_L$  is included, namely

$$f_s = 2.74 \times \frac{v_G - v_L}{D} \frac{H_L}{1 - H_L}$$

The steady state liquid holdup as well as the in-situ gas and liquid velocities  $v_G$  and  $v_L$  are computed using the dimensionless holdup equation based on the Martinelli parameter as outlined in section 5.5. Based on wave stability arguments, a similar slug frequency relation is obtained by Tronconi (1990), namely

$$f_s = 0.61 \times \frac{v_G}{D} \frac{1}{1 - h/D} \frac{\rho_G}{\rho_L}$$

in which  $h$  denotes the equilibrium stratified liquid height. Based on air-water experiments in horizontal pipes with 3 different diameters, Nydal (1991) reports the frequency correlation

$$f_s = 0.088 \frac{(U_{SL} + 1.5)^2}{gD}$$

High pressure experiments in horizontal pipes lead Manolis *et al* (1995) to modify the Gregory & Scott correlation, giving

$$fs = 0.0037 \frac{U_{SL}}{gD} \left( \frac{U_2^2 + U_{mix}^2}{U_{mix}} \right)^{1.8}$$

in which  $U_2 = 5\text{m/s}$ . Zabaras (2000) has also modified the Gregory & Scott correlation by including the influence of pipe inclination. His analysis of an extended data set suggests

$$fs = 0.0226 \left( \frac{U_{SL}}{gD} \right)^{1.2} \left( \frac{19.75}{U_{mix}} + U_{mix} \right)^{1.2} [0.836 + 2.75 \sin^{1/4}(\theta)]$$

An analysis of large-scale field and laboratory data lead Shea *et al* (2004) to the following relation

$$fs = 0.47 \frac{U_{SL}^{0.75}}{D^{1.2} L_p^{0.55}}$$

in which  $L_p$  denotes the pipe length (measured from the pipe inlet). Note that this is the only correlation in which the pipe length is included. Experiments with high-viscosity oils in a 50mm ID, horizontal pipe, leads Gockal *et al* (2009) to the correlation

$$fs = 2.816 \times \frac{U_{SL}}{D} \frac{1}{N_f}$$

in which the ratio between gravity and viscous forces is given by  $N_f = \frac{D^{3/2} \sqrt{\rho_L \Delta \rho g}}{\mu_L}$ . This is the only relation which suggests a linear dependence of the slug frequency on the liquid viscosity.

## References

- Abdul-Majeed G. H. 1999 Liquid slug holdup in horizontal and slightly inclined two-phase slug flow. *J. Petrol. Sci. Eng.*, **27**, 27-32.
- Akai, M, Inoue, A., Aoki, S. & Endo, K. 1980 A co-current stratified air-mercury flow with a wavy interface. *Int. J. Multiphase Flow*, **6**, 173-190.
- Angeli, P. & Hewitt, G.F. 2000a Flow structure in horizontal oil-water flow. *Int. J. Multiphase Flow*, **26**, 1117-1140.
- Angeli, P. & Hewitt, G.F. 2000b Drop size distributions in horizontal oil-water dispersed flows. *Chem. Eng. Sci.*, **55**, 3133-3143.
- Amundsen, L., Schulkes, R. & Melaaen, M. 2009 Oil-water flow: experiments and model development. Proceedings of 14th International Conference on Multiphase Production Technology. Cannes, France.
- Andersson, R. & Andersson, B. 2006 On the breakup of fluid particles in turbulent flows. *AIChE J.* **52**(6), 2020-2030.
- Andreussi P. & Bendiksen K. 1989 An investigation of void fraction in liquid slugs for horizontal and inclined gas-liquid pipe flow. *Int. J. Multiphase Flow*, **15**(6), 937-946.
- Andritsos, N. & Hanratty, T.J. 1987 Interfacial instability for horizontal gas-liquid flows in pipes. *Int. J. Multiphase Flow*, **13**, 583-603.
- Banerjee, S. & Chan, A.M.C 1980 Separated flow models. *Int. J. Multiphase Flow*, **6**, 1-24.
- Barnea, D., Shoham O. & Taitel, Y. 1982, Flow pattern transition for downward inclined two phase flow; horizontal to vertical. *Chem. Engng Science*, **37**(5), 735-740.
- Barnea, D. & Taitel, Y. 1993 Kelvin-Helmholtz stability criteria for stratified flow: viscous versus non-viscous (inviscid) approaches. *Int. J. Multiphase Flow* **19**(4), 639-649.
- Batchelor, G.K. 1967 *An introduction to fluid mechanics*. Cambridge University Press.
- Batchelor, G.K. 1972 Sedimentation in a dilute suspension of spheres. *J. Fluid Mech.* **52**, 245-268.
- Batchelor, G.K. 1977 The effect of Brownian motion on the bulk stress in a suspension of spherical particles. *J. Fluid Mech.* **83**, 97-117.
- Batchelor, G.K. & Wen, C-S. 1982 Sedimentation in a dilute polydisperse system of interacting spheres. Part 2. Numerical results *J. Fluid Mech.* **124**, 495-528.
- Beggs, H.D. & Brill, J.P. 1973 A study of two-phase flow in inclined pipes. *Journal of Petroleum Technology*, May 1973, 607.
- Bendiksen, K.H. 1984 An experimental investigation of the motion of long bubbles in inclined tubes. *Int. J. Multiphase Flow* **10**(4), 467-483.
- Bendiksen, K.H. 1985 On the motion of long bubbles in vertical tubes. *Int. J. Multiphase Flow* **11**, 797-812.
- Bendiksen, K.H., Malnes, D., Moe, R. & Nuland, S. 1989 The dynamic two-fluid model OLGA: theory and application. *SPE 19451*.

- Bendiksen, K., Brandt, I., Fuchs, P., Linga, H., Malnes, D. & Moe, R. 1986 Two-phase flow research at SINTEF and IFE. Some experimental results and a demonstration of the dynamic two-phase simulator OLGA. Presented at The Offshore Northern Seas Conf., Stavanger, Norway.
- Benjamin, T.B. 1968 Gravity currents and related phenomena. *J. Fluid Mech.* **31**(2), 209-248.
- Biberg, D. 1998. A simple friction model for two-phase stratified pipe flow. *3rd Int. Conf. Multiphase Flow ICMF'98, Lyon, France.*
- Biberg, D. 1999 An explicit approximation for the wetted angle in two-phase stratified pipe flow. *Can. J. Chem. Engng.* **77**(6), 1221-1224.
- Biberg, D. & Halvorsen, G. 2000 Wall and interfacial shear stresses in pressure driven two-phase laminar stratified pipe flow. *Int. J. Multiphase Flow* **26**, 1645-1673.
- Biberg, D. 2005 Mathematical models for two-phase stratified pipe flow. *PhD Thesis*, University of Oslo, Norway.
- Biberg, D. 2007 A mathematical model for two-phase stratified turbulent duct flow. *Multiphase Sci. Techn.* **19**(1), 1-48.
- Brauner, 2001 The prediction of dispersed flow boundaries in liquid-liquid and gas-liquid systems. *Int. J. Multiphase Flow* **27**, 885-910.
- Bremond, N., Thiam, A.R., & Bibette, J. 2008 Decompressing Emulsion Droplets Favors Coalescence *Phys. Rev. Lett.* **100**, 2008.
- Brennen, C.E. 2005 *Fundamentals of multiphase flow*. Cambridge University Press.
- Chen, X.T., Cai, X.D. & Brill, J.P. 1997 A general model for transition to dispersed bubble flow. *Chem. Eng. Sci.* **52**(23) 4373-4380.
- Choi, S.J., & Schowalter W.R. 1975 Rheological properties of non dilute suspensions of deformable particles. *Phys. Fluids* **18**, 420-427.
- Cohen, S.L. Hanratty, T.J 1968 Effects if waves at a gas-liquid interface on a turbulent air flow. *J. Fluid Mech.* **31**, 467-469.
- Collins, R., de Moraes, F.F., Davidson, J.F. & Harrison, D. 1978 The motion of large bubbles rising through liquid flowing in a tube. *J. Fluid Mech.* **89**, 497-514.
- Crouzier, O. 1978 Écoulement diphasiques gaz-liquide dans les conduites faiblement inclinées par rapport à l'horizontale. Thèse de 3e cycle,, Université de Paris VI.
- Crowe, C.T., Sommerfeld, M. & Tsuji, Y. 1998. *Multiphase flows with droplets and particles*. CRC Press LLC.
- Crowley, C.J. & Rothe, P.H. 1988 Assessment of mechanistic two-phase analysis method for gas-condensate pipelines. *PSIG Annual Meeting*, Toronto, Ontario, Canada.
- Di Felice, R. 1999 The sedimentation velocity of dilute suspensions of nearly monosized spheres. *Int. J. Multiphase Flow* **25**, 559-574.
- Drazin, P.G & Reid, W.H. 1981 *Hydrodynamic stability*, Cambridge Univeristy Press.
- Drew, D.A & Passman, S.L 1999 *Theory of multicomponent fluids*. Springer.
- Drew, D.A & Wood, R.T. 1985 Overview and taxonomy of models and methods for workshop on two-phase flow fundamentals.

- Dukler, A.E. & Hubbard, M.G. 1975 A model for gas-liquid slug flow in horizontal and near horizontal tubes. *Ind. Eng. Chem. Fundamen.* **14**(4), 337-347.
- Dumistrescu, D.T. 1943 Strömung an einer Luftbase in senkrechten Rohr. *Z. Angew. Math. Mech.* **23**, 139-149.
- Eilers, 1941 Die Viskosität von Emulsionen hochviskoser Stoffe als Funktion der Konzentration *Kolloid-Z.* **97**(3), 313-321.
- Einstein, A. 1906 A new determination of molecular dimensions. *Ann. Phys.* **19**, 289-306.
- Elseth, G. 2001 An experimental study of oil/water flow in horizontal pipes. PhD Norwegian University of Technology, Trondheim, Norway.
- Espedal, M. 1998 An experimental investigation of two-phase pipe flow at small inclinations. PhD Norwegian University of Technology, Trondheim, Norway
- Fabre, J. & Liné, A. 1992 Modelling of two-phase slug flow. *Ann. Rev. Fluid Mech.* **24**, 21-46.
- Fagundes Netto, J.R., Fabre, J. & Peresson, L. 1999 Shape of long bubbles in horizontal slug flow. *Int. J. Multiphase Flow*, **25**, 1129-1160.
- Ferschneider, G. 1983 Ecoulement diphasiques gaz-liquide à poches et à bouchons en conduites. *Revue Inst. Fr. Petrole*, **38**, 153.
- Gamio, J.C., Castor, J., Rivera, L., Alamilla, J., Garcia-Nocetti, F. & Aguilar, L. 2005 Visualisation of gas-oil two-phase flows in pressurised pipes using electrical capacitance tomography. *Flow Meas. Instrum.* **16**, 129-134.
- Gokcal, B., Al-Sarkhi, A.S., Sarica, C., Al-Safran, E.M. 2009 Prediction of slug frequency for high viscosity oils in horizontal pipes. SPE 124057. Annual Technical Conference and Exhibition, New Orleans, October, 2009.
- Grassi, B., Strazza, D., Poesi, P. 2008 Experimental validation of theoretical models in two-phase high-viscosity ratio liquid-liquid flows in horizontal and slightly inclined pipes. *Int. J. Multiphase Flow*, **34**, 950-965.
- Gregory, G.A., Nicholson, M.K. & Aziz, K. 1978 Correlation of the liquid volume fraction in the slug for horizontal gas-liquid slug flow. *Int. J. Multiphase Flow*, **4**, 33-39.
- Gregory, G.A. & Scott, D. S. 1969 Correlation of liquid slug velocity and frequency in horizontal cocurrent gas-liquid slug flow *AICHE J.* **15**, 833-835.
- Hamersma, P.J. & Hart, J. 1987 A pressure drop correlation for gas/liquid pipe flow with small liquid holdup. *Chem. Eng. Sci.* **42**(5), 1187-1196.
- Harmathy, T.Z. 1960 Velocity of large drops and bubbles in media of infinite or restricted extent. *AICHE J.* **6**, 281-288.
- Hart, J., Hamersma, P.J. & Fortuin, J.M. 1989 Correlations predicting frictional pressure drop and liquid holdup during horizontal gas-liquid pipe flow with small liquid holdup. *Int. J. Multiphase Flow*, **15**, 947-964.
- Hesketh, R.P., Fraser Russel, T.W. & Etchells, A.W. 1987 Bubble size in horizontal pipelines. *AICHE J.* **33**(4), 663-667.
- Heywood, N.I. & Richardson, J.F. 1979 Slug flow of air-water mixtures in a horizontal pipe: determination of liquid holdup by  $\gamma$ -ray absorption.

- Hibiki, T. & Ishii, M. 2003 One-dimensional drift-flux model and constitutive equations for relative motion between phases in various two-phase flow regimes. *Int. J. Heat Mass Transfer* **46**, 4935-4948.
- Hinze, J.O. 1955 Fundamentals of the hydrodynamic mechanism of splitting in dispersion processes. *AICHE J.* **1**(3), 289-295.
- Hinze, J.O. 1975. *Turbulence* (second ed.), McGraw-Hill.
- Holmås, H., Sira, T. Nordsveen, M., Langtangen, H.P. & Schulkes, R. 2008a Analysis of 1D incompressible two-fluid model including artificial diffusion. *IMA J. Appl. Math.*
- Holmås, H., Biberg, D., Johnson, J., Schulkes, R. & Sira, T. 2008b Stability analysis of the Biberg pre-integrated stratified two-phase flow model including profile factors. *Proc. 6th North-American Conf. Multiphase Technology*, Banff, Canada, 127-141.
- Huang, N & Bonn, D. 2007 Viscosity of a dense suspension in Couette flow. *J. Fluid Mech.* **590**, 497-507.
- Ishii, M. & Hibiki, T. 2006 *Thermo-fluid dynamics of two-phase flow*, Springer.
- Ishii, M. & Zuber, N. 1979 Drag coefficient and relative velocity in bubbly, droplet and particulate flows. *AICHE J.* **25**(5), 843-855.
- Julshamn, J.A. 2006 Hydraulic jumps in horizontal two-phase pipe flow. *PhD Thesis*, Telemark University College, Norway.
- Jeffreys, H. 1926 On the formation of water waves by wind. *Proc. R. Soc. A* **107**, 189-201
- Karabelas, A.J. 1978 Droplet size spectra generated in turbulent pipe flow of dilute liquid/liquid dispersions. *AICHE J.* **24**(2), 170-180.
- Kawaiji, M., Anoda, Y., & Kakamura, H. 1987 Phase and velocity distributions and holdup in high pressure steam/water stratified flow in large diameter horizontal pipe. *Int. J. Multiphase Flow*, **13**, 145-159.
- Khor, S.H. 1998 Three phase liquid-liquid-gas stratified flow in pipelines. *PhD Thesis*, Imperial College, UK.
- Kim, H.J., Lee, S.C. & Bankoff, S.G. 1985 Heat transfer and interfacial drag in counter-current steam-water stratified flow. *Int. J. Multiphase Flow*, **11**, 593-606.
- Kolev, N. 2002 *Multiphase Flow Dynamics*. Springer.
- Kolmogorov, A.N. 1949 On the disintegration of drops in turbulent flow. *Dokl. Akad. Nauk. USSR*, **66**, 825-828.
- Krieger, I.M. & Dougherty, T.J. 1959 A mechanism for non-Newtonian flow in suspensions of rigid spheres. *Trans. Soc. Rheol.* **3**, 137-152.
- Landman, M.J. Non-unique holdup and pressure drop in two-phase stratified inclined pipe flow. *Int. J. Multiphase Flow*, **17**(3), 377-394.
- Landau, L.D. & Lifshitz, E.M. 1987 *Course in Theoretical Physics Volume 6, Fluid Mechanics*. Pergamon Press.
- Langsholt, M., Pettersen, B. & Andersson, P. 2002 Pipe inclination effects on three-phase slug flow characteristics. IFE/KR/F-2002/064.
- Langsholt, M. & Holm, H. 2007 Liquid accumulation in gas-condensate pipe lines - an experimental study. *13th Int. Conf. Multiphase Production Technology*, Edinburgh, UK.

- Levich, V.G. 1962 *Pysicochemical hydrodynamics*. Prentice-Hall.
- Linehan, J.H. 1968 The interaction of two-dimensional, stratified, turbulent, air-water and steam-water flows. *PhD Thesis, Dept Mech. Engng.*, University of Wisconsin.
- Louaked, M., Hanich, L. & Thompson, C.P. 2003, Well-posedness of incompressible two- and three-phase flow. *IMA J. Appl. Math.*, **68**, 595-620.
- Lockhart, R.W & Martinelli, R.C 1949 Proposed correlation of data for isothermal two-phase, two-component flow in pipes. *Chem. Eng. Prog.* **45**, 39-45.
- Malnes, D. 1982 Slug flow in vertical, horizontal and inclined pipes. *Report IFE/KR/E-83/0002, V. Institute for Energy Technology, Kjeller, Norway.*
- Mandhane, J.M, Gregory, G.A. & Aziz, K. 1974 A flow pattern map for gas liquid flow in horizontal pipes. *Int. J. Multiphase Flow*, **1**, 534-553.
- Manolis, I.G. 1995 High pressure, gas-liquid flow. *PhD Thesis*, Imperial College, London.
- Millikan, C.B. 1939 A critical discussion of turbulent flows in channels and circular pipes. *Proc. Fifth Int. Congress for Appl. Mech.*, 386-392, Wiley.
- Monin, A.S. & Yaglom, A.M. 1973. *Statistical fluid mechanics, mechanics of turbulence*, volumes I and II. MIT Press.
- Mols, B & Oliemans, R.V.A 1998 A turbulent diffusion model for particle dispersion and deposition in horizontal tube flow. *Int. J. Multiphase Flow*, **24**(1), 55-75.
- Mouly, P. 1979 Écoulement stratifiés de gaz naturel et d'huile en conduite pétrolière. Thèse Docteur Ingénieur, Université de Paris VI.
- Nieuwstadt, F.T.M. 1992 Turbulentie. Epsilon Uitgave, Utrecht, The Netherlands.
- Nydal, O.J. 1991 An experimental investigation of slug flow. *PhD Thesis*, University of Oslo, Norway.
- Nydal, O.J., Pintus, S. & Andreassi, P. 1992 Statistical characterization of slug flow in horizontal pipes. *Int. J. Multiphase Flow*, **18**(2), 439-453.
- Omebere-Iyari, N.K., Azzopardi, B.J., Lucas, D., Beyer, M. & Prasser, H-M. 2008 The characteristics of gas-liquid flow in large risers at high pressures. *Int. J. Multiphase Flow*, **34**, 461-476.
- Ooi, Y.S.Y. 2001 Prediction of slug body void fraction. *Link Project Report*, Department of Chemical Engineering, Imperial College, London.
- Oseen, C.W. 1910 Über die Stokesschen Formel und über die verwandte Aufgabe in der Hydrodynamik. *Ark. f. Mat. Astr. og Fys.* **6**(29).
- Pal, R. 1993 Pipeline flow of unstable and surfactant-stabilized emulsions. *AICHE J.* **39**(11), 1754-1764.
- Pal, R. 2000 Viscosity-concentration equation for emulsions of nearly spherical droplets. *J. Colloid Interf. Sci.* **231**, 168-175.
- Pan, L. 1996 High pressure three-phase (gas/liquid/liquid) flow. *PhD Thesis*, Imperial College, UK.
- Park, R.W. 1970 Behaviour of water drops colliding in humid nitrogen. *PhD Thesis* Chem. Eng. Dept., University of Wisconsin-Madison.
- Peregrine, D.H. 1968 Long waves in a uniform channel of arbitrary cross-section. *J. Fluid Mech.* **32**(2), 353-365.

- Powell, R.L. 2008 Experimental techniques for multiphase flows. *Phys. Fluids* **20**, 040605.
- Proudman, I. & Pearson, J.A.R. 1957 Expansions at small Reynolds numbers for the flow past a sphere and a circular cylinder. *J. Fluid Mech.* **2**, 237-262.
- Razzaque, M.M., Afacan, A., Liu, S., Nandakumar, K., Masliyah, J.H. & Sanders, R.S. 2003 Bubble size in coalescence dominate regime of turbulent air-water flow through horizontal pipes. *Int. J. Multiphase Flow*, **29**, 1451-1471.
- Richardson, J.F. & Zaki, W.N. 1954 Sedimentation and Fluidization, part I *Trans. Inst. Chem. Engrs.* **32**, 35-53.
- Rosant, J.M. 1994 Liquid-wall shear stress in stratified liquid/gas flow. *J. Appl. Electrochemistry* **24**, 35-53.
- Russel, T.W.F., Etchells, A.W., Jensen, R.H. & Arruda, P.J. 1974 Pressure drop and holdup in stratified gas-liquid flow. *AIChE J.* **20**(4), 664-669.
- Sevik, M & Park, S.H. 1973 The splitting of drops and bubbles by turbulent fluid flow. *J. Fluid Eng. Trans. ASME* **95**, 54-59.
- Shea, R.H., Eidesmoen, H., Nordsveen, M., Rasmussen, J., Xu, Z.G. & Nossen, J. 2004 Slug frequency prediction method comparisons. Proc. 4th North American Conference on Multiphase Technology, 227-237.
- Shi, H., Holmes, J.A., Durlofsky, L.J., Aziz, K., Diaz, L.R., Alkaya, B., Oddie, G. 2005 Drift-flux modelling of two-phase flow in wellbores. *SPE J.* March 2005, 24-33.
- Shoham, O & Taitel, Y. 1984 Stratified turbulent-turbulent gas-liquid flow in horizontal and inclined pipes. *AIChE J.* **30**, 377-385.
- Simmons, M.J.H. & Azzopardi, B.J. 2001 Drop size distributions in dispersed liquid-liquid pipe flow. *Int. J. Multiphase Flow*, **27**, 843-859.
- Slattery, J.C. 1999 Advanced Transport Phenomena. Cambridge University Press.
- Soleimani, A. 1999 Phase distribution and associated phenomena in oil-water flows in horizontal tubes. *PhD Thesis*, Imperial College, UK.
- Spedding, P.L., Hand, N.P. & Ferguson, M.E.G. 1986 The effect of pipe diameter on prediction of holdup. *Encyclopedia of Fluid Mechanics.*, Supplement 3: Advances in Flow Dynamics, 31-50, Gulf Publishing Group.
- Srichai, S. 1994 High pressure separated two-phase flow. *PhD Thesis*, Imperial College, UK.
- Stickel, J.J. & Powel, R.L. 2005 Fluid mechanics and rheology of dense suspensions *Ann. Rev. Fluid Mech.* **37**, 129-149.
- Taitel, Y., Barnea, D. & Dukler, A.E. 1980, Modelling flow pattern transitions for steady upward gas-liquid flow in vertical tubes. *AIChE J.* **26**(3), 345-354.
- Taitel, Y. & Barnea, D. 1990 Two phase slug flow. *Adv. Heat Transf.* **20**, 83-132.
- Taitel, Y. & Dukler, A.E. 1976 A model for predicting flow transitions in horizontal and near-horizontal gas-liquid flow. *AIChE J.* **22**, 47-55.
- Tennekes, H. & Lumley, J.L. 1972 *A first course in turbulence*. MIT Press.
- Tronconi, E. 1990 Prediction of slug frequency in horizontal two-phase slug flow. *AIChE J.* **36**, 701-709.

- Tsiklauri, G.V., Besfamiliny, P.V. & Baryshev, Y.V. 1979 Experimental study of hydrodynamic processes for wavey water film in a co-current air flow. *Two-phase Momentum, Heat and Mass Transfer* **1**, 357-372, Hemisphere, New York.
- Ullmann, A., Zamir, M, Gat, S. & Brauner, N. 2003 Multi-holdups in co-current stratified flow in inclined tubes. *Int. J. Multiphase Flow*, **29**, 1565-1581.
- Van Hout, R., Shemer, L. & Barnea, D. 2003 Evolution of hydrodynamic and statistical parameters of gas-liquid slug flow along inclined pipes. *Chem. Eng. Sci.* **58**(1), 115-133.
- Vand, V. 1948 *J. Phys. Colloid. Chem.* **52** 217.
- Wallis, G.B. 1969 *One-Dimensional two-phase flow*. McGraw-Hill.
- Weber, M.E. 1981 Drift in intermittent two-phase flow in horizontal pipes. *Can. J. Chem. Eng.* **59**, 398-399.
- Whitham, G.B. 1974 *Linear and nonlinear waves*. Wiley-Interscience.
- Woods, B.D.& Hanratty, T.J. 1999 Influence of Froude number on physical processes determining frequency of slugging in horizontal gas-liquid flows. *Int. J. Multiphase Flow*, **25**, 1195-1223.
- Woods, B.D., Fan, Z. & Hanratty, T.J. 2006 Frequency and development of slugs in horizontal pipes at large liquid flows. *Int. J. Multiphase Flow*, **32**, 902-925.
- Wu, H.L., Pots, B.F.M., Hollenberg, J.F. & Meerhoff, R. 1987 Flow pattern transitions in two-phase gas/condensate flow at high pressure in an 8-inch horizontal pipe. *3rd Int. Conf. Multiphase Flow*, The Hague, The Netherlands.
- Xiao, J. 1990 A comprehensive mechanistic model for two-phase flow in pipelines. *MSc Thesis*, University of Tulsa, USA.
- Zabaras, G.J. 2000 Prediction of slug frequency for gas/liquid flows. *SPE J.* **5**(3), 252-258.
- Zuber, N. & Findlay, J.A. 1965 Average volumetric concentration in a two-phase system. *J. Heat Transfer Trans. ASME* **87**, 453-458.
- Zukoski, E.E. 1966 Influence of viscosity, surface tension and inclination angle on motion of long bubbles in closed tubes. *J. Fluid Mech.* **25**, 821-837.

# Index

- Annular flow, 30
- Area averaged two-fluid model, 52
- Artificial diffusion, 146
- Averaging, 38
  - Ensemble, 39
  - Eulerian average, 38
  - Lagrangian average, 38
  - Time average, 38
  - Volume average, 38
- Bernoulli effect, 150
- Bernoulli equation, 10, 114, 134
- Biberg model, 85
- Blasius friction factor, 26
- Bond number, 28
- Boussinesq closure hypothesis, 19, 20
- Capillary number, 28
- Channel flow
  - Laminar, 13
  - Turbulent , 20
- Characteristics, 140
- Chezy coefficient, 26
- Churn flow, 152
- Closure problem, 18, 52
- Closure relations, 58
- Coalescence, 103
- Colebrook friction factor, 26, 79
- Conductivity measurments, 40
- Conservation equation, 8
  - Energy, 8
  - Mass, 8
  - Momentum, 8
- Conservation equations, 6
- Conservation principles, 8
- Control volume method, 66
- Convective derivative, 9
- Core-annular flow, 38
- Correlations, 113
  - Gas entrainment, 122
- Couette flow, 85
- Curvature, 12
- Darcy friction factor, 25
- Diffusion coeffcient
  - Fluid diffusivity, 109
  - Particle diffusivity, 109
- Diffusion equation, 65, 108
- Diffusion stress, 64, 108
- Diffusion velocity, 64, 108
- Dilute suspension, 90
- Dimensional analysis, 24, 28
- Dirac's delta function, 47
- Dispersed bubble flow, 30
- Dispersed flow, 62
- Dispersion relation, 136, 138
- Dissipation rate of turbulent energy, 17
- Distribution coefficient, 114
- Distribution parameter, 61, 109
- Drag coefficient, 93, 94
  - Oseen's approximation, 93
- Drag force, 92
- Drift coefficient, 114
- Drift velocity, 61, 62, 65, 108, 115
- Drift-flux model, 60
  - Distribution parameter, 61
  - Drift velocity, 62
  - Slip law, 60
- Drop size, 104
  - Droplet breakup, 104
- Dynamic pressure force, 105
- Dynamic similarity, 25
- Eötvös number, 28
- Eddy viscosity, 19
- Effective medium theory, 102
- Effective viscosity, 96
  - Einstein's approximation, 100
- Emulsions, 100
- Elongated bubble, 113
- Elongated bubble flow, 30
- Emulsion viscosity, 37, 100
- Emulsions, 35
  - Stable and unstable emulsions, 35
  - Stable emulsions, 101
  - Unstable emulsions, 102
- Energy conservation, 8
- Ensemble avaraging, 18, 45
- Ensemble averaging, 39
- Entrance length, 152
- Ergodic hypothesis, 40
- Ergodic process, 40
- Eulerian average, 38
- Extensive property, 8
- Fanning friction factor, 25
- Favre average, 50
- Flow regime, 28, 29
  - Flow regime map, 31
- Flow regime map, 30, 149
- Flow regime transition, inclined flow
  - Slug to dispersed bubble flow, 150
  - Stratified smooth to stratified wavy flow, 150
  - Stratified to annular flow, 150
  - Stratified to slug flow, 150

Flow regime transition, vertical flow  
     Dispersed bubble to slug flow, 152  
     Slug to churn flow, 152  
 Flux, 61  
 Friction factor, 15, 23, 24, 79  
     Blasius friction factor, 26  
     Chezy coefficient, 26  
     Colebrook friction factor, 26  
     Darcy friction factor, 15, 25  
     Fanning friction factor, 25  
     Haaland friction factor, 26  
     Interfacial friction factor, 80  
     Liquid wall friction factor, 80  
 Friction velocity, 20  
 Froude number, 142  
  
 Gamma densitometer, 41  
 Gas entrainment, 30, 121  
 Gas entrainment rate, 122  
 Gas-oil ratio, 33  
 Gravitational Settling, 108  
  
 Haaland friction factor, 26, 79  
 Hinze-Levich model, 106  
 Hold-up, 31  
     Hold-up equation, 129  
 Holdup  
     Holdup equation, 73, 78  
     Holdup equation, hydraulic model, 75  
 Hydraulic diameter, 54, 79  
 Hydraulic flow model, 15, 52, 74  
 Hydraulic jump, 122  
 Hydraulic model  
     Single phase, laminar flow, 15  
     Stratified, laminar flow, 74  
  
 Ill posedness of two-fluid equations, 146  
 Ill-posed problem, 139  
 In-situ  
     Hold-up, 31  
     Slip velocity, 160  
     Velocity, 31, 160  
 Incompressible fluid, 10  
 Intensive property, 6  
 Interfacial shear stress, 74  
 Interfacial area concentration, 106  
 Interfacial boundary condition, 10  
 Interfacial friction factor, 80  
 Interfacial mass transfer, 49  
 Interfacial pressure, 72  
 Interfacial roughness, 81  
 Interfacial shear  
     Stratified flow in a pipe, 76  
 Interfacial shear stress, 56, 80  
 Interfacial shear, continuity, 72  
  
 Interfacial waves  
     Inviscid flow, 133  
 Internal energy, 8  
 Inversion water cut, 110  
 Inviscid flow, 133  
 Irrotational flow, 133  
  
 Jump conditions, 11, 50  
  
 Kolmogorov micro scales, 17, 105  
 Kolmogorov's relation, 17  
 Krieger-Dougherty emulsion viscosity model, 103  
  
 Lagrangian average, 38  
 Laminar flow  
     Hydraulic model, 74  
     Single phase flow between plates, 13  
     Single phase flow in a pipe, 26  
     Stratified flow between plates, 71  
     Stratified flow in pipe, 75  
 Laser-Doppler velocimetry, 40  
 Linear stability, 136, 143  
 Liquid fraction, 33  
 Liquid holdup, 31  
     In-situ holdup, 31  
 Liquid-liquid flow, 33  
 Lockhart-Martinelli parameter, 82, 89  
 Logarithmic friction law, 23  
  
 Macro structure of turbulent flow, 16  
 Martinelli parameter, 150, 160  
 Mass conservation, 7  
 Material  
     Volume, 6  
 Material  
     Derivative, 9  
 Maximum drop size, 106  
 Maximum packing fraction, 101, 102  
 Measuring techniques  
     Area measurements, 41  
     Line measurements, 41  
     Point measurements, 40  
     Tomography, 41  
     Volume measurements, 42  
 Micro structure of turbulent flow, 17  
 Mixing length, 85  
 Mixture density, 63, 107  
 Mixture velocity, 63, 107  
 Mixture viscosity, 96  
 Momentum conservation, 8  
 Momentum source  
     Interfacial, 49  
     Mass transfer, 49  
 Moody chart, 25

Navier Stokes equation, 10  
 Newtonian fluid  
     Derivative, 9  
 No-slip condition, 12  
  
 Ohnesorge number, 28  
  
 Particle Image Velocimetry, 40  
 Particle size distribution  
     Log-normal distribution, 107  
     Rosin-Rammler distribution, 107  
 Particle-particle interactions, 94  
 Phase function, 46  
 Prandtl mixing length, 19, 20, 85  
 Prandtl number, 16  
 Profile coefficient, 27, 53  
 Pseudo fluid, 95, 102, 106  
  
 Rate of work done, 99  
 Relative velocity, 64  
 Resonance frequency, 106  
 Reynolds equations, 17  
 Reynolds stress, 19, 57  
 Reynolds transport theorem, 6  
     Generalised form, 10  
 Roll waves, 147  
 Rosin-Rammler distribution, 107  
  
 Saffman lift force, 61  
 Sauter mean diameter, 104  
 Sedimentation velocity, 93  
 Settling velocity, 93  
 Single phase flow  
     Laminar flow, 13  
     Turbulent flow, 16  
 Slip, 31, 117  
 Slip law, 60  
 Slip ratio, 31  
 Slip velocity, 63  
 Slug flow, 30, 112  
     Bubble front velocity, 113  
     Bubble region, 113  
     Distribution coefficient, 116  
     Drift coefficient, 114, 116  
     Drift velocity, 114  
     Film region, 113  
     Slug body holdup, 123  
     Slug unit, 113  
 Slug frequency, 125, 160  
 Slug front, 118  
     Gas entrainment, 121  
     Pressure jump, 118  
 Slug statistics, 124  
 Slug unit  
     Average density, 130  
     Average hold-up, 130  
     Pressure drop, 130  
  
 Slug unit model, 127  
 Slugs  
     Developing, 125  
     Slug length, 125, 130  
 Spheroidal particles, 100  
 Stability condition, 137, 138  
 Stable emulsions, 102  
 Stokes drag, 93  
 Stokes flow, 90  
 Straining motion, 97  
 Stratified flow, 55  
     Hydraulic model, 74  
     Laminar flow in pipe, 75  
     Oil-water flow, 109  
     One-dimensional model, 77  
 Stratified flow between plates, 71  
 Streamline, 114  
 Stress tensor, 8  
     Deviatoric part, 9  
 Stress vector, 13, 14  
 Superficial velocity, 30, 72  
     Superficial gas velocity, 30  
     Superficial liquid velocity, 30  
 Surface tension, 12  
 Surfactants, 35  
  
 Terminal velocity, 66, 93  
 Test function, 48  
     Compact support, 48  
 Tomography, 41  
 Turbulence modelling, 19  
 Turbulent diffusion, 16, 19, 85  
 Turbulent flow, 16  
     Closure problem, 18  
     Core region, 22  
     Dissipation rate of turbulent energy, 17  
     Eddies, 16  
     Eddy viscosity, 19  
     Energy cascade, 17  
     Kinetic energy, 17  
     Kolmogorov micro scales, 17  
     Macro structure, 16  
     Micro structure, 17  
     Reynolds stress, 19  
     Turbulent diffusion, 16, 19  
     Turbulent stress tensor, 19  
     Viscous sub-layer, 21  
     Wall region, 21  
 Two-fluid model, 45, 49  
  
 Unit slug model, 127  
 Unstable emulsions, 101  
  
 Velocity potential, 134  
 Viscous sub-layer, 21

Volume fraction, 51  
Von Karman constant, 21  
Vorticity, 133

Wall shear stress, 14, 56, 74, 79  
Wall variables, 21  
Watercut, 35  
Weber number, 28  
Weighted mean  
Phase weighted mean, 50  
Well-posed equations, 138  
Work integral, 100